OU-RM-DOE-17-F1

Three-dimensional Modeling of Fracture Clusters in Geothermal Reservoirs

DE-PS36-08GO1896

Submitted by:

Ahmad Ghassemi

McCasland Chair Professor
Mewbourne School of Petroleum & Geological Engineering
The University of Oklahoma
Sarkeys Energy Center, Office 1314
100 East Boyd Street
Norman, OK
Tel. (405)-325-4347

A. Acknowledgements

The PI (A. Ghassemi) has benefited from the contributions of many individuals in completing this project, including graduate students, and post-doctoral fellows whose efforts are reflected in the publications listed at the end of this report and others that are forthcoming. Drs. Zhennan Zhang, and Kai Huang, and Kyoung Min as well as Naresh Sesetty worked on various aspects of the project for their post-doctoral work, and Ph.D. and M.S. theses.

B. Disclaimer

This information was prepared as an account of work sponsored by an agency of the U.S. Government (U.S. Department of Energy Office of Energy Efficiency and Renewable Energy under Award Number DE-PS36-08GO1896).

C. Introduction

Effective development of enhanced geothermal systems can significantly benefit from improved modeling of hydraulic fracturing. In geothermal reservoirs, where the temperature can reach or exceed 350 ^{o}C, thermal and poro-mechanical processes play an important role in fracture initiation and propagation. Models have been developed to study the fundamental mechanisms of fracture propagation in hot poroelastic rocks and fracture coalescence, particularly in the near wellbore region of geothermal reservoirs (e.g., Ghassemi and Zhang, 2005; Ghassemi and Zhang, 2004). However, a hydraulic fracture simulation model capable of addressing the propagation of fractures in tensile or shear in rock is not available and must be developed (MIT-led Report). Moreover, poro-thermo-mechanical analysis of injection into fractures shows that high stress zones develop in the vicinity of the main fracture, indicating potential for multiple initiation and propagation events (Ghassemi et al., 2007). Therefore, hydraulic fracture models need to include poro-thermoelastic effects on fracture initiation in rock penetrated by the main fracture. On the other hand, reservoir rock and in-situ stress heterogeneity often result in fracture propagation involving tensile, shear and tearing modes, and as shown in Healy and Jones (2006), 2-D numerical modeling and simple analytical approaches (Germanovich et al. 1997) are insufficient to predict the fracture and a 3-D numerical analysis is required. Therefore, the objective of this work was to develop 3-D numerical models for simulating models that can capture modes I, II, and III (tensile, shear, and out-of-plane) propagation in geothermal reservoir stimulation using damage mechanics and the novel approach of virtual multi-dimensional internal bond (VMIB).

The proposed research addresses the major technical issue of accurately predicting stimulation outcome, a technology barrier addressed in the MIT-led report (lack of tools to predict propagation of fracture cluster in mixed modes). Phase 1 of the work consisted of elastic model development. Starting with 2D work and then developing 3D VMIB and damage models implemented into the FEM codes with hydraulic propagation routines. This phase included simulations and comparison with published results and laboratory experiments. Phase 2 of the work includes addition of thermoelastic material models in FEM codes and addition of hydraulic fracture routine with joint elements and partitioning algorithms. Phase 3 was the testing and application phase and verification of the poro- and thermoelastic effects on fracturing; assessing the accuracy of the method and making improvements. Finally, we applied the model to Lab-scale stimulation experiments.

In this project hydraulic fracturing of hot subsurface rock mass is numerically modeled by extending the virtual multiple internal bond theory and implementing it in a 3D finite element code. In addition, we developed numerical model based on the non-local damage model. Detailed of these numerical strategies are discussed next.

CHAPTER 1: VIRTUAL MULTIDIMENSIONAL INTERNAL BONDS

Simulation of 3D fracture propagation is complex because it often simultaneously involves all three fracture modes (I, II, III) over a contour. This is in contrast to 2D case where the zone of interest is only a point, i.e., the fracture tips. Currently, a number of techniques are used to simulate fractures and their growth in hydraulic stimulation process, including boundary element method (Sesetty and Ghassemi, 2015; Kumar and Ghassemi, 2016; Dobroskok et al., 2005; Koshelev and Ghassemi 2003 and 2004; Vandamme and Curran, 1989; Curran and Carvalho, 1987) or the finite-element method (FEM). The BEM such as the displacement discontinuity technique provides efficient and accurate results when

modeling 2D fracture propagation in elastic media. A major challenge in modeling 3D fracture propagation using the linear elastic FEM or BEM is the need of re-meshing as the fracture propagates. To address the problem of re-meshing, nodal enrichment methods (Belytschko et al., 1999; Moes et al., 1999) are mostly used in 2D. An alternative includes the Virtual Internal Bond (VIB) method (Gao and Klein, 1998) which was proven to be effective in 2D simulations. In VIB method, the solid is considered to consist of micro material particles at micro scale and these material particles are bonded with internal virtual bond. The cohesive law contains the information of fracture so that external fracture criterion is not needed. (Zhang and Ge, 2005a; Zhang and Ge 2005b]; Zhang and Ge, 2006) modified the VIB method and introduced the shear effect between material particles so that the extended VIB model, defined as Virtual Multidimensional Internal Bond (VMIB), is applicable to material with different Poisson's ratio. In VIB-based constitutive model, the micro mechanism of Mode II and III is the same in that both the two fracture result from the bond ruptures. Via bond evolution function, the fracture criterion is actually implicitly embedded into the constitutive relation. Recently, this method has been extended to simulation of pre-existing fractures (Min et al., 2010; Zhang and Ghassemi, 2010). In this work, the VMIB is further developed, and is used to simulate the 3D propagation and interaction of multiple fractures in rock subjected to compressive stresses and fluid pressure, including pre-existing natural fracture. To represent the pre-existing fracture, the 3D element partition method (Huang and Zhang, 2010) is used to avoid re-meshing.

The VMIB model considers that the material is composited by the randomized mass particles connected by virtual bonds with both normal and shear stiffness. According to the concept of VMIB, the macro behavior of material is determined by the bond evolution in micro structure. In other words, a macro constitutive relation derived from the cohesive law between material particles represents the macro nonlinear behaviors.

1.1 Hyperelastic Theory

In the continuum mechanics, a change in the configuration of a continuum body results in displacement. The displacement is composed by rigid-body displacement and deformation. The material points in the undeformed configuration are described by the Lagrangian (Material) coordinates $X = (X_1, X_2, X_3)$. The corresponding material points in the deformed configuration is described by Eulerian (spatial) coordinates $x = (x_1, x_2, x_3)$. The deformation gradient is given by:

$$F_{iI} = \frac{\partial x_i}{\partial X_I} \tag{1}$$

From deformation gradient, the Green-Lagrange strain tensor is given by:

$$E_{IJ} = \frac{1}{2}(F_{iI}F_{iJ} - \delta_{IJ}) \tag{2}$$

where δ_{IJ} is the Kronecker delta. In the hyperelastic theory (Marsden and Hughes, 1983; Ogden, 1984), Φ is the strain energy density function. The Piola-Kitchhoff stress tensor is:

$$S_{IJ} = \frac{\partial \Phi}{\partial E_{IJ}} \tag{3}$$

The material elastic tensor is:

$$C_{IJKL} = \frac{\partial S_{IJ}}{\partial E_{KL}} = \frac{\partial^2 \Phi}{\partial E_{IJ} \partial E_{KL}} \qquad (4)$$

1.2 Material Constitutive Model of VMIB

The constitutive representation of a material varies with different scales, These are continuum based for materials at macro scale and are particle based at the micro scale, shown as Figure 1. The macroscopic mechanical behavior is determined by the material constitutive representation at micro scale. In the VMIB method, the solid is considered as randomized virtual material particles at the micro scale shown in Figure 1(b). Virtual internal bonds between the material particles have both normal and shear stiffness as shown in Figure 1(c). The bond constrains both normal displacement and rotation. The interactions of the bonds govern the mechanical response of the material according to the relative displacements of paired particles. These particles and bonds are not necessary to be realistic physical particles such as atom or molecule. In this simplifying of microscopic structure, VMIB avoids the complicated and massive atom simulation.

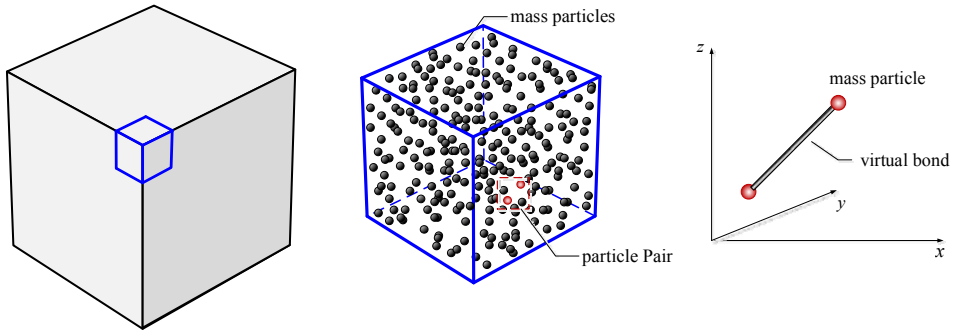

Figure 1. Material constitution at (a) macro scale and (b) micro scale consisting of randomized material particles that are bonded with (c) virtual bonds.

1.3 Relative Displacements and Energy Potentials of Particle Pairs

From micro structure of material, derivation of the macroscopic constitution starts with the relative position and displacements of each virtual particle pair. The relative displacements can be decomposed into bond stretch l and bond rotation with angle β . Therefore, the virtual bonds between particles are classified as normal bonds and shear bonds due to the different connecting and constraining mechanisms. Normal bonds govern the normal relative displacement and interacting effects of a particle pair. On the other hand, shear bonds restrict the relative rotations. In the small deformation cases, according to Cauchy-Born rule, the stretch of normal bond in ξ direction is

$$l = l_0 \xi_i \varepsilon_{ij} \xi_j \qquad (5)$$

where l_0 is the original bond length, $\xi = (\sin\theta\cos\phi, \sin\theta\sin\phi, \cos\theta)$ is the unit orientation vector of bond in sphere coordinate system and ε_{ij} is the strain tensor. The rotation angles of bond towards three coordinate axes are respectively:

$$\begin{cases}\beta_1 = \xi_i \varepsilon_{ij} \eta'_j \\ \beta_2 = \xi_i \varepsilon_{ij} \eta''_j \\ \beta_3 = \xi_i \varepsilon_{ij} \eta'''_j \end{cases} \tag{6}$$

where β_1, β_2 and β_3 are the rotation angle towards axis $\mathbf{x}_1$, $\mathbf{x}_2$ and $\mathbf{x}_3$ respectively, $\boldsymbol{\eta}'$, $\boldsymbol{\eta}''$ and $\boldsymbol{\eta}'''$ is the unit vectors perpendicular to the direction indicated by $\boldsymbol{\xi}$ of normal bond. Additionally, $\boldsymbol{\eta}'$, $\boldsymbol{\eta}''$ and $\boldsymbol{\eta}'''$ have to be in same planes determined with their correspondent coordinate axis vectors and $\boldsymbol{\xi}$ respectively. Their mathematical expressions are

$$\begin{aligned}\boldsymbol{\eta}' &= \boldsymbol{\xi} \times (\mathbf{x}_1 \times \boldsymbol{\xi}) \\ &= \left(\sin^2\theta \sin^2\phi + \cos^2\theta, -\sin^2\theta \cos\phi \sin\phi, -\sin\theta \cos\phi \cos\theta\right)\end{aligned} \tag{7}$$

$$\begin{aligned}\boldsymbol{\eta}'' &= \boldsymbol{\xi} \times (\mathbf{x}_2 \times \boldsymbol{\xi}) \\ &= \left(-\sin^2\theta \cos\phi \sin\phi, \cos^2\theta + \sin^2\theta \cos^2\phi, -\sin\theta \sin\phi \cos\theta\right)\end{aligned} \tag{8}$$

$$\begin{aligned}\boldsymbol{\eta}''' &= \boldsymbol{\xi} \times (\mathbf{x}_3 \times \boldsymbol{\xi}) \\ &= \left(-\sin\theta \cos\phi \cos\theta, -\sin\theta \sin\phi \cos\theta, \sin^2\theta\right)\end{aligned} \tag{9}$$

According to two decomposed displacement l and β, the total energy potential U is given as:

$$U = U_l + U_\beta \tag{10}$$

where U_l, U_β are the stretch energy potential and rotation potential respectively. U_l and U_β can be written as:

$$U_l = \frac{1}{2} k l^2 = \frac{1}{2} k \left(l_0 \varepsilon_{ij} \xi_i \xi_j\right)^2 \tag{11}$$

$$\begin{aligned}U_\beta &= U_{\beta_1} + U_{\beta_2} + U_{\beta_3} \\ &= \frac{1}{2} r \beta_1^2 + \frac{1}{2} r \beta_2^2 + \frac{1}{2} r \beta_2^2 \\ &= \frac{1}{2}\left(\varepsilon_{ij} \xi_i \eta'_j\right)^2 + \frac{1}{2}\left(\varepsilon_{ij} \xi_i \eta''_j\right)^2 + \frac{1}{2}\left(\varepsilon_{ij} \xi_i \eta'''_j\right)^2\end{aligned} \tag{12}$$

where k is normal bond stiffness, r is the shear bond stiffness coefficient.

1.3.1 Fourth-order elastic tensor

The mass particles randomly distribute in the infinitesimal of material according to the assumption above. Therefore, the bonds between the particles are also have randomized distributions and orientations, but following a given spatial distribution density $D(\phi, \theta)$ in the sphere coordinate system. Since the assumption of small deformation cases, E_{IJ} and S_{IJ} reduce to the strain $\boldsymbol{\varepsilon}_{ij}$ and stress σ_{ij} respectively of linear elasticity (Gao and Klein, 1998). By integrating the total energy potential and assuming the initial length of normal bond is identical, the energy density is written as

$$\Phi = \frac{W_l + W_\beta}{V} \quad (13)$$

where V is volume of infinitesimal, W_l is

$$W_l = \int_0^{2\pi}\int_0^{\pi} U_l D(\theta,\phi)\sin(\theta)d\theta d\phi \quad (14)$$

, and W_β is

$$\begin{aligned} W_\beta = &\int_0^{2\pi}\int_0^{\pi} U_{\beta_1} D(\theta,\phi)\sin(\theta)d\theta d\phi + \int_0^{2\pi}\int_0^{\pi} U_{\beta_2} D(\theta,\phi)\sin(\theta)d\theta d\phi \\ &+ \int_0^{2\pi}\int_0^{\pi} U_{\beta_3} D(\theta,\phi)\sin(\theta)d\theta d\phi \end{aligned} \quad (15)$$

According to Eqs. (3) and (4), by equaling the energy potential stored in the virtual bonds with the strain energy potential stored on the continuum level in the same volume due to an imposed deformation, the stress tensor is given as:

$$\begin{aligned} \sigma_{ij} = \frac{\partial\Phi}{\partial\varepsilon_{ij}} = &\frac{1}{V}\int_0^{2\pi}\int_0^{\pi} kl_0\left(\xi_m\varepsilon_{mn}\xi_n\right)\xi_i\xi_j D(\theta,\phi)\sin(\theta)d\theta d\phi \\ &+ \frac{1}{V}\int_0^{2\pi}\int_0^{\pi} r\beta_1\xi_i\eta_j' D(\theta,\phi)\sin(\theta)d\theta d\phi \\ &+ \frac{1}{V}\int_0^{2\pi}\int_0^{\pi} r\beta_2\xi_i\eta_j'' D(\theta,\phi)\sin(\theta)d\theta d\phi \\ &+ \frac{1}{V}\int_0^{2\pi}\int_0^{\pi} r\beta_3\xi_i\eta_j''' D(\theta,\phi)\sin(\theta)d\theta d\phi \end{aligned} \quad (16)$$

The fourth-order elastic tensor is written as:

$$\begin{aligned} C_{ijmn} = \frac{\partial^2\Phi}{\partial\varepsilon_{ij}\partial\varepsilon_{mn}} = &\frac{1}{V}\int_0^{2\pi}\int_0^{\pi} kl_0^2\xi_i\xi_j\xi_m\xi_n D(\theta,\phi)\sin(\theta)d\theta d\phi \\ &+ \frac{1}{V}\int_0^{2\pi}\int_0^{\pi} r\xi_i\eta_j'\xi_m\eta_n' D(\theta,\phi)\sin(\theta)d\theta d\phi \\ &+ \frac{1}{V}\int_0^{2\pi}\int_0^{\pi} r\xi_i\eta_j''\xi_m\eta_n'' D(\theta,\phi)\sin(\theta)d\theta d\phi \\ &+ \frac{1}{V}\int_0^{2\pi}\int_0^{\pi} r\xi_i\eta_j'''\xi_m\eta_n''' D(\theta,\phi)\sin(\theta)d\theta d\phi \end{aligned} \quad (17)$$

For an isotropic material, the bond distribution density in every direction is uniform, i.e. $D(\theta,\phi) = 1$.

In finite element method (FEM), the strain-stress relationship is expressed as:

$$\boldsymbol{\sigma} = \boldsymbol{\Omega}\cdot\boldsymbol{\varepsilon} \quad (18)$$

where $\boldsymbol{\sigma}$ is the stress vector, i.e. $\boldsymbol{\sigma} = \left[\sigma_{11},\sigma_{22},\sigma_{33},\sigma_{12},\sigma_{13},\sigma_{23}\right]^T$, $\boldsymbol{\varepsilon}$ is the strain vector, i.e. $\boldsymbol{\varepsilon} = \left[\varepsilon_{11},\varepsilon_{22},\varepsilon_{33},\varepsilon_{12},\varepsilon_{13},\varepsilon_{23}\right]^T$, and $\boldsymbol{\Omega}$ is the elastic tensor C_{ijmn} written in the elastic matrix form:

$$\mathbf{\Omega}=\begin{bmatrix} C_{1111} & C_{1122} & C_{1133} & \frac{1}{2}(C_{1112}+C_{1121}) & \frac{1}{2}(C_{1132}+C_{1123}) & \frac{1}{2}(C_{1113}+C_{1131}) \\ C_{2211} & C_{2222} & C_{2233} & \frac{1}{2}(C_{2212}+C_{2221}) & \frac{1}{2}(C_{2232}+C_{2223}) & \frac{1}{2}(C_{2213}+C_{2231}) \\ C_{3311} & C_{3322} & C_{3333} & \frac{1}{2}(C_{3312}+C_{3321}) & \frac{1}{2}(C_{3332}+C_{3323}) & \frac{1}{2}(C_{3313}+C_{3331}) \\ C_{1211} & C_{1222} & C_{1233} & \frac{1}{2}(C_{1212}+C_{1221}) & \frac{1}{2}(C_{1232}+C_{1223}) & \frac{1}{2}(C_{1213}+C_{1231}) \\ C_{2311} & C_{2322} & C_{2333} & \frac{1}{2}(C_{2312}+C_{2321}) & \frac{1}{2}(C_{2332}+C_{2323}) & \frac{1}{2}(C_{2313}+C_{2331}) \\ C_{1311} & C_{1322} & C_{1333} & \frac{1}{2}(C_{1312}+C_{1321}) & \frac{1}{2}(C_{1332}+C_{1323}) & \frac{1}{2}(C_{1313}+C_{1331}) \end{bmatrix} \tag{19}$$

Integrating Eq. (17) and substituting to Eq. (19) yields

$$\mathbf{\Omega}=\begin{bmatrix} 3kl_0^2+2r & kl_0^2-r & kl_0^2-r & 0 & 0 & 0 \\ & 3kl_0^2+2r & kl_0^2-r & 0 & 0 & 0 \\ & & 3kl_0^2+2r & 0 & 0 & 0 \\ & & & kl_0^2+0.5r & 0 & 0 \\ & \textit{symmetric} & & & kl_0^2+0.5r & 0 \\ & & & & & kl_0^2+0.5r \end{bmatrix} \tag{20}$$

Equaling Eq. (20) with elastic matrix expressed by macroscopic material constants Young's modulus E and Poisson ratio ν, the relationship between microscopic material constants k, r and macroscopic constants can be obtained

$$k=\frac{3EV}{4\pi(1-2\nu)l_0^2} \tag{21}$$

$$r=\frac{3EV(1-4\nu)}{4\pi(1+\nu)(1-2\nu)} \tag{22}$$

On the contrary, the Young's modulus and Poisson ratio can also be expressed using microscopic material constants k, r, which means the macroscopic mechanical behaviors are determined by the micro bond mechanical properties.

1.4 Bond Evolution Mechanisms

In the previous sections, the linear VMIB constitutive relationship was derived. For realistic materials such as rocks, normally, the mechanical response can be classified as linear elastic phase, strengthening phase and strain-softening phases as the deformation increases, shown in Figure 2. In VMIB system, the bond is not broken when simulating the fracture propagating. The nonlinear macro properties of a material such as softening and degradation are expressed by introducing the strength evolution of internal virtual bonds. Thus, by introducing an evolution function $f(\boldsymbol{\varepsilon})$, the nonlinear elastic tensor is given by:

$$\begin{aligned} C_{ijmn}=&\frac{1}{V}\int_0^{2\pi}\int_0^{\pi} f(\boldsymbol{\varepsilon})(kl_0^2\xi_i\xi_j\xi_m\xi_n+r\xi_i\eta'_j\xi_m\eta'_n \\ &+r\xi_i\eta''_j\xi_m\eta''_n+r\xi_i\eta'''_j\xi_m\eta''')D(\theta,\phi)\sin(\theta)d\theta d\phi \end{aligned} \tag{23}$$

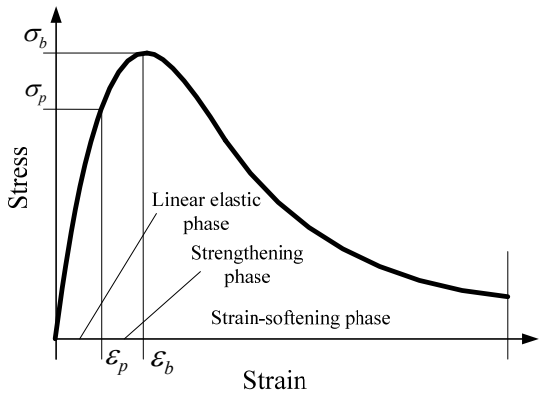

Figure 2. Nonlinear mechanical response of material under uniaxial tensile load.

In this work, the strain based evolution function can be written as following:

$$f(\boldsymbol{\varepsilon}) = \exp\left[-c\left(\frac{\left|\boldsymbol{\xi}^T\boldsymbol{\varepsilon}\boldsymbol{\xi}\right|}{\varepsilon_b}\right)^n\right]\cdot\exp\left[-c\left(\frac{\boldsymbol{\xi}^T\boldsymbol{\varepsilon}^T\boldsymbol{\varepsilon}\boldsymbol{\xi}-\left(\boldsymbol{\xi}^T\boldsymbol{\varepsilon}\boldsymbol{\xi}\right)^2}{\varepsilon_b^2}\right)^n\right] \quad (24)$$

where ε_b is a micro coefficient, $\varepsilon_b = \varepsilon_t$ if $\boldsymbol{\xi}^T\boldsymbol{\varepsilon}\boldsymbol{\xi} \geq 0$ whereas $\varepsilon_b = \varepsilon_c$ if $\boldsymbol{\xi}^T\boldsymbol{\varepsilon}\boldsymbol{\xi} < 0$. ε_t and ε_c indicate the strain at the peak stress in uniaxial tensile and compressive test, respectively. c, n are the shape coefficients which determine the shape of stress-strain curve. The term $\boldsymbol{\xi}^T\boldsymbol{\varepsilon}\boldsymbol{\xi}$ means the relative normal deformation of bond and the term $\boldsymbol{\xi}^T\boldsymbol{\varepsilon}^T\boldsymbol{\varepsilon}\boldsymbol{\xi}-\left(\boldsymbol{\xi}^T\boldsymbol{\varepsilon}\boldsymbol{\xi}\right)^2$ represents the relative shear deformation of bond shown in the Figure 3.

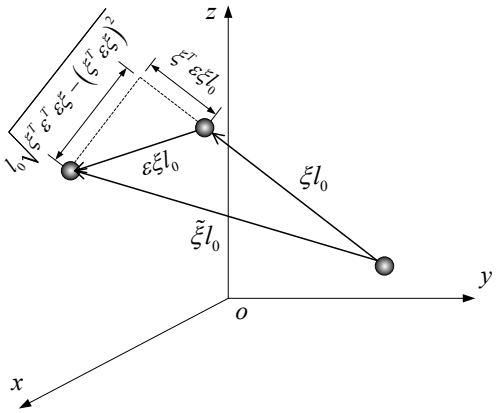

Figure 3. Geometrical relationship among undeformed bond vector $\boldsymbol{\xi} l_0$ and deformed bond vector $\tilde{\boldsymbol{\xi}} l_0$

2. Three Dimensional Representation of Fracture Using Element Partition Method

One of the challenges for 3D fracture simulation is the mechanical representation of pre-existing and newly extended fracture surfaces. Propagating fracture geometry associated with the moving boundary

conditions through fracture growth path makes hydraulic fracturing modeling especially difficult. Additionally, besides the opening fracture, the contact and friction of closed fracture surface are also significant mechanical behaviors for pre-existed fracture subjected to the compressive and shear stresses. Several special treatments for fracture surface have been used in the fracture modeling in the framework of finite element method. Remeshing and mesh refining for the newly extended fracture surface and tip are common techniques, which have great advantages on the computational accuracy and efficiency on the linear equation system solving. However, the remeshing and refining scheme implements are difficult to be performed since that it is time consuming and mathematically challenging especially for 3D problems with complex domain and fracture geometry. Extended finite element method (XFEM) (Belytschko and Black, 1999; Moes et al., 1999) based on the generalized finite element method and partition of unit method represents the fracture by enriching the solution space with discontinuous function for fracture surface and asymptotic function for the fracture. The XFEM avoids the remeshing problem and captures the stress singularity using the original mesh system, which compensates the inconvenience of traditional FEM. However, the XFEM still has disadvantage that the added degrees of freedom change the original structure of matrix and sparseness, numerical integration for each divided parts of element is time consuming and difficult particularly for the element contains multiple fractures.

Different from the XFEM, taking advantage of simple geometry character of triangle and tetrahedron element, element partitioning method (EPM) (Zhang and Chen, 2008, 2009; Huang and Zhang, 2010) construct triple-node and quad-node contact element that needs no remeshing and mesh refinement during the fracture propagation and uses original mesh configuration during the fracture propagation. Therefore, the greatest advantage of EPM saves computational time and is easier to encode since that EPM introduces no additional degree of freedom and global matrix structure remains the same. However, EPM has a limitation that the elastic deformation of partitioned element is not considered. The error is arising with increase of element size. Comparing the computational cost with the other fracture treatment techniques, EPM is still more desirable since that the simulating domain and element size chosen is relative small. In the functional test, performance of 3D EPM will be tested on representing mechanical behaviors of the closed fracture surface subjected to the compressive and shear stress.

2.1 General Idea of Element Partition Method

(Zhang and Chen, 2008, 2009) developed the two-dimensional element partition method (2D EPM) to represent the mechanical behaviors of fractured element cut through by pre-existing and newly extended fracture. Taking advantages of the simple geometrical characteristic of three-node triangular element, the stiffness matrix for a partitioned element is derived to account for the contact and friction effects between fracture faces. Through 2D EPM, the fracture could be represented by transferring intact element to partitioned element. Since the partitioned element shares the same nodes with intact element, no mesh modification is needed. Based on similar concept, 3D element partition method (3D EPM) is developed by (Huang and Zhang 2010) to describe the opening, contact and friction between the fracture surfaces. The 3D EPM takes advantage of the geometry features of tetrahedron element to construct a four-node contact element. When a fracture cuts through a tetrahedron element, two types of four-node contact element, i.e., Type I and Type II, are formed shown as Figure 4. Tetrahedron element is chosen because of its geometric simplicity. Therefore, only type I and II of the contact element with triangular and quadrilateral fracture sections, respectively, will be generated, which avoids the complexity from more types of partition element to be identified and calculated. The geometry aspects will be discussed in the follow sections.

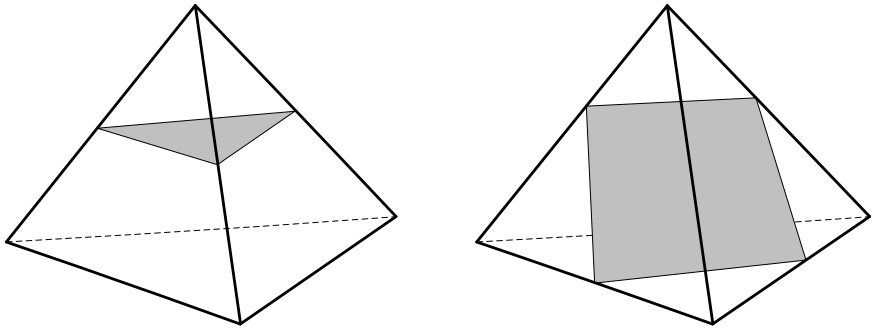

(a) (b)

Figure 4. Partition modes of tetrahedron element: (a) type I: triangular fracture plane; (b) type II: quadrilateral fracture plane.

2.2 Derivation of Stiffness Matrix for 3D EPM

To derive the stiffness matrix of 3D EPM, taking type I partition element shown in Figure 5 for example, a local coordinate system needs to be established. The original point, x' and y' axis of the coordinate system are on the fracture plane. The z' axis is perpendicular to the fracture plane. Therefore, the local coordinates x', y' and z' are defined as:

$$\begin{aligned} x' &= \left[-\frac{n_1 n_3}{\sqrt{1-n_3^2}}, -\frac{n_2 n_3}{\sqrt{1-n_3^2}}, \sqrt{1-n_3^2} \right] \\ y' &= \left[-\frac{n_2}{\sqrt{1-n_3^2}}, -\frac{n_1}{\sqrt{1-n_3^2}}, 0 \right] \\ z' &= \left[n_1, n_2, n_3 \right] \end{aligned} \tag{25}$$

where (n_1, n_2, n_3) is the unit vector indicating the normal direction of the fracture plane calculated by the plane equation $n_1(x-x_0)+n_2(y-y_0)+n_3(z-z_0)=0$. (x_0, y_0, z_0) is the center point on the fracture plane.

The following assumptions are made to derive the stiffness matrix of 3D EPM: (i) all the strain energy is stored in a contact volume with the thickness h and the area A shown in Figure 6 if the fracture surface is subjected to compression and shear stress; (ii) the contact volume is linear elastic; (iii) the displacements of points m', m'' and m''' are equal to the displacements of node M, the displacements of point i, j and k are equal to the displacements of I, J and K respectively; (iv) the contact areas $A_{im'}$, $A_{jm''}$ and $A_{km''}$ shown in Fig. 3 are controlled by contact pairs $i-m'$, $j-m''$ and $k-m'''$ respectively. The displacements of nodes I, J, K and M are denoted as u_x^I, u_y^I, u_z^I, u_x^J, u_y^J, u_z^J, u_x^K, u_y^K, u_z^K, u_x^M, u_y^M and u_z^M respectively.

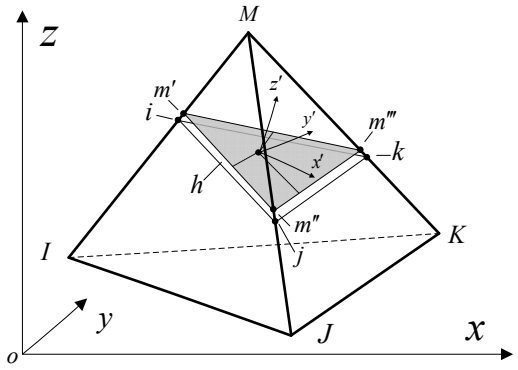

Figure 5. Local coordinate system and node pairs for type I partition element.

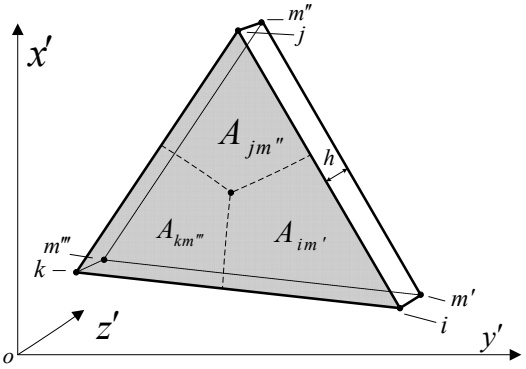

Figure 6. Contact volume and contact areas for each node pairs (type I).

Based on a special case that local and global coordinate systems are parallel to each other, the strain energy stored in the contact volume is:

$$W_{im'} = \frac{1}{2}K_n\varepsilon_n^{im'2}A_{im'}h + \frac{1}{2}K_s\varepsilon_s^{im'2}A_{im'}h = \frac{1}{2}\frac{\left(u_z^M - u_z^I\right)}{h}K_n\frac{\left(u_z^M - u_z^I\right)}{h}A_{im'}h$$
$$+\frac{1}{2}\frac{\left(u_y^M - u_y^I\right)}{h}K_s\frac{\left(u_y^M - u_y^I\right)}{h}A_{im'}h + \frac{1}{2}\frac{\left(u_x^M - u_x^I\right)}{h}K_s\frac{\left(u_x^M - u_x^I\right)}{h}A_{im'}h \quad (26)$$

where K_n, K_s are the shear and the normal stiffness coefficients of the contact element respectively. $\varepsilon_n^{im'}$, $\varepsilon_s^{im'2}$ are the normal strain and shear strain of the contact area $A_{im'}$.

Similarly, the strain energy stored in the contact areas $A_{jm''}$ and $A_{km'''}$ are

$$W_{jm''} = \frac{1}{2}K_n\varepsilon_n^{jm''2}A_{jm''}h + \frac{1}{2}K_s\varepsilon_s^{jm''2}A_{jm''}h = \frac{1}{2}\frac{\left(u_z^M - u_z^J\right)}{h}K_n\frac{\left(u_z^M - u_z^J\right)}{h}A_{jm''}h$$
$$+\frac{1}{2}\frac{\left(u_y^M - u_y^J\right)}{h}K_s\frac{\left(u_y^M - u_y^J\right)}{h}A_{jm''}h + \frac{1}{2}\frac{\left(u_x^M - u_x^J\right)}{h}K_s\frac{\left(u_x^M - u_x^J\right)}{h}A_{jm''}h \quad (27)$$

$$W_{km'''} = \frac{1}{2} K_n \varepsilon_n^{km'''2} A_{km'''} h + \frac{1}{2} K_s \varepsilon_s^{km'''2} A_{km'''} h = \frac{1}{2} \frac{\left(u_z^M - u_z^K\right)}{h} K_n \frac{\left(u_z^M - u_z^K\right)}{h} A_{km'''} h$$
$$+ \frac{1}{2} \frac{\left(u_y^M - u_y^K\right)}{h} K_s \frac{\left(u_y^M - u_y^K\right)}{h} A_{km'''} h + \frac{1}{2} \frac{\left(u_x^M - u_x^K\right)}{h} K_s \frac{\left(u_x^M - u_x^K\right)}{h} A_{km'''} h \quad (28)$$

where $A_{im'} = A_{jm''} = A_{km'''} = \frac{1}{3} A$, A is the area of fracture plane contained in the partition element.

To capture the opening, contact and slippage of the fracture plane in the partition element, two different conditions are considered. The first condition is that the fracture surface is free to open if it is subjected to tensile stress. The second one is that the fracture surface keeps the normal strength and surface friction to support the closure and represent the slippage resistance respectively, when the fracture is subjected to compressive and shear stresses. Therefore, the total strain energy stored in the contact volume is derived as:

$$W = W_{im'} H\left(u_z^M - u_z^I\right) + W_{jm''} H\left(u_z^M - u_z^J\right) + W_{km'''} H\left(u_z^M - u_z^K\right) \quad (29)$$

where $H(x) = \begin{cases} 1 & x \le 0 \\ 0 & x > 0 \end{cases}$. $x \le 0$ indicates the fracture is closed, $x > 0$ indicates the fracture is opened.

Substituting Eqs. (26), (27) and (28) into Eq. (29) yields

$$W = \frac{A_{im'}}{2h}\left[K_n\left(u_z^M - u_z^I\right)^2 + K_s\left(u_y^M - u_y^I\right)^2 + K_s\left(u_x^M - u_x^I\right)^2\right] H\left(u_z^M - u_z^I\right)$$
$$+ \frac{A_{jm''}}{2h}\left[K_n\left(u_z^M - u_z^J\right)^2 + K_s\left(u_y^M - u_y^J\right)^2 + K_s\left(u_x^M - u_x^J\right)^2\right] H\left(u_z^M - u_z^J\right) \quad (30)$$
$$+ \frac{A_{km'''}}{2h}\left[K_n\left(u_z^M - u_z^K\right)^2 + K_s\left(u_y^M - u_y^K\right)^2 + K_s\left(u_x^M - u_x^K\right)^2\right] H\left(u_z^M - u_z^K\right)$$

For sake of simplicity, the displacements of element nodes are written as:

$$u_i = \left[u_1, u_2, u_3, u_4, u_5, u_6, u_7, u_8, u_9, u_{10}, u_{11}, u_{12}\right] \quad (31)$$

$$F_i = \left[F_1, F_2, F_3, F_4, F_5, F_6, F_7, F_8, F_9, F_{10}, F_{11}, F_{12}\right] \quad (32)$$

where $u_1 = u_x^I, u_2 = u_y^I, u_3 = u_z^I, u_4 = u_x^J, u_5 = u_y^J, u_6 = u_z^J, u_7 = u_x^K, u_8 = u_y^K, u_9 = u_z^K, u_{10} = u_x^M, u_{11} = u_y^M,$ $u_{12} = u_z^M$ and $F_1 = F_x^I$, $F_2 = F_y^I$, $F_3 = F_z^I$, $F_4 = F_x^J$, $F_5 = F_y^J$, $F_6 = F_z^J$, $F_7 = F_x^K$, $F_8 = F_y^K$, $F_9 = F_z^K$, $F_{10} = F_x^M$, $F_{11} = F_y^M$, $F_{12} = F_z^M$.

Using the new notation, Eq. (30) can be written as:

$$W = \frac{A_{im'}}{2h}\left[K_n\left(\delta_{12i}u_i - \delta_{3i}u_i\right)^2 + K_s\left(\delta_{11i}u_i - \delta_{2i}u_i\right)^2 + K_s\left(\delta_{10i}u_i - \delta_{1i}u_i\right)^2\right] H\left(u_{12} - u_3\right)$$
$$+ \frac{A_{jm''}}{2h}\left[K_n\left(\delta_{12i}u_i - \delta_{6i}u_i\right)^2 + K_s\left(\delta_{11i}u_i - \delta_{5i}u_i\right)^2 + K_s\left(\delta_{10i}u_i - \delta_{4i}u_i\right)^2\right] H\left(u_{12} - u_6\right) \quad (33)$$
$$+ \frac{A_{km'''}}{2h}\left[K_n\left(\delta_{12i}u_i - \delta_{9i}u_i\right)^2 + K_s\left(\delta_{11i}u_i - \delta_{8i}u_i\right)^2 + K_s\left(\delta_{10i}u_i - \delta_{7i}u_i\right)^2\right] H\left(u_{12} - u_9\right)$$

where δ_{ij} is the Kronecker delta.

The complementary energy Φ is

$$\Phi = W - u_i F_i \quad (34)$$

According to the principle of minimum complementary energy in the elasticity theory, the stiffness matrix of type I partition element is derived as:

$$\begin{aligned} K_{ij}^{(I)} &= \frac{\partial^2 \Phi}{\partial u_i \partial u_j} \\ &= \frac{A_{im'}}{h}\left[K_n(\delta_{12i}-\delta_{3i})(\delta_{12i}-\delta_{3i}) + K_s(\delta_{11i}-\delta_{2i})(\delta_{11i}-\delta_{2i}) + K_s(\delta_{10i}-\delta_{1i})(\delta_{10i}-\delta_{1i})\right]H(u_{12}-u_3) \\ &+ \frac{A_{jm''}}{h}\left[K_n(\delta_{12i}-\delta_{6i})(\delta_{12i}-\delta_{6i}) + K_s(\delta_{11i}-\delta_{5i})(\delta_{11i}-\delta_{5i}) + K_s(\delta_{10i}-\delta_{4i})(\delta_{10i}-\delta_{4i})\right]H(u_{12}-u_6) \\ &+ \frac{A_{km'''}}{h}\left[K_n(\delta_{12i}-\delta_{9i})(\delta_{12i}-\delta_{9i}) + K_s(\delta_{11i}-\delta_{8i})(\delta_{11i}-\delta_{8i}) + K_s(\delta_{10i}-\delta_{7i})(\delta_{10i}-\delta_{7i})\right]H(u_{12}-u_9) \end{aligned} \quad (35)$$

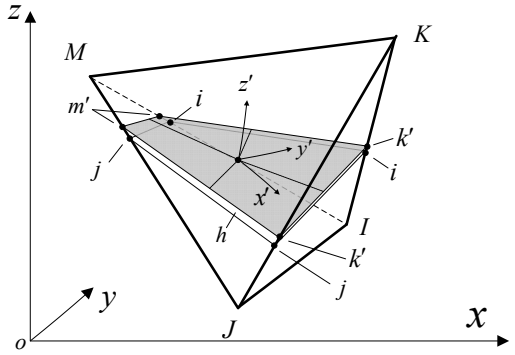

Figure 7. Local coordinate system and node pairs for type II partition element.

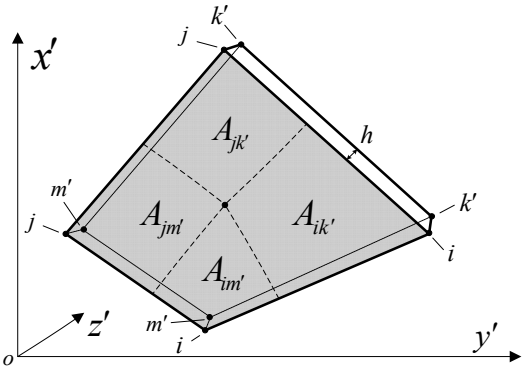

Figure 8. Contact volume and contact areas for each node pairs (type II).

Similarly, Figure (7)shows the local coordinate system and node pairs for type II partition element. The contact node pairs such as $i-m'$, $j-m'$, $i-k'$ and $j-k'$ control their contact areas $A_{im'}$, $A_{jm'}$, $A_{ik'}$ and $A_{jk'}$ respectively shown in Figure (8). The stiffness matrix of type II partition is derived as

$$
\begin{aligned}
K_{ij}^{(II)} &= \frac{\partial^2 \Phi}{\partial u_i \partial u_j} \\
&= \frac{A_{im'}}{h}\left[K_n(\delta_{12i}-\delta_{3i})(\delta_{12i}-\delta_{3i})+K_s(\delta_{11i}-\delta_{2i})(\delta_{11i}-\delta_{2i})+K_s(\delta_{10i}-\delta_{1i})(\delta_{10i}-\delta_{1i})\right]H(u_{12}-u_3) \\
&+ \frac{A_{jm'}}{h}\left[K_n(\delta_{12i}-\delta_{6i})(\delta_{12i}-\delta_{6i})+K_s(\delta_{11i}-\delta_{5i})(\delta_{11i}-\delta_{5i})+K_s(\delta_{10i}-\delta_{4i})(\delta_{10i}-\delta_{4i})\right]H(u_{12}-u_6) \\
&+ \frac{A_{ik'}}{h}\left[K_n(\delta_{9i}-\delta_{3i})(\delta_{9i}-\delta_{3i})+K_s(\delta_{8i}-\delta_{2i})(\delta_{8i}-\delta_{2i})+K_s(\delta_{7i}-\delta_{1i})(\delta_{7i}-\delta_{1i})\right]H(u_9-u_3) \\
&+ \frac{A_{jk'}}{h}\left[K_n(\delta_{9i}-\delta_{6i})(\delta_{9i}-\delta_{6i})+K_s(\delta_{8i}-\delta_{5i})(\delta_{8i}-\delta_{5i})+K_s(\delta_{7i}-\delta_{4i})(\delta_{7i}-\delta_{4i})\right]H(u_9-u_6)
\end{aligned}
\tag{36}
$$

where $A_{im'} = A_{jm'} = A_{ik'} = A_{jk'} = \frac{1}{4}A$.

Based on the stiffness matrixes derived above for special case that the local and global coordinate systems are parallel to each other, the general form of stiffness matrixes can be derived through the coordinate system transformation as follow:

$$K_{ij} = Q^T K' Q \quad (37)$$

where Q is the coordinate transform matrix.

2.3 Functional Test of 3D EPM

To test the performance of 3D EPM on representing the contact and slippage of the fracture surface, the mechanical behavior of a rock block with a cut-through joint is tested in the section. The object geometry and boundary conditions are shown in Figure 9. The number of element and node used in the simulation are 8000 and 3362 respectively. Figure 10(a) shows the tetrahedron elements intersected with the joint. Figure 10(b) gives the geometrical relationship between vertical and horizontal force components. Two different shear stiffness coefficients K_{s1} and K_{s2} are used in the simulations to test the influence of the coefficients on the slippage response of the joint surface. The material parameters are listed in Table 1. The normal stress applied on the top of object is $\sigma_n = 1.0MPa$. The simulation results are shown in Figure 11 indicating the curve of the resultant force and relative displacements on the joint surface and Figure 12 displays the relative slippage between joint surfaces by the deformed mesh configuration.

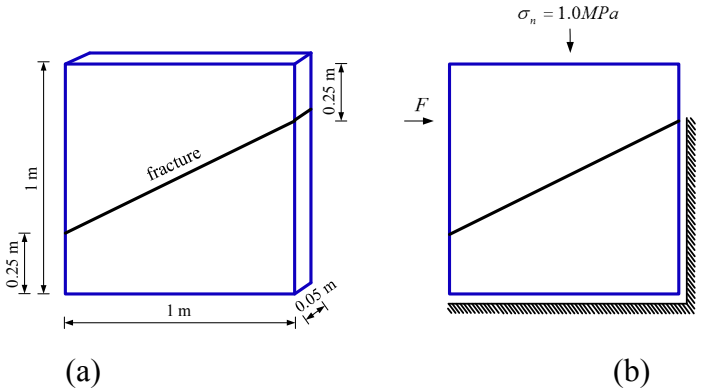

Figure 9. (a) Dimension of simulation object and (b) boundary conditions.

Table 1. Simulation Parameters for 3D EPM Functional Test.

Parameters of intact element:	
Young's modulus, E	10.0 GPa
Poisson's ratio, ν	0.16
Tensile strain strength, ε_t	0.1×10^{-3}
Parameters of 3D EPM:	
Normal stiffness coefficient, K_n / h	10.0 Gpa/m
Shear stiffness coefficient, K_{s1} / h	10^{-5} Gpa/m
Shear stiffness coefficient, K_{s2} / h	10^{-3} Gpa/m
Fracture width, h	1.0 mm

According to the geometrical relationship between vertical and horizontal force components, the lateral force balanced with the normal stress on the top is calculated to be $F = 25kN$. Therefore, the slippage initiation forces for two different shear coefficients are both $F = 25kN$ in Figure 11. Due to different shear stiffness coefficients, the consequent tendency of curves of lateral force F and relative slippage are different in slope. When the shear stiffness coefficient K_{s1} is relatively small, the upper block of simulation object is free to slide on the inclined surface due to the existing of cut-through joint. With the increase of relative displacement between upper and lower blocks, shown in Figure 11, the lateral force F keeps constant and balanced with the normal stress applied on the top indicating that the slipping surface is smooth. For larger shear stiffness coefficient K_{s2}, the lateral force increases linearly with the relative displacement growth shown in Figure 11. In Figure 12, the deformed mesh configuration shows the rigid body displacement of upper and lower blocks. The upper block is gradually climbing up along the inclined surface. Therefore, these results verified the capability of 3D EPM of representing the mechanical behavior of contact and slippage of the fracture surfaces.

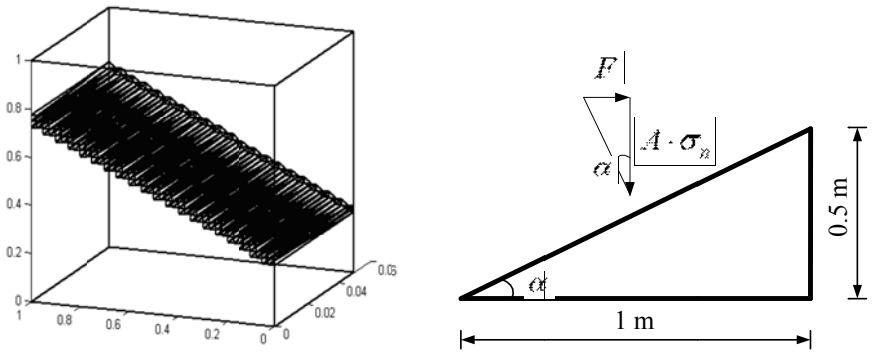

(a) (b)

Figure 10. (a) Tetrahedron elements intersected with fracture; (b) illustration of the geometrical relationship between vertical and horizontal force components.

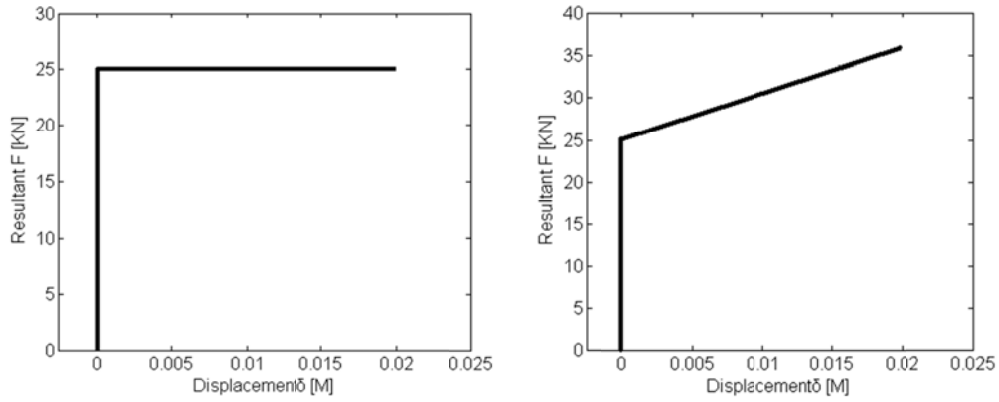

(a) (b)

Figure 11. Simulation results: relationship between the applied displacement and the resultant force F : (a) shear stiffness coefficient $K_{s1} = 10^{-5} MPa$; (b) shear stiffness coefficient $K_{s2} = 10^{-3} MPa$.

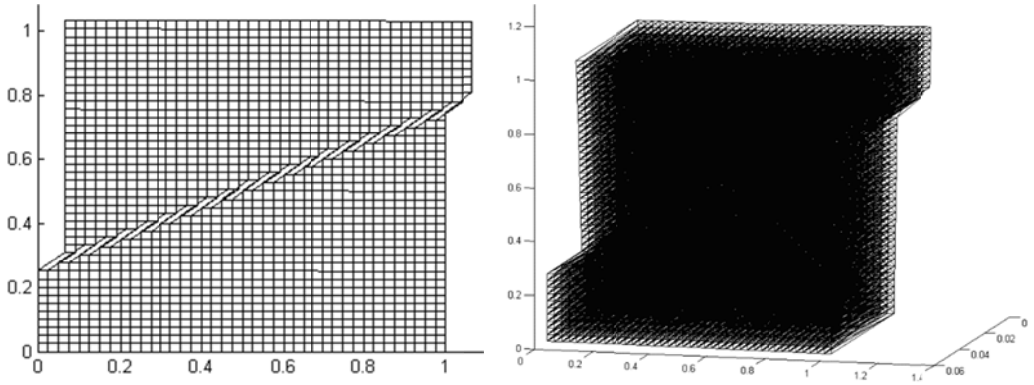

(a) (b)

Figure 12. Simulation results: the rigid body displacement indicating relative slippage between joint surfaces.

3. Poroelastic Model

3.1 Poroelastic Constitutive Relations

Based on the assumption of linear relations between stress σ_{ij} and strain ε_{ij} , pressure p and fluid content ζ respectively, the coupled mechanical equilibrium equations with pore pressure for isotropic porous material could be described by the Biot's theory(Biot, 1935, 1941):

$$\varepsilon_{ij} = \frac{\sigma_{ij}}{2G} - \frac{\nu}{2G(1+\nu)}\sigma_{kk}\delta_{ij} + \frac{\alpha(1-2\nu)}{2G(1+\nu)}p\delta_{ij} \qquad (38)$$

$$\zeta = \frac{\alpha(1-2\nu)}{2G(1+\nu)}\left(\sigma_{kk} + \frac{3}{B}p\right) \qquad (39)$$

where the first equation considers the constitutive response for the solid skeleton, the second equation correspond to the behaviors of porous fluid, ε_{ij} is strain tensor that is positive for tension, σ_{ij} denotes the total stress tensor, p and ζ are the pore pressure and the variation of the fluid content per unit volume of the porous media respectively. G is the shear modulus and ν is the Poisson ratio. α is the Biot's coefficient, B is the Skempton's coefficient. α and B are written as

$$\alpha = 1 - \frac{K}{K_s} \qquad (40)$$

$$B = \frac{3(\nu_u - \nu)}{\alpha(1-2\nu)(1+\nu_u)} \qquad (41)$$

where K is bulk modulus, K_s is the bulk modulus of solid phase, ν_u is the undrained Poisson ratio.

Eq. (38) can be written in terms of stress strain relation,

$$\sigma_{ij} = 2G\varepsilon_{ij} + \frac{2G}{1-2\nu}\varepsilon_{kk}\delta_{ij} - \alpha p\delta_{ij} \qquad (42)$$

Eq. (42) represents the constitutive equation for the linear system, in which we can find the effective stress σ'_{ij} by eliminates the last pore pressure term defined as

$$\sigma'_{ij} = 2G\varepsilon_{ij} + \frac{2G}{1-2\nu}\varepsilon_{kk}\delta_{ij} \qquad (43)$$

Effective stress σ'_{ij} physically means the resultant stress applied on the rock skeleton. It is the exact stress that the rock skeleton supports.

3.1.1 Balance law

Two equilibrium considerations compose the conservation law for poroelastic material. Firstly, the static equilibrium leads to stress balance equation or equilibrium equation written as

$$\sigma_{ij,j} = -F_i \qquad (44)$$

where F_i is the body force per unit volume. Usually the body force is assumed to be ignored if the volume or dimension of objective of interest is small. Second one is the continuity equation for the fluid phase considering the mass conservation:

$$\frac{\partial \zeta}{\partial t} + q_{i,i} = \gamma \qquad (45)$$

where γ is the density of injection source.

3.1.2 Field equations

The equations in the previous sections explain the physical meaning of porous material and fluid. However, only field equations lead to useful solution that is derived in this section. Associated with (i) the constitutive equations for the porous rock (Eq. (42)) and porous fluid (Eq. (39)), (ii) the equilibrium equation and continuity equation defined as Eqs. (44) and (45) respectively and (iii) Darcy's law that

governs the single phase fluid transport in the porous rock, the linear isotropic poroelastic coupling processes are captured. By ignoring the body force of fluid, the Darcy's law is written as

$$q_i = -\frac{k}{\mu} p_{,i} \qquad (46)$$

where k is intrinsic permeability and μ is the fluid viscosity.

By combining the strain-displacement relationship under assumption of small deformation,

$$\varepsilon_{ij} = \frac{1}{2}\left(u_{i,j} + u_{j,i}\right) \qquad (47)$$

with the constitutive equations and the momentum equilibrium. The deformation field equations are obtained as

$$G\nabla^2 u_i + \frac{G}{1-2\nu} u_{j,ji} - \alpha p_{,i} = 0 \quad (48)$$

The diffusion equation is derived by substituting Darcy's law (Eq. (46)) and constitutive equation (Eq. (39)) into fluid mass conservation (Eq. (45)) in terms of pore pressure p :

$$-\alpha \frac{\partial \varepsilon_{kk}}{\partial t} - \frac{1}{M}\frac{\partial p}{\partial t} + \frac{k}{\mu}\nabla^2 p = 0 \quad (49$$

where M is the Biot modulus defined as the fluid contents increase results from the unit increase of pore pressure under constant volumetric strain, written as

$$M = \frac{2G\left(\nu_u - \nu\right)}{\alpha^2\left(1-2\nu\right)\left(1-2\nu_u\right)} \qquad (50)$$

Based on the constitutive relations of porous rock and fluid, static equilibrium and mass conservation and transportation function, the governing equations representing the fully coupled poroelastic behaviors are therefore derived and written in terms of the displacement $\mathbf{u}$ and pore pressure p as

$$G\nabla^2 \mathbf{u} + \frac{G}{1-2\nu}\nabla\left(\nabla \cdot \mathbf{u}\right) - \mathbf{m}\alpha\nabla p = 0 \qquad (51)$$

$$-\alpha\left(\nabla \cdot \dot{\mathbf{u}}\right) - \frac{1}{M}\dot{p} + \frac{k}{\mu}\nabla^2 p = Q_i\delta \qquad (52)$$

where $\mathbf{m} = \left[1,1,1,0,0,0\right]^T$ for 3D problems and $\mathbf{m} = \left[1,1,0\right]^T$ for 2D problems since the coupling term $\mathbf{m}\alpha\nabla p$ is only active in case of volumetric change of porous solid, Q_i is injection rate at point source, δ is Kronecker's delta function.

By solving the field equation system shown as Eqs. (51) and (52) for the primary unknown variables-displacement $\mathbf{u}$ and pore pressure p , we can then calculate other unknowns such as strain $\boldsymbol{\varepsilon}$, total stress $\boldsymbol{\sigma}$, effective stress $\boldsymbol{\sigma}'$ and flux q according the constitutive relations. However, it is very difficult to get a close form solution due to the complexity of the partial differential equations, except the special cases with simple and symmetric geometries and material properties. Therefore, finding the

solution of coupled equations generally relies on numerical techniques, for example, finite element method, boundary element method and finite different method, etc. The problems contain more complicate geometries and various properties of porous solid and fluid such as nonlinearity, anisotropy, heterogeneity could be solved. In this work, we focus on the numerical solution using finite element method.

3.2 FEM Formulation

In the following, the finite element solution for the problem of poroelasticity is presented. The field equations (51) and (52) are spatially discrete by approximating the field variables of displacement, $\mathbf{u}$, pore pressure p through interpolation functions written as,

$$\mathbf{u} = \mathbf{N}_u \tilde{\mathbf{u}} \qquad (53)$$

$$p = \mathbf{N}_p \tilde{\mathbf{p}} \qquad (54)$$

where $\mathbf{N}_u$ and $\mathbf{N}_p$ are the shape functions for the solid displacement and pore pressure fields, respectively. $\tilde{\mathbf{u}}$ and $\tilde{\mathbf{p}}$ are the displacements and pore pressure on nodes in each elements described following an order as

$$\tilde{\mathbf{u}} = [u_x^1, u_y^1, u_z^1, u_x^2, u_y^2, u_z^2, \ldots, u_x^n, u_y^n, u_z^n] \qquad (55)$$

$$\tilde{\mathbf{p}} = [p^1, p^2, \ldots, p^n] \qquad (56)$$

The shape functions for displacement and pore pressure are respectively,

$$\mathbf{N}_u = \begin{bmatrix} N_u^1 & 0 & 0 & N_u^2 & 0 & 0 & \ldots & N_u^n & 0 & 0 \\ 0 & N_u^1 & 0 & 0 & N_u^2 & 0 & \ldots & 0 & N_u^n & 0 \\ 0 & 0 & N_u^1 & 0 & 0 & N_u^2 & \ldots & 0 & 0 & N_u^n \end{bmatrix} \qquad (57)$$

$$\mathbf{N}_p = \begin{bmatrix} N_p^1, N_p^2, \ldots, N_p^n \end{bmatrix} \qquad (58)$$

where n is the node order number depends on the chose type of element.

The strain-displacement relationship expressed as Eq. (47) can be written in discretized form,

$$\boldsymbol{\varepsilon} = \mathbf{B}\tilde{\mathbf{u}} \qquad (59)$$

where

$$\mathbf{B} = \mathbf{L}\mathbf{N}_u \qquad (60)$$

$$\mathbf{L} = \begin{bmatrix} \frac{\partial}{\partial x} & 0 & 0 & \frac{\partial}{\partial y} & 0 & \frac{\partial}{\partial z} \\ 0 & \frac{\partial}{\partial y} & 0 & \frac{\partial}{\partial x} & \frac{\partial}{\partial z} & 0 \\ 0 & 0 & \frac{\partial}{\partial z} & 0 & \frac{\partial}{\partial y} & \frac{\partial}{\partial x} \end{bmatrix}^T \qquad (61)$$

According to Eqs. (53) through (61), using Galerkin's method, the weak form of equation system Eqs. (51) and (52) can be derived as:

$$\mathbf{K}\tilde{\mathbf{u}} - \mathbf{A}\tilde{\mathbf{p}} = \mathbf{f} \quad (62)$$

$$-\mathbf{A}^T\dot{\tilde{\mathbf{u}}} - \mathbf{S}\dot{\tilde{\mathbf{p}}} + \mathbf{H}_H\tilde{\mathbf{p}} = \dot{\mathbf{q}} \quad (63)$$

where

$$\mathbf{K} = \int_{V_e}\mathbf{B}^T\mathbf{D}\mathbf{B}dV \quad (64)$$

$$\mathbf{A} = \int_{V_e}\mathbf{B}^T\alpha\mathbf{m}\mathbf{N}_p dV \quad (65)$$

$$\mathbf{S} = \int_{V_e}\mathbf{N}_p{}^T\frac{1}{M}\mathbf{N}_p dV \quad (66)$$

$$\mathbf{H}_H = \int_{V_e}\left(\nabla\mathbf{N}_p\right)^T\frac{k}{\mu}\left(\nabla\mathbf{N}_p\right)dV \quad (67)$$

In these equations, V_e is the volume of element, $\mathbf{f}$ is external mechanical loading, $\mathbf{q}$ is the injection rate from a point source. In the following Eq. (63) is discretized in time domain since it is first order time dependent. Though incremental formulation of matrix is required for strong nonlinear problem, the present work adopts the total formulation since that the constitutive models (VMIB, nonlocal damage model et al.) for the nonlinear rock behaviors are written in total form. Therefore the temporal discretization of field variables performed between t_0 and t can be expressed as:

$$\lambda\mathbf{K}_t\tilde{\mathbf{u}}_t - \lambda\mathbf{A}\tilde{\mathbf{p}}_t = -(1-\lambda)\mathbf{K}_{t0}\tilde{\mathbf{u}}_{t0} + (1-\lambda)\mathbf{A}\tilde{\mathbf{p}}_{t0} + \lambda\mathbf{f}_t + (1-\lambda)\mathbf{f}_{t0} \quad (68)$$

$$-\mathbf{A}^T\dot{\tilde{\mathbf{u}}}_t + (-\mathbf{S} - \Delta t\lambda\mathbf{H}_H)\tilde{\mathbf{p}}_t = -\mathbf{A}^T\dot{\tilde{\mathbf{u}}}_{t0} + [\Delta t(1-\lambda)\mathbf{H}_H - \mathbf{S}]\tilde{\mathbf{p}}_{t0} + \lambda\dot{\mathbf{q}}_t + (1-\lambda)\dot{\mathbf{q}}_{t0} \quad (69)$$

where $\Delta t = t - t_0$ is the time interval, λ is a coefficient with the range $0 < \lambda < 1$.

Eqs. (68) and (69) are written in the matrix form:

$$\begin{bmatrix}\mathbf{K}_t & -\mathbf{A}\\ -\mathbf{A}^T & -\Delta t\lambda\mathbf{H}_H - \mathbf{S}\end{bmatrix}\begin{bmatrix}\tilde{\mathbf{u}}_t\\ \tilde{\mathbf{p}}_t\end{bmatrix} = \begin{bmatrix}\frac{\lambda-1}{\lambda}\mathbf{K}_{t0} & -\frac{\lambda-1}{\lambda}\mathbf{A}\\ -\mathbf{A}^T & \Delta t(1-\lambda)\mathbf{H}_H - \mathbf{S}\end{bmatrix}\begin{bmatrix}\tilde{\mathbf{u}}_{t0}\\ \tilde{\mathbf{p}}_{t0}\end{bmatrix} + \begin{bmatrix}\mathbf{f}_t + \frac{1-\lambda}{\lambda}\mathbf{f}_{t0}\\ \Delta t\mathbf{q}_t + \frac{1-\lambda}{\lambda}\Delta t\mathbf{q}_{t0}\end{bmatrix} \quad (70)$$

For simplification purpose, set $\lambda = 1$ corresponding to an implicit schemes. Thus, the finite element formulation of field equations through special and temporal discretization in terms of displacement and pore pressure is obtained and Eq. (70) is reduced to

$$\begin{bmatrix}\mathbf{K}_t & -\mathbf{A}\\ -\mathbf{A}^T & -\Delta t\mathbf{H}_H - \mathbf{S}\end{bmatrix}\begin{bmatrix}\tilde{\mathbf{u}}_t\\ \tilde{\mathbf{p}}_t\end{bmatrix} = \begin{bmatrix}0 & 0\\ -\mathbf{A}^T & -\mathbf{S}\end{bmatrix}\begin{bmatrix}\tilde{\mathbf{u}}_{t0}\\ \tilde{\mathbf{p}}_{t0}\end{bmatrix} + \begin{bmatrix}\mathbf{f}_t\\ \Delta t\mathbf{q}_t\end{bmatrix} \quad (71)$$

Finally, by integrating the constitutive equations for the porous rock and fluid, the equilibrium equation, continuity equation and single phase Darcy's law, the fully coupled poroelastic field equations in FEM

form are obtained and coded in FORTRAN language. Due to the time dependency of poroelastic problem, using an appropriate time step is especially important. The stress and strain of porous rock propagates relatively faster than fluid diffusion that requires small enough time step for accuracy consideration. However, in fluid flow part, small time step will induce instable because of the pore pressure is nearly unchanged in this small time interval. Meantime, element size is another influence factor for adopting appropriate time step. Therefore, the time step is determined according to reasonable accuracy and stability.

3.4 FEM Formulation Validation of Poroelastic Model

To validate the present model for poroelastic model, the numerical solution is compared with the analytical solution of Terzaghi's one-dimensional consolidation. Terzaghi consolidation theory provided a solution for the fluid solid interaction in soil saturate with water, which has successfully inspired the following research in soil mechanics and geotechnical engineering. The settlement of a saturated soil column with thickness of h under a constant load from the top surface is analyzed. The column rests on a rigid and impermeable boundary. The constant normal loading with magnitude of P squeezes the pore water out from the top that induces a gradual settlement. The boundary conditions are written as follows:

$$\sigma_{zz} = -H(t)P \qquad z = 0 \quad (72)$$

$$p = 0 \qquad z = 0 \qquad \forall t \qquad (73)$$

$$\frac{\partial p}{\partial z} = 0 \qquad z = h \qquad \forall t \qquad (74)$$

(Detournay and Cheng 1993; Jaeger, Cook et al. 2009) give the detailed solutions for Terzaghi's one-dimensional consolidation. The solutions for pressure distribution are written as:

$$p(z,t) = \frac{B(1+\nu_u)}{3(1-\nu_u)}(-P)\sum_{m\ odd}\frac{4}{m\pi}\left(\sin\frac{m\pi}{2h}z\right)e^{-c\left(\frac{m\pi}{2h}\right)^2 t} \qquad (75)$$

$$\frac{p(z,t)}{p_0} = 1 - \sum_{n=0}^{\infty}(-1)^n\left\{erfc\left[\frac{2nh+z}{(4kt/\mu S)^{0.5}}\right] + erfc\left[\frac{2(n+1)h-z}{(4kt/\mu S)^{0.5}}\right]\right\} \qquad (76)$$

and the solution for top settlement is

$$w(z,t) = \frac{P}{\lambda+2G}\left[(z-h) + \frac{\alpha^2 Mh}{\lambda+2G+\alpha^2 M}\sum_{n=0}^{\infty}\frac{8}{n^2\pi^2}\cos\left(\frac{n\pi z}{2h}\right)\exp\left(\frac{-n^2\pi^2 kt}{4\mu Sh}\right)\right] \qquad (77)$$

where h is the thickness of soil column, M is the Biot modulus expressed as Eq. (50), B is the Skempton's coefficient written as Eq. (41), S is storativity coefficient written as:

$$S = \frac{\alpha^2(1-\nu_u)(1-2\nu)(1+\nu)}{3K(1-\nu)(\nu_u-\nu)} \qquad (78)$$

and $erfc(x)$ is the coerror function (Abramowitz and Stegun, 1970), defined as

$$erfc(x) = \frac{2}{\sqrt{\pi}}\int_x^{\infty} e^{-\eta^2}\,d\eta \qquad (79)$$

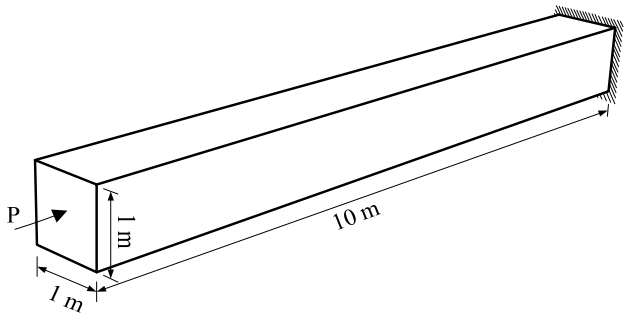

Figure 13. Problem geometry and boundary conditions of soil column.

The 3D finite element model with specified boundary conditions is used to reproduce Terzaghi 1D consolidation. The soil column has $1m \times 1m$ cross section and $10m$ height shown in Figure 13. The lateral surfaces are impermeable and their normal displacements are confined to fulfill the same boundary conditions as 1D Terzaghi's problem. The bottom side is also impermeable with no displacements. The top surface is exposed in air representing zero pore pressure boundary and subjected to a mechanical pressure load P. Therefore, the water is drained from the top during the loading process. Table 2 lists the input parameters used for analytical and numerical solutions. In the simulation, 38028 four nodes tetrahedron elements with 8556 nodes are used.

Table 2. Input Parameters for Terzaghi's 1D Consolidation.

Shear modulus, G	12.0 GPa
Poisson's ratio, ν	0.15
Undrained Poisson's ratio, ν_u	0.29
Biot's coefficient, α	1.0
Permeability, k	0.5 md
Fluid viscosity, μ	3.0×10^{-4} Pa·s
Load, P	1.0MPa

The comparisons of the transient pore pressure distributions between analytical and numerical solutions are shown in Figure 14. The pore pressure contours at different time are plotted in Figure 15. Figure 16 shows the transient settlements at various depth comparisons between analytical and numerical solutions. The comparisons indicate well agreement between the analytical and numerical solutions, which enhances the confidence that the model can be adopted to simulate the porous rock and fluid during the hydraulic stimulation in the following sections.

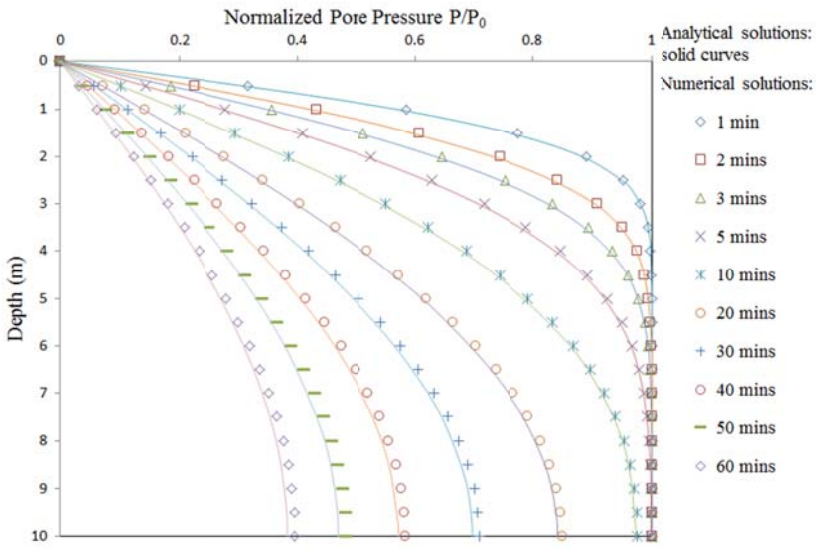

Figure 14. The transient pore pressure distributions comparisons between analytical and numerical solution.

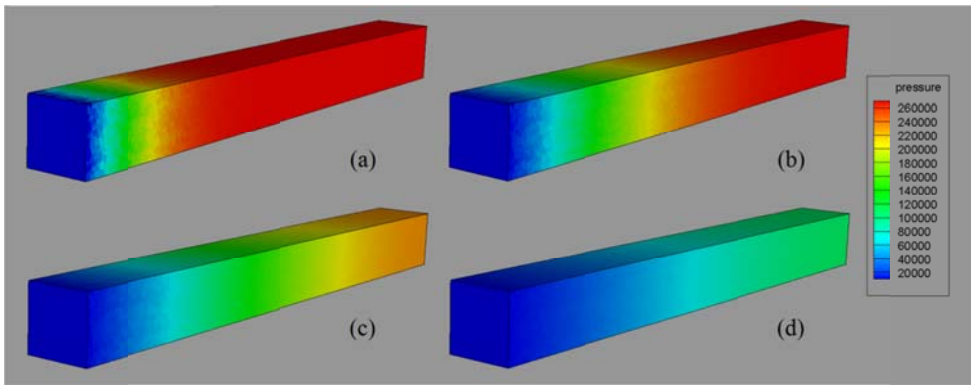

Figure 15. The transient pore pressure distributions at (a) 1mins; (b) 5 mins; (c) 20 mins; (d) 60 mins.

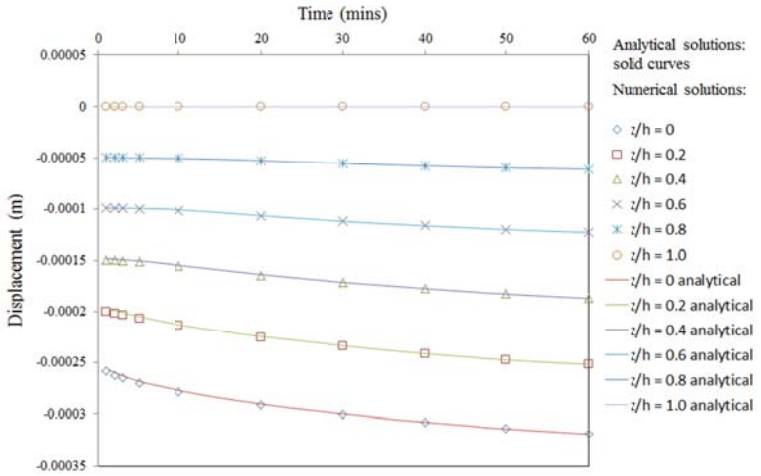

Figure 16. The transient settlements at various depth comparisons between analytical and numerical solution.

3.5 Fracture Flow Model

The theoretical aspects and mathematical derivation of classic poroelastic model are presented. The model is continuum-based and well explains the coupled process of the porous fluid flow and rock mass deformation for intact rock formation. However, to simulate the hydraulic fracturing process, a modification is necessarily needed because of the different flow mechanisms and boundary condition due to discontinuity of fracture surface. The conventional poroelastic model is not valid in an element that contains a fracture. On the aspect of fluid flow only, the permeability of fractured element is artificially increased to represent the conductivity enhancement by fracture creation. The pressure distribution along the fracture and diffusion in the rock formation can be calculated using an equation system. The challenge problem is applying the calculated pressure profile as pressure boundary on the fracture surface during the propagation process. As mentioned, the coupling part of the poroelastic model is not valid for the fractured element though the fluid diffusion part is still used to calculate the fluid pressure. Therefore, the modification is made on the coupling part of poroelastic model. The original coupled part $-\mathbf{A}$ in Eq. (71) is replaced with a new matrix derived based on the way of applying hydraulic pressure on the fracture surface using 3D EPM. The original poroelastic equations system is written as:

$$\begin{bmatrix} \mathbf{K}_t & -\mathbf{A} \\ -\mathbf{A}^T & -\Delta t\lambda\mathbf{H}_H - \mathbf{S} \end{bmatrix} \begin{pmatrix} \tilde{\mathbf{u}}_t \\ \tilde{\mathbf{p}}_t \end{pmatrix} = \begin{bmatrix} 0 & 0 \\ -\mathbf{A}^T & -\mathbf{S} \end{bmatrix} \begin{pmatrix} \tilde{\mathbf{u}}_{t0} \\ \tilde{\mathbf{p}}_{t0} \end{pmatrix} + \begin{pmatrix} \mathbf{f}_t \\ \Delta t\mathbf{q}_t \end{pmatrix} \tag{80}$$

In Eq. (80), $\mathbf{A}$ is the fully coupled term representing the porous fluid and solid mutual interaction. Eq. (80) is used for the intact element. For the fractured element, the following equation system is used:

$$\begin{bmatrix} \mathbf{K}_t^{EPM} & -\mathbf{A}^{EPM} \\ -\mathbf{A}^T & -\Delta t\lambda\mathbf{H}_H - \mathbf{S} \end{bmatrix} \begin{pmatrix} \tilde{\mathbf{u}}_t \\ \tilde{\mathbf{p}}_t \end{pmatrix} = \begin{bmatrix} 0 & 0 \\ -\mathbf{A}^T & -\mathbf{S} \end{bmatrix} \begin{pmatrix} \tilde{\mathbf{u}}_{t0} \\ \tilde{\mathbf{p}}_{t0} \end{pmatrix} + \begin{pmatrix} \mathbf{f}_t \\ \Delta t\mathbf{q}_t \end{pmatrix} \tag{81}$$

In Eq. (81), the stiffness matrix of solid $\mathbf{K}_t^{EPM}$ has been changed to the one calculated by 3D EPM and is no longer fully coupled with the porous fluid. The fluid flow in the fracture element will only follows the Darcy's law. In other words, the solid deformation will not influence the fluid pressure. The fluid pressure will affect the solid deformation in a one-way manner. Next, Eq. (81) is rearranged as

$$\begin{bmatrix} \mathbf{K}_t^{EPM} & 0 \\ 0 & -\Delta t\lambda\mathbf{H}_H - \mathbf{S} \end{bmatrix} \begin{pmatrix} \tilde{\mathbf{u}}_t \\ \tilde{\mathbf{p}}_t \end{pmatrix} = \begin{bmatrix} 0 & 0 \\ 0 & -\mathbf{S} \end{bmatrix} \begin{pmatrix} \tilde{\mathbf{u}}_{t0} \\ \tilde{\mathbf{p}}_{t0} \end{pmatrix} + \begin{pmatrix} \mathbf{f}_t \\ \Delta t\mathbf{q}_t \end{pmatrix} + \begin{pmatrix} \mathbf{A}^{EPM}\tilde{\mathbf{p}}_t \\ 0 \end{pmatrix} \tag{82}$$

After rearranging of Eq. (82), $\mathbf{A}^{EPM}\tilde{\mathbf{p}}_t$ term can be considered as nodal forces applied on the right hand side of equation system. Meantime, the pressure boundary condition on the fracture surface can be successfully applied if $\mathbf{A}^{EPM}$ is well constructed. Another advantage is that the pressure boundary will be possibly applied real-timely since that displacement and pressure are calculated simultaneously. Let's recall the method of representing the hydraulic pressure in fractured element, which is helpful for understanding the mathematical and mechanical meaning of $\mathbf{A}^{EPM}\tilde{\mathbf{p}}_t$. The hydraulic pressure $\mathbf{P}$ in an element is represented by the equivalent nodal forces $\mathbf{F} = \mathbf{P} \cdot A$, where A is the area of fracture in one element. Take type I partition element for example, the pressure in the fracture surface uses the averaged value of the pressure on these 4 nodes written as

$$\mathbf{P}=\frac{1}{4}(\tilde{p}_t^I+\tilde{p}_t^J+\tilde{p}_t^K+\tilde{p}_t^M)\cdot\mathbf{n} \quad (83)$$

where $\mathbf{n}=[n_x,n_y,n_z]$ is the direction vector indicating the normal direction of fracture surface.

The equivalent nodal forces are rewritten as

$$\mathbf{F}=[F_{Mx'},F_{My'},F_{Mz'}]=\mathbf{P}\cdot A=\frac{1}{4}(\tilde{p}_t^I+\tilde{p}_t^J+\tilde{p}_t^K+\tilde{p}_t^M)\cdot\mathbf{n}\cdot A \quad (84)$$

$$-\frac{1}{3}\mathbf{F}=[F_{Ix'},F_{Iy'},F_{Iz'}]=-\frac{1}{3}\mathbf{P}\cdot A=-\frac{1}{3}\frac{1}{4}(\tilde{p}_t^I+\tilde{p}_t^J+\tilde{p}_t^K+\tilde{p}_t^M)\cdot\mathbf{n}\cdot A \quad (85)$$

$$-\frac{1}{3}\mathbf{F}=[F_{Jx'},F_{Jy'},F_{Jz'}]=-\frac{1}{3}\mathbf{P}\cdot A=-\frac{1}{3}\frac{1}{4}(\tilde{p}_t^I+\tilde{p}_t^J+\tilde{p}_t^K+\tilde{p}_t^M)\cdot\mathbf{n}\cdot A \quad (86)$$

$$-\frac{1}{3}\mathbf{F}=[F_{Kx'},F_{Ky'},F_{Kz'}]=-\frac{1}{3}\mathbf{P}\cdot A=-\frac{1}{3}\frac{1}{4}(\tilde{p}_t^I+\tilde{p}_t^J+\tilde{p}_t^K+\tilde{p}_t^M)\cdot\mathbf{n}\cdot A \quad (87)$$

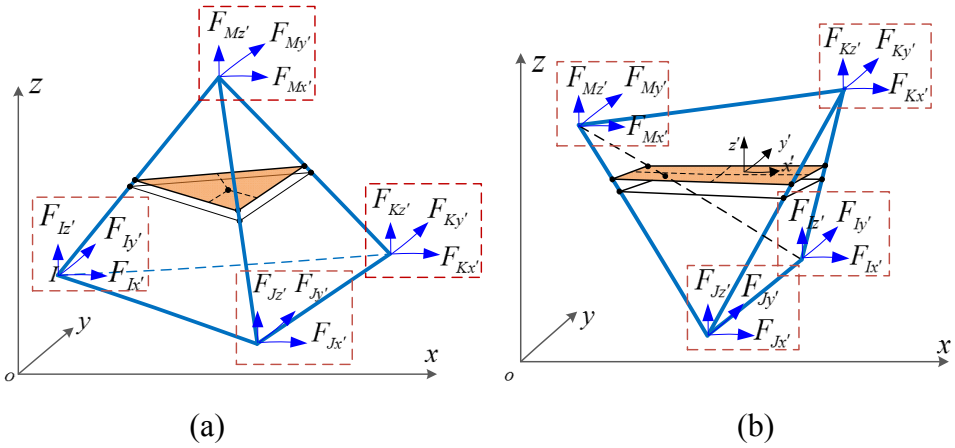

Figure 17. Equivalent nodal forces representing hydraulic pressure for (a) type I partition element; (b) type II partition element.

Write Eq. (84)~(87) in matrix form shown as following:

$$[F_{Mx'},F_{My'},F_{Mz'}]=\mathbf{A}_{typeI}^{M}\tilde{\mathbf{p}}_t^e=\begin{bmatrix}\frac{1}{4}An_x & \frac{1}{4}An_x & \frac{1}{4}An_x & \frac{1}{4}An_x\\ \frac{1}{4}An_y & \frac{1}{4}An_y & \frac{1}{4}An_y & \frac{1}{4}An_y\\ \frac{1}{4}An_z & \frac{1}{4}An_z & \frac{1}{4}An_z & \frac{1}{4}An_z\end{bmatrix}\begin{pmatrix}\tilde{p}_t^I\\ \tilde{p}_t^J\\ \tilde{p}_t^K\\ \tilde{p}_t^M\end{pmatrix} \quad (88)$$

$$[F_{Ix'}, F_{Iy'}, F_{Iz'}] = \mathbf{A}^{I}_{typeI}\tilde{\mathbf{p}}^{e}_{t} = \begin{bmatrix} -\frac{1}{12}An_x & -\frac{1}{12}An_x & -\frac{1}{12}An_x & -\frac{1}{12}An_x \\ -\frac{1}{12}An_y & -\frac{1}{12}An_y & -\frac{1}{12}An_y & -\frac{1}{12}An_y \\ -\frac{1}{12}An_Z & -\frac{1}{12}An_Z & -\frac{1}{12}An_Z & -\frac{1}{12}An_Z \end{bmatrix} \begin{pmatrix} \tilde{p}^{I}_{t} \\ \tilde{p}^{J}_{t} \\ \tilde{p}^{K}_{t} \\ \tilde{p}^{M}_{t} \end{pmatrix} \quad (89)$$

$$[F_{Jx'}, F_{Jy'}, F_{Jz'}] = \mathbf{A}^{J}_{typeI}\tilde{\mathbf{p}}^{e}_{t} = \begin{bmatrix} -\frac{1}{12}An_x & -\frac{1}{12}An_x & -\frac{1}{12}An_x & -\frac{1}{12}An_x \\ -\frac{1}{12}An_y & -\frac{1}{12}An_y & -\frac{1}{12}An_y & -\frac{1}{12}An_y \\ -\frac{1}{12}An_Z & -\frac{1}{12}An_Z & -\frac{1}{12}An_Z & -\frac{1}{12}An_Z \end{bmatrix} \begin{pmatrix} \tilde{p}^{I}_{t} \\ \tilde{p}^{J}_{t} \\ \tilde{p}^{K}_{t} \\ \tilde{p}^{M}_{t} \end{pmatrix} \quad (90)$$

$$[F_{Kx'}, F_{Ky'}, F_{Kz'}] = \mathbf{A}^{K}_{typeI}\tilde{\mathbf{p}}^{e}_{t} = \begin{bmatrix} -\frac{1}{12}An_x & -\frac{1}{12}An_x & -\frac{1}{12}An_x & -\frac{1}{12}An_x \\ -\frac{1}{12}An_y & -\frac{1}{12}An_y & -\frac{1}{12}An_y & -\frac{1}{12}An_y \\ -\frac{1}{12}An_Z & -\frac{1}{12}An_Z & -\frac{1}{12}An_Z & -\frac{1}{12}An_Z \end{bmatrix} \begin{pmatrix} \tilde{p}^{I}_{t} \\ \tilde{p}^{J}_{t} \\ \tilde{p}^{K}_{t} \\ \tilde{p}^{M}_{t} \end{pmatrix} \quad (91)$$

The nodal force vector on the right hand of elemental matrix system is written as:

$$\mathbf{f} = [F_{Ix'}, F_{Iy'}, F_{Iz'}, F_{Jx'}, F_{Jy'}, F_{Jz'}, F_{Kx'}, F_{Ky'}, F_{Kz'}, F_{Mx'}, F_{My'}, F_{Mz'}] \quad (92)$$

Combining and rearranging Eq. (88)~(92) yields:

$$\mathbf{f} = \mathbf{A}^{EPM}_{typeI}\tilde{\mathbf{p}}_{t} \quad (93)$$

where $\mathbf{A}^{EPM}_{typeI} = [\mathbf{A}^{I}_{typeI} \quad \mathbf{A}^{J}_{typeI} \quad \mathbf{A}^{K}_{typeI} \quad \mathbf{A}^{M}_{typeI}]^{T}$ for type I partition element.

Similarly, for type II partition element,

$$[F_{Mx'}, F_{My'}, F_{Mz'}] = \mathbf{A}^{M}_{typeII}\tilde{\mathbf{p}}^{e}_{t} = \begin{bmatrix} \frac{1}{8}An_x & \frac{1}{8}An_x & \frac{1}{8}An_x & \frac{1}{8}An_x \\ \frac{1}{8}An_y & \frac{1}{8}An_y & \frac{1}{8}An_y & \frac{1}{8}An_y \\ \frac{1}{8}An_z & \frac{1}{8}An_z & \frac{1}{8}An_z & \frac{1}{8}An_z \end{bmatrix} \begin{pmatrix} \tilde{p}^{I}_{t} \\ \tilde{p}^{J}_{t} \\ \tilde{p}^{K}_{t} \\ \tilde{p}^{M}_{t} \end{pmatrix} \quad (94)$$

$$[F_{Kx'}, F_{Ky'}, F_{Kz'}] = \mathbf{A}^{K}_{typeII}\tilde{\mathbf{p}}^{e}_{t} = \begin{bmatrix} \frac{1}{8}An_x & \frac{1}{8}An_x & \frac{1}{8}An_x & \frac{1}{8}An_x \\ \frac{1}{8}An_y & \frac{1}{8}An_y & \frac{1}{8}An_y & \frac{1}{8}An_y \\ \frac{1}{8}An_z & \frac{1}{8}An_z & \frac{1}{8}An_z & \frac{1}{8}An_z \end{bmatrix} \begin{pmatrix} \tilde{p}^{I}_{t} \\ \tilde{p}^{J}_{t} \\ \tilde{p}^{K}_{t} \\ \tilde{p}^{M}_{t} \end{pmatrix} \quad (95)$$

$$[F_{Ix'}, F_{Iy'}, F_{Iz'}] = \mathbf{A}^{I}_{typeII}\tilde{\mathbf{p}}^{e}_{t} = \begin{bmatrix} -\frac{1}{8}An_x & -\frac{1}{8}An_x & -\frac{1}{8}An_x & -\frac{1}{8}An_x \\ -\frac{1}{8}An_y & -\frac{1}{8}An_y & -\frac{1}{8}An_y & -\frac{1}{8}An_y \\ -\frac{1}{8}An_z & -\frac{1}{8}An_z & -\frac{1}{8}An_z & -\frac{1}{8}An_z \end{bmatrix} \begin{pmatrix} \tilde{p}^{I}_{t} \\ \tilde{p}^{J}_{t} \\ \tilde{p}^{K}_{t} \\ \tilde{p}^{M}_{t} \end{pmatrix} \quad (96)$$

$$[F_{Jx'}, F_{Jy'}, F_{Jz'}] = \mathbf{A}^{J}_{typeII}\tilde{\mathbf{p}}^{e}_{t} = \begin{bmatrix} -\frac{1}{8}An_x & -\frac{1}{8}An_x & -\frac{1}{8}An_x & -\frac{1}{8}An_x \\ -\frac{1}{8}An_y & -\frac{1}{8}An_y & -\frac{1}{8}An_y & -\frac{1}{8}An_y \\ -\frac{1}{8}An_z & -\frac{1}{8}An_z & -\frac{1}{8}An_z & -\frac{1}{8}An_z \end{bmatrix} \begin{pmatrix} \tilde{p}^{I}_{t} \\ \tilde{p}^{J}_{t} \\ \tilde{p}^{K}_{t} \\ \tilde{p}^{M}_{t} \end{pmatrix} \quad (97)$$

Combining and rearranging Eq. (92) and Eq. (94)~(97) yield

$$\mathbf{f} = \mathbf{A}^{EPM}_{typeII}\tilde{\mathbf{p}}_{t} \quad (98)$$

where $\mathbf{A}^{EPM}_{typeII} = [\mathbf{A}^{I}_{typeII} \quad \mathbf{A}^{J}_{typeII} \quad \mathbf{A}^{K}_{typeII} \quad \mathbf{A}^{M}_{typeII}]^{T}$ for type II partition element.

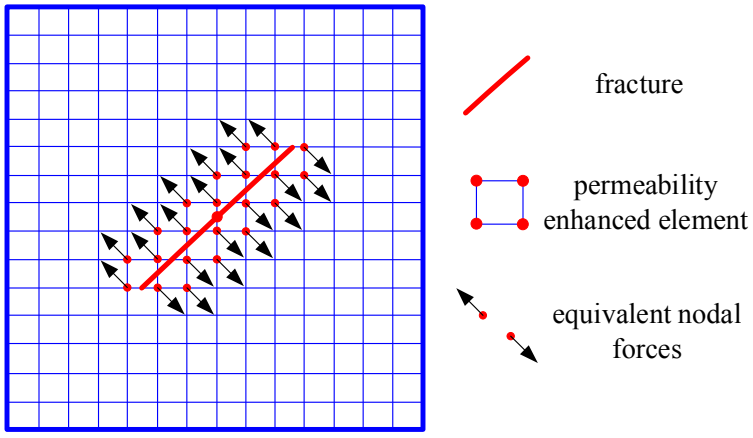

Figure 18. Illustration of modified poroelastic model

Finally, the modified poroelastic model is derived and illustrated in Figure 18. In Figure 18, the red line indicates a fracture. The blue rectangular with the red dot corner displays the permeability enhanced element cut by the fracture. The arrows show the equivalent nodal forces normal to the fracture surface. The fully coupled poroelastic model shown in Eq. (80) is adopted to simulate the fluid diffusion and deformation in the intact rock formation. The modified poroelastic model shown in Eq. (81) changed the matrix component based on 3D EPM that is capable to apply real-time hydraulic pressure calculated simultaneously in the same equation system. For newly extended fracture, the elemental matrix will be changed to 3D EPM formulation if the element is cut by the new fracture surfaces.

In traditional poroelastic modeling, the time step Δt is predetermined to fit the problem of interests. However, for hydraulic fracture simulation, the time step between each propagation step has specific physical meaning that governs the fracture pressure distribution and leak-off volume into the formation. Therefore, a reasonable value of Δt is required. In present model, the injection time increment Δt in Eq.

(80) and (81) is calculated using the similar way as the one used in lubrication theory written as $\Delta t = \int_{A_f} \Delta w dA / Q_i$. The equation means that the Δt only takes account in the fluid volume that stays in the fracture surface. The volume of diffuse fluid is neglect in Δt calculation since that the leak-off volume is difficult to get especially for complex fracture surface and moving boundary during the fracture propagation. Therefore, Δt is underestimated and needs more work in the future.

4. Thermo-mechanical Model

The influences of thermo-mechanical processes on fracture initiation and propagation are important to geothermal systems development. Cold water injection and heat extraction in the geothermal reservoir will cause dramatic temperature changes in the rock subjecting it to volumetric contraction (expansion). A volumetric expansion or contraction results in variation of rock stress and rock properties. The processes of thermal and mechanical coupling occur on various time scales and may have different influence upon the problem of interest. The influence of thermo-poroelastic process on the near wellbore flow and stresses has been addressed analytically (McTigue, 1990) and numerically (e.g., Ghassemi and Zhang, 2004; Zhou and Ghassemi, 2009). Generally, the thermal effects should be considered during long term injection owing to low thermal diffusivity of rocks. High tensile stress are induced by cooling of the rock fractures surfaces, indicating a potential for extension of the secondary thermal fractures (Bazant and Ohtsubo, 1979, Tarasovs and Ghassemi, 2014, Feng and Jin, 2009, Tarasovs and Ghassemi, 2011, Huang and Ghassemi, 2012). There is also experimental investigation (Geyer and Nemat-Nasser, 1982) showing thermally induced crack in glass. (Bauer and Handin, 1979, 1983) presented experiments to measure the thermal expansion of various water-saturated heated rocks under different effective confining pressure. Microcrack developments have been found associated with thermal expansions from 25 C to 800 C . The work inferred the permeability enhancement of interconnected micro crack due to thermal stimulation. As a result, thermal stimulation has been suggested as a means of enhancing reservoir permeability.

Thermal fractures can result from the nonlinear deformation of the solid in response to thermal stress. Before the rock reaches the final failure stage, material softening and bulk modulus degradation can cause changes in the thermo-mechanical properties of the solid. In order to capture this aspect of the solid fracture, a VMIB-based thermo-mechanical model is derived to track elastic, softening, and the final failure stages of the rock response with the change of its temperature field in time. The thermo-mechanical properties of rock changes as its bulk modulus evolves are derived from a nonlinear constitutive model. On the other hand, to represent the thermo-mechanical behavior of pre-existing fractures, the element partition method (EPM)(Huang and Zhang, 2010) is employed. The 3D EPM has been used to simulate the propagation of 3D embedded mix-mode fracture (Huang, Zhang and Ghassemi, 2012). Taking advantage of EPM, the contact and friction of the fracture can be simulated without a dedicated mesh.

By including an additional thermal term into the governing equations, a nonlinear thermo-mechanical constitutive equation can be obtained as (Nowacki, 1976),

$$\sigma_{ij} = C_{ijmn}\varepsilon_{mn} - \hat{\gamma}\Delta T\delta_{ij} \quad (99)$$

where σ_{ij} and ε_{ij} are the components of stress and strain tensor (tension is considered positive), ΔT is the temperature change equal to $(T - T_0)$, in which T and T_0 are the current temperature and initial temperature, respectively. δ_{ij} is the Kronecker's detla. The thermal coefficient $\hat{\gamma}$ in Eq. (99) is defined as:

$$\hat{\gamma} = \hat{K}\alpha_m \qquad (100)$$

where $\hat{K}$ is bulk modulus defined as $\hat{K} = \frac{1}{3}C_{11kl}\delta_{kl} = \frac{1}{3}C_{22kl}\delta_{kl} = \frac{1}{3}C_{33kl}\delta_{kl}$ for an isotropic material, and α_m is the thermal expansion coefficient of solid matrix. The above constitutive equations combined with stress equilibrium and energy balance equations, yield the following Navier's and thermal diffusion field equations,

$$C_{ijkl}u_{k,li} - \hat{\gamma}\Delta T_{,i}\delta_{ij} = 0 \qquad (101)$$

$$\dot{T} - c^T\nabla^2 T = 0 \qquad (102)$$

In the following, the finite element method for the nonlinear thermo-mechanical problems is presented. To approximate the field variables of displacement, $\mathbf{u}$, temperature $\mathbf{T}$, and total temperatures change, $\Delta\mathbf{T}$, shape functions are used: $\mathbf{u} = \mathbf{N}_u\tilde{\mathbf{u}}$, $\mathbf{T} = \mathbf{N}_T\tilde{\mathbf{T}}$, $\Delta\mathbf{T} = \mathbf{N}_T\Delta\tilde{\mathbf{T}}$, where $\mathbf{N}_u$ and $\mathbf{N}_T$ are the shape functions for the solid displacement and temperature fields, respectively. $\tilde{\mathbf{u}}$ and $\Delta\tilde{\mathbf{T}}$ are nodal displacements and total temperatures change. These approximations are substituted into Eq. (101) and (102) (Galerkin method) yielding the following equations

$$\mathbf{K}\tilde{\mathbf{u}} - \mathbf{V}\Delta\tilde{\mathbf{T}} = \tilde{\mathbf{f}} \qquad (103)$$

$$\mathbf{R}\dot{\tilde{\mathbf{T}}} - \mathbf{U}\tilde{\mathbf{T}} = 0 \qquad (104)$$

where

$$\mathbf{K} = \int_{V_e}\mathbf{B}^T\mathbf{D}\mathbf{B}dV \qquad (105)$$

$$\mathbf{V} = \int_{V_e}\mathbf{B}^T\hat{\gamma}\mathbf{m}\mathbf{N}_T dV \qquad (106)$$

$$\mathbf{R} = \int_{V_e}\mathbf{N}_T{}^T\mathbf{N}_T dV \qquad (107)$$

$$\mathbf{U} = \int_{V_e}(\nabla\mathbf{N}_T)^T\mathbf{c}^T(\nabla\mathbf{N}_T)dV \qquad (108)$$

Using Crank-Nicolson method for time approximation scheme to discretize the heat diffusion equation shown as Eq. (104), the final finite element formula can be obtained

$$-(\mathbf{R} + \theta\Delta t\mathbf{U})\Delta\tilde{\mathbf{T}}_n = \Delta t\mathbf{U}\tilde{\mathbf{T}}_{n-1} \qquad (109)$$

Where $\widetilde{\mathbf{T}}_{n-1}$ is the temperature in the previous time step, and $\Delta\widetilde{\mathbf{T}}_n$ is the temperature change in the present step.

Since the thermal-mechanical problem is not a fully coupled one, i.e., mechanical deformation does not influence the thermal diffusion, the thermal coupling term in the elasticity equations can be taken as a mechanical load caused by temperature changes during the calculation. Once the temperature field is known, the thermal stress load can be obtained. Considering the coupling part, after rearrangement of Eqn. (103), the field equation becomes

$$\mathbf{K}\widetilde{\mathbf{u}} = \widetilde{\mathbf{f}} + \mathbf{V}\Delta\widetilde{\mathbf{T}} \quad (110)$$

The second term on the right side describes how the temperature changes influences the stress-strain field through displacements.

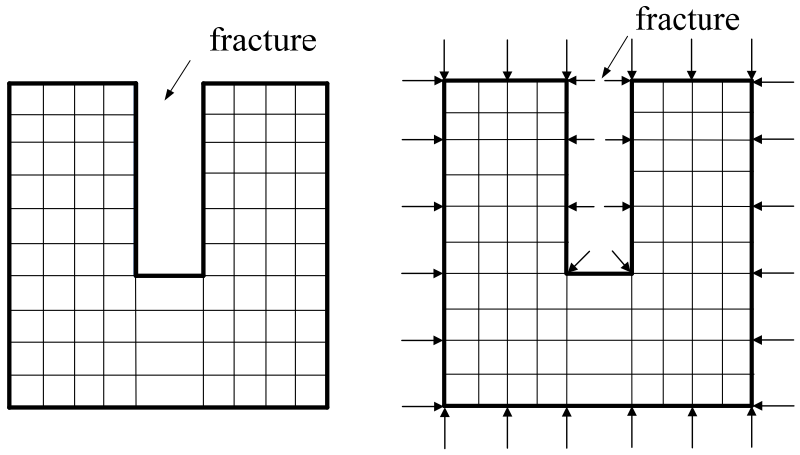

Figure 19. Thermo-mechanical response of a fracture in traditional FEM. The arrows show the cooling-induced nodal forces for contraction.

To achieve the volume change such as expansion by heating and shrinking by cooling in the finite element modeling, equivalent node forces (ENFs) caused by the nodal temperature changes are applied on the corresponding nodes and in the corresponding directions. The mathematical expression of equivalent node forces (ENFs) is shown in Eq. (110), which is $\mathbf{V}\Delta\widetilde{\mathbf{T}}$. For example, we assume that the temperature over a domain changes instantaneously and uniformly. The ENFs are canceled on the interior nodes because of their same temperature change, and only the enforced ENFs on the boundary nodes will cause a volumetric change (shown in 2D in Figure 19 for cooling process).

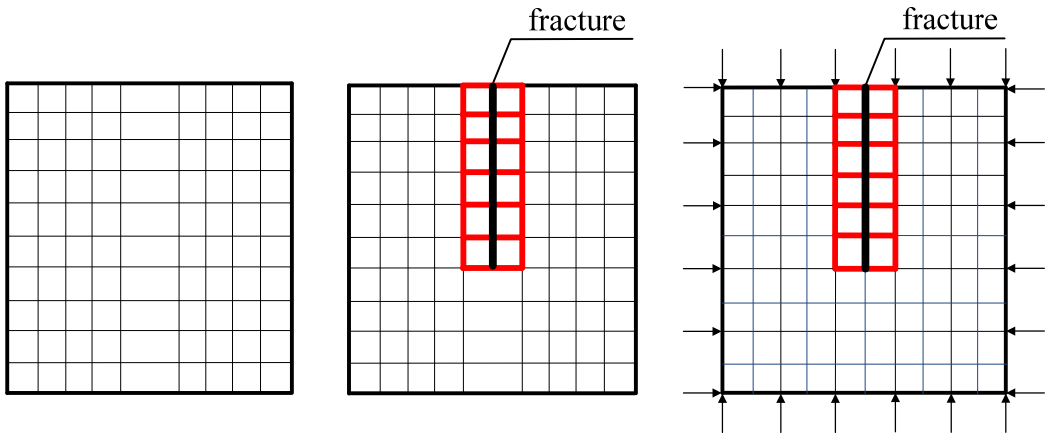

Figure 20. Thermo-mechanical response with original thermal properties.

In this work we use a 3D element partition method (3D EPM) for fracture creation so there is no need to mesh for pre-existing fracture. If the ith element is cut through by a fracture, the element will be transferred to the partition element based on the original structured. The ith element stiffness matrix $\mathbf{K}_i^e$ will be replaced by $\mathbf{K}_i^{EPM}$ before being assembled into global stiffness matrix $\mathbf{K}$. However, the thermal and thermo-mechanical coupling part of the partition element also needs to be modified. In Figure 20, the elements with red boundaries have been changed into partition elements after being cut by fracture shown as thick line. Having their original thermal and coupling properties, the object in the figure will perform like a non-fractured one, because that the ENFs status in Figure 20 is equal to the resultant nodal forces in Figure 21(a) and (b). If the thermally induced ENFs of the fractured elements are removed, shown in Figure 21(a), the resultant nodal force shown in Figure 21(b) will be the same as the one in Figure 19. Mathematically, before being assembled into the coupling part of global matrix $\mathbf{V}$, the thermo-mechanical coupling term in element level $\mathbf{V}_i^e$ should be multiplied by β which equals 0 if the ith element is fractured. Therefore, the fractured element is now partitioned both with respect to its mechanical properties and its volumetric thermal deformation so that deformation behavior of a fracture under thermo-mechanical load is numerically represented. The same modification will be applied to newly extended fractures. As a result, the fracture will be represented in a blunt sharp that related the size and shape of the fractured elements. This could influence the precision of calculation if the element size is relative large.

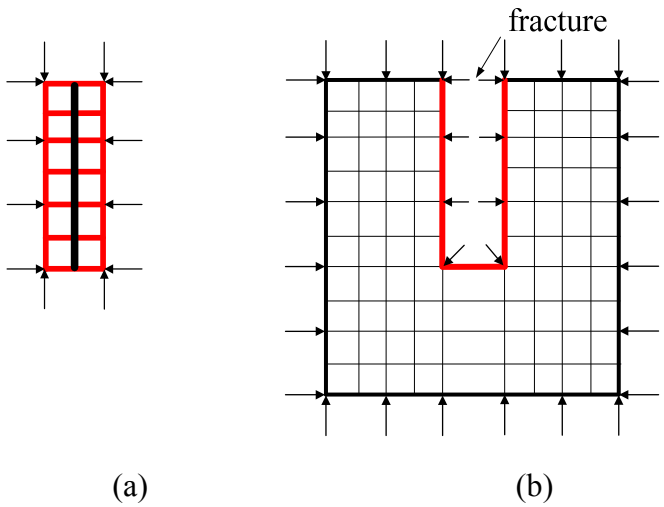

Figure 21. (a) Thermo-mechanical response of fractured element; (b) thermo-mechanical response of partition element after modification.

4.1 Numerical Simulation of Fracture Propagation under Mechanical Loading

4.1.1 Mode I fracture

To examine the performance of VMIB and 3D EPM in simulating tensile (Mode I) fractures propagation and their interaction, a cubic specimen with two sawed horizontal rectangular fractures is simulated. The geometry is shown in Figure 22. The uniaxial vertical tensile load is applied on the top of the specimen. Table 4 shows the parameters used. The mesh consists of 12, 24 and 34 rows of nodes plotted on the x, y and z direction respectively. The total element number is 41745 and the total node number is 9792. Displacement controlled loading is employed in this simulation.

Table 4. Parameters of Simulations Using VMIB Model

Parameters of intact element:	
Young's modulus, E	30.5 GPa
Poisson's ratio, ν	0.20
Tensile strain strength, ε_t	0.105×10^{-3}
Parameters of 3D EPM:	
Normal stiffness coefficient, K_n / h	10.0 GPa/m
Shear stiffness coefficient, K_s / h	10^{-8} GPa/m
Fracture width, h	1.0 mm
Parameters of 3D VMIB:	
c	0.15
n	4.0

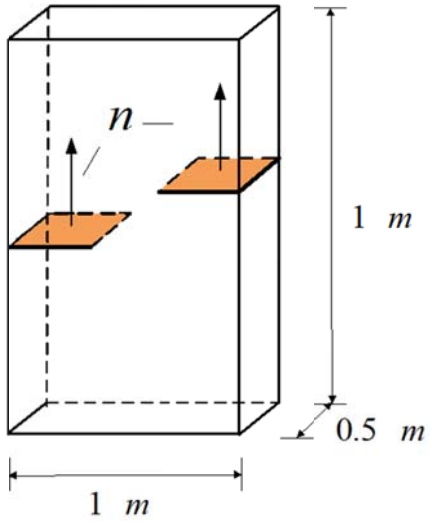

Figure 22. Problem geometry and boundary condition of a specimen with two horizontal rectangular fractures, subjected to vertical tension.

Figure 23(a) shows the initial and final fracture patterns. From Figure 23(b) to (d), the fractures develop from initial crack tips and propagate horizontally as typical Mode I fractures. As the fractures interact with each other, the stress field around the fracture tips is disturbed. Consequently, the newly extended fracture deviates towards the other one and coalesce. Figure 23(e) and (f) show the fracture surface and deformed mesh configuration upon specimen failure.

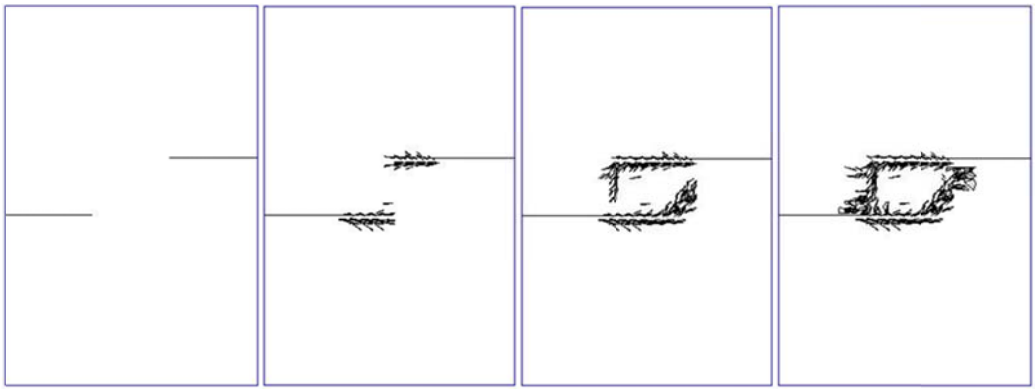

(a) (b) (c) (d)

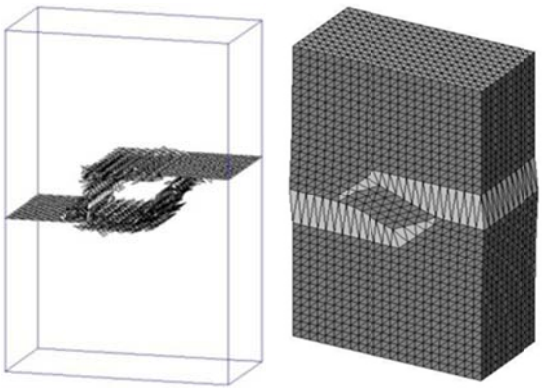

(e) (f)

Figure 23. Fracture propagation: (a) initial fracture; (b-d) fracture propagation; (e) fracture surface at failure,and (f) deformed mesh configuration (node displacements magnified 300 times).

4.1.2 Mode II fracture

The second simulation explores Mode II fracture propagation and interaction. A cubic specimen with two sawed inclined rectangular fracture is simulated. The dimensions and boundary conditions are shown as Figure 24. Material and model parameters showed in Table 4. The mesh consists of 26 rows of nodes plotted on the each direction. The total element number is 78125 and the total node number is 17576. Displacement controlled load is used in this simulation. Figure 25(a) shows the initial fracture. From Figure 25(b) to (d), the fractures propagate from both wings of the initial cracks. The left wing of lower initial fracture and the right wing of upper fracture yield newly-extended fracture firstly along the direction perpendicular to the fracture surface.

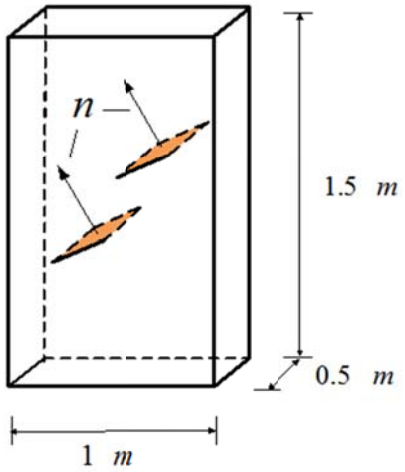

Figure 24. Problem geometry and boundary conditions for the cubic specimen with two sawed inclined rectangular fractures, subjected to vertical compression.

Then, the newly extended fractures develop along the vertical direction axis of the specimen in the direction of the applied maximum stress. This agrees with experimental observation (Bobet and Einstein, 1998). The fractures extend from near side initial fracture tips and converge in the middle of the specimen. Figure 25(e), (f) shows the fracture surface and deformed mesh configuration at failure. This agrees with experimental observations in Figure 26.

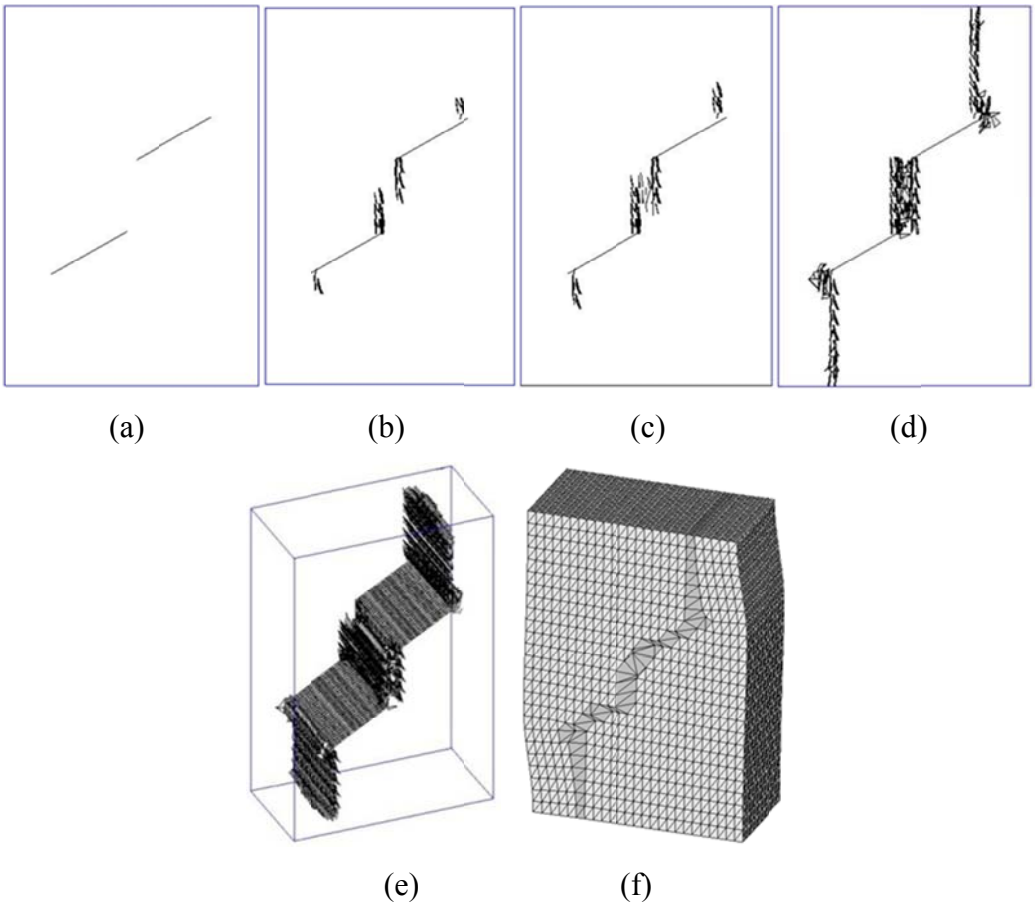

Figure 25. Fracture propagation: (a) initial fracture; (b-d) fracture propagation; (e) fracture surface at failure, and (f) deformed mesh configuration (node displacements magnified 300 times).

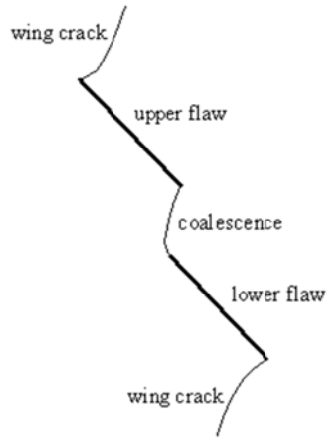

Figure 26. Experimental observation of wing crack growth in uniaxial compression (Bobet and Einstein, 1998).

4.1.3 Embedded fracture (Mix Mode-I, II, III)

Simulating the propagation of an embedded fracture subjected to shear stresses is a challenging problem in geomechanics. In this case, the fracture simultaneously involves Modes I, II and III. To model this phenomenon, consider the simulation of embedded elliptical fracture. The dimensions and boundary conditions are shown in Figure 27. Material and model parameters are given in Table 4. In presented meshing scheme, there are 45 rows of nodes each plotted on the x, y and z direction. The total element number is 425920 and the total node number is 91125. Figure 28(a) shows the initial fracture. The processes of fracture propagation are shown in Figure 28(b)~(f). The normal direction of the initial fracture plane is given as 60°.

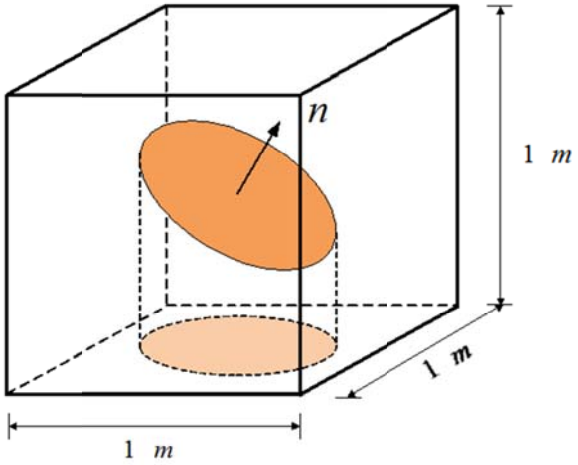

Figure 27. Problem geometry and boundary conditions of a cubic specimen with an embedded elliptical fracture.

The appearance of the crack tip after some crack growth has occurred is shown in Figure 28(b). It is observed that the crack has not grown by extending its own plane but by generating multiple tiny fracture surfaces which deviate from its original crack front. Similar phenomenon is captured in the experiment for observing the crack propagation in anti-plane shear tested by (Knauss, 1970), which is shown in Figure 29. The newly-extended fractures "straddle" the pre-existing straight crack tip. Then these tiny fractures around the original crack tip will form new crack tip which will influence the orientation of consequently opened fracture. Figure 28(c)-(f) shows that the fracture develops from upper and lower tips of initial fracture in a typical Mode II fracture. The fracture propagation is slower on the sides tip as it propagates outwardly to the lateral side of specimen. From Figure 28, the side fracture that initiated from the side tip rotates from the initial crack tip toward the lateral side of specimen, which represents the Mode III response.

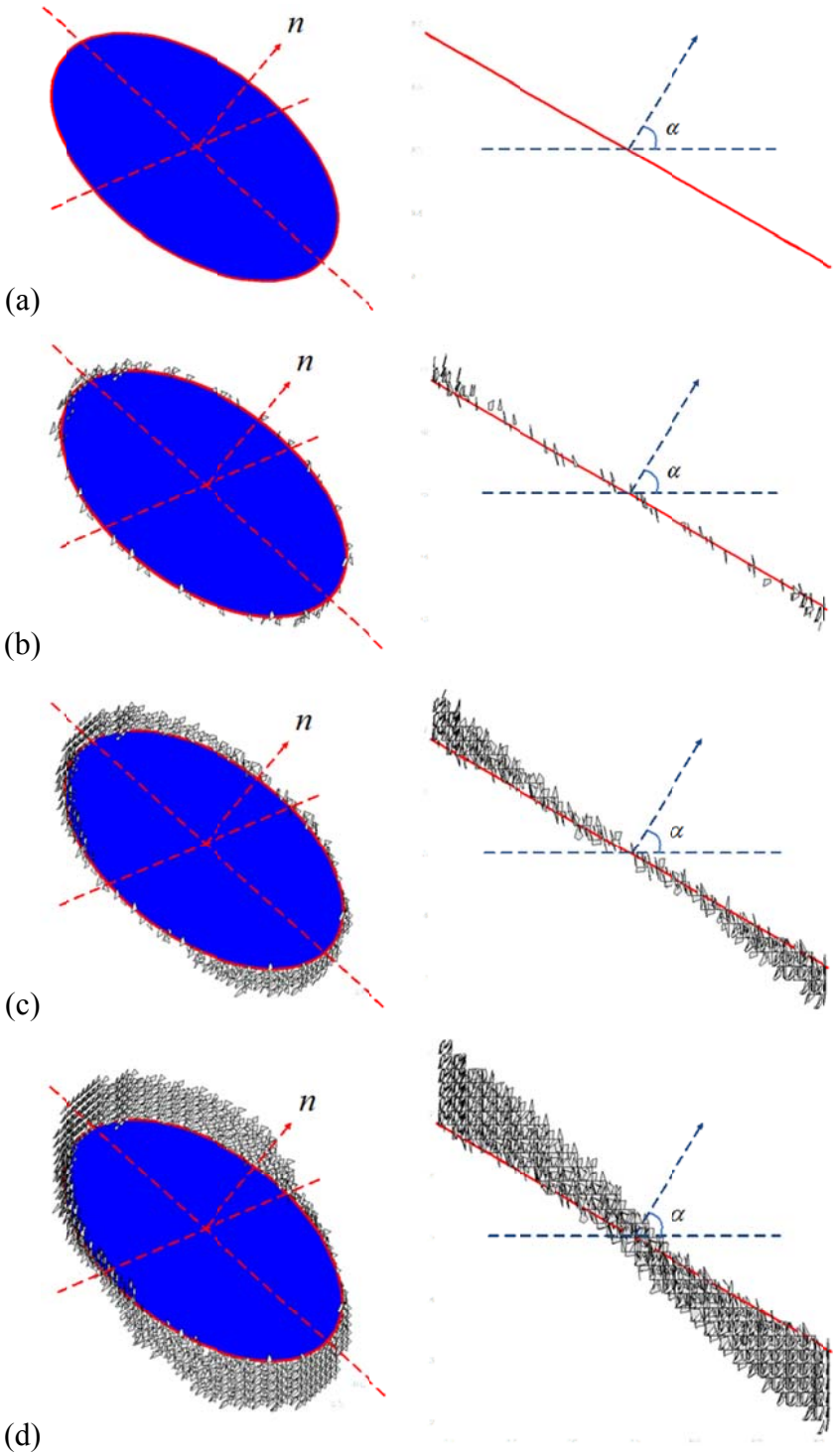
n
α
(a)
n
α
(b)
n
α
(c)
n
α
(d)

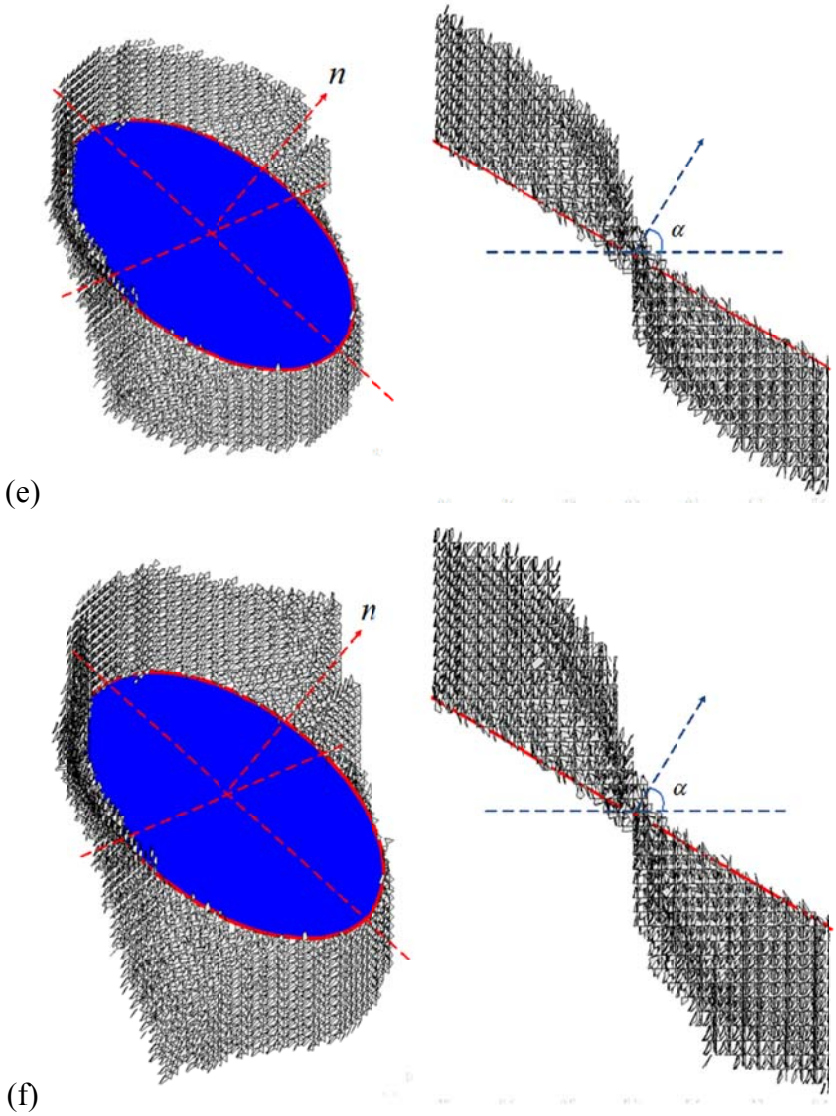

Figure 28. Fracture propagation stages: (a) initial fracture and (b–f) propagated fracture.

Figure 30 shows the fracture surface at failure from different viewpoints. For the purpose of visualization, the failure specimen is sliced into 6 pieces which is shown in Figure 31 and Figure 32. Figure 33 indicates the rotation angle of Mode III fracture between the middle slice and lateral surface of specimen. Also, it shows the fracture surface tends to propagate along vertical direction, or the maximum stress direction. As a result, according to the observed phenomenon, if the specimen is large enough, mode III fracture will gradually turn to be mode I which open in the direction of maximum tensile stress. Mode II fracture has the similar tendency that gradually propagates into mode I pattern which is shown in mode II fracture simulation above.

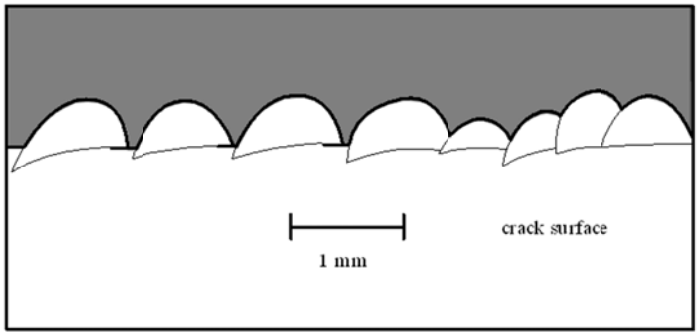

Figure 29. Close-up view of crack extension from the direction normal to the original crack as observed in experiments (Knauss, 1970).

This pattern of fracture propagation has been observed in experimental modeling of 3-D crack growth from pre-existing circular crack by (Adams and Sines 1978). Also, (Dyskin et al., 2003) tested wing crack model using a brittle material with the presence of the contact effect. In their experiments, (Dyskin et al., 2003) observed secondary cracks (called “wings") branched towards the axis of compression from the upper and lower tips of the initial circular crack due to mixed mode of K_{II} and K_{III} related to the contact between pre-existing crack surface (Figure 34)

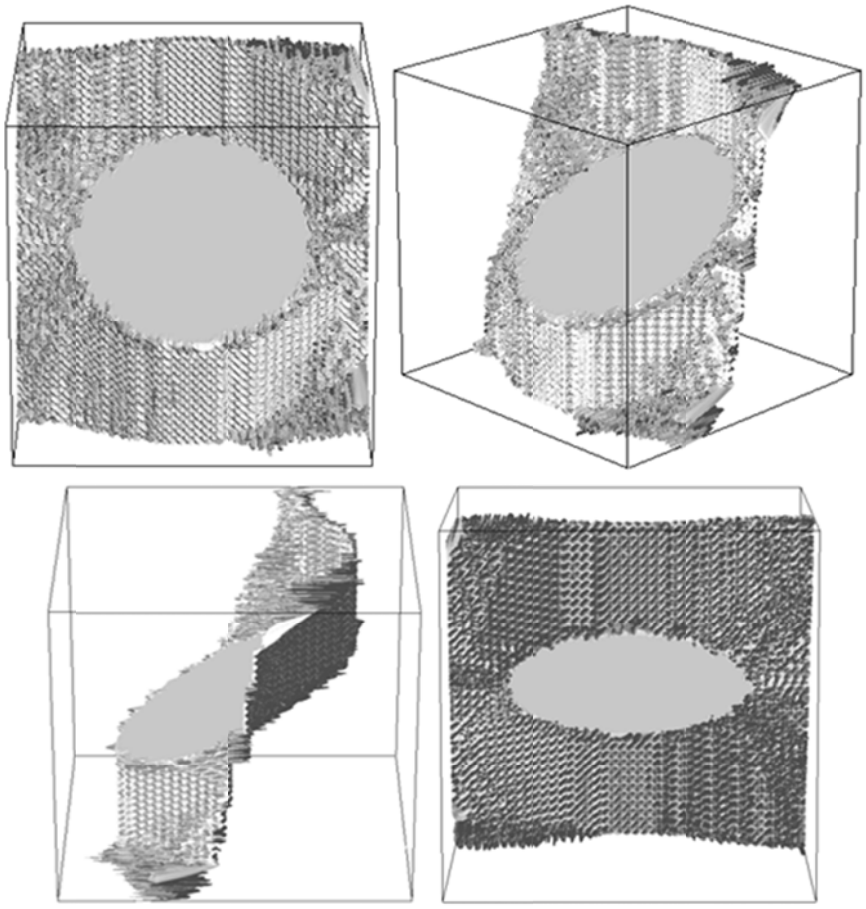

Figure 30. Illustration of fracture surface at failure.

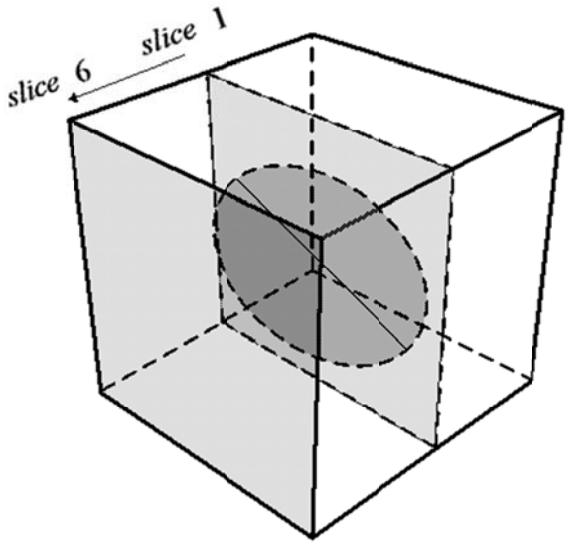

Figure 31. Illustration of the location of the slices in the specimen.

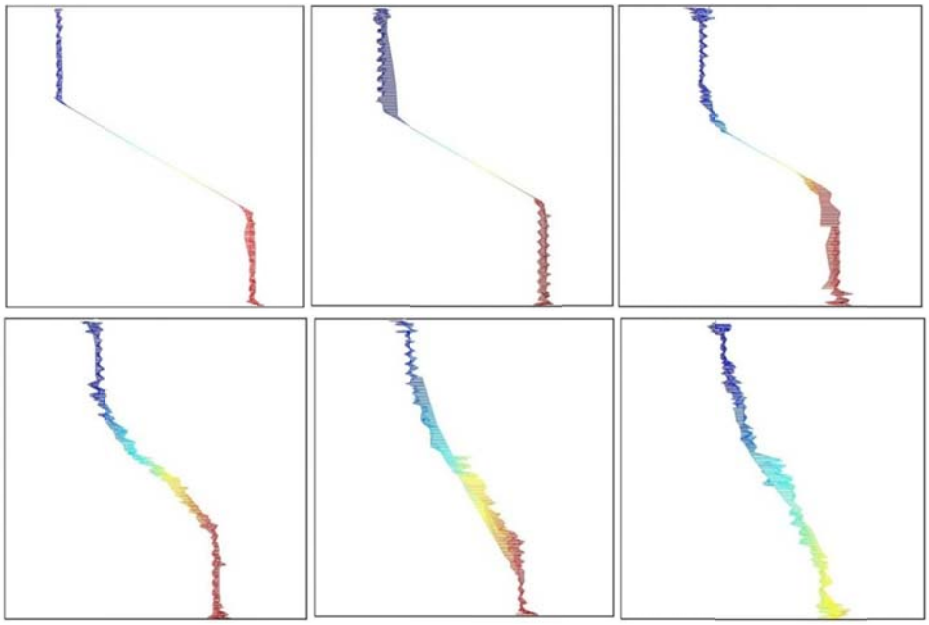

Figure 32. Illustration of fracture geometry (surface orientation) in the specimen for different slices from slice 1 to slice 6.

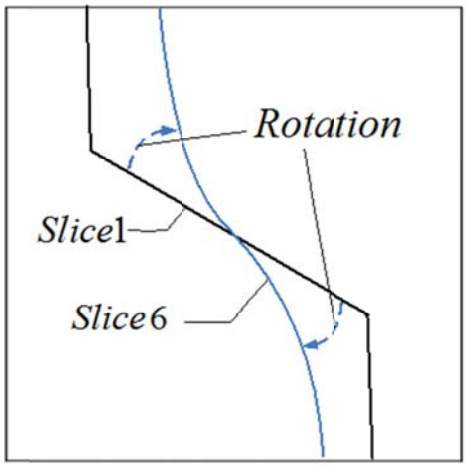

Figure 33. The fracture rotates between the middle slice and the side slice of the specimen as it propagates in mode III.

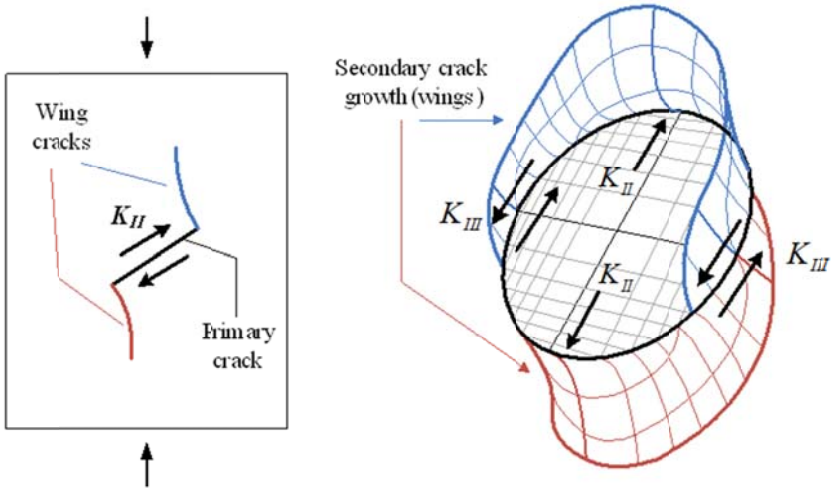

Figure 34. Two-dimensional wing crack growth (K_{II}) and 3D wing crack growth (mixed mode of K_{II} and K_{III}).

4.2 Simulation Examples of Thermal Fracturing

4.2.1 Functional test I: Single fracture

To examine the performance of thermo-mechanical VMIB formulation and 3D EPM in simulating thermal fracture propagation, a cubic sample of rock having a fracture at its top is simulated. The rock block and fracture dimensions are shown in Figure 35. Table 5 shows the parameters used in the present simulations. This dissertation assumed no friction between shearing fracture surfaces. Therefore, K_S is set to be very small. A small sample is used so that we may focus on the ability of the new VMIB constitutive model and its numerical implementation to capture softening by thermal stress. Since the size of the object is relatively small, the conduction of heat through the rock sample occurs in a short period of time. Therefore, a uniform cooling is assumed to test the mechanical response due to temperature change without taking into account the transience of temperature diffusion (this is consideration in the next section). The displacements of all rock surfaces except the top one are confined in the direction

perpendicular to them. The total number of elements is 156,975 and the total number of node number is 35,280. For each simulation step, a temperature drop of $0.15^{\circ}C$ is used with a total number of 120 steps.

Table 5. Simulation Parameters.

Parameters of intact element:	
Young's modulus, E	30.5 GPa
Poisson's ratio, ν	0.20
Tensile strain strength, ε_t	0.105×10^{-3}
Parameters of 3D EPM:	
Normal stiffness coefficient, K_n / h	10.0 GPa/m
Shear stiffness coefficient, K_s / h	10^{-8} GPa/m
Fracture width, h	1.0 mm
Parameters of 3D VMIB:	
c	0.15
n	4.0
Thermal properties of rock	
Thermal diffusivity, c^T	$1.6\times10^{-6} m^2/s$
Thermal expansion coefficient, α_m	$1.8\times10^{-5} K^{-1}$

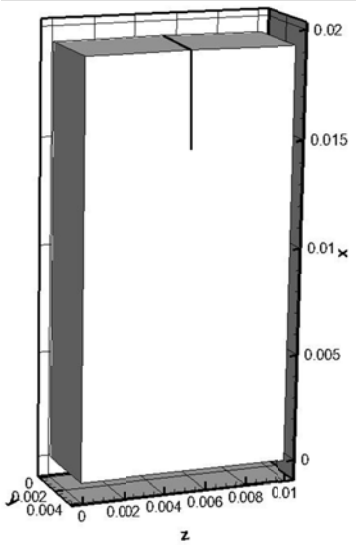

Figure 35. The problem geometry showing size and fracture set.

Figure 36(a)~(f) shows the deformed mesh configuration amplified 1200 times for different temperature drops. Figure 37(a)~(f) shows the middle slice of the maximum principal stress contour in the deformed configuration. Firstly, significant thermally induced volumetric displacements takes place near the pre-existing fracture surfaces due to the shrinkage of rock as shown in Figure 36(a). The fracture is forced to

open, causing stress concentration at its tip. With increasing cooling, the thermal stress and displacement increase, causing stress concentration at the fracture tip to rise bringing the tip region rock into softening stage, and finally resulting in the formation of a newly extended fracture. Figure 38 shows a plot of $\alpha_m K$ verses the maximum principal strain for the element at the initial fracture tip. Bulk modulus K retains its original value for a few steps and then, gradually degrades as the tensile strain reaches strain level at ultimate strength. This example verifies that the present model is capable of simulating the nonlinear process of thermal fracturing.

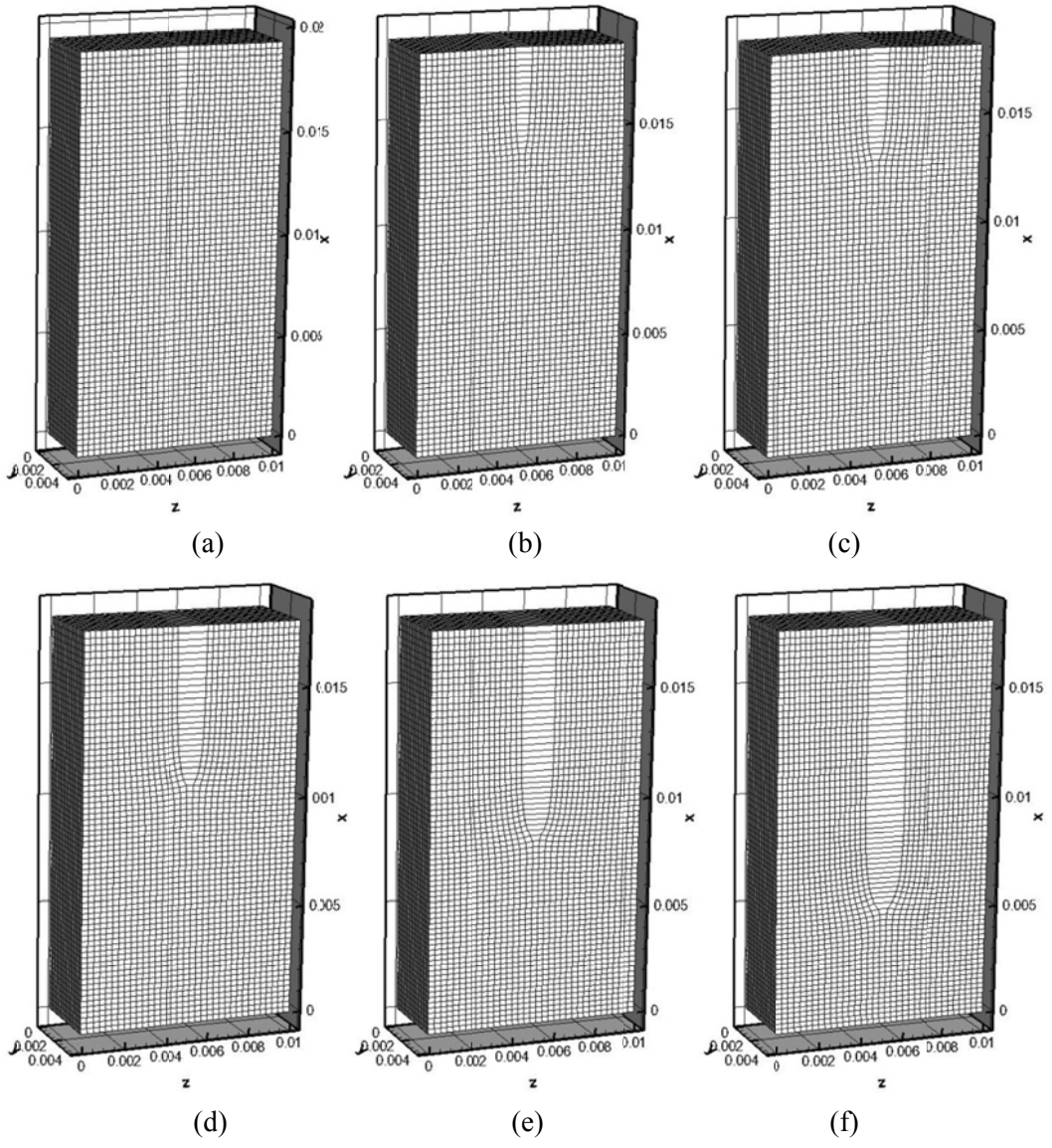

Figure 36. Deformed mesh configuration (amplified 1200 times) when the rock was cooled by: (a) $-3^{\circ}C$; (b) $-6^{\circ}C$; (c) $-9^{\circ}C$; (d) $-12^{\circ}C$; (e) $-15^{\circ}C$; (f) $-18^{\circ}C$.

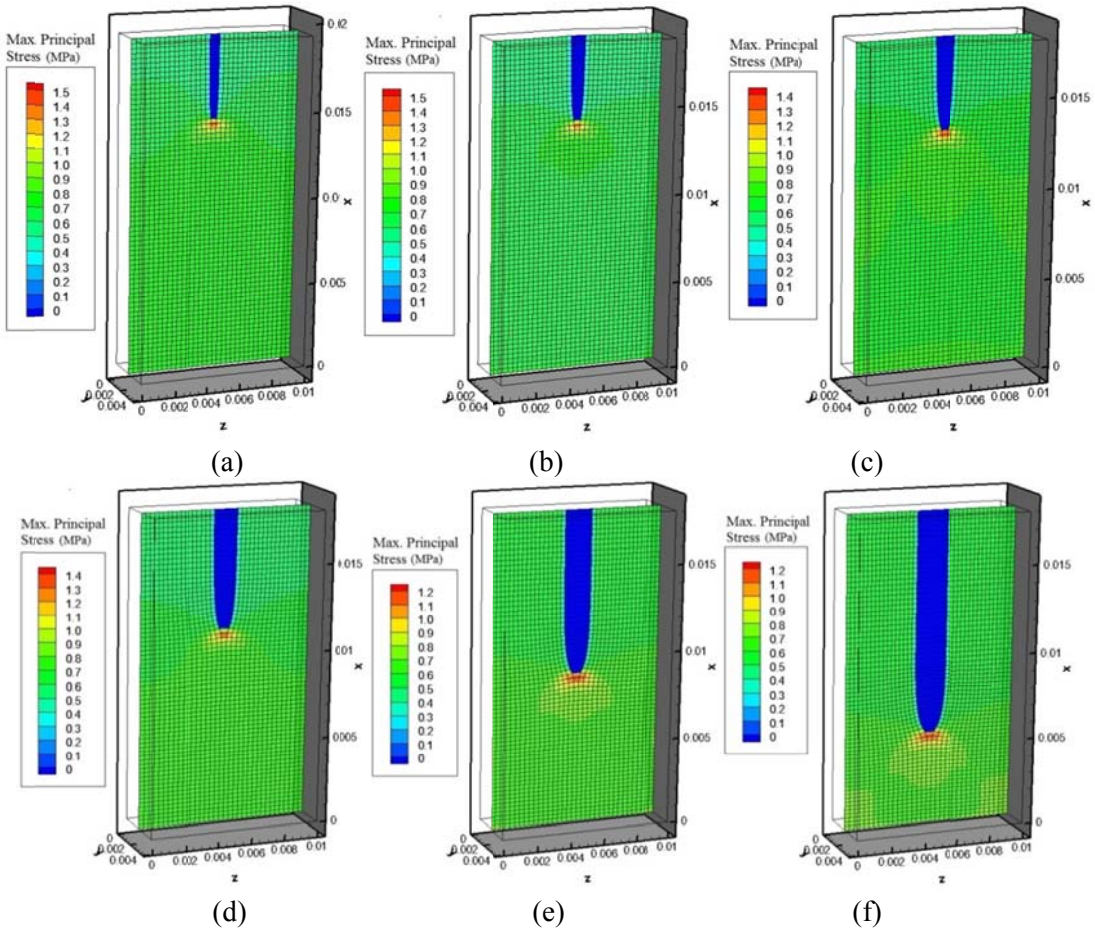

Figure 37. The middle slice of maximum principal stress contour with deformed mesh configuration (amplified 1200 times) when the rock was cooled by: (a) $-3^{\circ}C$; (b) $-6^{\circ}C$; (c) $-9^{\circ}C$; (d) $-12^{\circ}C$; (e) $-15^{\circ}C$; (f) $-18^{\circ}C$.

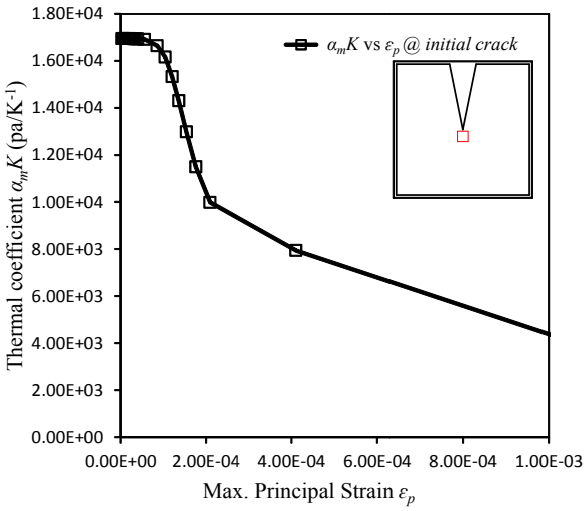

Figure 38. Thermal coefficient $\alpha_m K$ verse maximum principal strain for the element at the initial fracture tip.

4.2.2 Functional test II: Randomly distributed multiple fractures

The second simulation explores thermal fracture propagation and interaction. Taking advantage of 3D EPM to represent thermal response of fractures, multi-fractures can be simulated with a structured mesh without remeshing in the process of fracture propagation. A cubic specimen with 20 randomly distributed small fractures is considered. The dimensions are shown in Figure 39 and the material and model parameters are listed in Table 5. As before, uniform cooling is assumed to test the mechanical response of fractures to a temperature change. The total number of element is 380,880 and the total number of node number is 83,300. For each step, the temperature drop is $2.0^{\circ}C$ with a total number of 19 steps.

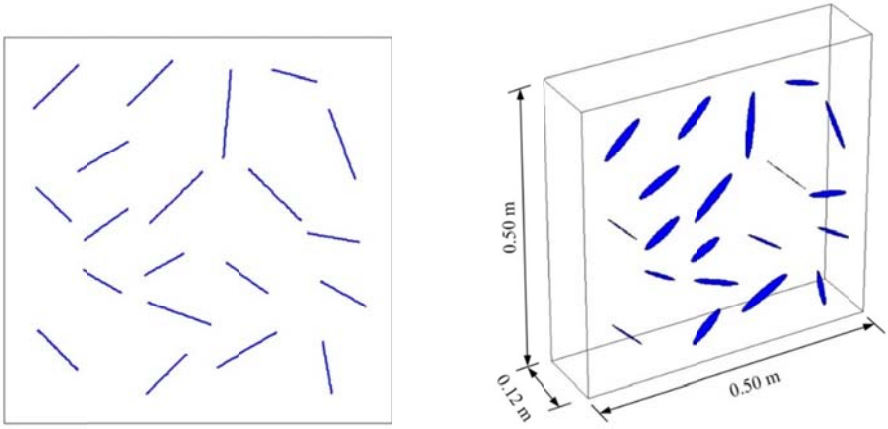

Figure 39. The problem geometry showing size and fracture set.

Figure 40 shows the propagation of thermal fractures. Initial fractures tend to open in the cooling process and then propagate in their initial plane. However, the displacement and stress fields are changed due to the existence of neighboring fractures. Therefore, fractures tend to converge during the cooling shown red lines in Figure 40(c) and red circle in Figure 41(c). Figure 41 (a)~(c) shows the maximum principal stress contour when the rock is cooled by (a) $-28^{\circ}C$, (b) $-34^{\circ}C$, and (c) $-38^{\circ}C$. Thermal stress is concentrated at each fracture tip as the fractures open due to material shrinkage. For the same reason, fracture opening releases the stress on the both side of the fracture surfaces (displayed by green and blue color). Logically, the thermal stress of areas surrounded by the fractures is largely released due to gradual loss of confinement during the propagation of fractures as shown Figure 41(c) highlighted in the red dash box.

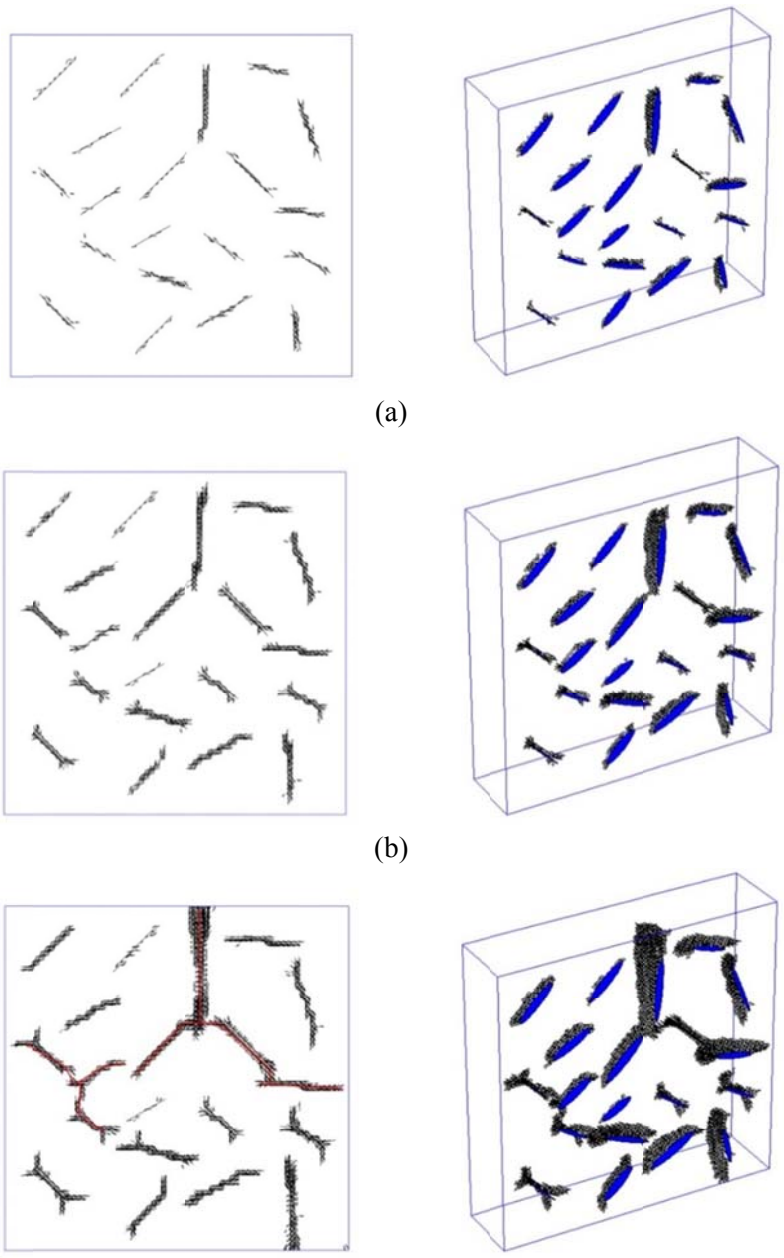

Figure 40. Propagation of thermal fracture when the rock was cooled by: (a) $-28^{\circ}C$; (b) $-34^{\circ}C$; (c) $-38^{\circ}C$.

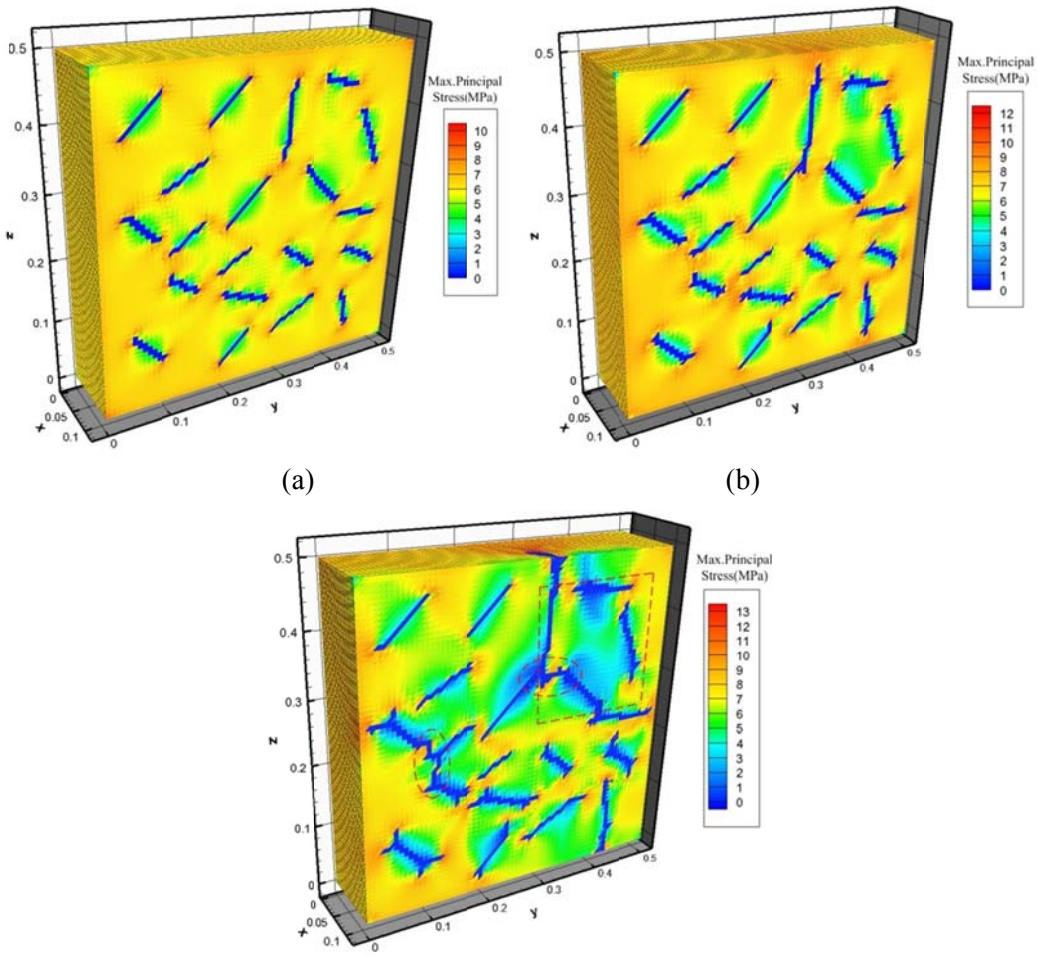

Figure 41. Maximum principal stress contour when the rock was cooled by: (a) $-28^{\circ}C$; (b) $-34^{\circ}C$; (c) $-38^{\circ}C$.

4.2.3 Multiple fractures emanating from a wellbore

Next, a wellbore is simulated with multiple pre-existing cracks emanating from it. A number of 16 initial cracks (3.33 to 4 cm in length) are equally spaced around the wellbore shown in Figure 42. Simulation parameters for this example are listed in Table 5. The initial temperature in the matrix is $220^{\circ}C$ and $40^{\circ}C$ on the surface of wellbore. Because it is assumed that all fractures cut through the rock in z direction and propagate in the x-y plane, a single layer of elements in z-direction is used, and all displacements in the z-direction are constrained to be zero. In the present meshing scheme, the total element number is 100,800 and the total node number is 40,800. Since the diffusion rate of temperature tends to become slower as time goes on, a gradually increasing time step scheme is utilized. The initial time step is 2 minutes, and then it is increased to 20 minutes after 20th step, 40 minutes after 50th step, 80 minutes after 100th step, 160 minutes after 150th step, 320 minutes after 200th step, 640 minutes after 250th step, respectively.

To simulate the impact of the in-situ stress, 2 different in-situ stress schemes are used in the examples, which are (a) $S_H = 6MPa$, $S_h = 6MPa$; (b) $S_H = 6MPa$, $S_h = 4MPa$. The results are summarized in

Figure 43 and Figure 44. Figure 43 shows the temperature field at 52.4 days after cooling process started. Figure 44 displays the maximum principal stress (tensile stress considered positive). The magnitude of thermal stress are indicated by the legends. The lighter shade shows higher thermal stress values (around the wellbore) where the cooling zone is located. Figure 44 also shows fracture propagation. Since the fracture creation relieves the stress of a fractured element to zero, the fractures are shown in dark color as they propagate near the wellbore. Moreover, lighter zones are found at the fracture tips where stress concentration occurs due to opening of fractures.

For the isotropic in-situ stress field, in Figure 44 (a), thermal fractures tend to propagate in radially. In this case, the in-situ stresses have no impact on the main direction of fracture opening. On the other hand, in Figure 44 (b), for anisotropic stress field, the dominant cracks grow in the direction of SH. It should be noted that the fractures do not propagate symmetrically although the domain is symmetric. This is caused by use of an asymmetric mesh scheme and the EPM in which newly extended fractures are combined with the discontinuous fracture surface of the cracked elements. Moreover, the thermal fracture propagation is very sensitive to the length of the fractures and the space between them, especially when multiple fractures are competing to grow. A higher thermal-induced stress arises at the tips of the longer fractures or the fractures with larger area in between (Tarasovs and Ghassemi, 2014, Geyer and Nemat-Nasser, 1982). The fractures length and spacing could be slightly different during the transient cooling so that the thermal fractures propagate in an asymmetric pattern. The contrast in magnitudes of the maximum and minimum in-situ stress still plays the major role on the propagation orientations.

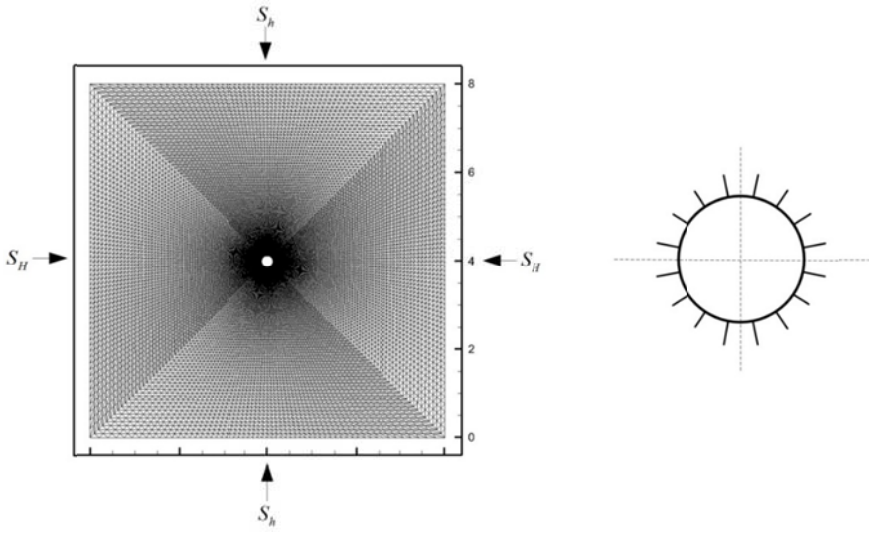

Figure 42. (a)The problem geometry and (b)fractures distribution.

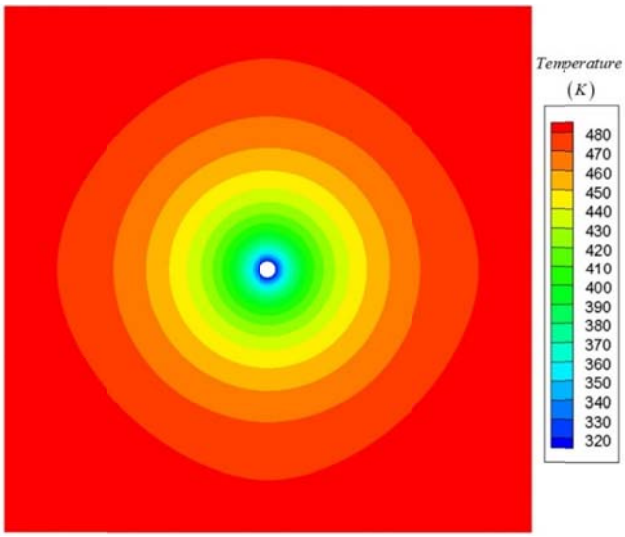

Figure 43. Temperature contour at 52.4 days after cooling process started

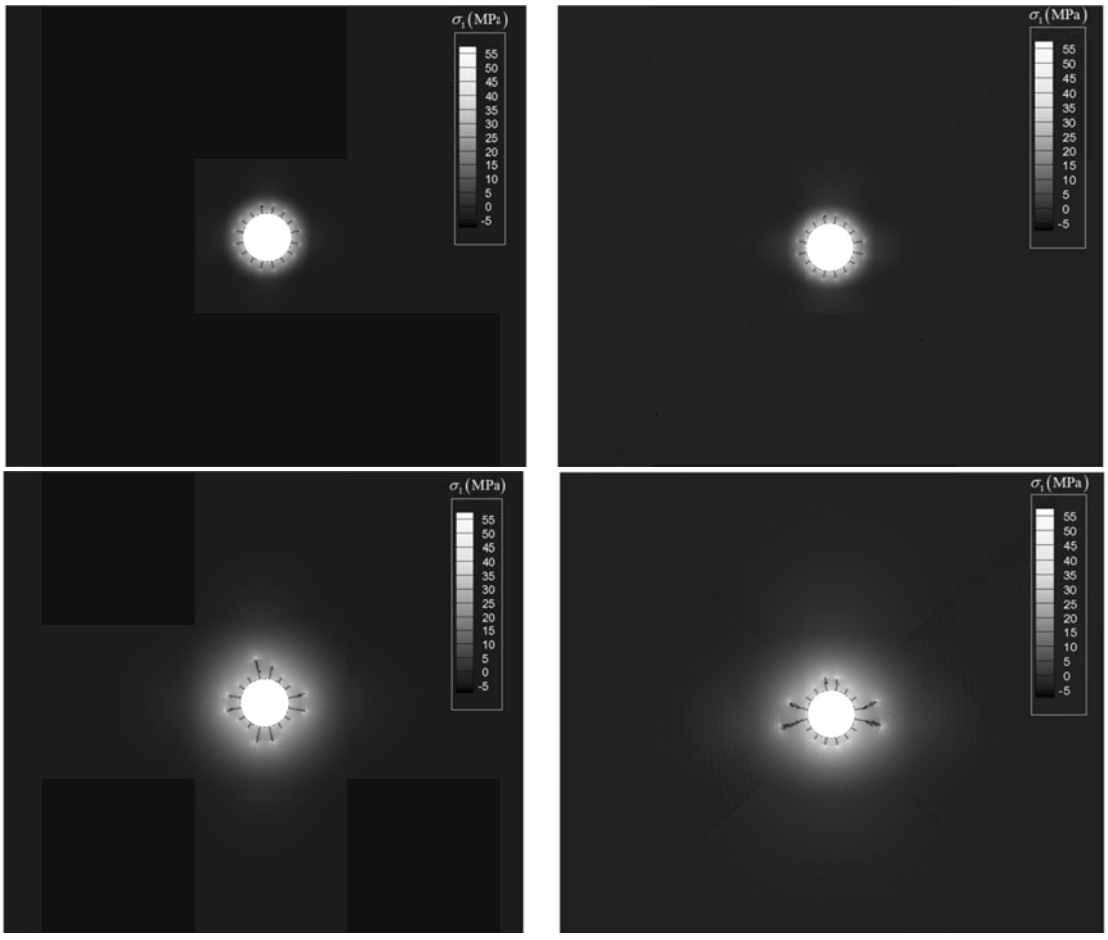

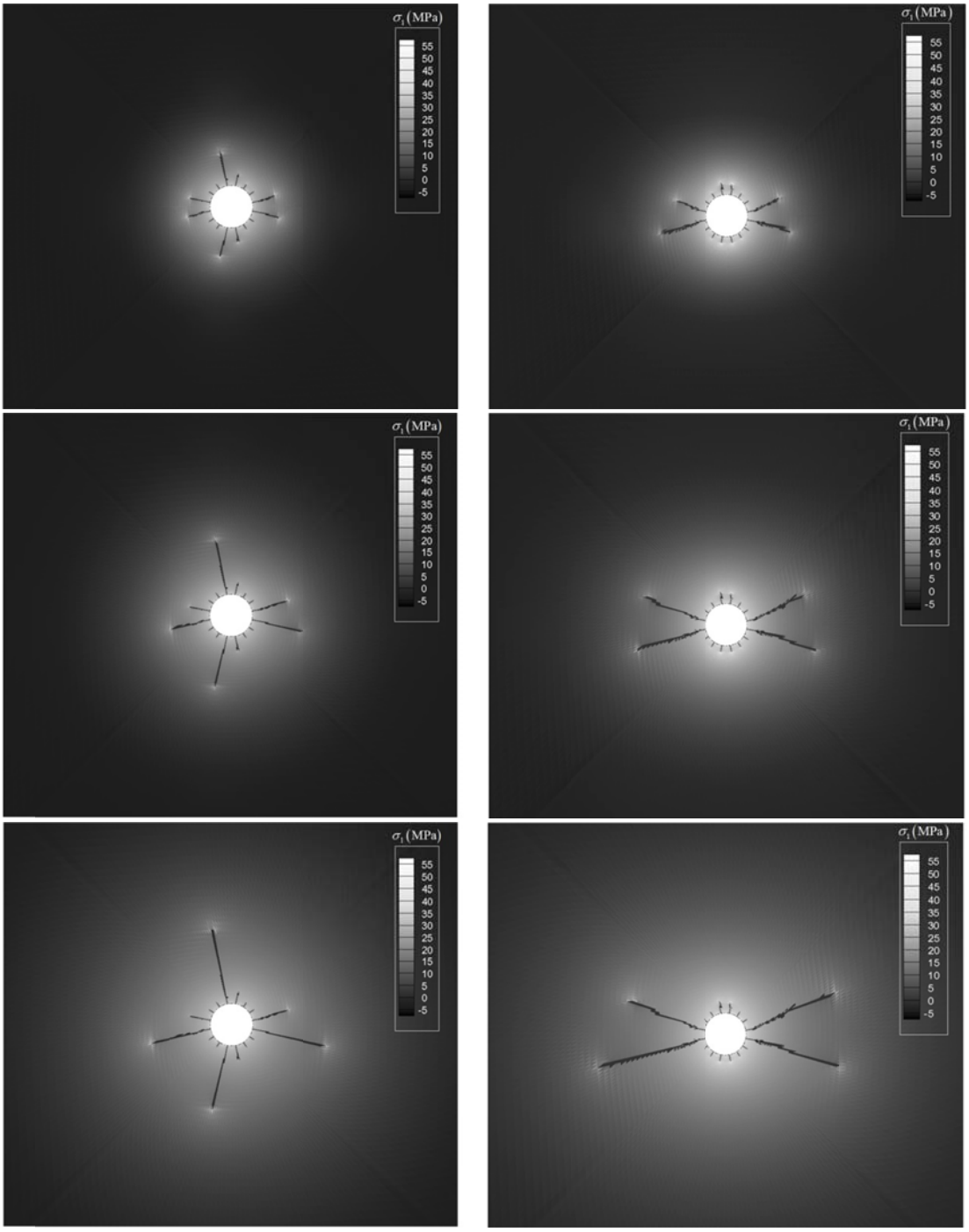
σ_1 (MPa)
55
50
45
40
35
30
25
20
15
10
5
0
-5

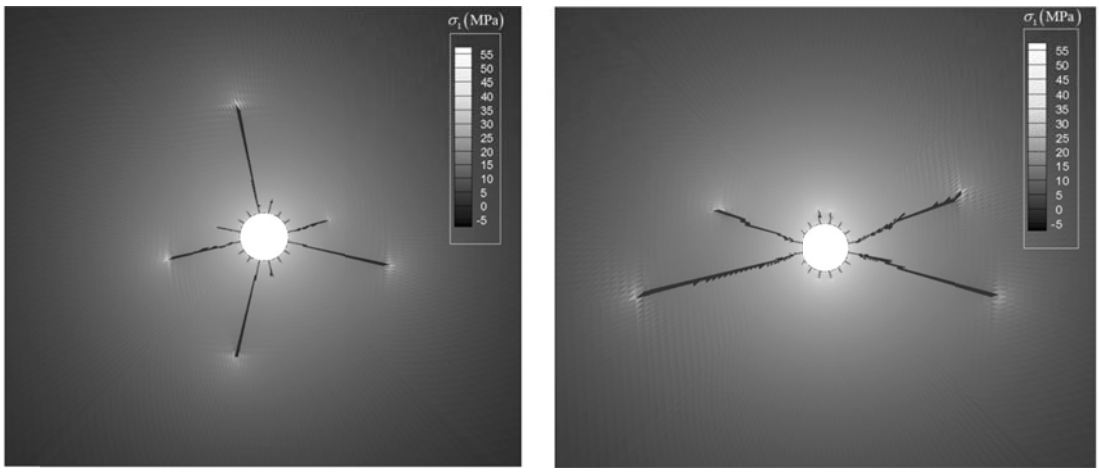

(a) (b)

Figure 44. Maximum principal thermal stress contour: (a) $S_H = 6MPa$, $S_h = 6MPa$; (b) $S_H = 6MPa$, $S_h = 4MPa$.

Numerical simulation of 3D thermal fracture propagation in brittle rock was studied using VMIB model combined with 3D EPM method. Nonlinearities of mechanical behaviors and thermal parameters of the solid material were captured by introducing a nonlinear VMIB constitutive model. The 3D EPM associated with thermal parameters modification for fractured elements provided a simple way to represent the pre-existing fracture in structured mesh. The examples of functional test provided evidences for the validation of presented method. Test I showed the reasonable results of nonlinear thermal response and fracture development of rock when it is under uniform cooling. Test II was designed to perform the ability of the model to treat the random distributed fractures with structured mesh. The simulations in wellbore condition studied the thermal fracturing emanating from wellbore surface and the impact on the propagation patterns from the in-situ stress. The present model provided a new way to predict 3D thermal fracturing.

5. Modeling 3D Hydraulic Fracture Propagation Using VMIB

The hydraulic fractures in geothermal reservoirs and unconventional petroleum resources are subjected to high in-situ stresses that highly influence the fracture propagation. To examine this, consider an embedded elliptical fracture of finite area that is driven by a uniform hydraulic pressure in an infinite underground space. The problem geometry is shown in Figure 45, and the material and the corresponding model parameters are listed in Table 4. To increase the efficiency of the simulation, half of the embedded fracture is simulated using the problem symmetry. In the presented meshing scheme, there are 26 rows of nodes plotted on x direction, and both 42 rows of nodes on y and z direction. The total element number is 210125 and the total node number is 45864. Initially, a hydraulic pressure p_0 is applied to the fracture. Then the fracture is increasingly pressurized by an increment of $\Delta p = 0.07MPa$. A series of fracture propagation case are studied using the following four in-situ stresses:

Case I: $\sigma_V = 0.8$, $\sigma_h = 0.8$, $\sigma_H = 0.8$, $p_0 = 1.6MPa$;

Case II: $\sigma_V = 1.6$, $\sigma_h = 0.8$, $\sigma_H = 0.8$, $p_0 = 2.4MPa$;

Case III: $\sigma_V = 2.0$, $\sigma_h = 0.8$, $\sigma_H = 0.8$, $p_0 = 2.8MPa$;

Case IV: $\sigma_V = 2.4$, $\sigma_h = 0.8$, $\sigma_H = 0.8$, $p_0 = 3.2MPa$;

In Case I the angle of inclination, α, is set to be 45 degree to decrease the boundary effect. α in other cases is set to be 30 degree. The simulation results for these cases are shown in Figure 46 to Figure 48.

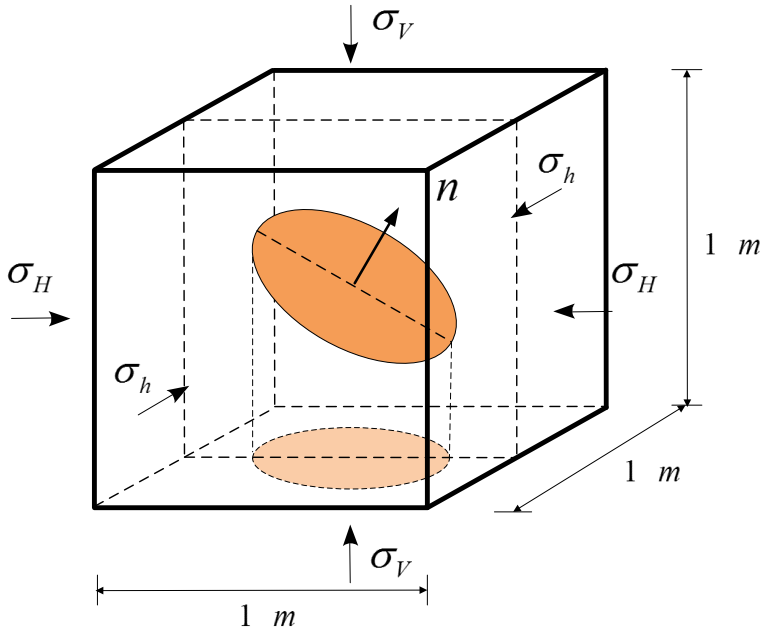

Figure 45. Problem geometry and in-situ stress directions.

When the fracture is pressurized, both the strain and the stress are concentrated near its tip. However, in case of the 3D embedded elliptical fracture, the fracture tip is an ellipse, and the stress strain state is different along the tip contour depending on the certain geometry and in situ stress. Thus, different fracture propagation modes might occur at different locations of the fracture tip contour. Figure 46a shows the fracture propagation in the isotropic stress field (Case I). As the applied stress state is symmetric for the 45-degree crack, the fracture propagates on its original plane under the action of the applied stress field. The fracture advances straightforward when the applied uniform hydraulic pressure exceeds the normal stress on the plane of the fracture. Figure 46b shows the fracture propagation for the Case II. The upper and lower fracture tips develop slightly inclined to the vertical direction, that is, the maximum stress direction. This can be observed more clearly in Case III, shown in Figure 46c. The final path is steeper than that of Case II, tending to the maximum in situ stress direction. As σ_V increases, the pattern of fracture propagation at the upper and lower wings of original fracture changes from Mode I to combined Modes I and II. To illustrate this, the middle slice of the rock block, which contains only the upper and lower end tips, is considered, and the resulting fracture path is shown for each stress state in Figure 47. Figure 48 shows the final propagation of the half elliptical fracture. In Case I, shown in Figure 48a, the fracture propagates as Mode I despite the location of the fracture tip. From Figure 48b–c, mixed mode propagation (Modes I and II) occurs at both upper and lower edges of the original fracture. On the side tips, the fracture develops outward and connects with the fractures on the upper and lower ends to form a curved surface, a typical behavior of Mode III fracture.

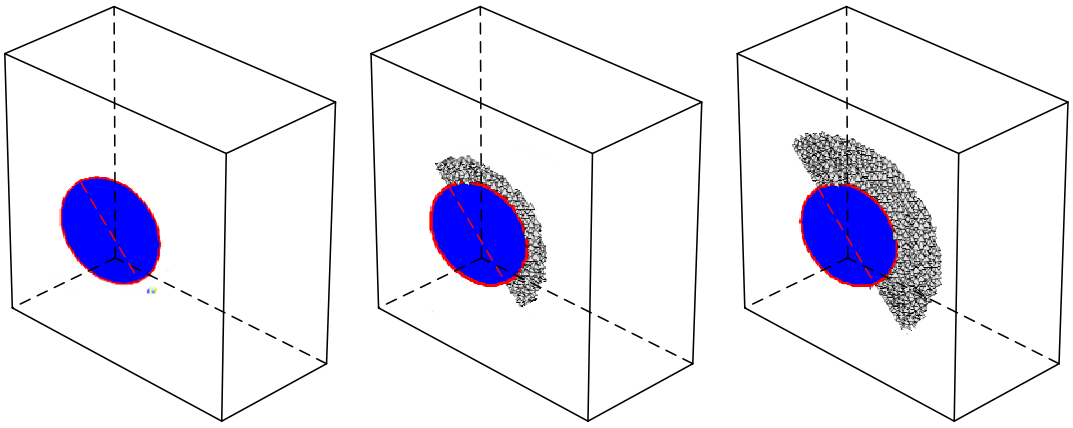

(a)

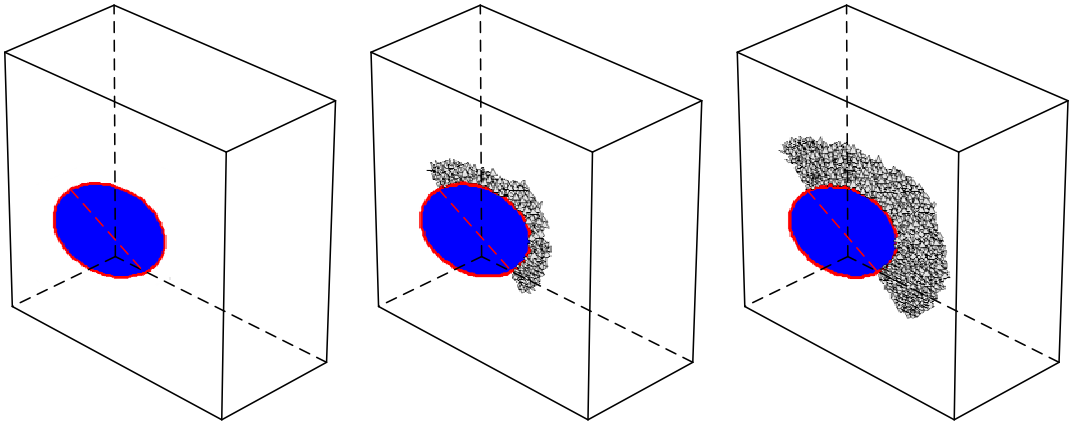

(b)

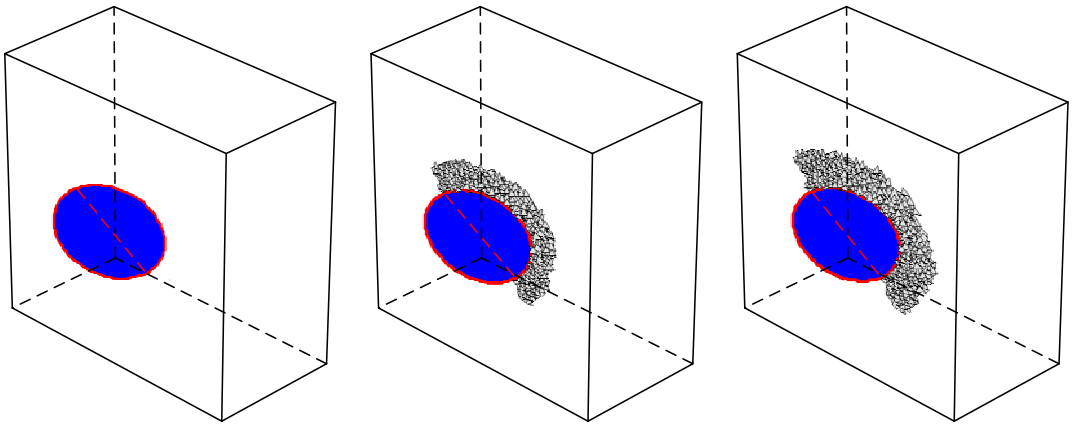

(c)

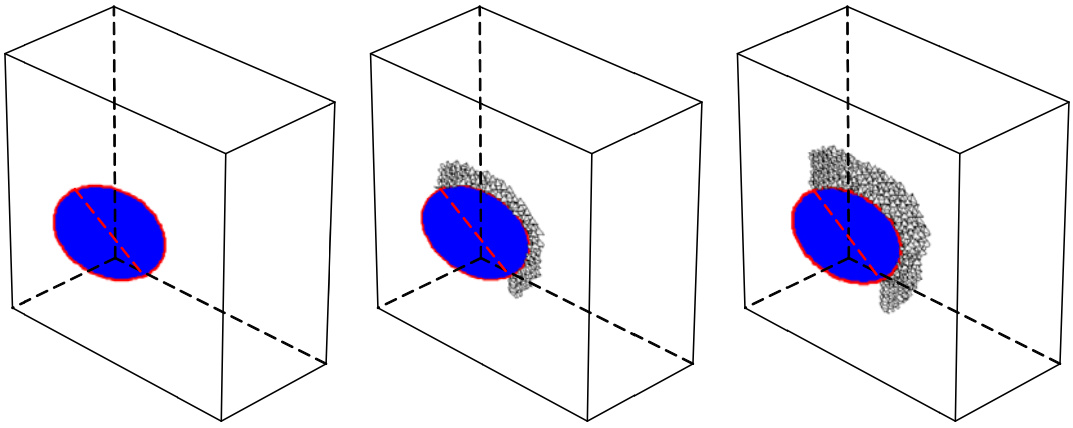

(d)

Figure 46. Simulated hydraulic fracture propagation paths: (a) Case I, (b) Case II, (c) Case III, and (d) Case IV

Case IV, when σ_V is three times σ_h and σ_H, is particularly interesting. As shown in Figure 47d and Figure 48d, the tips of the upper and lower wings develop parallel to the vertical in situ stress. However, the fracture propagation is different on the side tip. Two separate fractures are formed at the side tip shown in Figure 48d. The reason for this is the strong tendency of the fracture propagation at the upper and lower tips to develop vertically. Moreover, hydraulic pressure in the newly extended fracture tends to force the fracture open in the direction normal to the hydraulic pressure. Consequently, the new fracture on the side tip cannot connect the upper and lower parts of fracture. In other words, the upper and lower parts are more favorable to propagate in their own direction, resulting in segmentation on the fracture front. This is an important aspect of Mode III fracture propagation that is very challenging to numerically simulate.

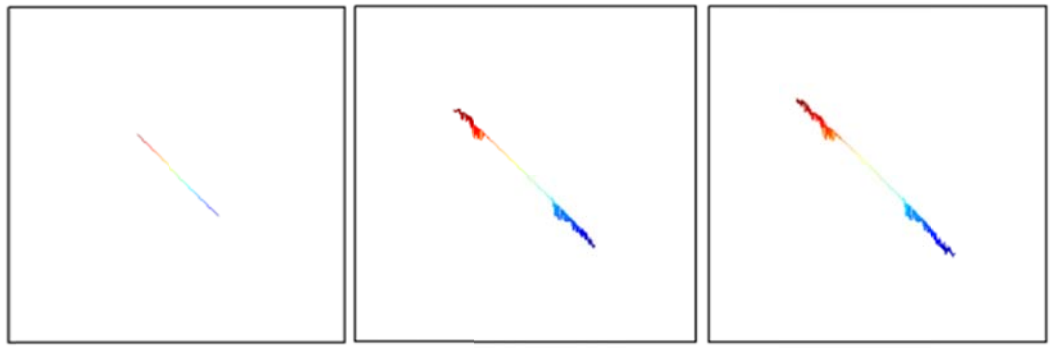

(a)

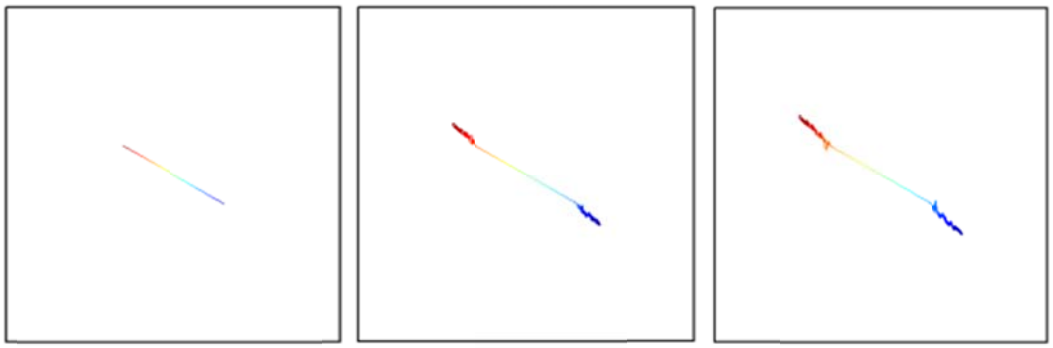

(b)

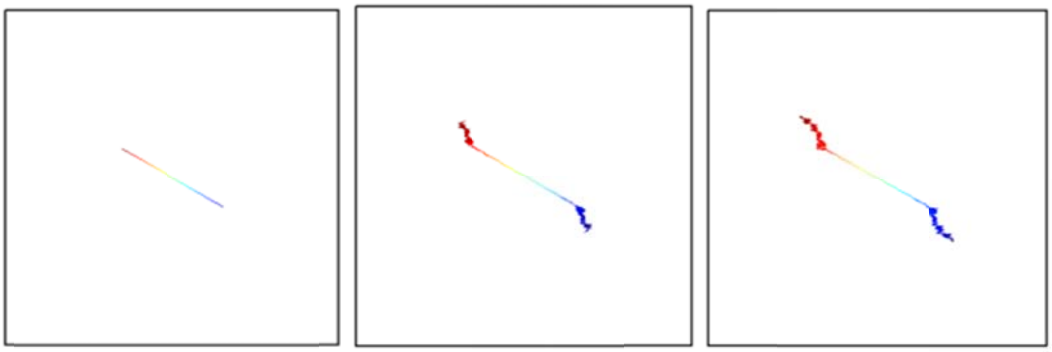

(c)

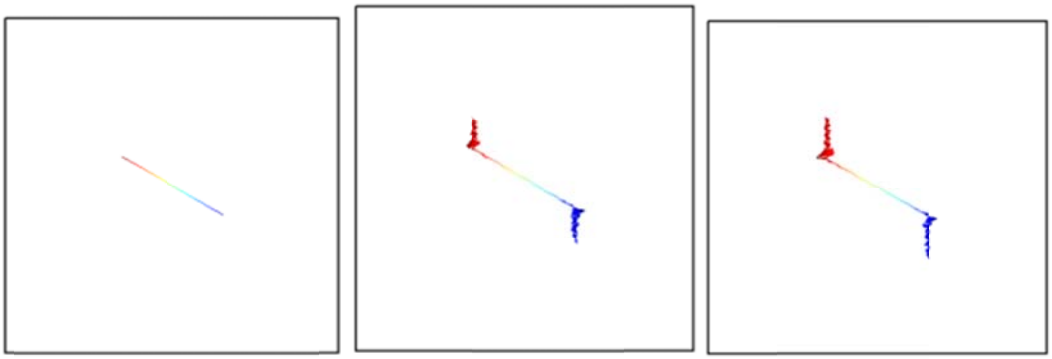

(d)

Figure 47. . Illustration of fracture propagation path for the middle slice: (a) Case I, (b) Case II, (c) Case III, and (d) Case IV.

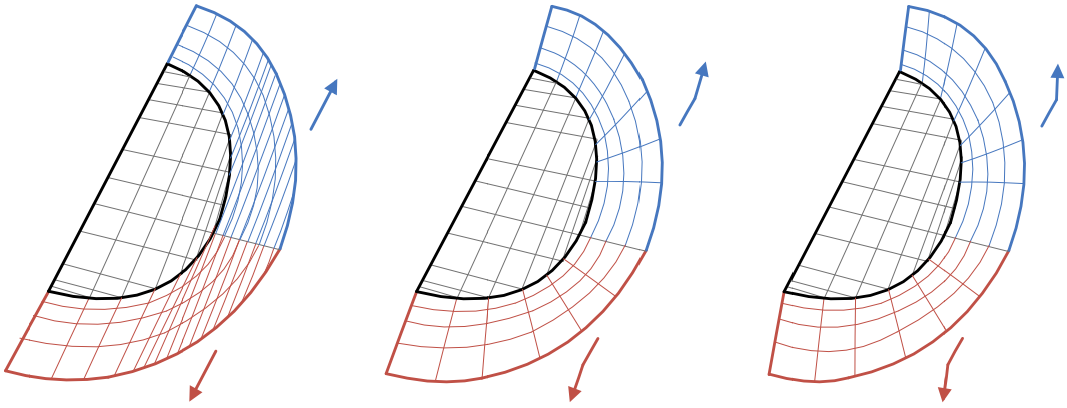

(a) (b) (c)

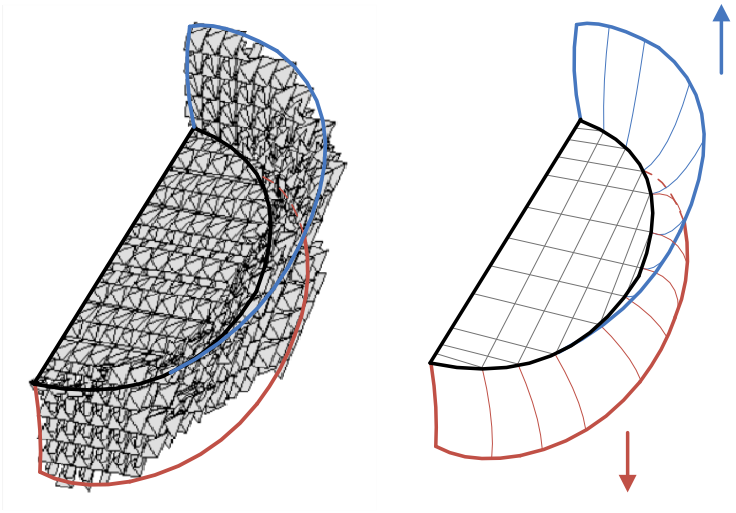

(b)

Figure 48. . Final shape of propagated hydraulic fracture: (a) Case I, (b) Case II, (c) Case III, and (d) Case IV.

5.1 Mesh Size Sensitivity

In realistic material, the strength degradation causes by micro crack and void development. The material failure results from interconnection of micro crack and emerging of macro crack. In element based methods and strain softening constitutive models like VMIB, the micro-cracks growth are homogenized in an implicit way within a representative volume that usually is the element size. Since one element size is the minimum representative volume, the softening usually localized in a narrow region that is controlled by the size of the element. Therefore, VMIB model becomes highly affected by the mesh size and alignment causing non-physical predictions of fracture proceeding area.

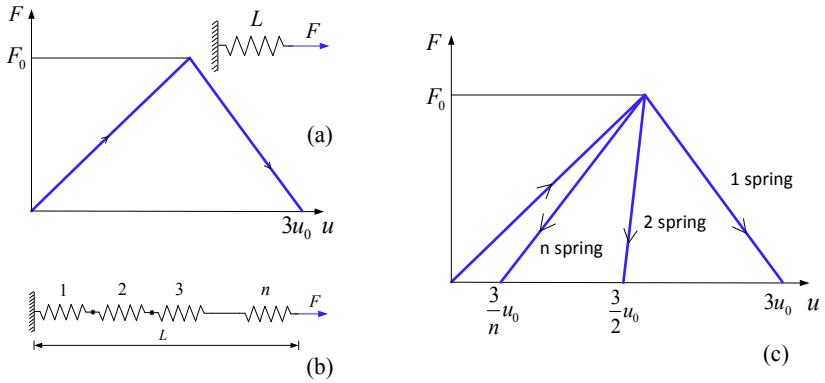

Figure 49. (a) Softening behavior of a single spring; (b) spring system and (c) displacement-force diagrams from different number of springs (Bazant and Planas, 1998).

(Bazant and Planas, 1998) described the phenomenon as mesh size dependency. It has been discussed in numerical results from a 1D spring system with total length L shown in Figure 49(a). Figure 49(a) shows the softening behavior of a single spring by stretching. Figure 49(c) shows the displacement-force curves

from different number of springs in the system. The post-peak behaviors, therefore, depend on the number of springs in the system. When n springs are used, the post-peak curve will snap back to $\frac{3}{n}u_0$. The tendency of post-peak curve is turning back to the original point if the number of springs n goes infinite that indicates the energy dissipation during the whole loading and failure process tends to be zero, which is physically unrealistic.

The original VMIB model used unique cohesive law for all elements with different size. However, the fracture energy is not conserved and model is subjected to mesh size dependency. Through analysis using J-integral (Rice, 1968), the outline of localization zone is taken as the integral path Γ, the J-integral (23) along Γ can be computed as

$$J = \int_{\Gamma}\left(\mathbf{W}dy - T\cdot\frac{\partial \mathbf{U}}{\partial x}ds\right) = -\int_{coh}\sigma_n\frac{du_n}{dx}dx = \int_0^{u_n^*}\sigma_n du_n \approx h\int_0^{\varepsilon_u}\sigma_n d\varepsilon_y \tag{111}$$

where W is the strain energy density, T and U are the traction and separation vector of cohesive zone respectively, h is the length scale of localization zone, $u_n = h\boldsymbol{\varepsilon}$ is the normal separation, u_n^* is the critical separation when cohesive stress becomes zero, $\varepsilon_u = u_n^*/h$. In J integral along Γ, a length scale h that is proportional to the fracture energy in the VMIB model. Therefore, the bond density potential has to consider strength and fracture energy conjugated with the localization zone size to eliminate the mesh size dependency.

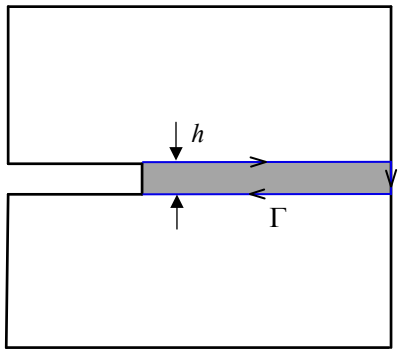

Figure 50. The path of J-integral contours along the outline of localization zone.

5.2 VMIB Model with Hyperelastic Bilinear Potential Considering Fracture Energy Conservation

At different scales, the constitution of material has different representation. Generally, material is considered as continuum at macro scale and particle at microscale shown as Figure 51. In VMIB theory, material is consisted by randomized mass particles at the micro scale. The particles are connected by virtual bonds that provide both longitudinal and rotational resistances in Figure 51(c). The behaviors of bonds govern the mechanical response of material according to relative displacements of paired particles. These particles are not realistic physical particles such as atom or molecule. The macroscopic continuum behavior is descripted by microscopic interaction of particles through homogenization. By Cauchy–Born

rule, the strain energy function in the VMIB model is characterized. A change in the configuration of a continuum body results in displacement that is composed by rigid-body displacement and deformation. The material points in the undeformed configuration are described by the Lagrangian (Material) coordinates $X = (X_1, X_2, X_3)$. The corresponding material points in the deformed configuration is described by Eulerian (spatial) coordinates $x = (x_1, x_2, x_3)$. The deformation gradient is given by

$$F_{iI} = \frac{\partial x_i}{\partial X_I} \tag{112}$$

From deformation gradient, the Green-Lagrange strain tensor is given by

$$E_{IJ} = \frac{1}{2}\left(F_{iI}F_{iJ} - \delta_{IJ}\right) \tag{113}$$

where δ_{IJ} is the Kronecker delta. In the hyperelastic theory (Marsden and Hughes, 1983; Ogden, 1984), Ψ is the strain energy density function. The Piola-Kitchhoff stress tensor is

$$S_{IJ} = \frac{\partial \Psi}{\partial E_{IJ}} \tag{114}$$

The material elastic tensor is

$$C_{IJKL} = \frac{\partial S_{IJ}}{\partial E_{KL}} = \frac{\partial^2 \Psi}{\partial E_{IJ}\partial E_{KL}} \tag{115}$$

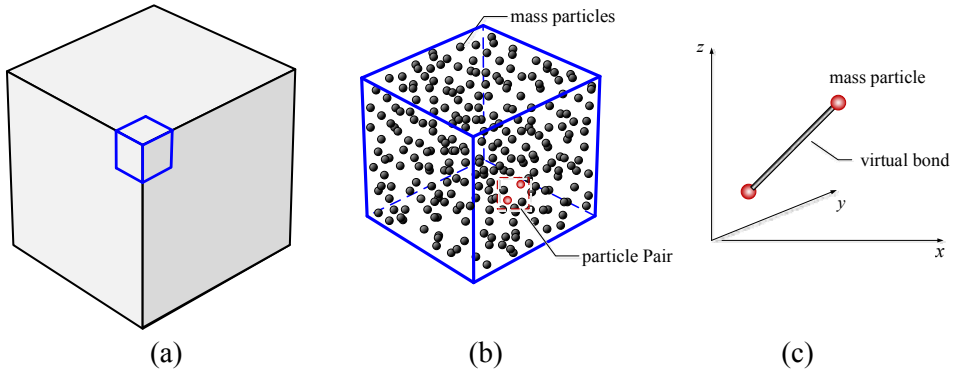

(a) (b) (c)

Figure 51. Material constitution at (a) macro scale and (b) micro scale consisting of randomized material particles that are bonded with (c) virtual bonds.

Each micro bond is described by a potential:

$$\Phi = \Phi_l + \Phi_\beta \tag{116}$$

where l is bond stretch and β is bond rotation angle. In small deformation case, E_{IJ} and S_{IJ} reduce to the strain ε_{ij} and stress σ_{ij} respectively of linear elasticity (Gao and Klein, 1998). According to the Cauchy–Born rule (Milstein,1980; Tadmor et al., 1996), the bond deformation Δ contain:

$$l = l_0 \xi_i \varepsilon_{ij} \xi_j, \ \beta_1 = \xi_i \varepsilon_{ij} \eta'_j, \ \beta_2 = \xi_i \varepsilon_{ij} \eta''_j, \ \beta_3 = \xi_i \varepsilon_{ij} \eta'''_j \tag{117}$$

where l_0 is the original bond length, $\boldsymbol{\xi} = (\sin\theta\cos\phi, \sin\theta\sin\phi, \cos\theta)$ is the unit orientation vector of bond in sphere coordinate system and ε_{ij} is the strain tensor. β_1, β_2 and β_3 are rotation angles of bond towards three coordinate axes $\mathbf{x}_1$, $\mathbf{x}_2$ and $\mathbf{x}_3$ respectively. $\boldsymbol{\eta}'$, $\boldsymbol{\eta}''$ and $\boldsymbol{\eta}'''$ are unit vectors perpendicular to the direction indicated by $\boldsymbol{\xi}$ of normal bond.

The average strain energy density of the representative volume element can be written as follows

$$\Psi = \frac{1}{V}\left\langle \Phi_l + \Phi_\beta \right\rangle \tag{118}$$

where V is the volume of representative element and $\langle \cdots \rangle = \int_0^{2\pi}\int_0^{2\pi} (\cdots) D(\theta,\phi)\sin\theta d\theta d\phi$. $D(\theta,\phi)$ is the bond density function. The bracket $\langle \cdots \rangle$ represents a homogenization process. The homogenization process integrals and diminishes the individual behaviors of all micro bonds in the representative volume.

From Eqs. (3) and (4) and assumption of small deformation, the stress tensor of the representative element is derived as

$$\sigma_{ij} = \frac{\partial \Psi}{\partial \varepsilon_{ij}} = \frac{1}{V}\left\langle \Phi_l' \cdot \frac{\partial l}{\partial \varepsilon_{ij}} + \frac{\partial \Phi_\beta}{\partial \beta_1}\cdot\frac{\partial \beta_1}{\partial \varepsilon_{ij}} + \frac{\partial \Phi_\beta}{\partial \beta_2}\cdot\frac{\partial \beta_2}{\partial \varepsilon_{ij}} + \frac{\partial \Phi_\beta}{\partial \beta_3}\cdot\frac{\partial \beta_3}{\partial \varepsilon_{ij}} \right\rangle \tag{119}$$

We assume $\Phi_\beta' = \frac{\partial \Phi_\beta}{\partial \beta_1} = \frac{\partial \Phi_\beta}{\partial \beta_2} = \frac{\partial \Phi_\beta}{\partial \beta_3}$ and rewrite Eq. (9) yields

$$\sigma_{ij} = \frac{\partial \Psi}{\partial \varepsilon_{ij}} = \frac{1}{V}\left\langle \Phi_l' \cdot l_0 \xi_i \xi_j + \Phi_\beta' \cdot (\xi_i \eta_j' + \xi_i \eta_j'' + \xi_i \eta_j''') \right\rangle \tag{120}$$

The modulus matrix C_{ijkl} is derived as

$$C_{ijkl} = \frac{\partial^2 \Psi}{\partial \varepsilon_{ij}\partial \varepsilon_{kl}} = \frac{1}{V}\left\langle \Phi_l'' \cdot l_0^2 \xi_i \xi_j \xi_k \xi_l + \Phi_\beta'' \cdot (\xi_i \eta_j' \xi_k \eta_l' + \xi_i \eta_j'' \xi_k \eta_l'' + \xi_i \eta_j''' \xi_k \eta_l''') \right\rangle \tag{121}$$

For elastic and isotropic case, Φ_l'', Φ_β'' are constant and $D(\theta,\phi) = 1.0$. For material nonlinearity, a phenomenological cohesive law is introduced to represent hyperelastic and softening behaviors. The following exponential function (Gao and Klein 1998; Klein and Gao 1998; Zhang et al. 2002; Klein et al. 2001; Nguyen et al. 2004; Thiagarajan et al. 2004) is typical one used as bond density potential in VIB model

$$\Phi_l' = A(l - l_0)\exp\left[-(l - l_0)/B\right] \tag{122}$$

where A is a Young's modulus related parameter and B is related to fracture energy. The nonlinear macro properties of material such as softening and degradation are expressed by introducing the bond strength or density evolution. The evolution law is characterized by mechanical behaviors of material failure test.

5.3 VMIB With Fracture Energy Conservation

Many works (Hillerborg et al., 1976, Bazant and Planas, 1998, Kyoungsoo et al., 2008) introduced a localization zone size according to this length scale for the simulations. This is feasible for problems with simple geometry and known fracture propagating direction and patterns. For complex stress state in three

dimension and mix-mode fracture problem, the localization zone remains unknown before analysis. Therefore, to capture fracture propagation without pre-assuming localization zone, the present work considers every element as potential localization zone. If element type and shape are known, the length scale h of each element is proportion to element volume. (Bazant and Becq-Giraudon, 2002) introduced two fracture energies to G_f and G_F that are needed for accurate structural analysis considering size effect. G_F is total fracture energy that corresponds to total work under the softening curve. G_f is the initial fracture energy that primary depends on peak strength. Accordingly, (Park etc., 2008) described a bilinear softening model for concrete shown as Fig.4. The bilinear softening curve was defined tensile stress f_t', initial fracture energy G_f and total fracture energy G_F. The vertical coordinate of kink point is $\beta f_t'$. w_{cr}, w_1, w_k and w_f are crucial crack openings width during the softening process, which are determined by the peak strength, fracture energy and location of kink point. According to Figure 52, the stress responds to given crack opening is

$$\sigma = \begin{cases} \dfrac{w}{w_{cr}} f_t & \text{if} \quad 0 < w < w_{cr} \\ \dfrac{(w - w_1) f_t}{w_{cr} - w_1} & \text{if} \quad w_{cr} < w < w_k \\ \dfrac{(w - w_f) f_t}{w_k - w_f} & \text{if} \quad w_k < w < w_f \\ 0 & \text{if} \quad w_f < w \end{cases} \tag{123}$$

and tangential stiffness is

$$k = \begin{cases} f_t / w_{cr} & \text{if} \quad 0 < w < w_{cr} \\ f_t / (w_{cr} - w_1) & \text{if} \quad w_{cr} < w < w_k \\ f_t / (w_k - w_f) & \text{if} \quad w_k < w < w_f \\ 0 & \text{if} \quad w_f < w \end{cases} \tag{124}$$

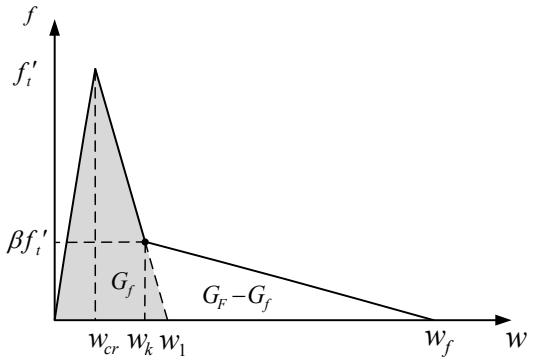

Figure 52. Bilinear softening model for concrete where f_t is tensile strength, G_f is initial fracture energy; and G_F is total fracture energy.

Adapting the idea of bilinear softening model, the bond cohesive law of VMIB incorporate the material's fracture energy shown as Figure 53, where g_F and g_f are the fracture energy related coefficients calculated by $G_F A = g_F V$ and $G_f A = g_f V$. A is the fracture area in the element and V is element volume.

From Eq. (6), the bond longitudinal stretch l and rotational angle β are the functions of strain $\boldsymbol{\varepsilon}$ according to the Cauchy–Born rule. Therefore, the longitudinal potential is rewrote as $\Phi_l(\varepsilon)$. The present model assume the longitudinal potential Φ_l and rotational potential Φ_β in Eq. (10) evolution follow same bond cohesive law. In loading process, the evolutions of rotational potential Φ''_β is proportional to Φ''_l, and $\Phi''_\beta \propto \Phi''_l$ in brief. In Eq.(10), Φ''_l and Φ''_β follows similar softening tendency in Figure 52 and are rewritten as $\Phi''_l = f(\boldsymbol{\varepsilon})k$ and $\Phi''_\beta = f(\boldsymbol{\varepsilon})r$, where $f(\boldsymbol{\varepsilon})$ is bond evolution function, k and r are longitudinal and rotational bond material constants respectively, which can be interconnected and expressed by macroscopic material constants Young's modulus E and Poisson ratio ν as

$$k = \frac{3EV}{4\pi(1-2\nu)l_0^2}$$
$$r = \frac{3EV(1-4\nu)}{4\pi(1+\nu)(1-2\nu)} \tag{125}$$

Eq. (10) is written as

$$C_{ijkl} = \frac{\partial^2 \Psi}{\partial \varepsilon_{ij} \partial \varepsilon_{kl}} = \frac{1}{V}\left\langle f(\boldsymbol{\varepsilon})_l k l_0^2 \xi_i \xi_j \xi_k \xi_l + f(\boldsymbol{\varepsilon}) r(\xi_i \eta'_j \xi_k \eta'_l + \xi_i \eta''_j \xi_k \eta''_l + \xi_i \eta'''_j \xi_k \eta'''_l)\right\rangle \tag{126}$$

Similar to Eq. (14), the bond evolution function $f(\boldsymbol{\varepsilon})$ is written as

$$f(\varepsilon) = \begin{cases} 1 & \text{if} \quad 0 < \varepsilon < \varepsilon_b \\ 1/(\varepsilon_b - \varepsilon_r) & \text{if} \quad \varepsilon_b < \varepsilon < \varepsilon_p \\ 1/(\varepsilon_p - \varepsilon_c) & \text{if} \quad \varepsilon_p < \varepsilon < \varepsilon_c \\ 0 & \text{if} \quad \varepsilon_c < \varepsilon \end{cases} \tag{127}$$

where ε_b, ε_p, ε_r and ε_c are shape parameters determined by the peak strength σ_t, fracture energies, location of kink point $\beta\sigma_t$ and the size of representative volume.

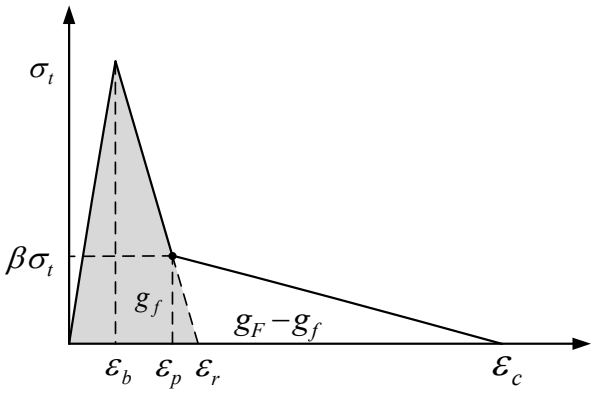

Figure 53. Bond cohesive law for VMIB considering fracture energy g_f and g_F.

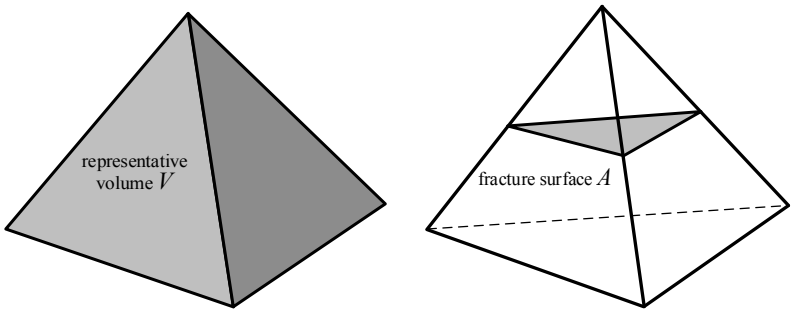

Figure 54. (a)Continuum based representative volume consumes strain energy and (b)fracture surface and its area consumes fracture energy.

The VMIB is a particle-based and continuum-based model. The softening and energy consumption occur in the representative volume that is element in FEM implementation, which is shown in Figure 54(a). The fracture energy, on the other hand, is dissipated over the fracture surface shown as Figure 54(b). The shape parameters ε_b, ε_p, ε_r and ε_c are quantified by relating the bond work to fracture energy. Firstly, ε_b is the critical strain at tensile strength of material. ε_p, ε_r and ε_c are related to the initial fracture energy G_f, total fracture energy G_F and representative element volume. ε_p is the strain at the kink point of softening segments in the bilinear cohesive law. ε_r is the extended line of segment ε_b - ε_p to horizontal axis. The strength vanishes at ε_c. According to Figure 53 and Eq. (17), the work of bond in representative element is divided into three segments,

$$\begin{aligned} W_1 &= \frac{1}{2} V \varepsilon_b f_t \\ W_2 &= \frac{1}{2} V (\varepsilon_r - \varepsilon_b) f_t \\ W_3 &= \frac{1}{2} V (\varepsilon_c - \varepsilon_r) f_t \end{aligned} \tag{128}$$

where V is element volume, W_1 is the work on loading from zero to tensile strength, $W_1 + W_2$ is related to initial fracture energy G_f, W_3 corresponds to $G_F - G_f$.

As the representative element is deformed and cracked, a crack is created in the element. The geometrical parameters like the length scale of localization zone h and fracture area A need to characterized from the volume of element,

$$\begin{aligned} h &= V^{\frac{1}{3}} \\ A &= \gamma V^{\frac{2}{3}} \end{aligned} \tag{129}$$

where γ is a coefficient related to the element geometry and shape.

The total strain energy dissipation by stretching volumetric element is equal to fracture energy required to create crack surface in the element. We have

$$\begin{aligned} G_f A &= W_1 + W_2 \\ G_F A &= W_1 + W_2 + W_3 \end{aligned} \tag{130}$$

The shape parameters ε_p, ε_r and ε_c shown in Figure 53 are derived with Eqs. (18)-(20)

$$\begin{aligned}\varepsilon_r &= \varepsilon_b + \frac{2(\theta G_F \gamma / h - W_1)}{f_t} \\ \varepsilon_c &= \varepsilon_r + \frac{2(1-\theta) G_F \gamma}{h \beta f_t} \\ \varepsilon_p &= \varepsilon_r - \beta(\varepsilon_r - \varepsilon_b)\end{aligned} \tag{131}$$

where $\theta = G_f / G_F$, β is bond force ratio indicating the location of kink point in softening curve.

In certain cases, the calculated ε_r is smaller than ε_b that makes present model no more validate to capture fracture energy correctly. The present VMIB model can be applied if the length scale of localization zone h is smaller than a critical value

$$h = \frac{\theta G_F \gamma}{W_1} \tag{132}$$

And the critical element volume is

$$V = \left(\frac{\theta G_F \gamma}{W_1} \right)^3 \tag{133}$$

5.3.1 Verification

To verify the bilinear softening potential model in remedying the spurious mesh sensitivity, the three-point bonding test of notched concrete beam made of micro-concrete (Ruiz G. 1998, Yu et al., 2008) is simulated. The dimension and geometry of simulating specimen is shown in Figure 55. The parameters of materials (Yu et al., 2008) are the Young's modulus is $E = 30.5\text{GPa}$, the Poisson ratio is $\nu = 0.2$, the uniaxial tensile strength $f_t = 3.8\text{MPa}$ and the total fracture energy $G_F = 62.5\text{J/m}^2$. The critical strain is calibrated as $\varepsilon_b = 0.286 \times 10^{-3}$. The fracture energy ratio θ is set as $\theta = G_f / G_F = 0.5$ and the ratio of bond force is $\beta = 0.2$. The element geometry and shape coefficient is calibrated as $\gamma = 0.23$. To examine the effectiveness of the present method on element size dependency, three different mesh schemes are simulated and shown in Figure 56. Finer meshes are generated above the notch sections with approximate sizes of 5 mm, 2.5 mm and 1 mm respectively.

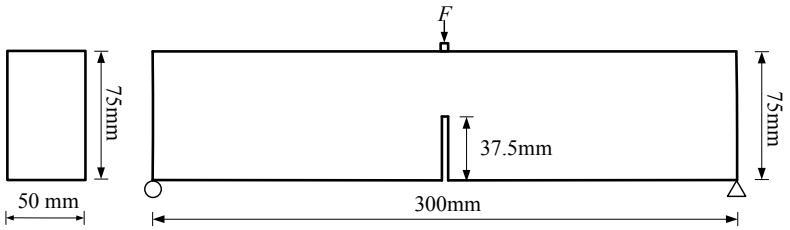

Figure 55. The dimensions of the simulated three points bending specimen.

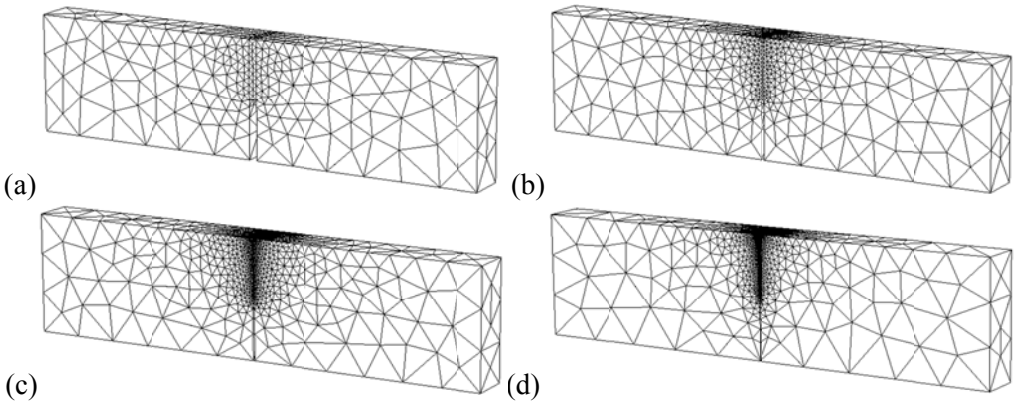

Figure 56. Mesh schemes with element sizes of: (a) 5 mm; (b) 2.5 mm; (c) 1 mm; (d)0.5mm.

The simulation results are shown in Figure 57. Figure 57 (a) shows the comparison between the experimental data (Ruiz G. 1998, Yu et al., 2008) and the numerical results by the VMIB with fracture energy conservation. By comparing, the three numerical curves reasonably agree with the experimental data. This suggests that the mechanical response can be quantitatively predicted in propagation process, and the mesh size dependency is minimized considering the fracture energy dissipation and their relationship with mesh geometry and size. Figure 57(b) used the VMIB model described in (Huang et al., 2013) that applied one bond evolution function for all element size. Contrast to Figure 57(a), Figure 57(b) shows the results that are strongly dependent on the element size. The curves not only show the weaker peak loads when using smaller element size, but also less works indicated by areas under envelopes of displacement-force curve with shrinking element size in three different mesh scheme. (Zhang et al., 2015) discussed the influence of the fracture energy ratio θ and the ratio of bond force β on mechanical properties representation of material. Though, this paper uses constitutive relation with different conception and expression, θ and β represent same meaning to the fracture energy and post peak behaviors respectively. (Zhang et al., 2015) indicated the fracture energy ratio θ dominates the peak strength and the bond force ratio β dominates the post-peak ductility. Figure 58 shows the influence of elemental geometry and shape coefficient γ that is a key parameter representing the fracture surface area in an element by known element volume. Based on Eq. (19), higher γ indicates higher fracture area A in the element and higher fracture energy dissipation during the failure process. It interconnects the strain energy and fracture energy dissipation. Therefore, the loading-displacement envelops become larger. Figure 59 shows the deformed mesh configuration at failure for 1 mm mesh scheme.

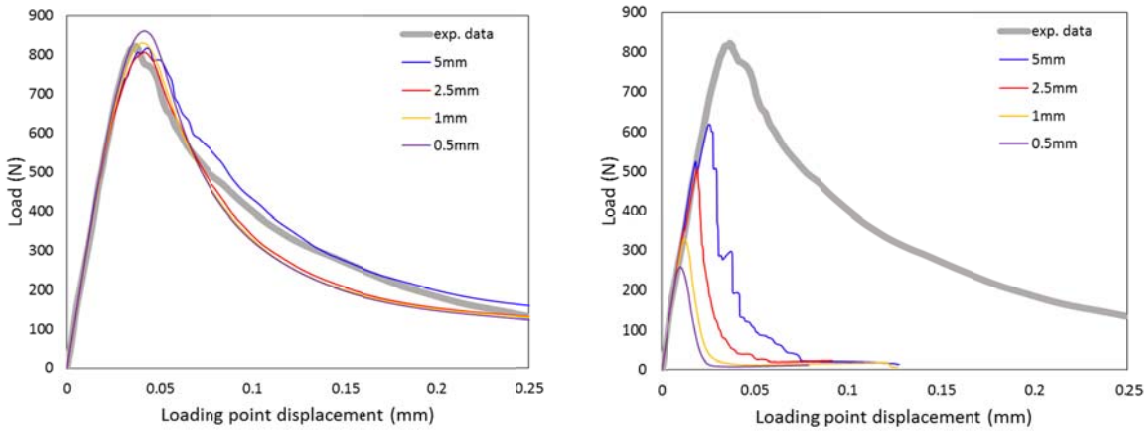

Figure 57. Comparison of the numerical force–displacement curves with different mesh sizes with experimental results from (Yu et al., 2008). (a) VMIB with fracture energy conservation; (b) VMIB model described in (Huang et al., 2013).

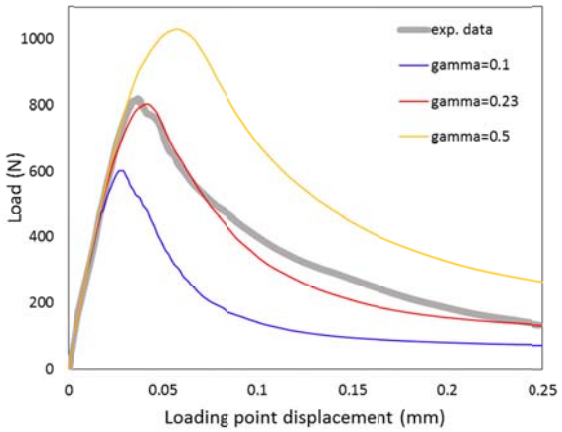

Figure 58. Influence on the macro mechanical response of coefficient γ.

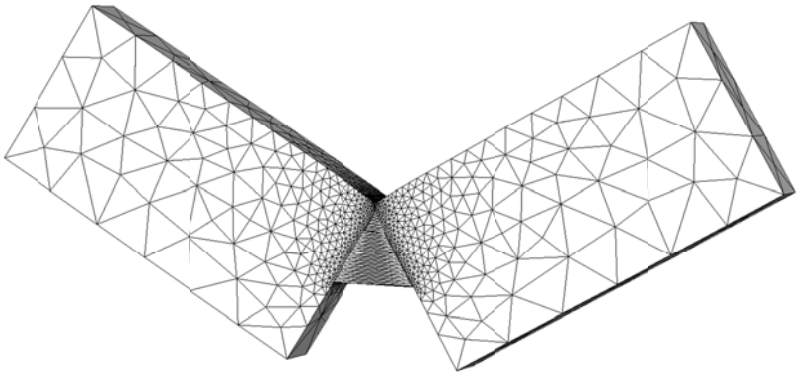

Figure 59. Deformed mesh configuration at failure for mesh scheme 1 mm.

5.4 Fluid-solid Coupled Model for Matrix and Fluid-Filled Fracture

The intact porous rock employs fully coupled poroelastic model. The nonlinear deformation and failure of rock matrix are captured by VMIB model with fracture energy conservation. The fracture is initiated and propagates through failure elements. For fractured elements, the fluid is equivalently modeled by porous

media formulation and the permeability is enhanced since the high conductive zone created by fracture in the element. For moving boundary hydraulic fracturing process, a modification to the continuum model is necessary due to discontinuity of fracture surface. For intact element, the original poroelastic equations system in FEM formulation is written as

$$\begin{bmatrix} \mathbf{K}_t & -\mathbf{A} \\ -\mathbf{A}^T & -\Delta t\lambda \mathbf{H}_H - \mathbf{S} \end{bmatrix} \begin{pmatrix} \tilde{\mathbf{u}}_t \\ \tilde{\mathbf{p}}_t \end{pmatrix} = \begin{bmatrix} 0 & 0 \\ -\mathbf{A}^T & -\mathbf{S} \end{bmatrix} \begin{pmatrix} \tilde{\mathbf{u}}_{t0} \\ \tilde{\mathbf{p}}_{t0} \end{pmatrix} + \begin{pmatrix} \mathbf{f}_t \\ \Delta t\mathbf{q}_t \end{pmatrix} \tag{134}$$

where $\mathbf{K}$ is rock stiffness matrix, $\mathbf{A}$ is the poroelastic coupled term representing the mutual interaction of porous fluid and matrix, $\mathbf{S}$and $\mathbf{H}_H$ are diffusion matrix, $\tilde{\mathbf{u}}$ and $\tilde{\mathbf{p}}_{\tilde{p}}$ are the nodal displacements and pore pressure. $\mathbf{f}$is external mechanical loading, $\mathbf{q}$ is the injection rate from a point source, $_t$ is the present time, $t0$ is the time at previous step, $\Delta t = t - t0$ is the time interval, λ is a coefficient with the range $0 < \lambda < 1$.

For the fractured element, the following equation system is used:

$$\begin{bmatrix} \mathbf{K}_t & 0 \\ 0 & -\Delta t\lambda \mathbf{H}_H - \mathbf{S} \end{bmatrix} \begin{pmatrix} \tilde{\mathbf{u}}_t \\ \tilde{\mathbf{p}}_t \end{pmatrix} = \begin{bmatrix} 0 & 0 \\ 0 & -\mathbf{S} \end{bmatrix} \begin{pmatrix} \tilde{\mathbf{u}}_{t0} \\ \tilde{\mathbf{p}}_{t0} \end{pmatrix} + \begin{pmatrix} \mathbf{f}_t \\ \Delta t\mathbf{q}_t \end{pmatrix} + \begin{pmatrix} \mathbf{A}^{EPM}\tilde{\mathbf{p}}_t \\ 0 \end{pmatrix} \tag{135}$$

where $\mathbf{A}^{EPM}\tilde{\mathbf{p}}_t$ term is nodal forces applied on the right hand side of equation system to apply the fluid pressure on the fracture surface. The fluid flow in the fracture element will only follows the Darcy's law. The fluid and solid are no longer coupled in the way described by the Biot's theory. Eq. (25) is rewritten as

$$\begin{bmatrix} \mathbf{K}_t & -\mathbf{A}^{EPM} \\ 0 & -\Delta t\lambda \mathbf{H}_H - \mathbf{S} \end{bmatrix} \begin{pmatrix} \tilde{\mathbf{u}}_t \\ \tilde{\mathbf{p}}_t \end{pmatrix} = \begin{bmatrix} 0 & 0 \\ 0 & -\mathbf{S} \end{bmatrix} \begin{pmatrix} \tilde{\mathbf{u}}_{t0} \\ \tilde{\mathbf{p}}_{t0} \end{pmatrix} + \begin{pmatrix} \mathbf{f}_t \\ \Delta t\mathbf{q}_t \end{pmatrix} \tag{136}$$

After rearranging, the pressure boundary condition on the fracture surface can be applied by matrix $\mathbf{A}^{EPM}$. It is not needed to apply the nodal forces representing the fluid pressure on fracture after the pressure is calculated. The pressurizing displacement and fluid pressure are calculated simultaneously.

The hydraulic pressure $\mathbf{p}$ in a fracture element is represented by the equivalent nodal forces $\mathbf{f} = A\mathbf{p}$, where A is the fracture area in the element. For example, considering fractured element with triangle fracture area, the pressure on the fracture surface is calculated by averaging the pressures on all 4 nodes of the element:

$$\mathbf{p} = \frac{1}{4}\left(\tilde{p}_t^I + \tilde{p}_t^J + \tilde{p}_t^K + \tilde{p}_t^M\right)\mathbf{n} \tag{137}$$

where $\mathbf{n}$ is the unit normal to the fracture surface, $\tilde{p}_t^I$ is the nodal fluid pressure on node I at time t. As shown in Figure 60(a), the element contains a triangle crack surface. Node M is the only one on the upper side of fracture. The equivalent force of node M is representing the fluid pressure on the fracture,

$$\mathbf{F}_M = (F_x^M, F_y^M, F_z^M) = A\mathbf{P} = \frac{1}{4}A\left(\tilde{p}_t^I + \tilde{p}_t^J + \tilde{p}_t^K + \tilde{p}_t^M\right)\mathbf{n} \tag{138}$$

Each node I, $J$and K on the other side are carrying 1/3 of the fluid load on the fracture. Their equivalent nodal forces are

$$\mathbf{F}_I = \mathbf{F}_J = \mathbf{F}_K = -\frac{1}{3}\frac{1}{4} A\left(\tilde{p}_t^I + \tilde{p}_t^J + \tilde{p}_t^K + \tilde{p}_t^M\right)\mathbf{n} \tag{139}$$

The nodal force vector on the right hand of the elemental matrix system is written as

$$\mathbf{f} = \left(F_x^I, F_y^I, F_z^I, F_x^J, F_y^J, F_z^J, F_x^K, F_y^K, F_z^K, F_x^M, F_y^M, F_z^M\right)\mathbf{n} \tag{140}$$

According to (Huang, dissertation), nodal force vector is derived as

$$\mathbf{f} = \mathbf{A}^{EPM}\,\tilde{\mathbf{p}}_t^e \tag{141}$$

where $\mathbf{A}^{EPM} = \left[\mathbf{A}^I \quad \mathbf{A}^J \quad \mathbf{A}^K \quad \mathbf{A}^M\right]$ for fractured element with triangle crack intersection.

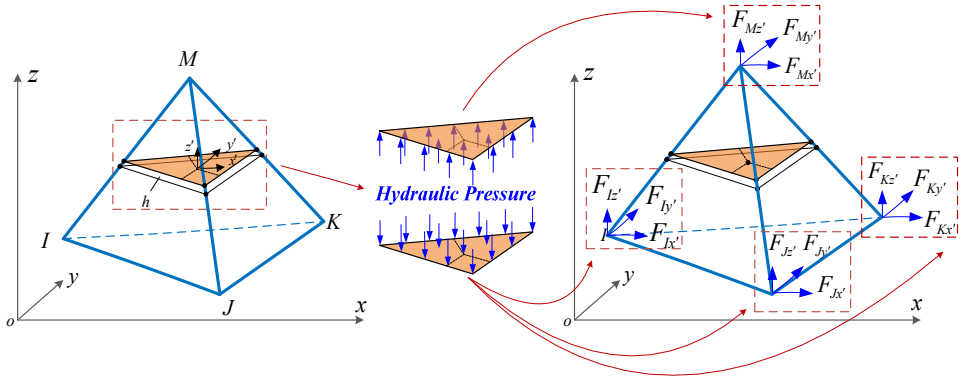

(a)

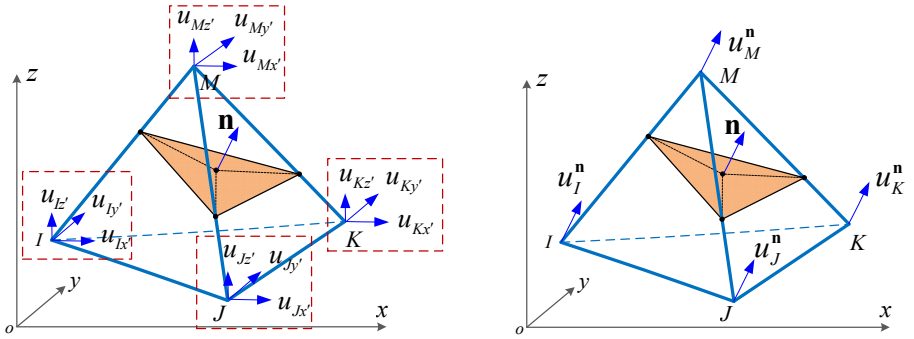

(b)

Figure 60. (a)Equivalent nodal force representing the fracture fluid pressure and (b) aperture representing by relative displacement in element with triangle crack plane.

Based on similar concept, the fracture aperture w is calculated based on the relative displacement and orientation of the fracture surface, shown as Figure 60(b). The displacements of nodes along the normal direction of fracture are written as $\tilde{\mathbf{u}}^n = \left[u_I^n \quad u_J^n \quad u_K^n \quad u_M^n\right]$. The aperture is calculated as

$$w = \frac{1}{3}\left[(u_M^n - u_I^n) + (u_M^n - u_J^n) + (u_M^n - u_K^n)\right] \tag{142}$$

5.5 Numerical Modeling of Laboratory Scale Multiple Hydraulic Fractures

Fracture spacing is a crucial factor in the interactions between hydraulic fractures which can affect fracture geometry and productivity. (Bunger et al., 2011) numerically studied the issue of curved growth of a hydraulic fracture interacting with a previously placed hydraulic fracture. Figure 61(a) is the configuration considered in (Bunger et al., 2011) that illustrates a small notch (HF2) at a distance H above the pre-existing fracture (HF1). As HF2 grows, its growing path deflected due to the stress state and mechanical interaction between hydraulic fractures. In Figure 61(b), local reopening of HF1 in response of tensile stress around the tips of HF2 results in that HF2 propagates towards HF1. If HF1 remains closed during growth of HF2, shown as Figure 61(c), slip of HF1 results in HF2 curving away from HF1. The closely spaced hydraulic fracture laboratory experiments (Kear et al., 2013) show sequential hydraulic fracture growth in different spacing under various confining stresses. In Figure 62(a), the experiment result of Block-4 shows that in the presence of Fracture-1, Fracture-2 tended to curve towards Fracture-1 and eventually coalesced with Fracture-1. Fracture-4 repeated the curve in behavior similar to Fracture-2. In the test on Block-6 shown in Figure 62(b), the fractures show nearly parallel pattern due to higher vertical confining stress that suppressed the reopening of pre-existing fracture. These two experiments gave excellent example of the phenomenon described above in Figure 61.

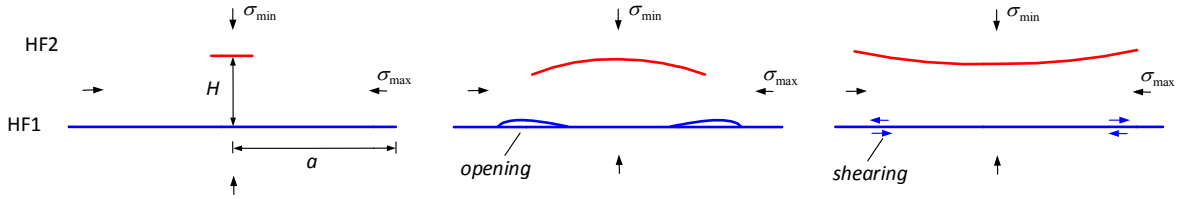

Figure 61. Two fractures interaction, a) problem configuration, b) HF2 grows towards HF 1, c) HF2 to curve away from HF1 (Bunger et al, 2011).

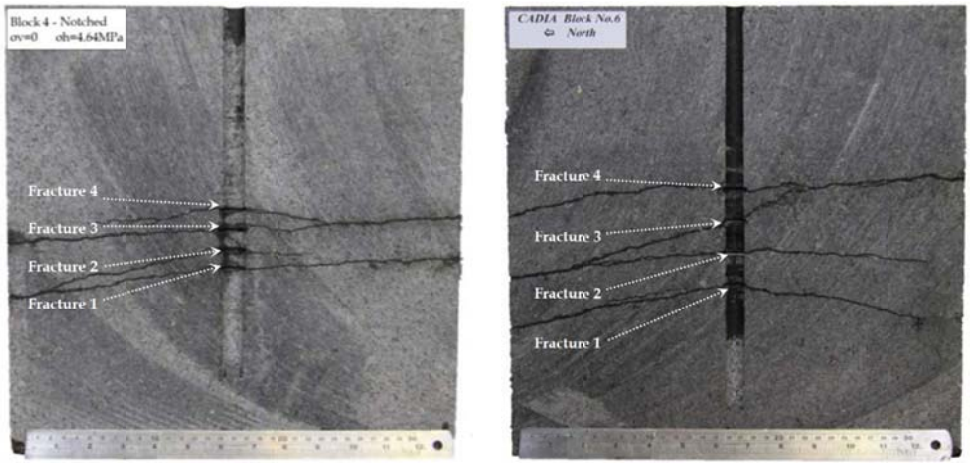

Figure 62. Geometry of fractures for (a) block 4 with zero vertical confining stress and (b) block 6 with vertical confining stress reported by (Kear et al. 2013).

We simulate the mentioned closely spaced hydraulic fracture experiments. The experiments tested $350 \times 350 \times 350\ mm$ blocks of Adelaide Black Granite. A 16 mm diameter borehole is drilled to a depth of 290 mm. 4 notches with 1 mm depth into the borehole circumference are scribed and the notch array is

centered. The spacing between the notch intervals is 15 mm. Figure 62 illustrates the geometry of rock block sample. Take advantage of symmetry of problems, a quarter of rock sample is simulated and shown as gray. Two fractures are simulated to emphasis on their interaction illustrated in Figure 61. The fluid is injected in the notch with red outline that is 15 mm above the previously placed fracture with blue outline. Two limiting scenarios are designed in the experiments, which are cases with zero vertical confining stress and with vertical stress restraining the reopening of underneath fracture. The simulation properties is used according to the rock block used in the test. The Young's modulus, E and Poisson's ratio, ν are $102GPa$ and 0.27, respectively. The rock fracture toughness is $K_{IC} = 2.3MPa \cdot m^{1/2}$. (Bazant and Kazemi, 1990) discussed the relation between the fracture toughness K_{IC}, fracture energy release rate G_I and fracture energy G_f. In linear elastic fracture mechanics it is shown that $G_I = K_I^2 / E$ and further yields $R = K_{IC}^2 / E$, where R is critical fracture energy release rate. According to the size effect law, fracture energy G_f is expressed by $G_f = \lim_{d \to \infty} R$, where d is the sample size. (Hashida .and Takahashi, 1985) presented R value as a function of sample size d. When the sample size d reaches 350 mm, the value of R / G_f is larger than 0.9 and approaching 1.0 as the size increasing. The present simulation uses $G_f = R$ and its value is 51.86 J / m^2. The critical strain is calibrated as $\varepsilon_b = 0.922 \times 10^{-4}$. The fracture energy ratio θ is set as $\theta = G_f / G_F = 0.5$ and the ratio of bond force is $\beta = 0.25$. The element geometry and shape coefficient is calibrated as $\gamma = 0.12$. For fluid flow in the rock and fractures, we consider that the rock is nearly impermeable since extreme low permeability and short term injection. Therefore, a very low permeability $k_{\text{intact}} = 1.0\text{nd}$ is given for the intact rock in the simulation. Major fluid flow and storage occur in the fractures. As the theory mentioned above, the fractured elements are also treated as porous media with constant enhanced permeability that is given by cubic law using constant aperture of 5×10^{-5} meter. For fluid parameters, the viscosity is $\mu = 0.3\text{e}^{-3}\text{Pa}$, the injection rate is constant $Q_{\text{inj}} = 0.0038\text{ml/min}$. The total number of elements is 975,454 and the total number of nodes is 160,806.

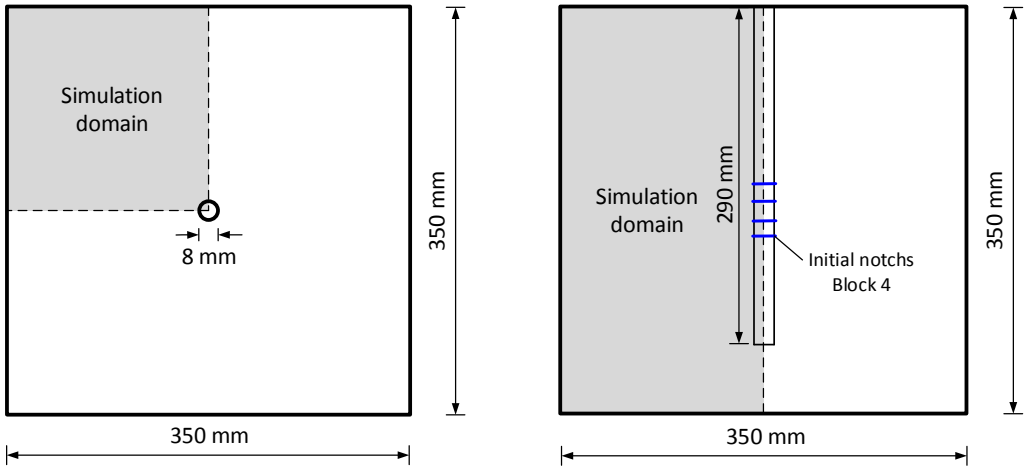

Figure 63. Geometry of rock block sample and simulation domain.

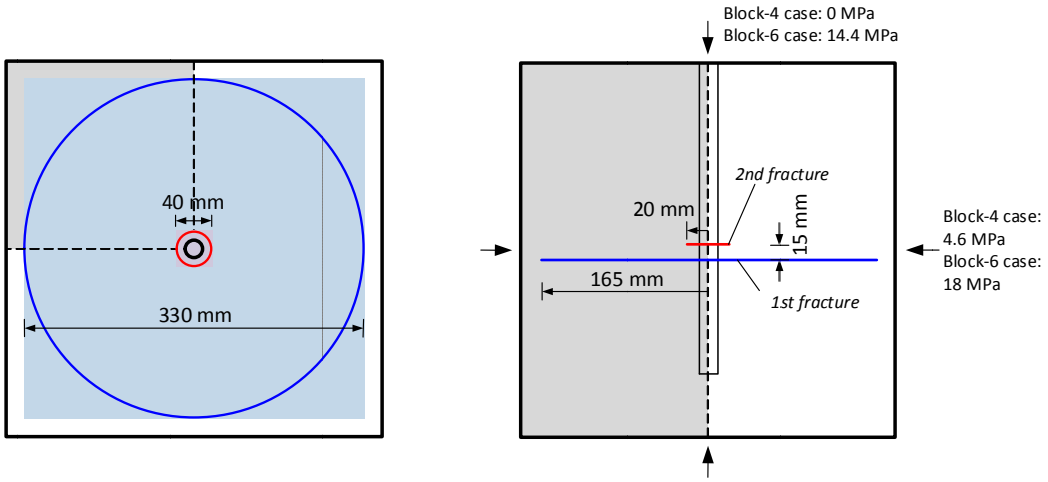

Figure 64. Geometry of fractures in the numerical analysis.

Figure 65 gives the comparison of injection pressure evolution between numerical and experiment. Though the rate of pressure build up and breakdown is not agree between the numerical results and experiments, the magnitude of breakdown pressures are matched very well for both cases. Since that the present work focus on the nonlinear mechanical response of rock, the fluid diffusion in fractured rock is not rigorously captured, but is approximately calculated by constant permeability and applied as fluid pressure boundary condition on the fracture surface. Take advantage of mechanical model presented above, the breakdown pressure is captured that is indirectly indicating the initiation of fracture propagation. The simulated breakdown pressure of Fracture-2 for case Block-4 and Block-6 are 21.25 Mpa and 46.34 MPa respectively. The experiment breakdown pressure for each fracture of Block-4 range from 23.46 MPa to 26.98 MPa. For Block-6, the range is from 39.44 MPa to 45.70 MPa.

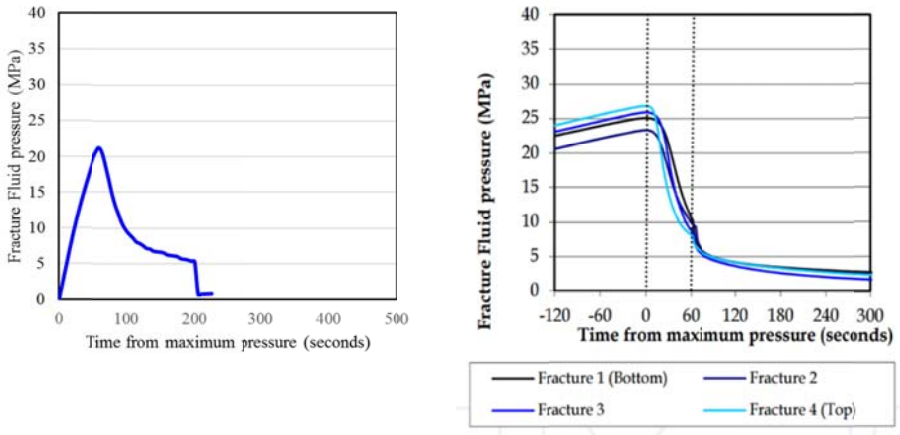

(a)

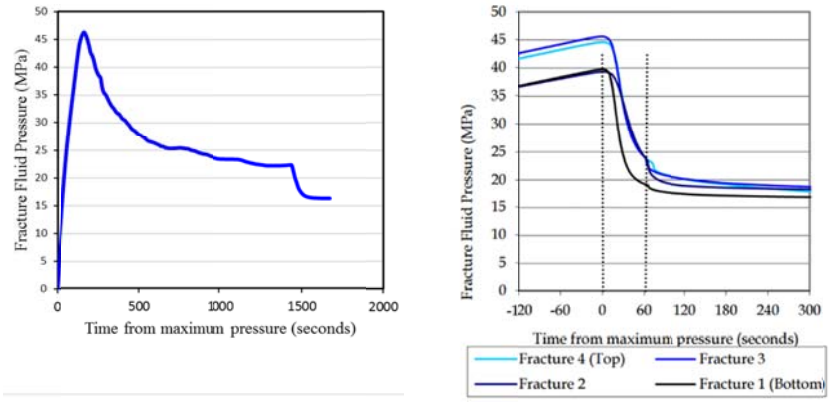

(b)

Figure 65. Comparison of injection pressure vs time between numerical and experiment results for the cases (a)without and (b)with vertical confining stress.

Figure 66 and 67 show the numerical results for the fracture aperture. The changes in color also indicate the evolution of fracture geometry with injection. The red dots in Figure 66(i) and 19(i) indicate injection pressure and time for each fracture geometry. For Block-4 case with zero vertical stress, upper fracture tends to curve towards and eventually coalesces with the underneath fracture. In the numerical model, the previously created fractures are treated as joint elements. Since no suppression by vertical confining stress and the presence of a larger applied horizontal stress, the 1st fracture is reopened locally in response to the induced tensile stresses by the propagating fracture tip. As the upper fracture growing, the location and aperture of opening area are changing with the growing fracture. After two fractures coalesced, the injection pressure dropped rapidly since the fluid leaked into the larger fracture. Therefore, the aperture is decreased once the 2nd fracture contacts the 1st one. For Block-6 case, the 1st fracture almost remains closed during the injection process restrained by higher 14.4 MPa vertical stress. Therefore, nearly parallel fracture is formed. Such behaviors are also observed in the numerical simulations of the same experiment by (Ghassemi, 2016). As the fracture developing in Block-6 case, the injection pressure gradually approach the vertical confining stress that is also observed in the laboratory test shown in Figure 65(b). The partial reopening caused by propagating fracture is shown in Figure 68. The blue area indicates where the fracture remain closed since the compression from fluid pressure from the another fracture. The opening area relocates outwardly as the growing fracture becomes larger and the moving of fracture tip. Figure 69 finalizes the fracture pattern for case Block-4 and Block-6 by comparing with experimental fracture patterns. Though only two fractures are simulated, the simulated fracture patterns agree with the fracture pairs of Fracture-1 and Fracture-2 for both case that are curve in and parallel to the pre-existing fracture respectively.

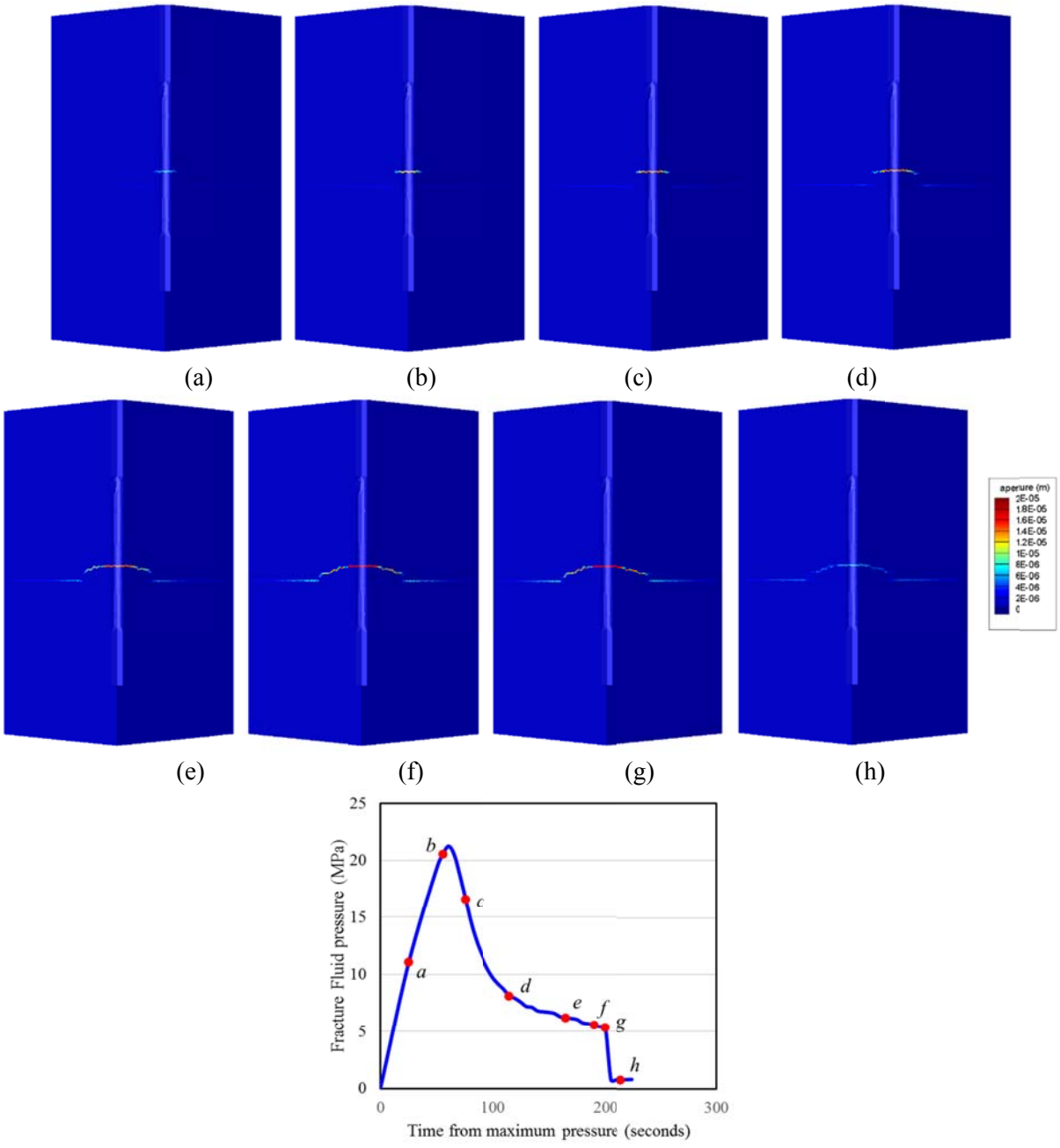

Figure 66. Fracture aperture and pressure indicators for case Block-4.

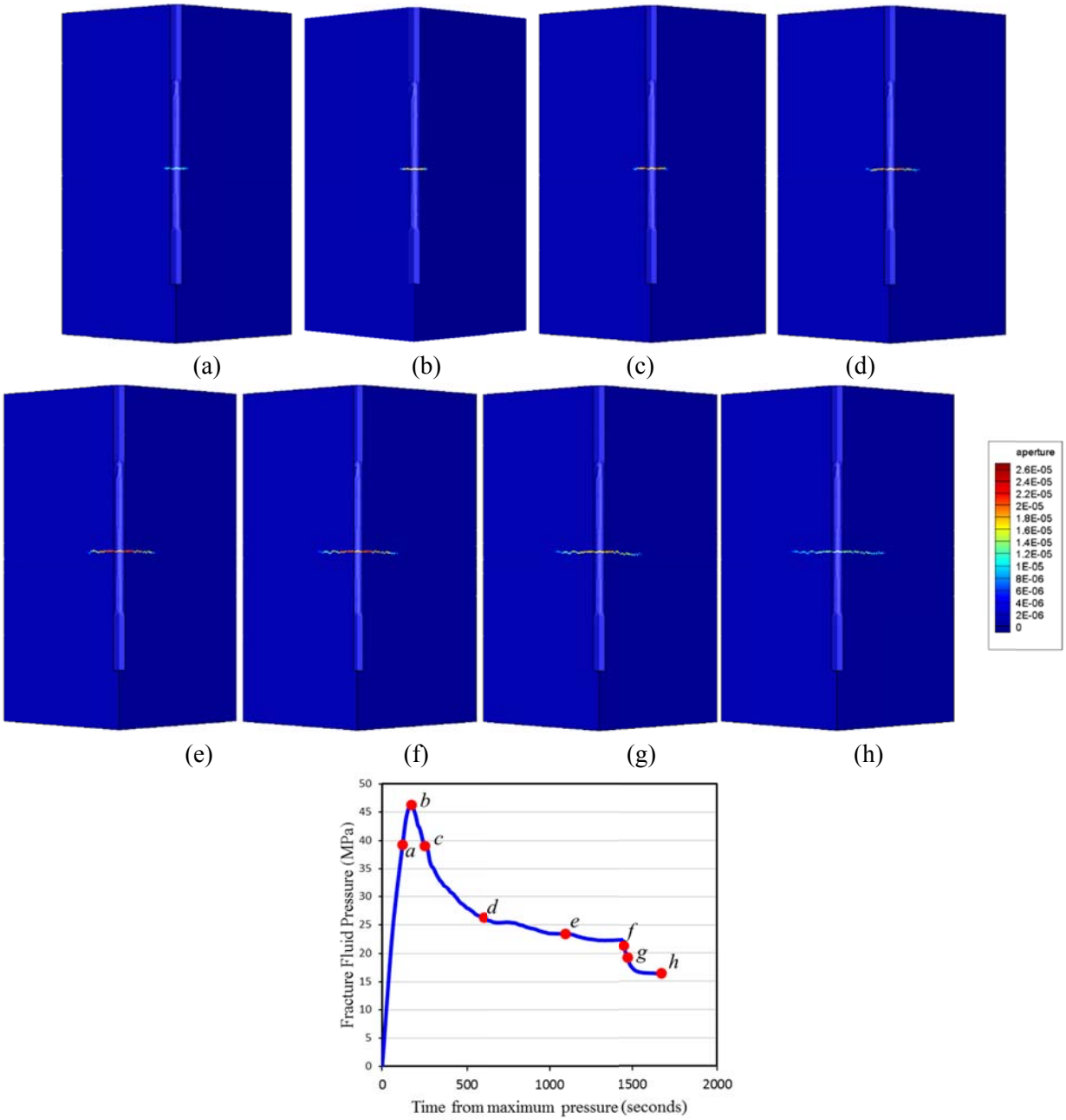

(a) (b) (c) (d)

(e) (f) (g) (h)

(i)

Figure 67. Fracture pattern and pressure indicators for case Block-6.

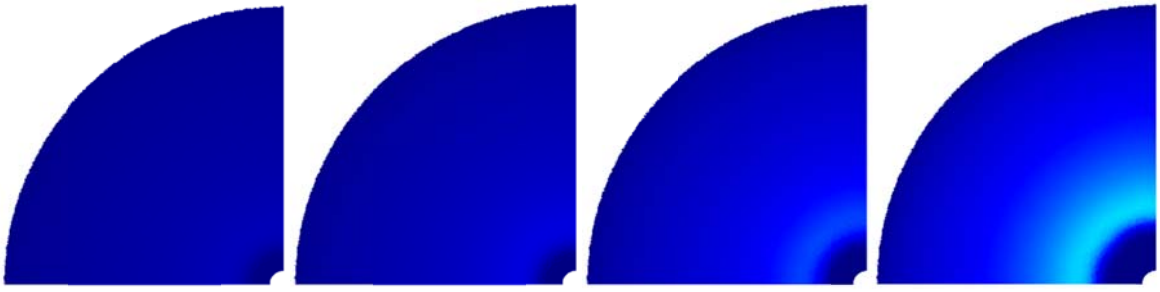

(a) (b) (c) (d)

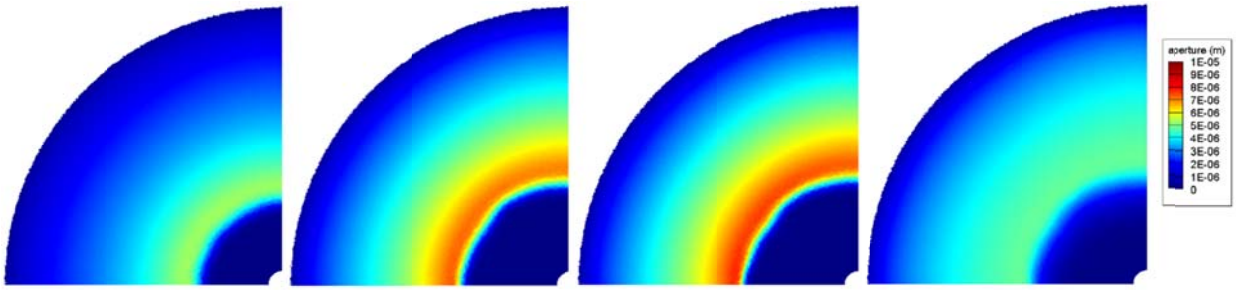

(e) (f) (g) (h)

Figure 68. Aperture of 1st facture showing the partial reopening caused by propagating fracture.

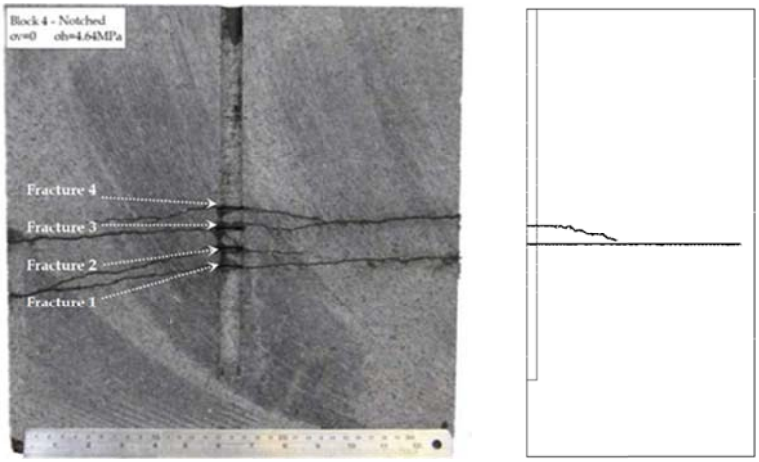

(a)

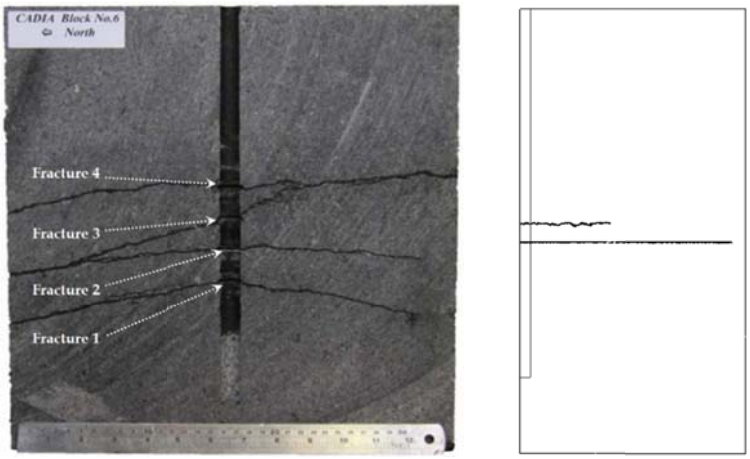

(b)

Figure 69. Fracture pattern for case Block-4 and Block-6 by comparing with experimental results.

6. Conclusions

Special algorithms were developed and used to address the mesh-sensitivity of the VMIB approach. In particular, the fracture energy conservation was considered in the proposed VMIB model. Through incorporation of the fracture energy in the bond evolution function, the mesh-size sensitivity was minimized for the element size simulated in this work. The model served as a mechanical constitutive relation in a fully 3D hydraulic fracturing model to simulate laboratory scale experiments. Taking

advantage of 3D EPM, the pre-existing fractures were treated as "joints" so that the contact and reopening behaviors were captured when interacting with a propagating fracture. For each case, curved and parallel growth of fractures under different confining stresses was captured with reasonable agreement with experimental observations. The critical element size, however, limits the maximum size that satisfies fracture energy conservation and the effectiveness of the model. Therefore, it limits the size of simulation domains to small and possibly meso-scale.

7. References

1. Bahr, H.A., Weiss, H.-J., Maschke, H.G., Meissner, F. 1988. Multiple crack propagation in a strip caused by thermal shock. Theoretical and Applied Fracture Mechanics, 10:219–226.
2. Bauer, S.J. and Handin, J., 1983. Thermal Expansion and Cracking of Three Confined, Water-saturated Igneous Rocks to 800˚C. Rock Mechanics and Rock Engineering, 16, 181-198.
3. Bauer, S. J. and Johnson, B., 1979. Effects of Slow Uniform Heating on the Physical Properties of Westerly and Charcoal Granites. Proc. 20th U.S. Syrup. Rock Mechanics, Univ. Texas, Austin, 7--18.
4. Bunger, A.P., Jeffrey, R.G., Kear, J., Zhang, X. and Morgan, M., 2011, January. Experimental investigation of the interaction among closely spaced hydraulic fractures. In 45th US Rock Mechanics/Geomechanics Symposium. American Rock Mechanics Association.
5. Bažant, Z.P. and Kazemi, M.T., 1990. Size effect in fracture of ceramics and its use to determine fracture energy and effective process zone length. Journal of the American Ceramic Society, 73(7), pp.1841-1853.
6. Bazant, Z. P., and Planas, J., 1998. Fracture and size effect in concrete and other quasibrittle materials, CRC, Boca Raton.
7. Bažant, Zdeněk P., Hideomi Ohtsubo, and Kazuo Aoh, 1979. Stability and post-critical growth of a system of cooling or shrinkage cracks. International Journal of Fracture 15.5: 443-456.
8. Bažant, Z.P. and Becq-Giraudon, E., 2002. Statistical prediction of fracture parameters of concrete and implications for choice of testing standard. Cement and concrete research, 32(4), pp.529-556.
9. Belytschko, T., Black, T. 1999. Elastic crack growth in finite elements with minimal remeshing. International Journal for Numerical Methods in Engineering; 45(5): 601-620.
10. Boone TJ, Ingraffea AR. A numerical procedure for simulation of hydraulically-driven fracture propagation in poroelastic media. International Journal for Numerical & Analytical Methods in Geomechanics, 1990: 14: 27-47.
11. Curran, J..H, Carvalho, J.L., 1987. A displacement discontinuity model for fluid-saturated porous media, Proceedings 6th Congress of the ISRM, Montreal, Ca; 1, 73-78.
12. Dobroskok, A. A., Ghassemi, A., and Linkov, A.M., 2005. Novozhilov structural criterion: an extension for numerical simulation of mode I and II crack growth and coalescence. Int. J. of Fracture. 133, 223-246.
13. Feng, Yuezhong, and Zhihe Jin, 2009. Thermal fracture of functionally graded plate with parallel surface cracks. Acta Mechanica Solida Sinica 22.5: 453-464.
14. Gao H, Klein P., 1998. Numerical simulation of crack growth in an isotropic solid with randomized internal cohesive bonds. Journal of Mechanics, Physics, Solids. 46(2), 187-218.
15. Germanovich, L. N., Ring, L. M., Shlyapobersky, J., Mayerhofer, M. J., and Astakhov, D. K., 1997. Hydraulic fracture with multiple segments, II, Modeling, Int. J. Rock Mech. Min. Sci. 34, No 3/4, Paper no. 98

16. Germanovich, L.N., Carter, B.J., Ingraffea, A.R., Dyskin, A.V., Lee, K.K. 1996. Mechanics of 3D Crack Growth in Compression, 2nd North Am. Rock Mech. Symp., Montreal, Canada, Aubertin, Hassani & Mitri (eds), Balkema, Rotterdam, 1151-1160, 1996. FRANC3D
17. Geyer, John F., and S. Nemat-Nasser., 1982. Experimental investigation of thermally induced interacting cracks in brittle solids. International Journal of Solids and Structures 18.4: 349-356.
18. Ghassemi, A., 1996. A three-dimensional poroelastic hydraulic fracture simulator using the displacement discontinuity method. Ph.D. Dissertation, University of Oklahoma.
19. Ghassemi, A., Tarasovs, A., and Cheng, A.H.-D., 2003. An Integral equation method for modeling three-dimensional heat extraction from a fracture in hot dry rock. Int. J. Num. & Anal. Methods in Geomech., 27, 989-1004.
20. Ghassemi, A., Zhang, Q., 2004. A transient fictitious stress boundary element method for porothermoelastic media. J. Eng. Analysis with Boundary Elements. 28/11, 1363-1373.
21. Ghassemi, A., Tarasovs, A. and Cheng, A.D.-H., 2005. Integral equation solution of heat extraction induced thermal stress in enhanced geothermal reservoirs. Int. J. Num. & Anal. Methods in Geomech., 27, No. 12, 989-1004.
22. Ghassemi, A., Zhang, Q., 2005. Poro-thermoelastic response of a stationary crack using the displacement discontinuity method. J. Engineering Mechanics (in press).
23. Hashida, T. and Takahashi, H., 1985. Simple determination of the effective Young's modulus of rock by the compliance method. Journal of Testing and Evaluation, 13(1), pp.77-84.
24. Healy, D., R.R. Jones, and H. R.E., 2006.Three-dimensional brittle shear fracturing by tensile crack interaction. Nature, 439: p. 64-67.
25. Hillerborg, A., Modéer, M. and Petersson, P.E., 1976. Analysis of crack formation and crack growth in concrete by means of fracture mechanics and finite elements. Cement and concrete research, 6(6), pp.773-781.
26. Huang, K., Zhang, Z. and Ghassemi, A., 2013. Modeling three-dimensional hydraulic fracture propagation using virtual multidimensional internal bonds. International Journal for Numerical and Analytical Methods in Geomechanics, 37(13), pp.2021-2038.
27. Huang, K., and Ghassemi, A., 2012. Modeling 3D hydraulic fracture propagation and Thermal fracturing using virtual multidimensional internal bonds. Presented at the 36th Workshop on Geothermal Reservoir Engineering, Stanford University, Stanford, California.
28. Kear, J., White, J., Bunger, A.P., Jeffrey, R. and Hessami, M.A., 2013. Three dimensional forms of closely-spaced hydraulic fractures. In Effective and Sustainable Hydraulic Fracturing. InTech.
29. Klein, P, Gao H., 1998. Crack nucleation and growth as strain localization in a virtual-bond continuum. Engineering Fracture Mechanics. 61(1), 21-48.
30. Klein, P.A., Foulk, J.W., Chen, E.P., Wimmer, S.A. and Gao, H.J., 2001. Physics-based modeling of brittle fracture: cohesive formulations and the application of meshfree methods. Theoretical and Applied Fracture Mechanics, 37(1), pp.99-166.
31. Koshelev, V. & Ghassemi, A., 2003. Numerical Modeling of Stress Distribution and Crack Trajectory near a Fault or a Natural Fracture. Soil-Rock America Symp., Boston.
32. Koshelev, V. & Ghassemi, A. 2004. Complex variable BEM for stationary thermoelasticity & poroelasticity. J. Eng. Anal. Boundary Elements, 28/7, 825-832.
33. Kumar, D., and Ghassemi, A., 2016. Three-Dimensional modeling and analysis of sequential and simultaneous hydraulic fracturing of horizontal wells. J. Petroleum Science and Engineering, 46, 1006-1025.
34. Marsden, T.J.R. Hughes, 1983. Mathematical Foundations of Elasticity, Prentice-Hall, Englewood Cliffs, NJ.
35. Mao, J., 2005. A finite element approach to solve contact problems in geotechnical engineering. Int. J. Num. Anal. Methods Geomech., 29: 525-550.
36. McTigue, D.F., 1986. Thermoelastic response of fluid-saturated porous rock. J. Geophys. Research, 91(B9), 9533-9542.

37. Milstein, F., 1980. Theoretical elastic behaviour of crystals at large strains. Journal of Materials Science, 15(5), pp.1071-1084.
38. Min, K.S., Zhang, Z.N., Ghassemi, A., 2010. Numerical Analysis of Multiple Fracture Propagation in Heterogeneous Rock induced by Hydraulic Fracturing. Proc. 44th US Rock Mechanics Symposium, Salt Lake City.
39. MIT Report,2006. The future of Geothermal Energy. Impact of Enhanced Geothermal Systems (EGS) on the United States in the 21st Century. Assessment by a MIT-led interdisciplinary panel (J.F. Tester, Chairman), 372pp.
40. Moes, N., Dolbow J., Belytschko, T. A., 1999. finite element method for crack growth without remeshing. International Journal for Numerical Methods in Engineering; 46:131–150.
41. Nguyen, T.D., Govindjee, S., Klein, P.A. and Gao, H., 2004. A rate-dependent cohesive continuum model for the study of crack dynamics. Computer methods in applied mechanics and engineering, 193(30), pp.3239-3265.
42. Ogden, R. W., 1984. Non-linear elastic deformations. Engineering Analysis. 1(2), 119.
43. Park, K., Paulino, G. H., and Roesler, J. R., 2008. Virtual Internal Pair-Bond Model for Quasi-Brittle Materials. Journal of engineering mechanics. 134(10), 856-866.
44. Ruiz G. Influencia del Tamano y de la Adherencia en la Armadura mınima de Vigas en Flexion. Grupo Espanol del Hormigon. ISBN:84-89670-08-0. Madrid, Spain; 1998.
45. Sesetty, V. K., Ghassemi, A., 2015. Modeling and analysis of sequential and simultaneous hydraulic fracturing in single and multi-lateral horizontal wells. Int. J. Petroleum Sci. and Eng., 132, 65-76.
46. Tarasovs, S., and Ghassemi, A., 2011. Propagation of a system of cracks under thermal stress. 45th US Rock Mechanics/Geomechanics Symposium.
47. Tarasovs, S. and Ghassemi, A., 2014. Self-similarity and scaling of thermal shock fractures. Physical Review E 90 (1), 012403-1-6.
48. Thiagarajan, G., Hsia, K. J., and Huang, Y. 2004. Finite-element implementation of virtual internal bond model for simulating crack behavior. Eng. Fract. Mech., 713, 401–423.
49. Tadmor, E.B., Ortiz, M. and Phillips, R., 1996. Quasicontinuum analysis of defects in solids. Philosophical magazine A, 73(6), pp.1529-1563.
50. Tarasovs, S., and Ghassemi, A., 2012. On the Role of Thermal Stress in Reservior Stimulation. Thirty-Seventh Workshop on Geothermal Reservoir Engineering, Stanford University.
51. Vandamme, L., Curran, J.H., 1989. A three-dimensional hydraulic fracturing simulator. International Journal for Numerical Methods in Engineering; 28: 909–27.
52. Yu, R.C., Ruiz, G., Chaves, E.W.V., 2008. A comparative study between discrete and continuum models to simulate concrete fracture. Engng Frac Mech; 75:117–27.
53. Zhang, Z., Ding, J., Ghassemi, A. and Ge, X., 2015. A hyperelastic-bilinear potential for lattice model with fracture energy conservation. Engineering Fracture Mechanics, 142, pp.220-235.
54. Zhang, P., Klein, P., Huang, Y., Gao, H. and Wu, P.D., 2002. Numerical simulation of cohesive fracture by the virtual-internal-bond model. Computer Modeling in Engineering and Sciences, 3(2), pp.263-277.
55. Zhang, Z.N., Ge, X. R., 2005a. Micromechanical consideration of tensile crack behavior based on virtual internal bond in contrast to cohesive stress. Theoretical and Applied Fracture Mechanics, 43(3): 342-359.
56. Zhang, Z.N., Ge, X.R., 2005b. A new quasi-continuum constitutive model for crack growth in an isotropic solid. European Journal of Mechanics - A/Solids, 24(2): 243-252.

57. Zhang, Z.N., Ge, X.R., 2006. Micromechanical modelling of elastic continuum with virtual multi-dimensional internal bonds. International Journal for Numerical Methods in Engineering; 65: 135-146.
58. Zhang, Z.N., Ghassemi, A. 2010. Simulation of hydraulic fracture propagation near a natural fracture using virtual multidimensional internal bonds. Int. J. Num. Anal. Methods. Geomech., (DOI: 10.1002/nag.905).
59. Zhou, X., and Ghassemi, A., 2009. Finite element analysis of coupled chemo-poro-thermo-mechanical effects around a wellbore in swelling shale. International Journal of Rock Mechanics and Mining Sciences 46.4: 769-778.

CHAPTER 2: MODELING HYDRAULIC FRACTURE PROPAGATION USING A THERMO-HYDRO-MECHANICAL FINITE ELEMENT METHOD WITH BRITTLE DAMAGE MODEL

this chapter we use a related but alternative approach to model the complex hydraulic fracturing processes including rock deformation induced by hydraulic pressurization, fluid flow (fluid pressure) within the fractures caused by fluid injection, and fracture propagation. To simulate the coupled processes, the following key factors are considered for hydraulic fracturing design in complex settings:

- First, the nonlinear mechanical behavior of a rock mass is described by elastic/brittle constitutive modeling using continuum damage mechanics (CDM). The failure mechanism of brittle rock is described using a mechanical damage evolution law at the elemental scale within the finite element method. So, at current stage, no rate/time-dependent behaviors such as plasticity are taken into account.
- Second, the heterogeneity of rock mass is considered using spatial distributions of material properties (Young's modulus, strength, and permeability). The spatial distribution curves are described by the Weibull distribution function (Weibull, 1939). The random variable approach of the Weibull function is popularly used to represent rock heterogeneity because of its simplicity (Fang and Harrison, 2002a; Tang and Hudson, 2011; Tang et al., 2002; Wong et al., 2006; Yuan and Harrison, 2005) and have been used in stimulation (Lee and Ghassemi, 2010).
- Third, the porous rock mass is assumed to be fully saturated with fluid flow governed by Darcy's law, and the reservoir response by the coupled processes of rock deformation, pore pressure, and temperature during hydraulic fracture propagation were described using the fully coupled thermo-hydro-mechanical (THM) analysis under the governance of mass, momentum and energy conservation laws (Noorishad and Tsang, 1996).
- Fourth, the fluid flow inside fractures is assumed as incompressible and single phase, with Newtonian flow, so that the hydraulic pressure distribution inside fractures is solved using the lubrication equation with a no-flow boundary condition at the fracture tip.
- Fifth, the quasi-static crack growth algorithm is developed to describe hydraulic fracture propagation. The Mohr-Coulomb failure criterion with tension cut-off was used to capture shear and tensile crack initiation. A moving-boundary scheme is developed to describe the transition of hydraulic pressure through the fracturing paths.

1. Methodologies

Developing a numerical model for the hydraulic fracturing process requires clear understanding of the rock failure mechanism, fluid flow in deformable fractures, and numerical modeling for crack propagation. Especially, numerical capability to capture fracture propagation under different failure modes is critical for hydraulic fracturing model design. Rock heterogeneity is also an important factor because of its influence on fluid flow and fracture pattern. Numerically, crack paths are very difficult to replicate because of the complexity of mechanical behavior and strong discontinuity of cracks in

heterogeneous rock. To solve for the fracturing problems, different numerical approaches based on the boundary element method (BEM), the finite element method (FEM) with VMIB and the discrete element method (DEM) can be used for crack propagation, depending on different purposes. However, each method has both cons and pros. DEM, which uses interaction between bonds of particles, gives good crack-path estimation for the discontinuous aspect of crack propagation. But it requires numerous particles to obtain accurate results, which lead to high computation costs and limit the method to small-scale geological models. Also, especially for fully coupled poroelastic analysis, it is very difficult to model realistic particle geometries and to determine the material parameters required to define mechanical relationships between these "micro-scale" particles, causing significant errors during simulation. BEM has the advantages of reducing computational model dimensions and generating a simple mesh, compared with FEM and DEM that use a full-domain discretization method (Jing and Hudson, 2002). BEM is especially suitable for linear-elastic fracture problems in homogeneous material. BEM formulations can be extended for coupled hydro-mechanical processes (Ghassemi et al., 2001; Pan and Maier, 1997). However, when dealing with rock heterogeneity in numerical domains, the BEM may not be a suitable method, because the basic BEM formulation cannot have sufficient sub-domains to represent the material's heterogeneity, in contrast with FEM and DEM. In addition, the BEM is not as efficient as the FEM for simulating nonlinear material behavior such as plasticity and damage evolution, because it requires sub-domain integrals (Jing, 2003). On the other hand, FEM has disadvantages when the discontinuous crack behavior is embedded on a continuum-mechanics-based FEM formulation. When many fracture elements are included, the FEM solution tends to yield an unstable and ill-conditioned state. Despite these disadvantages, FEM is the most popularly used numerical method in the engineering field because of its wide applicability. Particularly, the FEM is efficient for handling of rock heterogeneity, nonlinear material behavior, complex boundary conditions, and dynamic problems (Jing and Hudson, 2002). The FEM method has been used for hydraulic fracturing simulation by several researchers (Boone and Ingraffea, 1989; Boone et al., 1991; Carrier and Granet, 2012; Sarris and Papanastasious, 2011). However, a simple fracture plane has generally been assumed in these simulations. The VMIB presented in the last chapter remedies some of these shortcomings. An alternative approach is presented in based on damage mechanics approach. Several failure mechanisms of brittle rock and influences of pore pressure and confining pressure are investigated and the Weibull distribution function is introduced for rock heterogeneity as a stochastic approach.

1.1 Failure of Brittle Rock

Rock failure is a very complex process because of anisotropy and heterogeneity, so that numerically replicating the rock failure mechanism is still a very challenging issue in rock engineering. Thus only simplified descriptions of real rock behavior based on convenient mathematical descriptions are available (Fjær et al., 2008). Typically, rock specimen is tested in the laboratory using uniaxial and triaxial tests to measure mechanical properties of the rock. From these experiments, rock strength, which is a critical parameter for rock failure, is measured. Figure is a typical stress/strain curve from a uniaxial compression test. During the rock-failure process, three regions are generally observed: the elastic region, where elastic rock deformation is reversible; the ductile region, where rock deformation (microcrack growth) is irreversible; and the brittle region, where sudden loss of strength leads to totally irreversible rock deformation (microcrack coalescence and macrocrack growth).

Typically the ductile region is very small, so the deformed behavior can be modeled as a simplified elastic/brittle constitutive relationship. In a triaxial compression test, the compressive rock strength is

varied with confining pressure variation, and post-failure behavior also changes accordingly. In this study, the complex failure mechanism is numerically modeled as a simplified stress/strain relationship using CDM, rock heterogeneity, and a crack propagation model with an FEM formulation.

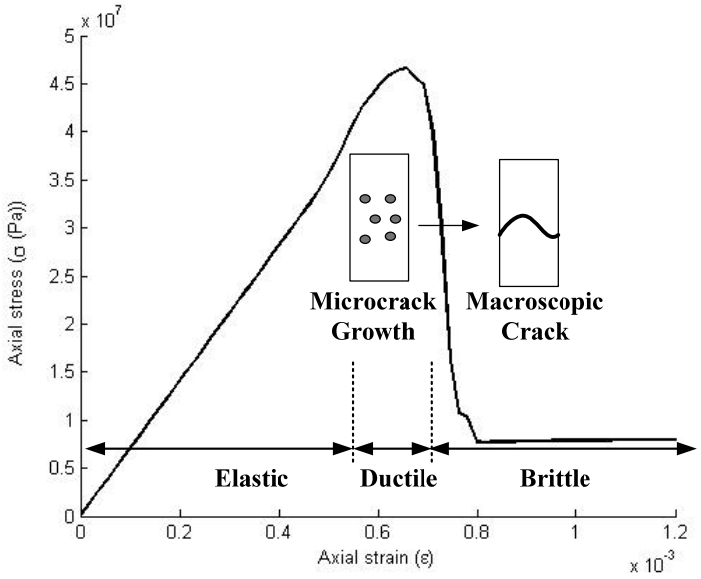

Figure 1. Typical stress-strain curve of brittle material from microcrack to macroscopic crack-growth.

1.1.1 Fracture modes

Three basic modes of fracture are illustrated in Figure 2Figure 2. Mode I is a tensile mode: the crack tip is opening; Mode II is an in-plane shear mode: the crack tip is sliding; and Mode III is an anti-plane shear mode: the crack tip is tearing. The tensile mode is the most important and dominant mode in hydraulic fracturing, but the importance of the shear-mode fractures is increasing during hydraulic fracturing treatments in naturally fractured and heterogeneous reservoirs. This is because most fractures are initiated by mixed modes and in practice; there are no single mode fractures because of heterogeneity.

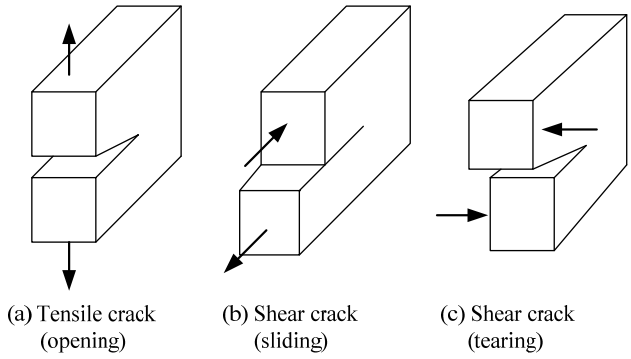

Figure 2. Schematic of fracture modes: (a) Mode I, (b) Mode II, (c) Mode III

1.1.2 Tensile failure

When the effective tensile stress at the crack tip exceeds the critical stress limit called *tensile strength,* Eqn. (4.1), tensile failure occurs. That is, the tensile crack initiates when the minimum principal stress, or the maximum tensile stress component during compression, reaches the critical tensile strength of the material. The tensile strength represents the opening mode of fracture toughness. The tensile failure criterion is usually combined with the Mohr-Coulomb failure criterion as a tension cut-off condition as explained in Figure 3.

$$\sigma_3 \geq -\sigma_T \,, \tag{4.1}$$

where σ_T is tensile strength of material and σ_3 is the minimum principal stress, which is also the maximum tensile stress.

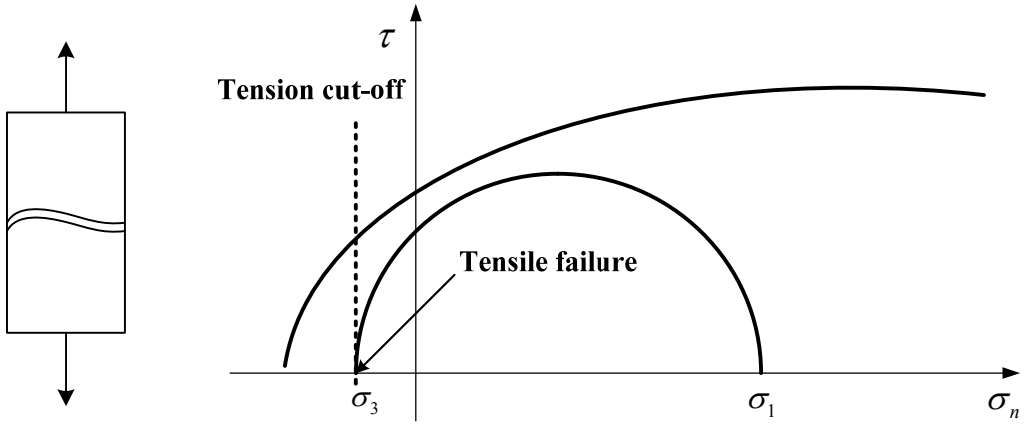

Figure 3. Tensile failure with the Mohr-Coulomb failure criterion.

1.1.3 Shear failure

When rock is subjected to compressive loading, shear mode failures are commonly observed. In the uniaxial and triaxial tests, shear localized fracturing dominates fracture growth. Generally, a shear crack initiates when effective compressive stress in the material reaches a specific value, which called *compressive strength*. Failure occurs along the failure plane when the shear stress increases on the failure plane to a specific value which is a function of the normal stresses in Eqn. (4.2). The Mohr-Coulomb criterion is commonly used to explain this shear localized fracturing behavior; it can predict the angle of the fracture plane and the stress state when the shear failure occurs.

$$\tau_f = c_F + \sigma_{nf} \tan \phi_f \tag{4.2}$$

where τ_f and σ_{nf} are the shear and normal effective stresses on the failure plane respectively, and the cohesion strength c_F and friction angle ϕ_f are rock-strength parameters.

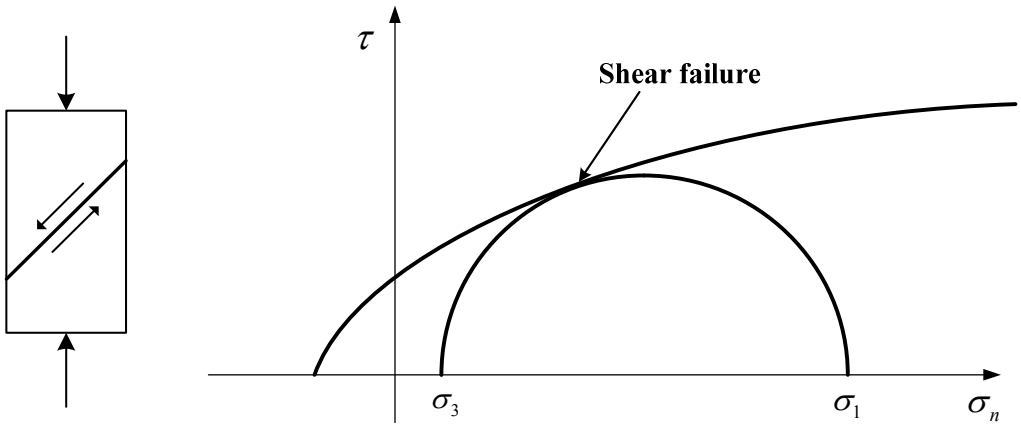

Figure 4. Shear failure on the Mohr-Coulomb failure plane.

1.1.4 Compaction failure

In highly porous or heterogeneous materials, pore collapse and grain reorientation are normally observed under compaction, as shown in Figure 5. 5. The pore collapse might be caused by breaks of grains and then filled into open pore space under pure hydrostatic loading. For instance, when a highly porous chalk is under compaction, the possibility of pore collapse increases because the grain size is much smaller than the pore-space dimension, so that the pore-collapse mechanism becomes the dominating fracture mode in that case (Fjær et al., 2008).

However, microscopically, after compaction failure, shear fracture is initiated by the contact between breaking grains; hence, the pore collapse can be regarded as shear-failure distribution in macroscopic view. Therefore, in this study, the compaction failure mechanism is not considered because of its complexity and uncertainty. And our target is tight reservoirs which have relatively low porosity, so the compaction failure has not effectively happened.

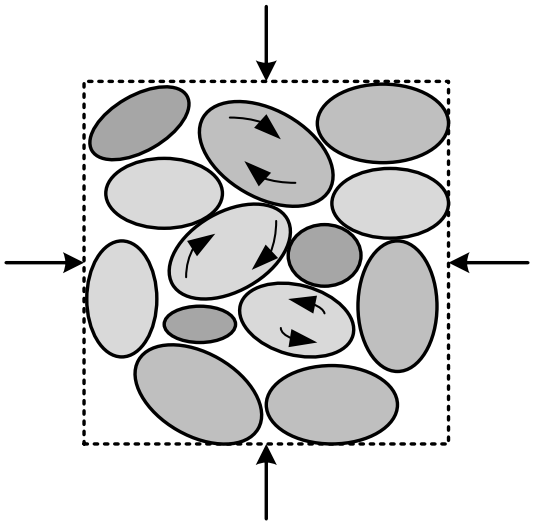

Figure 5. Grain reorientation by compaction forces.

1.1.5 Pore pressure effect

In porous rock, the pore space is filled with water, oil, or gas under in-situ stresses. The pore fluid may affect the failure of the rock, because the pore pressure is equally acting in all normal directions but not affected by shear stresses (Jaeger et al., 2007). In the Mohr diagram of Figure 6, the effect of pore pressure is translated to all the stress circles to the left and close to the failure line for shear and tensile failures. Therefore, increasing pore pressure significantly affects the destabilizing process of a rock and causes the rock to soften.

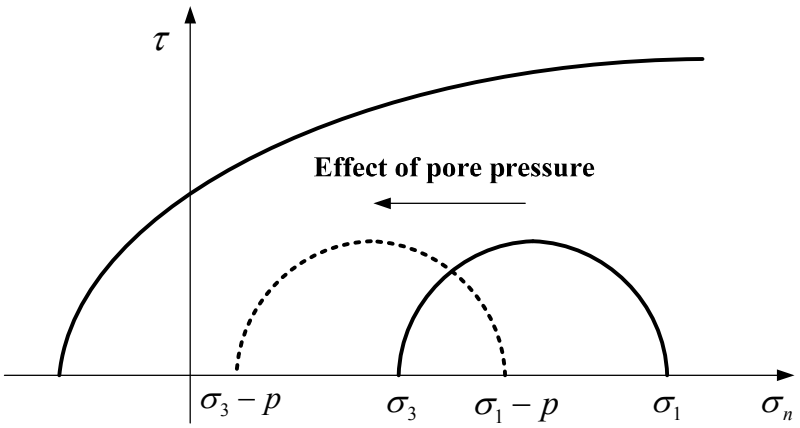

Figure 6. Effect of pore pressure on effective stress state.

Conventional triaxial tests illustrate that the stress/strain relations of geological materials change as applied confining pressure increases. In Figure 7(a), the slope of the stress/strain curve of Rand quartzite is nearly linear elastic, and both the yield strength and the compressive strength increase as the confining stress increases. Complete brittle fracture behavior is found after the yield points regardless of the confining stress variation. In Figure 7(b), a different type of behavior is shown with Carrara marble. As the confining stress increases, more ductile behavior is exhibited. The rock fails by brittle fracture at a low confining zone, transitions from brittle to ductile, and undergoes stress hardening at a high confining zone. The brittle behavior is also seen in other results at various confining stresses (Samieh and Wong, 1997). Figure 8.(a) shows the stress/strain responses of Athabasca oil sand specimens at different confining stresses. Figure 8 (b) presents the results of triaxial compression tests on Labiche shale. Except for swollen shale and Carrara marble, the general mechanical behavior of rock is observed as elastic/brittle behavior during triaxial compression tests.

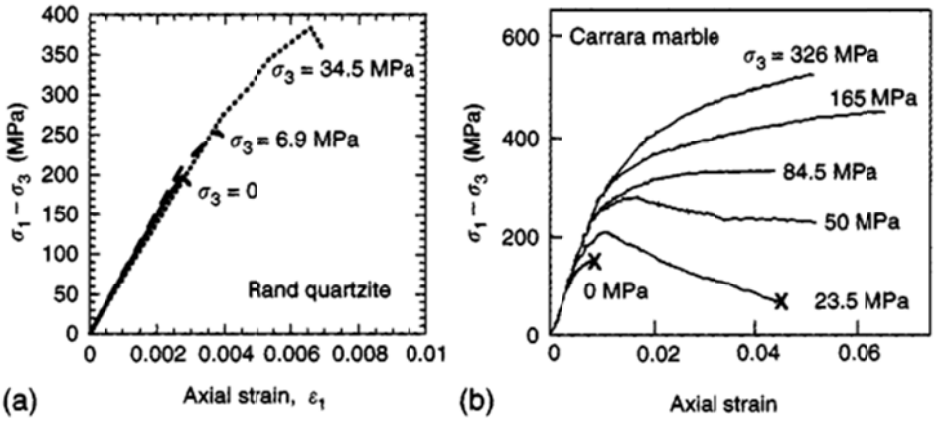

Figure 7. Stress/strain curves for (a) Rand quartzite and (b) Carrara marble (Jaeger et al., 2007).

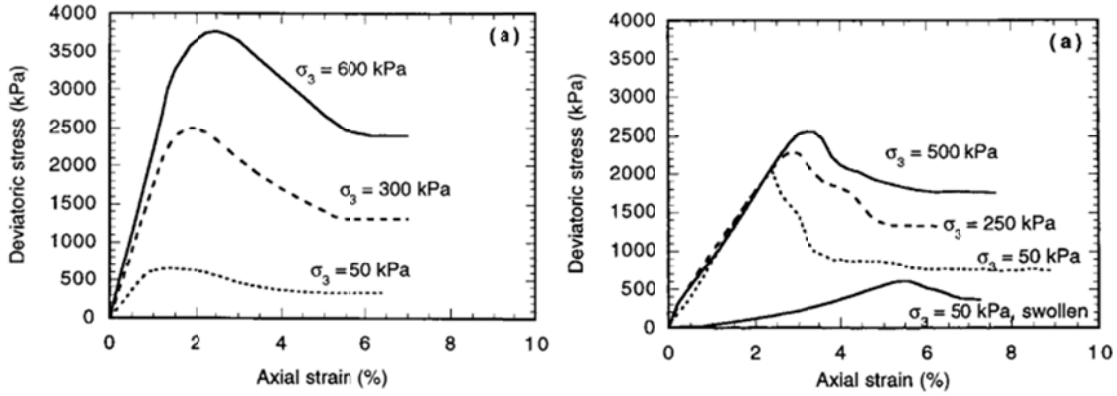

Figure 8. Results of drained triaxial compression tests on oil sand and clay shale (Samieh and Wong, 1997).

For capturing the failure of the brittle rock, the simplest and most commonly used criterion is Mohr-Coulomb theory. The Mohr-Coulomb failure criterion is the most general failure criterion for brittle material such as concrete, rock, and soils. The shear stress causing failure across a plane is resisted by the cohesion of the material and the normal stress across the plane. The Mohr-Coulomb criterion is expressed as:

$$\pm\frac{\sigma_3-\sigma_1}{2}=\left[\frac{\sigma_3+\sigma_1}{2}\right]\sin\phi_f+c_F\cdot\cos\phi_f \tag{4.3}$$

where σ_1 and σ_3 are the maximum and minimum principal stresses. ϕ_f and c_F represent the internal friction angle and cohesion strength, respectively. This criterion has the form of an irregular hexagonal cone in a 3D principal stress space. The principal stress space is obtained in 3D coordinates of the principal stresses, and it is more convenient to use stress invariants to obtain the principal stresses. So the stress invariants (I_s, I_t, I_θ) are defined in Cartesian coordinates:

$$I_s=\frac{1}{\sqrt{3}}\left(\sigma_{xx}+\sigma_{yy}+\sigma_{zz}\right) \tag{4.4}$$

$$I_t = \frac{1}{\sqrt{3}}\sqrt{\left(\sigma_{xx}-\sigma_{yy}\right)^2+\left(\sigma_{yy}-\sigma_{zz}\right)^2+\left(\sigma_{zz}-\sigma_{xx}\right)^2+6\sigma_{xy}^2+6\sigma_{xz}^2+6\sigma_{yz}^2} \tag{4.5}$$

$$I_\theta = \frac{1}{3}\sin^{-1}\left(\frac{-3\sqrt{6}J_3}{I_t^{\,3}}\right) \tag{4.6}$$

where

$$J_3 = s_x s_y s_z - s_x\sigma_{yz}^2 - s_y\sigma_{xz}^2 - s_z\sigma_{xy}^2 + 2\sigma_{xy}\sigma_{xz}\sigma_{yz} \tag{4.7}$$

$$s_x = \frac{\left(2\sigma_{xx}-\sigma_{yy}-\sigma_{zz}\right)}{3} \tag{4.8}$$

Mean effective stress and deviatoric stress are defined as:

$$p' = \frac{1}{\sqrt{3}}s,\;\; q' = \frac{\sqrt{3}}{\sqrt{2}}t \tag{4.9}$$

The principal stresses are expressed as stress invariants as:

$$\sigma_1 = p' + \frac{2}{3}q'\sin\left(I_\theta - \frac{2\pi}{3}\right) \tag{4.10}$$

$$\sigma_2 = p' + \frac{2}{3}q'\sin I_\theta \tag{4.11}$$

$$\sigma_3 = p' + \frac{2}{3}q'\sin\left(I_\theta + \frac{2\pi}{3}\right) \tag{4.12}$$

Then, the Mohr-Coulomb failure surface is expressed as shown below. The shear strength of rock at failure, τ_f, is given by the Coulomb failure criterion,

$$\tau_f = c_F + \sigma_{nf}\tan\phi_f, \tag{4.13}$$

where τ_f and σ_{nf} are the shear and normal effective stresses on the failure plane respectively. The cohesion strength, c_F, and friction angle, ϕ_f, are rock strength parameters. The Coulomb failure criterion can be rewritten in terms of stress invariants using Mohr's effective stress circle as follows;

$$f = -p'\sin\phi_f + q\left(\frac{\cos I_\theta}{\sqrt{3}} - \frac{\sin I_\theta \sin\phi_f}{3}\right) - c_F\cos\phi_f = 0 \tag{4.14}$$

So for the stress state falls inside of the yield surface, $f < 0$, while it is on the yield surface for $f = 0$, and it is outside the yield surface, $f > 0$. When the effective stress state is on the yield surface or outside the yield surface, the rock is indicated by shear failure. In addition, to introduce the tensile failure, the maximum tensile strength criterion, Eqn. (4.1), is combined with Mohr-Coulomb failure criterion as a tension cut-off condition as described in Figure 9. .

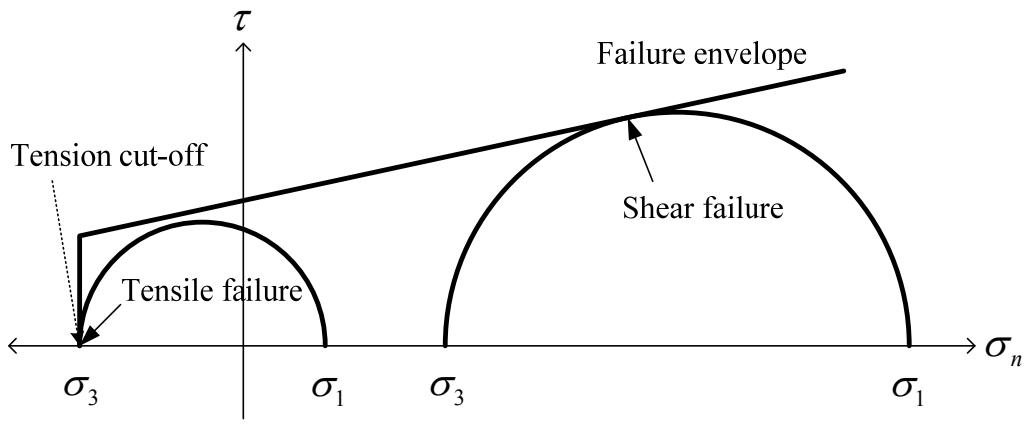

Figure 9. Schematic of Mohr Coulomb failure criterion with tension cut-off.

1.2 Rock Heterogeneity

Micromechanically, rock is a heterogeneous material that contains lots of different sizes, properties, and types of particle stack. That is, local rock properties may vary by composition and fabrication of the particle stack. Rock heterogeneity leads to various formations of multiple-crack branching during hydraulic fracture propagation. The effect of the rock heterogeneity has been studied experimentally by several researchers (Brace, 1961; Fredrich et al., 1990; Mahabadi et al., 2012; Wong et al., 2006), but the effect on strength and deformation has not been well understood. Especially, when the heterogeneity of large geological media is considered, it is almost impossible to characterize the heterogeneity from field observations. This uncertainty has led to use of a stochastic approach to represent a distribution of material properties and to take into account rock heterogeneity on numerical models.

Characteristics of various microdefects such as size, strength, and location can be determined by statistical aspects of a random function. The Weibull distribution function is widely used for modeling rock failure because of its simplicity (Fang and Harrison, 2002b; Liu et al., 2004; Tang and Hudson, 2011; Wong et al., 2006; Yuan and Harrison, 2005). Although failure processes of heterogeneous rock are complex, the stochastic approach can account for a variety of possibilities of rock heterogeneity. However, the stochastic approach cannot explain all different types of rock heterogeneity because each rock has a different form of heterogeneity and each unique statistical model can explain these heterogeneities (Wong et al., 2006). Also, the parameters of the Weibull distribution function are uncertain and highly dependent on the choice of input parameters, so the stochastic model may need to be evaluated on the basis of microstructure analysis and image analysis. For further improvement, the correlation between Weibull parameters and rock composition must be investigated. This issue is essential for numerical design for rock experiments; however, it is beyond the scope of my study, since lots of uncertainties in rock heterogeneity make it quite difficult.

The Weibull distribution function is used to account for a variety of rock fabric possibilities and has been used by several researchers (Fang and Harrison, 2002a; Lee and Ghassemi, 2010; Tang and Hudson, 2011; Tang et al., 2002; Yuan and Harrison, 2005). The Weibull distribution function is defined by the following probability density function (Weibull, 1939):

$$f(m) = \frac{a_i}{m_i}\left(\frac{m}{m_i}\right)^{a_i-1} \exp\left[-\left(\frac{m}{m_i}\right)^{a_i}\right], \qquad (4.15)$$

where m_i, a scale parameter, determines the mean value of the random variable, and a_i, a shape parameter, determines shape of the distribution function. A random variable m for heterogeneity is generated using the Weibull distribution function with parameters m_i and a_i. In Figure 10, the effect of a scale parameter showed that the distribution curve was shifted by the scale parameter change. A shape parameter determines the range of the distribution function. In

Figure 11(a), the distribution curve becomes narrow when the shape parameter increases. That means the material heterogeneity decreases as the shape parameter increases and until it nears homogeneous material behavior. In

Figure 11(b), since the scale parameter represents a mean value of the distribution curve, a larger value of m_i indicates a hard, heterogeneous rock, while a smaller m_i indicates a soft heterogeneous rock.

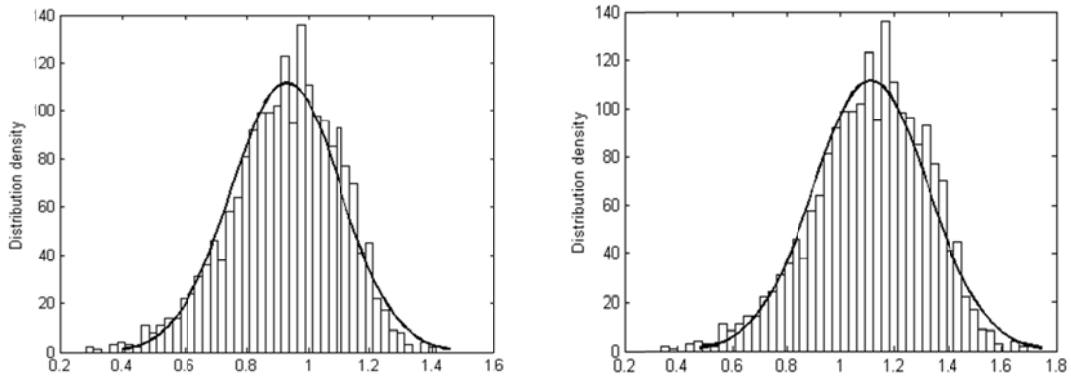

(a) m_i=1, a_i=6 (b) m_i=1.2, a_i=6

Figure 10. Distribution curves of random variable m by a scale parameter.

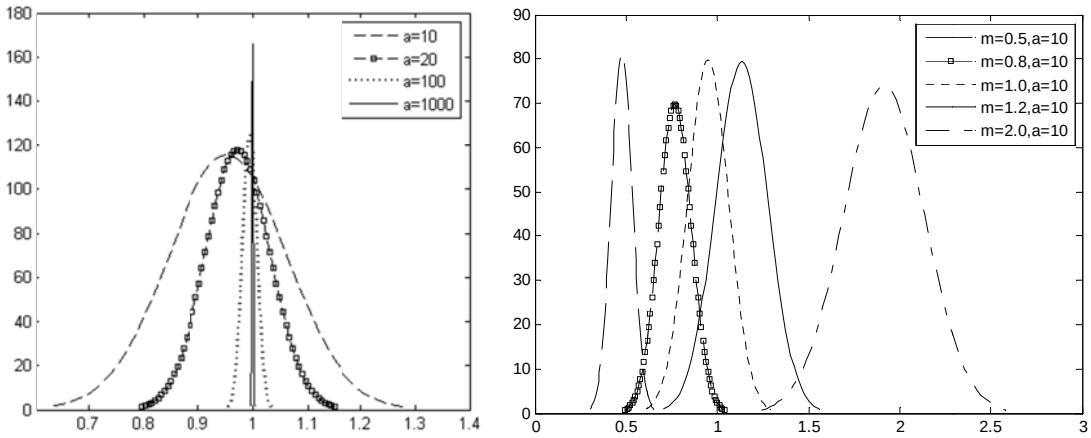

(a) Shape parameter changes (b) Scale parameter changes

Figure 11. Distribution curves by Weibull parameter changes.

2. Constitutive Modeling of Brittle Rock Failure

Various types of mathematical theories such as linear elastic, hyperelastic, plastic, viscoelastic, and viscoplastic are available to describe a realistic constitutive model of material behavior. However, constitutive modeling of realistic behavior of heterogeneous rock is quite difficult using mathematical formulation via numerical methods, because of the largely discontinuous, anisotropic, inhomogeneous and nonelastic behavior of a rock mass (Harrison and Hudson, 2000). Failure mechanism and fracture patterns are strongly dependent on the mechanical behavior of rock, so that finding a suitable constitutive model for the rock is an essential part of rock engineering.

In this work, the idealized elastic/brittle constitutive relations used for brittle materials are illustrated in Figure 12. The idealized elastic/brittle behavior of brittle rock is modeled by employing the elastic/brittle constitutive model using continuum damage mechanics. When brittle rock is under compressive forces, the mechanical behavior of the rock is changed by its confining pressure. Normally, as the confining pressure increases, the brittle rock has larger compressive strength and more ductile behavior, so confining pressure-dependent constitutive relations were developed using compressive-strength data from the experimental results. The constitutive relations needed to be calibrated with experimental results, since realistic strain-softening behavior must be described physically to predict damage and failure mechanisms of brittle materials and capture macroscopic cracking behavior (Bazant, 1986; Mazars and Pijaudier-Cabot, 1989). The material degradation of the brittle rock, where a localized, severely damaged zone defines a failure plane in the form of a macrocrack, was macroscopically characterized using the idealized elastic/brittle damage model. The damage variable represents average material degradation and considers various damage types at the micro scale such as nucleation, coalescence, and growth of voids, microcracks, cavities, and other microscopic defects (Budiansky and O'connell, 1976; Lubarda and Krajcinovic, 1993; Voyiadjis and Kattan, 2009).

The failure mechanism of brittle material is believed to involve growth of microcracks through the interaction of material inhomogeneities and applied stresses. Coalescence of these microcracks leads to macroscopic crack and damaged zone expansion as microcrack population and intensity increase. The brittle behavior is characterized by a sudden drop of the stress/strain curve right after the yield point caused by loss of cohesion, while ductile behavior is characterized by continuous deformation without downward change of the stress/strain curve after the yield point (Mogi, 2007). The initiation and growth of damage variables can be described using CDM (Kachanov, 1986). Usually, the critical value of the damage variable is used to decide the macroscopic crack growth. However, an important issue is how a macroscopic crack can be defined and at what amount of damage. Usually, the critical value chosen is in the range of 0.5 to 0.9 (Al-Rub and Darabi, 2010; Kachanov, 1986; Krajcinovic, 1989, 2000). In principle, CDM can be applied to porous materials weakened by microvoids of all shapes (Krajcinovic, 2000).

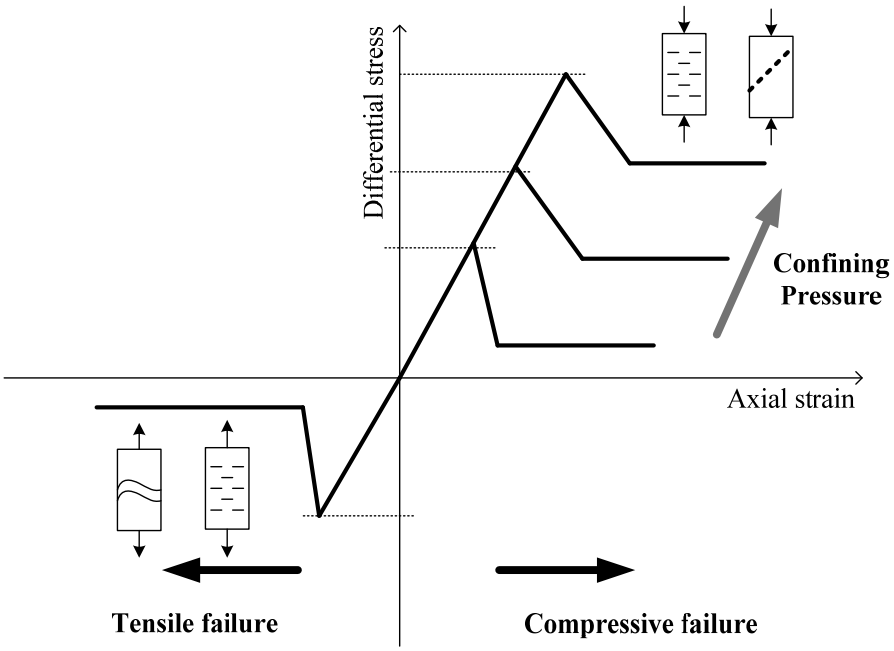

Figure 12. Idealized stress/strain behaviors based on compressive and tensile failure corresponding to confining pressure variation.

2.1 Continuum Damage Mechanics

The initial model of CDM was proposed by Kachanov(1958). From a microscopic point of view, breakage of atomic bonds causes damage and crack initiation. The breakage means degradation of material strength, and material strength degradation can be represented by a damage variable. Depending on material behavior (isotropic, transversely isotropic, anisotropic, etc.), a scalar, vector, or tensor damage variable (D, D_{ij}, D_{ijkl}) can be used to describe the isotropic or anisotropic stiffness degradation (Krajcinovic and Fonseka, 1981; Voyiadjis and Kattan, 2009). Among the different types of damage variable, the scalar damage variable is frequently used for an isotropic material for simplicity. The assumption of an isotropic damage variable has been found to be effective in predicting local failure in structural components (Lemaitre, 1984). The concept of scalar damage parameter and the "effective stress" approach were introduced by Kachanov(1958) and Rabotnov(1969). From the force balance $\sigma A = \sigma_{eff}\overline{A}$, where $\overline{A} = A - A_D$ is the effective area or the undamaged area in the total area A in Figure 13(a)-(b).

$$\sigma = \frac{\overline{A}}{A}\sigma_{eff} \tag{5.1}$$

For an isotropic case, the damage parameter has the same value in all directions, and it can be defined as:

$$D = 1 - \frac{\overline{A}}{A} = \frac{A_D}{A}, \tag{5.2}$$

where A is the total area of the specimen and A_D is the total damaged parts of the area (all microcracks, voids formed) of the specimen in Figure 13(a). Propagation and coalescence of the microcracks lead to

growth of the damage variable. By substituting Eqn. (5.2) into Eqn. (5.1), the effective stress is expressed as:

$$\sigma_{eff} = \frac{\sigma}{1-D}, 0 \le D < 1 \tag{5.3}$$

Because the damage model is isotropic, either damaged or undamaged material is still under linear elastic behavior before the strain level reaches breaking point, so the effective stress is governed by the Hooke's law (Kachanov, 1986):

$$\sigma_{eff} = E\varepsilon \tag{5.4}$$

Combining Eqn. (5.3) and (5.4), the stress/strain relation is obtained as:

$$\sigma = (1-D)E\varepsilon \tag{5.5}$$

In CDM, the damage parameter D is considered a macroscopic-state variable that affects stiffness degradation of the material (Kachanov, 1986), so that the effective Young's modulus is defined as:

$$E' = (1-D)E \tag{5.6}$$

The damage evolution equation can be characterized by a function of strain as the simplest method, as described in Figure 13(c) (Jirasek, 2004; Jirasek and Zimmermann, 1998).

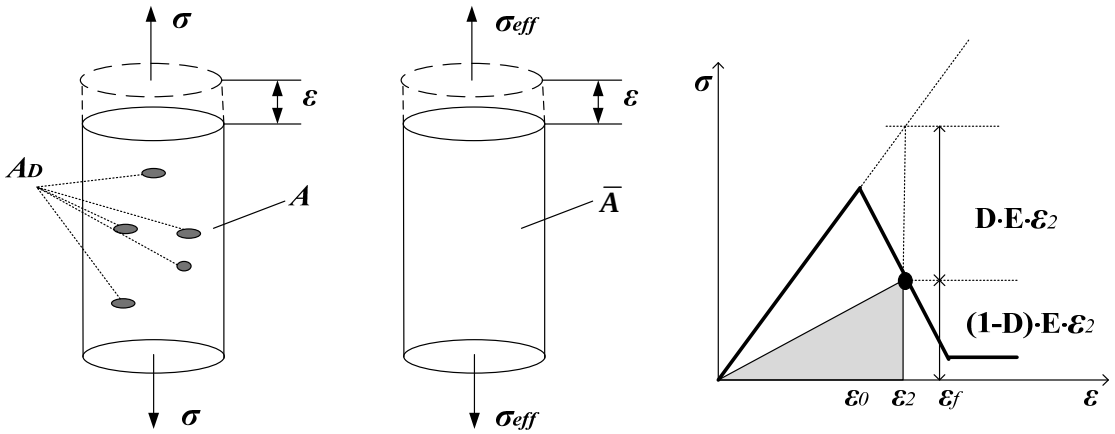

Figure 13. (a) Damaged configuration, (b) Effective stress equivalence principle (Kachanov, 1986) (c) Linear softening damage evolution (Jirasek and Zimmermann, 1998).

2.1.1 Nonlocal damage Model

Local strain-softening phenomena modeled using finite element analysis causes spurious mesh sensitivity due to strain localization in the damaged zone. In order to avoid the strain localization, nonlocal continuum approach was introduced (Erigen and Edelen, 1972; Kunin, 1968) and the nonlocal theory was extended to the nonlocal damage model by (Bazant and Pijaudier-Cabot, 1988; Pijaudier-Cabot and Bazant, 1987). The nonlocal damage model is formulated to explain the mesh size effects and prevent instability of strain localization. In the nonlocal theory, the stress is considered as a function of the mean

of the strain from a certain representative volume of the material, which plays a central role in the physics of heterogeneous materials to predict their effective properties. The representative volume is defined by a characteristic length. The characteristic length is usually determined by microstructural statistics using image analysis (Graham and Yang, 2003). For concrete, the characteristic length can be roughly estimated as 2 to 7 times the maximum aggregation size (Bazant and Pijaudier-Cabot, 1988).

The principle idea of the nonlocal damage theory is that the nonlocal damage variable is defined by spatial averaging over the representative volume (Bazant and Pijaudier-Cabot, 1988). The spatial averaging form was derived from a thermodynamic approach, and the state of material can be characterized by its free energy density, which is defined as:

$$\rho\psi = \frac{1}{2}\sigma_{ij}\varepsilon_{ij}\,, \tag{5.7}$$

where ψ is the free energy density, ρ is mass density, and σ_{ij} and ε_{ij} are the stress and strain tensors. From the stress/strain relation for an isotropic damage:

$$\sigma_{ij} = (1-D)C_{ijkl}\varepsilon_{kl} \tag{5.8}$$

Substituting Eqn. (5.8) into Eqn. (5.7), the following relation is obtained for the specific free energy, $\rho\psi$, per unit volume:

$$\rho\psi = \frac{1-D}{2}\varepsilon_{ij}C_{ijkl}\varepsilon_{kl} \tag{5.9}$$

In Figure 13(c), when the material is damaged, the strain energy in the failed zone begins release the stored energy during the failure process, so that the damage variable could be defined by the rate of strain energy dissipation. The energy dissipation rate is expressed as:

$$\varphi = -\frac{\partial(\rho\psi)}{\partial t} = -\frac{\partial(\rho\psi)}{\partial D}\frac{\partial D}{\partial t} = Y\dot{D}\,, \tag{5.10}$$

and the damage energy release rate, which is the driving force for the growth of damage, is defined as (Pijaudier-Cabot and Bazant, 1987):

$$Y = -\frac{\partial(\rho\psi)}{\partial D} = \frac{1}{2}\varepsilon_{ij}C_{ijkl}\varepsilon_{kl} \tag{5.11}$$

Based on the nonlocal damage theory (Pijaudier-Cabot and Bazant, 1987), the mean value of the damage energy release rate is evaluated over the representative volume. The spatial average of the damage energy release rate over the representative volume is defined as:

$$\tilde{Y}_e = \frac{1}{V_r}\int_V Y\ dV\,, \tag{5.12}$$

where V_r is a representative volume.

2.1.2 Damage evolution law for brittle rock

Employing an idea from the nonlocal damage theory, the damage energy release rate was evaluated by spatial averaging integral over the damaged volume instead of the representative volume:

$$\tilde{Y}_{ed} = \frac{1}{V_d}\sum\int_{V_{ed}} Y\ dV_{ed} \tag{5.13}$$

where V_d is a total volume of damaged elements and V_{ed} is a damaged element volume. In Figure 14, constitutive relationships of the brittle rock are differently described by failure type, so that a threshold value for the damaged release rate is calculated for tensile and shear failure, respectively. Each damage evolution equation for tensile and shear failure can be defined by a function of the damage energy release rate for monotonic damage growth. The type of softening curve could be obtained from a realistic shape of the stress/strain relationship on the basis of experiments. In this work a linear strain softening, schematically shown in Figure 14. 14, was assumed for numerical simplicity. The tensile strength (σ_T) and compressive strengths (σ_{c1}, σ_{c2}) by various confining pressures are obtained from experimental data. Based on the material strength information, the material coefficients (ε_t, ε_{tr}, ε_{c1}, ε_{c1r}, ε_{c2}, ε_{c2r}) are determined to control the relationships. In case of a heterogeneous material, the constitutive relationship of each element is varied by employing random variables.

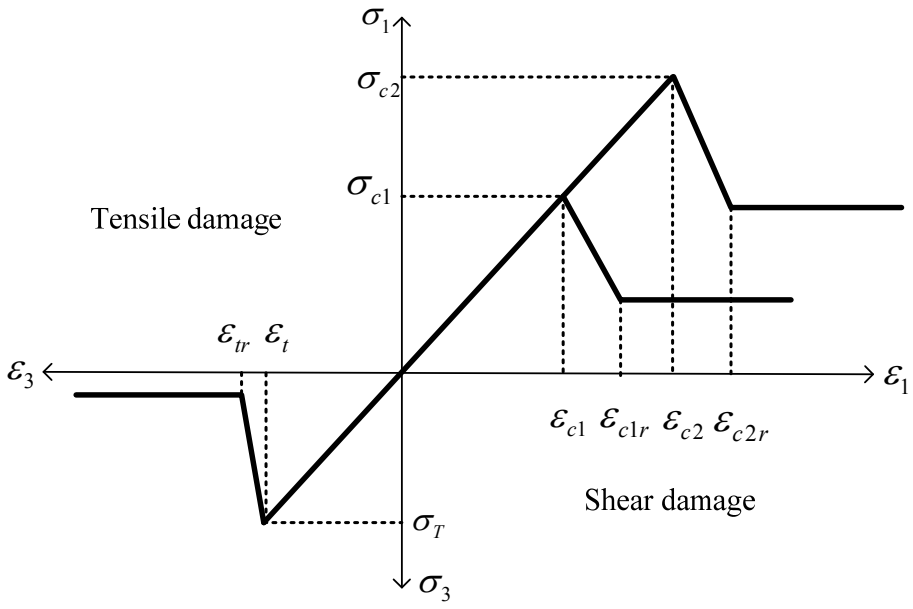

Figure 14. Schematic constitutive relationship based on tensile and shear damage.

To calculate the damage energy release rate of Eqn. (5.11), the elastic strain energy per unit volume of linear elastic material is used as follows:

$$\tilde{U}_e = \frac{1}{2}\sigma_{ij}\varepsilon_{ij} \tag{5.14}$$

The elastic strain energy per unit volume is rewritten using the stress/strain relation of an isotropic solid, which is described as:

$$\sigma_{ij} = \lambda\delta_{ij}\varepsilon_{kk} + 2\mu_L\varepsilon_{ij} \tag{5.15}$$

where δ_{ij} is the Kronecker delta, and Lamé's constants λ, μ_L are defined as below:

$$\lambda = \frac{\nu E}{(1+\nu)(1-2\nu)}, \mu_L = \frac{E}{2(1+\nu)} \tag{5.16}$$

Then, substituting into Eqn. (5.14), the elastic strain energy per unit volume can be expressed in terms of strains:

$$\tilde{U}_e = \frac{1}{2}\lambda\delta_{ij}\varepsilon_{kk}\varepsilon_{ij} + \mu\varepsilon_{ij}\varepsilon_{ij} \tag{5.17}$$

In this thesis, the damage dissipated energy rate is assumed to decrease linearly with the principal strain and the damage variable has a different stain softening curve for tensile and shear failure, which are determined by the Mohr-Coulomb failure criterion. The evolution equation of the damage variable is modeled by the damage energy release rate and the softening function, $g(\varepsilon)$ which is determined using:

$$g(\varepsilon) = \begin{cases} 0 & \text{if } \bar{\varepsilon} \le \varepsilon_t, \bar{\varepsilon} \ge \varepsilon_{tr} \\ \dfrac{(s-1)\tilde{Y}_{e0}}{\varepsilon_t - \varepsilon_{tr}} & \text{if } \varepsilon_t < \bar{\varepsilon} < \varepsilon_{tr} \end{cases} \tag{5.18}$$

where ε_t, is the maximum tensile stain, and ε_{tr}, released tensile strain for tensile damage and $\tilde{Y}_{e0}$ is the initial value of damage energy release rate, ε_t is determined by the tensile strength, σ_T, in Figure 15 and s is a parameter for strain softening rate, which has $0<s<1$. The softening parameter for the tensile damage is assumed 0.1, while the softening parameter for the shear damage is decided by a confining pressure. We assumed the softening parameter is increasing linearly with the confining pressure. So, the softening parameter for the shear damage is calculated by s=Pc(i)/max(Pc(n))*0.99, where Pc(i) indicates a current confining pressure and max(Pc(n)) represents the maximum confining pressure during triaxial compression tests. If the confining pressure is high, the softening parameter becomes closed to 0.99. That means the stress/stress curve does not softening and the material is nearly perfect plasticity. When the state of the current equivalent strain, $\bar{\varepsilon}$, is between ε_t and ε_{tr}, the dissipated strain energy is computed by multiplying of the softening function with $(\bar{\varepsilon} - \varepsilon_t)$. After the equivalent strain is over the softening region ($\bar{\varepsilon} \ge \varepsilon_{tr}$), the damage variable is gradually increased up to 0.99, which is calculated by an equation of $1 - s \cdot \tilde{Y}_{e0} / \tilde{U}_e$. The damage evolution law can then be expressed as:

$$D = \begin{cases} 0 & \text{if } \bar{\varepsilon} \le \varepsilon_t \\ 1 - \dfrac{g(\varepsilon)\cdot(\bar{\varepsilon} - \varepsilon_t) + \tilde{Y}_{e0}}{\tilde{U}_e} & \text{if } \varepsilon_t < \bar{\varepsilon} < \varepsilon_{tr} \\ 1 - \dfrac{s \cdot \tilde{Y}_{e0}}{\tilde{U}_e} & \text{if } \bar{\varepsilon} \ge \varepsilon_{tr} \end{cases} \tag{5.19}$$

In cases of shear damage, ε_{c1} and ε_{c2} are used instead of ε_t in Eqn. (5.18) and (3.19). ε_{c1r} and ε_{c2r} are calculated when the shear failure is detected. The shear strains are determined by compressive strength σ_{c1} and σ_{c2}, which are obtained from experimental results for a rock. All these tensile and shear strengths are also varied through the simulation domain (when needed) by employing random variables. Hence, the constitutive relationship of each element could vary by confining pressure, material heterogeneity, and type of failure.

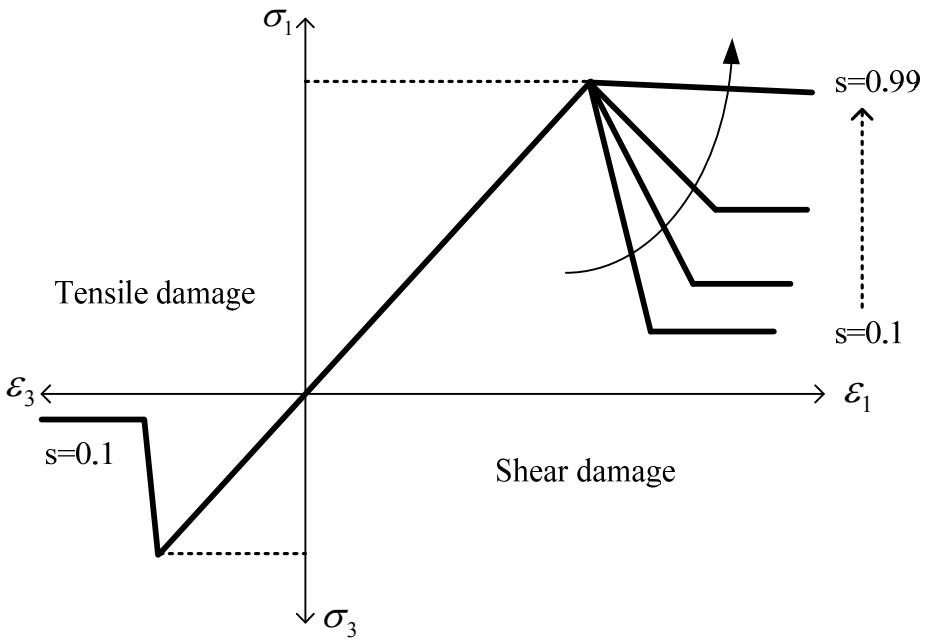

Figure 15. Schematic of softening parameter variation by tensile and shear damage.

3. Thermo-Hydro-Mechanical Rock Response

The fully coupled processes involving thermal, hydrologic and mechanical effects have been studied for a nuclear-waste repository in fractured rocks during the early 1980s (Stephansson et al., 1996; Tsang, 1987, 1991; Tsang et al., 2004). Through the international cooperative DECOVALEX (acronym for DEvelopment of COupled models and their VALidation against Experiments) project, these coupled processes have made significant progress and results have been published in a series of reports and books (Jing et al., 1993, 1995, 1996; Stephansson et al., 1996). Similar coupling procedure operates in the gas/oil recovery industry and geothermal energy development. The coupled THM process can be extended for chemical effect by the swelling of shale for wellbore stability analysis (Ghassemi and Diek, 2003; Ghassemi et al., 2009; Zhou and Ghassemi, 2009). The coupled THM process is described using the constitutive relations for the porous matrix, the pore space, and the fluid and heat diffusions within the conservation laws for momentum, mass, and energy. Terzaghi's 1D consolidation theory of soils was proposed for its pore-pressure effect on soil deformation (Terzaghi, 1923) and it was extended to linear poroelasticity for elastic porous media considering effective stress change by variations of pore pressure under fluid loading using the isothermal consolidation problem (Biot, 1941). Hooke's law of elasticity with the concept of infinitesimal displacement hypothesis, Darcy's law of flow in porous media, and Fourier's law of heat transfer were adopted. The effective heat transfer concept, which generally assumes that temperature is the same in both rock solids and pore fluid, was also adopted since local heat transfer is rapid enough for equilibrium of temperature, unlike in global heat and fluid diffusion models.

Then, based on the framework of Rice and Cleary formulation (Rice and Cleary, 1976) and Kurashige's approach for thermal effects (Kurashige, 1989), the thermo-poroelastic model was extended to combined

thermal and hydraulic stress for fully-saturated homogeneous rock (Mctigue, 1986; Palciauskas and Domenico, 1982). The deformation processes are considered as quasistatic states, since the inertia effect of rock mass is assumed to be neglected (Li, 1998).

3.1 Constitutive Relations

In deriving the coupled THM equations, the total stress, σ_{ij}, (*tensile positive convention*); pore pressure, p, for compressive positive; and temperature, T, are considered as the coupled variables. The general constitutive equations for fully saturated thermoelastic porous material can be written based on thermodynamics principles as follows (Cleary, 1976, 1977);

$$\varepsilon_{ij} = C_{ijkl}\sigma_{kl} + B_{ij}p + \alpha_{ij}^{T}\delta_{ij}T \tag{5.20}$$

$$\zeta = B_{kl}\sigma_{kl} + \beta p + \alpha_{p}^{T}T \tag{5.21}$$

where σ_{ij} denotes the components of the total stress tensor, ε_{ij} is the strain tensor from the solid displacements, p and T are the pore pressure and temperature, ζ is the variation of the fluid content per unit volume of the porous material, α_{ij}^{T} is the linear thermal expansion coefficient tensor, and α_{p}^{T} is the thermal expansion coefficient of the pore space. The elastic tensors C_{ijkl} and B_{ij} for isotropic materials are described as:

$$C_{ijkl} = \frac{1}{4G}\left(\delta_{ik}\delta_{jl} + \delta_{il}\delta_{kl} - \frac{2}{1+\nu}\delta_{ij}\delta_{kl}\right) \tag{5.22}$$

$$B_{ij} = \frac{3\left(\nu_u - \nu\right)}{2GB\left(1+\nu\right)\left(1+\nu_u\right)}\delta_{ij} \tag{5.23}$$

where B is Skempton's pore pressure coefficient defined as (Skempton, 1954):

$$B = \frac{3\left(\nu_u - \nu\right)}{\alpha\left(1-2\nu\right)\left(1+\nu_u\right)} \tag{5.24}$$

$$\beta = \frac{1}{B}\left(\frac{1}{K} - \frac{1}{K_s}\right) - \frac{\phi}{K_f} \tag{5.25}$$

$$K = \frac{2G\left(1+\nu\right)}{3\left(1-2\nu\right)} \tag{5.26}$$

Kurachige's work introduced an assumption that pores thermally expand while their volume remains the same, so the volumetric thermal expansion coefficient of pore space can be expressed as:

$$\alpha_{p}^{T} = \phi\alpha_{m} \tag{5.27}$$

K and G are bulk and shear moduli, ϕ is the porosity, K_s are the bulk of solid matrix, α is Biot's coefficient, and ν and ν_u are the drained and undrained Poisson's ratio. Rearranging Eqn. (5.20) using above relations and presenting it in a more convenient form,

$$\varepsilon_{ij} = \frac{1}{2G}\left(\sigma_{ij} - \frac{\nu}{1+\nu}\sigma_{kk}\delta_{ij}\right) + \frac{\alpha\left(1-2\nu\right)}{2G\left(1+\nu\right)}p\delta_{ij} + \frac{\alpha_m}{3}T\delta_{ij} \tag{5.28}$$

where σ_{kk} is the first invariant of the stress tensor:

$$\sigma_{kk} = \frac{2G(1+\nu)}{(1-2\nu)}\varepsilon_{kk} - 3\alpha p - \frac{2G(1+\nu)}{3(1-2\nu)}\alpha_m T \tag{5.29}$$

Eqn. (5.28) can be presented in terms of strain:

$$\sigma_{ij} = 2G\varepsilon_{ij} + \left(K - \frac{2G}{3}\right)\varepsilon_{kk}\delta_{ij} + \alpha p\delta_{ij} + \frac{2G(1+\nu)}{3(1-2\nu)}\alpha_m T\delta_{ij} \tag{5.30}$$

The change of fluid content also can be presented as:

$$\zeta = \frac{3(\nu_u - \nu)}{2GB(1+\nu)(1+\nu_u)}\delta_{ij}\sigma_{ij} + \frac{1}{B}\left(\frac{1}{K} - \frac{1}{K_s}\right)p - \left(\left(\alpha_f - \alpha_m\right)\phi\right)\Delta T \tag{5.31}$$

Simplifying Eqn. (4.12) by applying Eqn. (1.10) gives the following relationship:

$$\frac{1}{B}\left(\frac{1}{K} - \frac{1}{K_s}\right) = \frac{9(\nu_u - \nu)}{2GB^2(1+\nu)(1+\nu_u)} \tag{5.32}$$

$$\zeta = \frac{3(\nu_u - \nu)}{2GB(1+\nu)(1+\nu_u)}\sigma_{kk} + \frac{1}{B}\left(\frac{1}{K} - \frac{1}{K_s}\right)p - \left(\left(\alpha_m - \alpha_f\right)\phi\right)\Delta T \tag{5.33}$$

Substituting Skempton's coefficient, B, into the equation above and simplifying Eqn. (5.33), then summarizing from Eqn. (5.30) and (5.35), finally obtains the following constitutive relations:

$$\sigma_{ij} = 2G\varepsilon_{ij} + \left(K - \frac{2G}{3}\right)\varepsilon_{kk}\delta_{ij} + \alpha p\delta_{ij} + K\alpha_m T\delta_{ij} \tag{5.34}$$

$$\zeta = \frac{\alpha(1-2\nu)}{2G(1+\nu)}\left(\sigma_{kk} + \frac{3}{B}p\right) - \left(\left(\alpha_f - \alpha_m\right)\phi\right)\Delta T \tag{5.35}$$

where α_m and α_f are the thermal expansion coefficients of solid and fluid.

3.2 Conservation Laws

Three conservation laws are applied for the coupled THM processes. First, a momentum balance or equilibrium equation with no body force assumption is described as:

$$\sigma_{ij,j} = 0 \tag{5.36}$$

Second, to express effective force of the fluxes of fluid, the fluid flow in porous rock was assumed to be governed by Darcy's law with no phase change:

$$q_i = -\frac{k}{\mu}p_{,i} \tag{5.37}$$

The fluid mass balance equation is obtained as:

$$\frac{\partial\zeta}{\partial t} + q_{i,i} = 0 \tag{5.38}$$

Finally, to express the effective force of the heat transfer, the Fourier equation is used for heat transfer.

$$h_i = -k^T T_{,i} \tag{5.39}$$

The energy balance equation is used for an element unit volume (Combarnous and Bories, 1975):

$$\frac{\partial\left(\rho C_t T\right)}{\partial t}+h_{i,i}=0 \tag{5.40}$$

where ρ and C_t are the mass density and specific heat capacity for the bulk material, k is the permeability, μ is the fluid viscosity, and k^T is the thermal conductivity.

3.3 Governing Equations

The momentum, fluid mass, and energy balance equations can be combined with the above constitutive and transport equations and yield the following field equations. First, substituting these small deformation relationships into Eqn. (5.34):

$$\varepsilon_{ij}=\frac{1}{2}\left(u_{ij}+u_{ji}\right) \tag{5.41}$$

$$\varepsilon_{kk}=u_{kk} \tag{5.42}$$

The deformation field equation is obtained from Eqn. (5.34) and (5.36):

$$Gu_{i,ij}+\frac{G}{1-2\nu}u_{j,ji}-\alpha p_{,i}-\frac{2G\alpha_m\left(1+\nu\right)}{3\left(1-2\nu\right)}T_{,i}=0 \tag{5.43}$$

Second, for the fluid-diffusivity field equations, differentiating Eqn. (5.30) and (5.42) twice leads to:

$$\sigma_{ii,jj}=2G\left(\frac{1+\nu}{1-2\nu}\varepsilon_{kk,jj}\right)-3\alpha p_{,jj}-\frac{1+\nu}{1-2\nu}2G\alpha_m T_{,jj} \tag{5.44}$$

$$\varepsilon_{kk,jj}=u_{ii,jj} \tag{5.45}$$

Differentiating Eqn. (5.43) with respect to x_i, solving for $u_{ii,jj}$ and substituting into Eqn. (5.45) and then into Eqn. (5.44), the compatibility equation can be obtained in terms of stresses:

$$\sigma_{ii,jj}+\frac{2\alpha\left(1-2\nu\right)}{1-\nu}p_{,jj}+\frac{4G\left(1+\nu\right)}{3\left(1-\nu\right)}\alpha_m T_{,jj}=0 \tag{5.46}$$

Differentiating Eqn. (5.43) with respect to x_j and substituting into Eqn. (5.46), the following equation can be described:

$$\zeta_{,jj}=\frac{\alpha\left(1-2\nu\right)}{2G\left(1+\nu\right)}\left[\left(\frac{3}{B}-\frac{2\alpha\left(1-2\nu\right)}{\left(1-\nu\right)}\right)p_{,jj}-\frac{4G\left(1+\nu\right)}{3\left(1-\nu\right)}\alpha_m T_{,jj}\right]-\gamma_2\Delta T_{,jj} \tag{5.47}$$

Then, solving for $p_{,jj}$ from Eqn. (5.47) and substituting into Eqn. (5.38), the fluid diffusivity field equation can be obtained as:

$$\dot{\zeta}=C^f\left[\zeta_{,jj}+\left(\frac{2\alpha\left(1-2\nu\right)}{3\left(1-\nu\right)}-\gamma_2\right)T_{,jj}\right] \tag{5.48}$$

where, C^f is the fluid diffusion coefficient, which is defined as:

$$C^f=\frac{2kB^2G\left(1-\nu\right)\left(1+\nu_u\right)^2}{9\mu\left(1-\nu_u\right)\left(\nu_u-\nu\right)} \tag{5.49}$$

Then, differentiating Eqn. (5.35) with respect to time and substituting into Eqn. (5.38) with Darcy's law, Eqn. (5.37), and applying the relationships of σ_{kk} and ε_{kk}, the fluid diffusion field equation can be expressed in terms of pore pressure:

$$\dot{p} = M\left[kp_{,jj} - \alpha\dot{\varepsilon}_{kk} + \left(\alpha\alpha_m + \left(\alpha_f - \alpha_m\right)\phi\right)\Delta\dot{T} \right] \tag{5.50}$$

where M is the Biot modulus, which is defined as the change of fluid contents as a result of pore pressure variation under constant volumetric strain per unit volume.

$$M = \frac{2G\left(\nu_u - \nu\right)}{\alpha^2\left(1-2\nu\right)\left(1-2\nu_u\right)} \tag{5.51}$$

Finally, for the thermal diffusivity field equation can be obtained from Eqn. (5.39) and (5.40) as:

$$\dot{T} = c^T\nabla^2 T \tag{5.52}$$

where c^T is the thermal diffusivity coefficient for the bulk material.

$$c^T = \frac{k^T}{\rho\, C_t} \tag{5.53}$$

where ρ and C_t are the mass density and specific heat capacity for the bulk material, and k^T is the thermal conductivity.

Finally, three governing equations (Eqn. (5.48), (5.50), (5.52)) for the coupled THM processes are derived from the momentum, fluid mass, and energy balance equations combined with the constitutive and transport equations above. For convenient forms for the fully coupled Thermo-Hydro-Mechanical model, following governing equations could be written;

$$\left(K + \frac{G}{3}\right)\nabla\left(\nabla\cdot\mathbf{u}\right) + G\nabla^2\mathbf{u} + \mathbf{m}\left(\alpha\nabla p + \gamma_1\nabla T\right) = 0 \tag{5.54}$$

$$\alpha\left(\nabla\cdot\dot{\mathbf{u}}\right) + \beta_p\dot{p} - \frac{k}{\mu}\nabla^2 p - \gamma_2\nabla\dot{T} = 0 \tag{5.55}$$

$$\dot{T} - c^2\nabla^2 T = 0 \tag{5.56}$$

where $\mathbf{u}$ is displacement vector and $\mathbf{m}=[1,1,1,0,0,0]^T$ for 3D problems. The coefficients in Eqn. (5.54) and (5.55) are defined as following;

$$\beta_p = \frac{\alpha-\phi}{K_s} + \frac{\phi}{K_f} \tag{5.57}$$

$$\gamma_1 = K\alpha_m \tag{5.58}$$

$$\gamma_2 = \alpha\alpha_m + \left(\alpha_f - \alpha_m\right)\phi \tag{5.59}$$

Then the coupled equations are usually treated by numerical solution techniques using FEM, BEM, FDM, and FVM for practical conditions such as nonlinearity, anisotropy, heterogeneity, and complex geometries (Börgesson et al., 2001; Li, 1998; Millard, 1996; Noorishad and Tsang, 1996; Noorishad et al., 1992; Rutqvist et al., 2001; Schrefler, 2001). Among these numerical methods, FEM formulation is popularly used; and previously, the 3D, fully coupled, and nonlinear THM model has been developed within a finite element formulation using damage mechanics (Lee, 2011; Zhou and Ghassemi, 2009).

3.4 Poroelastic Parameter Changes

Since mechanical behavior of the fully coupled THM model is controlled by damage mechanics. It is necessary to consider the change of the poroelastic parameters such as bulk modulus, Biot's coefficients, and other related parameters (β_p, γ_1, γ_2) and when failure is detected and stress-strain relation is no longer

elastic. So, based on the status of the effective stress at a gauss point of an element, type of failure is decided by the Mohr-Coulomb failure criterion with tension cut-off and damage variables are calculated by the damage evolution law proposed in Chapter 3. We used linear 3-node triangular element for 2D simulation and 4-node tetrahedron element for 3D simulation in this thesis and both triangular and tetrahedron elements have one Gaussian point. So, according to the damage variable at the gauss point of the failed element, the poroelastic parameters are newly calculated. Since the effective Young's modulus is updated by $E' = (1-D)E$, the bulk modulus should be re-calculated by $K = E'/3(1-2\nu)$. In addition, we assumed that Biot's coefficient is changed to 0.99 when the damage variable is over 0.8. By the changes of the bulk modulus and Biot's coefficient, related parameters (β_p, γ_1, γ_2) are updated accordingly.

3.4.1 Time step of the coupling process

The complexity of the THM problem is often attributed to uncertainty of parameter values and unpredictable geometrical complexities of rock fractures with various dimensions under thermal, hydraulic, and mechanical loadings (Jing, 2003). Numerically, the coupled THM process is a challenge issue because of wide differences among the three processes in temporal and spatial scales (Tsang et al., 2004). While the thermal effect has relatively longer time and spatial scales, mechanical effect has a shorter time scale. This is because mechanical response can transfer with the speed of elastic waves, and various dimensions of fractures, joints and faults dominated its deformability (Tsang, 1991). Also, hydraulic effect is sensitive in both small-scale pore distribution and fracture networks with longer flow and solute transport time. Hence, finding an appropriate value for the time step is a critical aspect of the coupling process. The time increment should be small enough to capture the rock deformation accurately because of the high speed of stress waves in porous rock, however, too small of a time increment is not suitable for the fluid flow and the heat transfer equation as changes from one time step to another would be too small. Therefore, generally the smaller time increment is preferred to use. Moreover, smaller time step requires larger computational costs in time-dependent problems, thus the largest possible time step should be chosen by stability and accuracy analysis.

3.4.2 Fluid flow analysis in fractures

A common approach to fluid flow analysis in rock fractures is to assume idealized parallel plates separated by a constant aperture. In that approach, as described in Figure 16, fracture propagation is driven by injection of an incompressible Newtonian fluid at a constant volumetric injection rate Q_i. The incompressible fluid is described by the Poiseuille (lubrication) equation (Batchelor, 1967). The lubrication equation can be used to solve the fluid pressure distribution along the fracture. Fluid flow inside the fracture length depends on the aperture, roughness of the walls, and geometry of fractures. When the aperture is large and the fracture surface is smooth, large bulk flow dominates and Darcy's law is no longer valid. The various laboratory results showed that the assumption of laminar flow in the fractures is valid for Reynolds number less than about 2300 (Witherspoon et al., 1980). The Reynolds number can be defined for fluid flow in the fracture:

$$\mathrm{Re} = \frac{\rho_f \bar{u} w_f}{\mu_f} \tag{5.60}$$

where $\bar{u}$ is an average flow velocity in the fracture, μ_f the fluid viscosity of the fracturing fluid, w_f the fracture aperture, and ρ_f is an density of the fracturing fluid. The lubrication equation for the fluid flow is described as:

$$q = -\frac{w_f^3}{12\mu_f}\frac{\partial p_f}{\partial x} \tag{5.61}$$

Two-dimensional fluid flow in the fracture plane is expressed as:

$$\nabla_2 p_f(x,y,t) = -\frac{12\mu_f}{w_f^3(x,y,t)} q(x,y,t) \tag{5.62}$$

$$\nabla_2 \cdot \left[\frac{w_f^3(x,y,t)}{12\mu_f} \nabla_2 p_f(x,y,t) \right] = -v_l(x,y,t) - Q_i(t)\,\delta(x - x_i, y - y_i) \tag{5.63}$$

$$\text{Boundary conditions, } \frac{\partial p_f}{\partial n} = 0 \text{ on } \partial A_f$$

$$Q_i(t) = Q_{i0} \text{ at injection point}$$

where ∇_2 is the two-dimensional divergence operator in the fracture plane, μ_f is the fluid viscosity, v_l is the leakoff fluid from the fracture plane, p_f(x,y,t) is the fluid pressure in the fracture, w_f is the fracture aperture, $Q_i(t)$ is the fluid injection rate, and A_f is area of the fracture plane.

So, the fluid flow inside fractures is governed by the Poiseuille equation. The continuity equation and boundary conditions for the fluid flow in the fracture plane describe the point where the fluid injection rate is equal to the fluid flux at a wellbore and no flow at the crack tip is assumed. This boundary condition is valid when the fracturing fluid is fully filled inside the fracture. That is, there is no fluid lag, defined as an empty zone ahead of the fluid front to the fracturing tip, in the fluid flow analysis. If the fluid lag is included, there is additional unknown of the problem (Garagash and Detournay, 2000). Tracking of both the fluid front and the fracturing tip is required to account for the fluid lag, however it is not easy since the fluid lag length is unknown. In addition, the no fluid flux boundary condition is difficult to implement in finite element methods, because an arbitrary constant pressure assumption between the fracturing tip and neighbor is impracticable in the coupling algorithm. Because the pressure level inside the fracture is unknown, the zero flux boundary condition is not applicable to use in FEM. Therefore, zero pressure boundary condition at the fracturing tip is assumed instead of the zero flux boundary condition. Due to opening mode of fracture by hydraulic pressurization near the fracturing tip, pressure level at this region is near zero so the zero pressure assumption is appropriate and practicable to use in FEM.

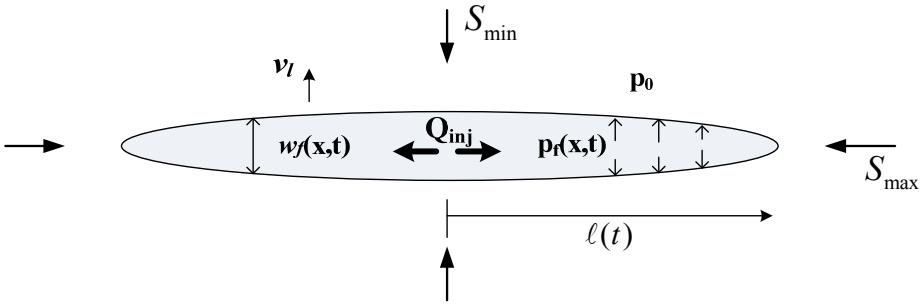

Figure 16. The fluid-driven hydraulic fracture propagation process.

3.4.3 Fluid leakoff

Leakoff during hydraulic fracturing has been shown to significantly affect fracture growth (Economides and Nolte, 2000). The leakoff volume affects the efficiency of the treatment. The injection efficiency, ε_{inj}, can be defined as the volume of fluid in the fracture divided by the total volume of injected fluid. The volume of fluid in the fracture can be defined as the total volume of injected fluid minus the leakoff volume.

$$\varepsilon_{inj} = \frac{V_f}{V_i} = \frac{V_i - V_l}{V_i} \tag{5.64}$$

where V_f is the total volume of the fractures, V_l is the leakoff volume, and V_i is the total injected fluid volume. In this paper, the fluid lost by the injected fluid leaking off into the rock matrix is expressed using Darcy's law:

$$v_l(x,y,t) = -\frac{k_m}{\mu_f}\frac{\partial p(x,y,z,t)}{\partial n} \tag{5.65}$$

where k_m is the rock matrix permeability and n is the normal direction of the fracture plane. The pressure differential between the fracture and the rock matrix and the permeability change of the rock formation are key factors that affect the volume of the leakoff.

3.4.4 Numerical modeling of fracture propagation

In this thesis, the fracture propagation model was developed based on three requirements: a possibility to describe continuous crack geometry, a capability to apply a moving-boundary scheme for transition of hydraulic forces through fracturing path, and simplicity of implementation with low computational effort.

To satisfy these requirements, a few guidelines for the fracture propagation model have been established. First, the crack path can only propagate through the inside of elements, as with cohesive element modeling and XFEM. Second, for low computational cost, the crack path should be expressed without modifying the mesh information. No redefinition of the element mesh is required after crack propagation. Third, there is no pre-assigned crack path, which means cracks can grow in arbitrary directions without restriction; this approach puts no limitation on the direction of the crack propagation. Last, to apply a moving-boundary scheme of hydraulic forces, crack surfaces are assumed inside the cracked element, and the direction of crack propagation is decided by the proportional direction of the maximum principal

stress at a fracture tip. Furthermore, a specialized 2D and 3D crack partitioning algorithm was employed to calculate the splitting surface in the cracked element for several scenarios.

When the fully coupled thermo-hydro-mechanical (THM) analysis is modeled via finite-element methods (FEM), an 8-node quadrilateral element is recommended for use; the 4 corner nodes are used for pore pressures and temperature, while all 8 nodes are used for displacements (Aboustit et al., 1985; Christian, 1977). However, in our fracture propagation modeling, the conventional rectangular element mesh is not efficient, because our fracture propagation model assumes that the crack path can grow arbitrarily without redefining mesh information. This approach is hugely beneficial for computational time and simplicity in numerical implementation. From the standpoint of the fracture propagation approach, if a rectangular mesh is used, the fracture propagation path shows a zig-zag crack band (Figure (a)). Moreover, mathematical formulation of the EPM is unavailable and should be developed. Splitting a rectangular element is more complicated than using a triangular element and it may increase computational costs. A triangular mesh (Figure 5.1(b)) clearly represents the arbitrary fracture propagation more flexibly than a rectangular mesh. By the same token, in the 3D crack propagation problem, a 4-node tetrahedron element has more flexibility to express the arbitrary growth of the 3D crack than an 8-node or 16-node cubic element. We used 3-node triangular and 4-node tetrahedron elements for the fracture propagation model in this project.

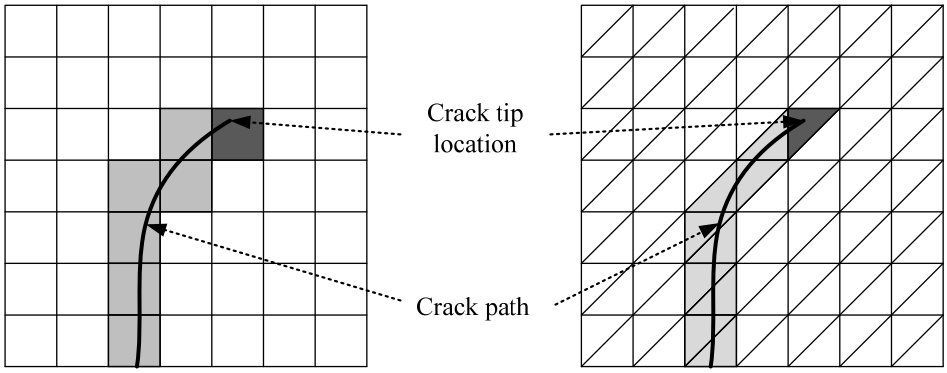

(a) Rectangular element (b) Triangular element

Figure 17. Description of fracture path by mesh type (re-drawing from (Bazant and Planas, 1997)).

3.4.5 Fracture initiation for hydraulic fracturing

Stresses applied to the rock by various loading mechanisms introduce crack nucleation, propagation, interaction, and coalescence, but there is no universally accepted theory for the fracture initiation and propagation. Practically, fractures can be initiated by various failure mechanisms such as tensile, shear and compaction. Among these failure mechanisms, the tensile fracture is dominating failure mechanism in the hydraulic fracture propagation. So, we assumed there is only tensile mode fracture available at a fracture tip. The fracture initiation criterion is checked at Gaussian point of the crack tip elements. For capturing the hydraulic fracturing failure of the brittle rock, the most commonly used criterion is the maximum tensile strength criterion, defined as:

$$\sigma_3 \geq -\sigma_T, \tag{5.66}$$

where σ_T is a tensile strength of material, and σ_3 is the minimum principal effective stress, which is also the maximum effective tensile stress for poroelastic analysis. So, we checked the fracture initiation criterion at a fracture tip. Once the fracture initiation criterion met, the fracture tip is extended by the fracture propagation algorithm, described in following.

3.4.6 Fracture propagation algorithm

Once the fracture initiation criterion was met at crack tips, the hydraulic fracture is extended with certain length and direction as shown in Figure 19. . So, tracking the fracture propagation is one of the main issues for hydraulic fracturing simulation. Developing a tracking algorithm for the crack-tip location and path information was necessary to apply correct boundary conditions for fluid pressure inside fractures and for estimating the propagating location of fracture. In order to extend the fracture, crack length criterion for quasi-static crack increments and crack direction criterion for angle of the fracture propagation are required.

First, the crack length criterion is adopted from Paris' law, which is proposed to compute a crack increment by the stress intensity factor under fatigue stress regime (Paris and Erdogan, 1963). Usually, the crack tip is assumed to advance in a quasi-static manner meaning that the crack is propagating at a constant speed in the hydraulic fracture propagation simulation. So every time a crack tip fails, the crack is assumed to advance by a fixed length, but crack should grow at different speeds during various stages because the energy required to propagate the crack could be different at different stages, particularly through heterogeneous materials. So, we adopted the propagation criterion suggested by (Renshaw and Pollard, 1994) to extend crack tips at every step. The crack increment is calculated by the energy accumulated at the crack tips.

$$l_{\text{adv}} = l_{\max}\left(\frac{U_{\text{tip}}}{U_{\max}}\right)^{\chi} \tag{5.67}$$

where U_{tip} is the strain energy accumulated at the crack tip, $U_{\max}$ is the maximum stain energy concentration at the crack tip, l_{adv} is an increment crack length, $l_{\max}$ is the maximum increment crack length at any propagation step, and χ is an empirical velocity index. The crack incremental method is a Paris-type law (Paris and Erdogan, 1963). Renshaw and Pollard (1994) defined $l_{\max}$ as the initial flaw size, because they assumed the maximum incremental length could be representative of the fracture processing zone (Irwin, 1958), which is a nonlinear zone characterized by progressive softening (stress decreases as increasing deformation). Renshaw and Pollard (1994) demonstrated by experimentation that the empirical velocity index of 0.35 yields realistic fracture propagation for the opening mode fractures of brittle rock. However, there is no detail information for the hydraulic fracturing simulation, so that we assumed input parameters by Renshaw and Pollard's crack incremental method. We assumed that $l_{\max}$ is same as a pre-existing crack length and the empirical velocity index is assumed as 0.35. In addition, $U_{\max}$, the maximum strain energy concentration at the crack tip, is assumed ten times larger than $U_{\min}$, which is the minimum strain energy required to advance the crack tip and defined;

$$U_{\min} = \frac{1}{2}\sigma_T \varepsilon_T = \frac{1}{2E}{\sigma_T}^2 \tag{5.68}$$

where σ_T is the tensile strength of rock, E is Young's modulus.

Second, the fracture propagation angle is assumed to follow the direction of perpendicular to the maximum circumferential tensile stress. It is determined by the normal direction of the maximum tensile stress. Because the fracture propagation induced by hydraulic pressurization is usually attributed to tensile mode opening, the orientation of the failure may simply be determined by the maximum principal stress direction as described in Figure 18. The principal angle is computed at the crack tip (Figure 19). The rotation angle, θ_p, is calculated using the normal stresses and the shear stress as follows:

$$\tan\left(2\theta_p\right) = \frac{2\tau_{xy}}{\sigma_x - \sigma_y} \tag{5.69}$$

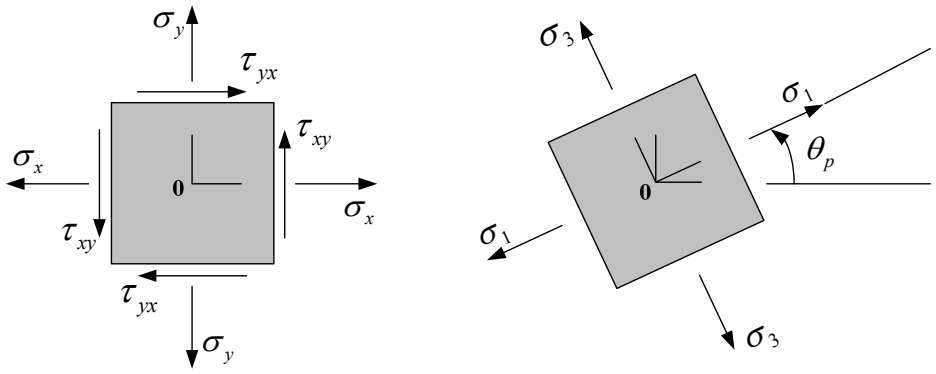

Figure 18. Illustration of the maximum principal stress direction.

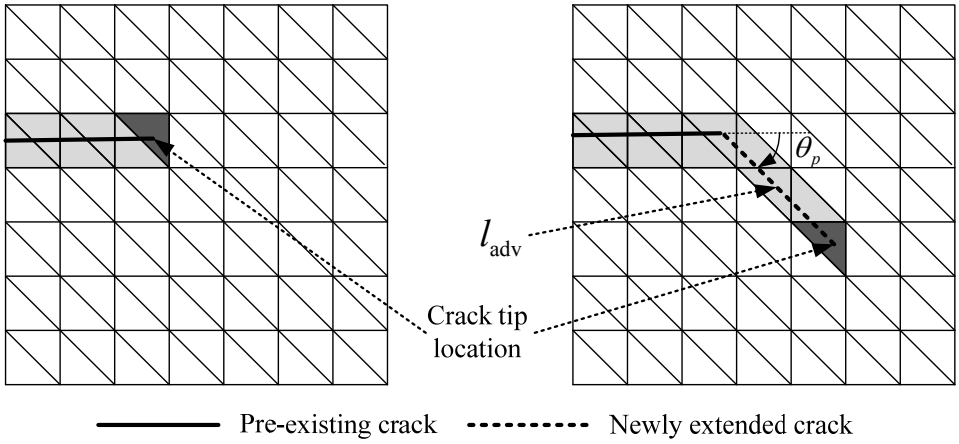

Figure 19. Illustration of crack propagation with crack increment and angle.

3.4.7 Moving boundary scheme using element partition methodology (EPM)

Another challenging issue for the hydraulic fracture propagation is applying transient boundary conditions on the propagating fracture surfaces at every step. The hydraulic pressure through the updated fracturing path, which is computed by the fluid flow analysis, must be applied as a boundary condition for the rock deformation analysis. So, a "quasi-static" hydraulic loading algorithm is used to provide the proper

boundary conditions for fluid pressure inside fractures. In this approach, when the propagation criterion is satisfied at the crack tip, the fracture geometry is extended by the propagation algorithm and the new crack geometry is calculated by EPM algorithm. Figure 20 briefly shows the boundary procedure to transfer from internal fluid pressure distribution to nodal forces. The pre-existing and newly propagated cracks are identified as equivalent crack elements (Zhang and Chen, 2008). The major features of the quasi-static hydraulic loading algorithm are identifying the newly extended fracture surface using the intersection points on the edges of the cracked element and applying the resulting nodal forces on the equivalent crack elements.

The EPM is used to compute the fracture areas subjected to the hydraulic pressurization. In this methodology, a crack plane intersecting the existing triangular element is defined using points on the edges of the existing element. When an element is cut by the newly propagated crack plane, the intersection points on the element edges are stored and updated at every time step. The EPM takes advantage of the continuous geometric features in both triangular and tetrahedron elements to construct fracture surfaces when a newly propagated crack path is cut through the triangular element (Huang and Zhang, 2010; Zhang and Chen, 2008). So the method does not require redefined mesh information during crack propagation, and the total number of degrees of freedom and the dimensions of the general stiffness matrix are not changed. The greatest advantage of the fixed mesh approach is low computation time and easier to encode for numerical implementation. However, the fixed meshes can lead poor definition of the fracture tips when the mesh size is too big, so that moderate size of the mesh is desired to use the EPM approach. When mesh size is too coarse to represent the fracture tips correctly, special care like the sub-mesh scheme near the fracture tip should be employed to obtain accurate results in the fixed mesh case. However, the sub-mesh scheme is computationally expensive and difficult to implement. Another disadvantage of the fixed mesh approach is resolution issue. This is because fracture elements representing the fracture geometry is too few at the early time, while the fracture elements are too many at the later time. In order to reduce the resolution issue, re-meshing scheme can be employed to make efficient use of computation time by controlling number of elements. Since the re-meshing method has great benefits to save computation time and to reduce the resolution issue, the method is recommended to use for larger scaled problem (i.e. reservoir scaled problem). However, developing the re-meshing scheme is not quite easy. Especially, the 3D re-meshing algorithm may require lots of efforts and mathematical challenges. As a result, we conclude that the fixed mesh approach is more desired than other approaches (sub-mesh, re-meshing), because numerical domains shown in this thesis is relatively small scale.

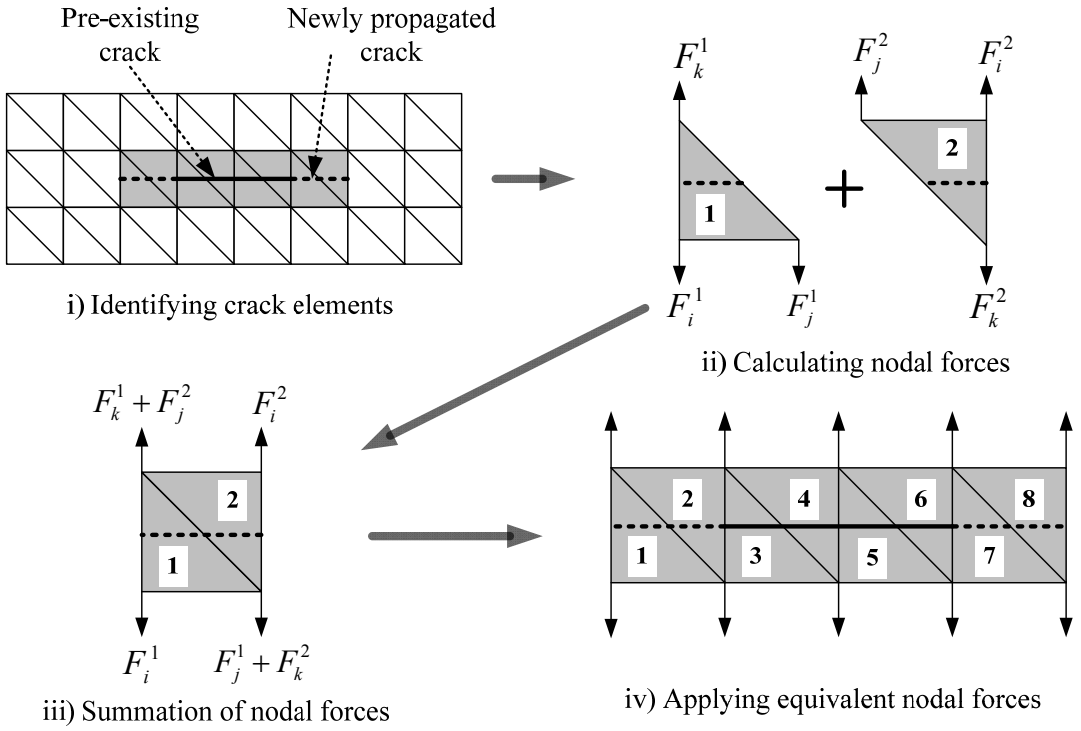

Figure 20. Schematic illustration of boundary condition description using EPM ((Huang and Zhang, 2010; Zhang and Chen, 2008).

4. Implementation of Damage Mechanics Hydraulic Fracturing Model

As mentioned above, the hydraulic fracturing could be defined as a fully coupled fluid-solid interaction problem. Each fluid and solid part is calculated by a separate solution, so that it is necessary to construct coupling algorithm between the fluid and solid analysis. When constructing the coupling algorithm between two analyses is handled, the consistency of solutions from these analyses remains an important issue. Especially for the hydraulic fracturing problem, the mechanical analysis of fracture opening is coupled with the fluid flow analysis. That is, the fluid pressure obtained from the fluid flow analysis is used to compute the fracture opening in the mechanical analysis. So, the opening amount should be consisted with the amount of injected fluid into the fractures by the mass conservation law. Since the fluid pressure and the fracture opening are calculated by a separate analysis, the iterative method is necessary to introduce to get converged solution between the fluid and solid analysis.

The coupling of the solution scheme for the fluid-driven fracturing problem was studied previously. Numerical modeling of the hydraulic fracturing was studied using mathematical formulation for the fluid-driven fracturing problem of simple planar geometry (Adachi and Detournay, 2008; Detournay, 2004). The fluid-driven propagation in poroelastic media was simulated using FEM technique and the influence of the poroelastic effects on fracture propagation was studied (Boone and Ingraffea, 1989; Boone et al., 1991).

The major difficulty in solving the coupled processes is the non-linear relationship between the fracture opening and the fluid pressure (Adachi and Detournay, 2008). Boone and Ingraffea (1990) proposed a partially coupled solution scheme with constant time step (Boone and Ingraffea, 1990). Adachi (2008) adopted the Picard iteration method (Picard, 1890) to solve the coupled fluid-driven fracturing problem. The Picard iterative process is useful to get approximation solution using iteration from a given trial solution. Figure 21 is a flowchart of the fully coupled iteration process.

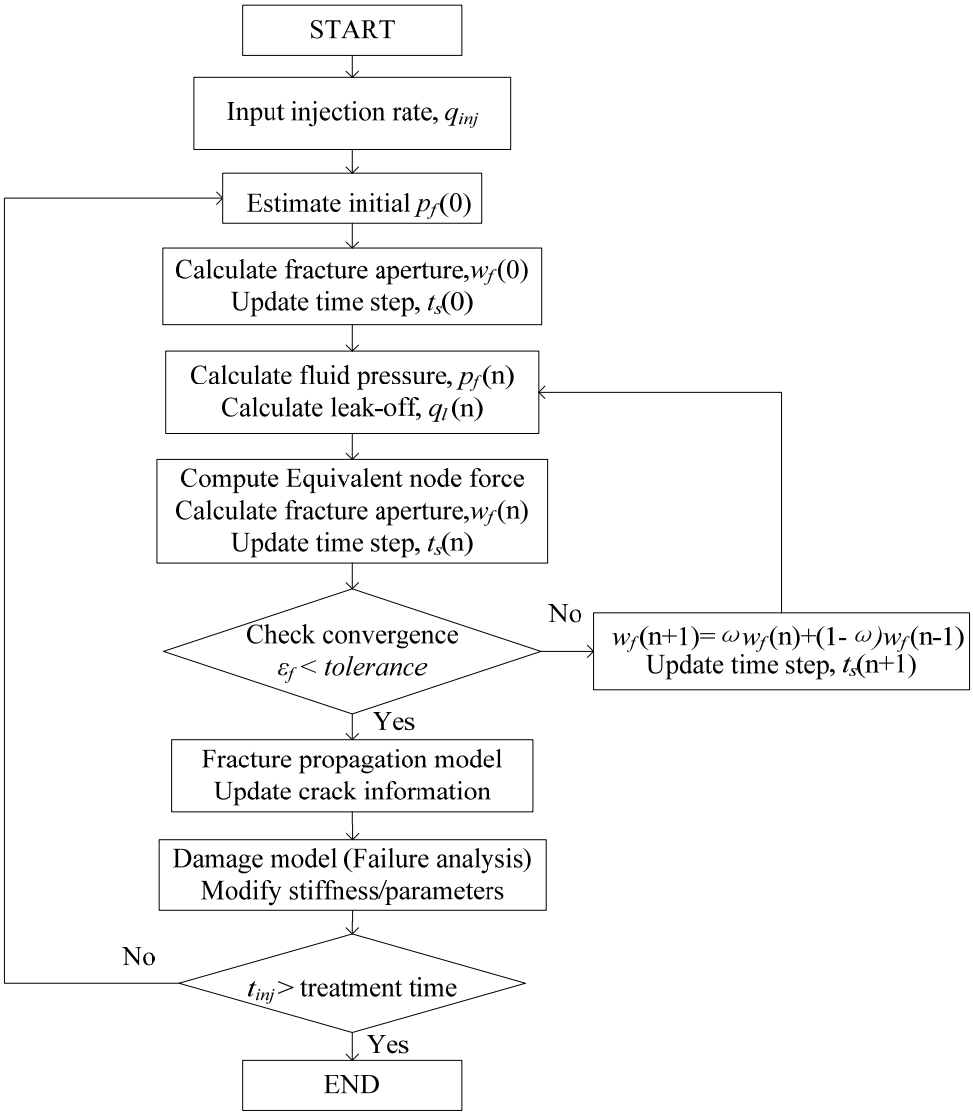

Figure 21. Flow chart of the fully coupled solution procedure.

Once a numerical model is constructed with an initial fracture, and input material parameters (E, v, k_m, etc) and necessary boundary conditions (in-situ stresses, Injection rate, etc) are estimated, it is needed to get a converged solution within a given initial fracture geometry before advancing to the next step. We used the iterative method to achieve the converged solution.

The basic procedure of the iterative process is straightforward: i) estimate initial fluid pressure distribution in the fractures, $p_f(0)$ and initial time step for an injection time, $t_s(0)$; ii) solve the coupled poroelastic equation for fracture opening, $w_f(0)$ and update time step, $t_s(0)$ using the total mass balance equation (Eqn. (6.2)) ; iii) solve the fluid flow equation for new fluid pressure inside the fractures, $p_f(\mathrm{n})$ and calculate leakoff rate, $q_l(\mathrm{n})$; iv) solve the poroelastic equation for new fracture opening, $w_f(\mathrm{n})$ and update the time step, $t_s(\mathrm{n})$ using the total mass balance equation (Eqn. (6.2)); v) the convergence of iterations is examined with given tolerance of the average error in the fluid pressure distribution in fractures as described in Eqn. (6.1), if not converged, return to iii) re-solve the fluid flow equation with the newly updated aperture profile and the time step, $w_f(\mathrm{n+1})$ and $t_s(\mathrm{n+1})$. The newly updated aperture profile is computed by $w_f(\mathrm{n+1}) = \omega w_f(\mathrm{n}) + (1-\omega) w_f(\mathrm{n\text{-}1})$, where ω is a convergence parameter, $0< \omega <0.5$, to control extreme changes of the solutions. $t_s(\mathrm{n+1})$ is also calculated based on the newly updated aperture profile using the total mass balance equation (Eqn. (6.2)). If the solution converges within a given tolerance, the iteration process is terminated and the fracture propagation and failure analysis processes, described in below, are begun to update the crack information (tip location, path).

The convergence of the iteration is determined by the average error in the fluid pressure during the iteration process (Adachi and Detournay, 2008; Adachi et al., 2007; Taleghani, 2009).

$$\varepsilon_f = \frac{\sum_{i=1}^{NE} \left| p_{f(i)}(\mathrm{n}) - p_{f(i)}(\mathrm{n-1}) \right|}{\sum_{i=1}^{NE} \left| p_{f(i)}(\mathrm{n}) \right|} \leq \text{tolerance} \tag{6.1}$$

where ε_f is an average error of fluid pressure distribution during iteration, $p_f(\mathrm{n})$ is the fluid pressure at the current iteration, and $p_f(\mathrm{n\text{-}1})$ is the fluid pressure at previous iteration.

The time step in the simulation is calculated from the total mass balance. The total injected fluid volume is a summation of the fracture volume and the fluid leakoff volume. Schematic description of the summation of the leakoff volume is described in Figure 22:

$$q_{inj} \cdot t_s = V_f + q_l \cdot t_s \tag{6.2}$$

where t_s is the time step, V_f is the fracture volume, q_{inj} is an injection rate as an input value, and q_l is calculated by summation of the leakoff volume on the fracture surface from Eqn. (5.65). The total leakoff volume is computed by a following equation:

$$\frac{1}{2} q_l = \sum_{i=1}^{nf} \left(-\frac{k_m}{\mu_f} A_f^i \left(p_m^i - p_f^i \right) \right) \tag{6.3}$$

where nf is the number of fracture elements, A_f^i is the area of fracture surface in the fracture element, p_m^i is an average of pore pressure in rock matrix, and p_f^i is an average of fluid pressures in the fracture element. So, we know the fluid injection rate, q_{inj}, the volume of the fractures, V_f, and the leakoff volume, q_l. Then, the time step, t_s, can be obtained from Eqn. (6.2).

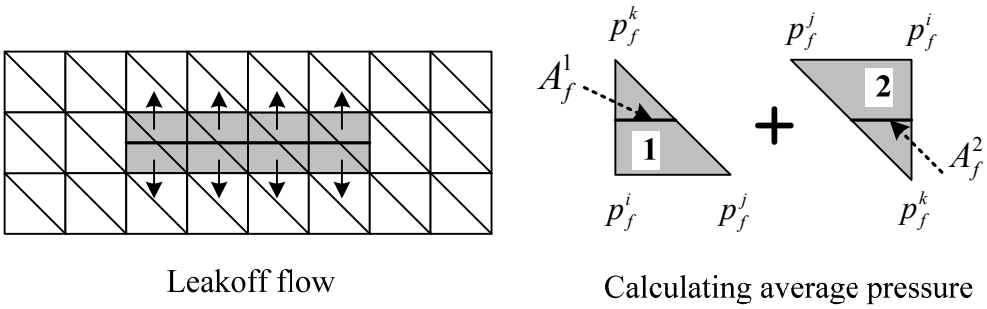

Figure 22. Schematic description of leakoff flow and summation.

Before proceeding to the fracture propagation analysis, the crack initiation criterion is examined at the crack tips. If the maximum tensile stress at the crack tip does not meet with the maximum tensile failure criterion, the hydraulic fracturing simulation is terminated and we should change input parameters such as fracturing fluid injection rate or viscosity of the fracturing fluid to increase the hydraulic fracturing. Once the crack initiation criterion is met, the hydraulic fracture will be extended based on quasi-static crack growth assumption. In the fracture propagation process, the hydraulic fracture is extended by the propagation angle and the incremental length computed from Eqn. (5.69) and (5.67). And then, fracture elements are identified by the newly extended crack path, and the cutting fracture surfaces are calculated by EPM for equivalent nodal forces of the hydraulic pressurization inside the fracture elements. In this process, the crack path is traced and stored information of the fracture elements at every time step.

One of the advantages of our model is using fixed mesh information for both solid and fluid analysis. That is, it is unnecessary to modify the size of global matrix at every time step, and this feature is beneficial for significant savings of computational cost when a large geological problem is considered. In the fluid-flow analysis, the hydraulic conductivity and pressurization are continuously updated using the crack path information. If the hydraulic fracture is extended, fracture elements are activated in the global matrix. For fluid flow modeling inside the fracture, the fractured elements are considered as fluid networks. As for applying boundary conditions on identified crack tips and injection points, the fluid flow equations are solved in this geometry.

Apart from the crack propagation model, intact elements in the rock matrix are examined by the failure criterion to identify failures. Beside with the crack propagation path, the rock is failed when the failure criterion is met. Especially in a heterogeneous reservoir, the rock failures near the primary fracturing path by the hydraulic pressurization is increasing and the failure events have critical role for the leakoff rate increase. Based on state of the effective stress at the intact element, the M-C failure criterion provides type of failure and can calculate the damage variable by a damage evolution law proposed in Chapter 3. By the calculated damage variable, the effective Young's modulus is calculated by $E' = (1-D)E$. Poroelastic parameters (β_p, γ_1, γ_2) related with bulk modulus and Biot's coefficients updated in the failed elements as described in Chapter 4.

4.1 Model Verification

The hydraulic fracture propagation is a complicated and coupled problem of fluid-solid interaction; thus, it is very difficult to find suitable analytical solutions. In the fluid-driven fracture problem, the correct

relationship between the fracture aperture and the fluid pressure is important. According to the lubrication theory, the fluid pressure distribution has cubic relationship with the fracture aperture, so that the solution from the lubrication equation is quite sensitive to the fracture aperture value. Hence, to verify the numerical model, the fracture opening and stress near the crack tip are compared with available analytical solutions using a pressurized, penny-shaped crack problem (Sneddon, 1946).

4.1.1 A pressurized crack

When the infinitely thin crack is subjected to uniform pressure Δp at the crack surface described in Figure 23, the stress and displacement fields are given by the solution with Possion's ratio v and shear modulus G along the x-direction (Sneddon, 1946).

$$D_y(x,0^+) = \frac{2\Delta p a(1-\nu)}{G}\sqrt{1-\frac{x^2}{a^2}}, 0 < x < a \tag{6.4}$$

where D_y is a displacement in y-direction, a the half-length of the fracture, and x the computational point within the half length of the fracture. The normal stresses σ_{yy} along the uncracked part of the crack plane are expressed as:

$$\sigma_{yy} = -\frac{\Delta p}{\sqrt{1-\frac{x^2}{a^2}}} - \Delta p, x > a \tag{6.5}$$

The rock material is assumed as a linear elastic material and fracture length is 2 m within a 10-m×10-m rectangular model. The material parameters are set as described in Table 1 and uniform pressure, Δp=5 MPa, is applied at the fracture surface as a boundary condition. The uniform triangular mesh is used for the numerical solution, and element size is 0.1-m ×0.1-m each. Figure 24 compares the numerical and analytical solutions about the fracture opening and normal stresses near the crack tip under uniform pressurization on the line crack. Therefore, the fracture permeability estimated by the lubrication equation is validated, since the simulated fracture opening has good agreement with the analytical result in Figure 23. However, error increased for the numerical results near the crack tip is, because a uniform mesh was used instead of a fine mesh near the crack tip (Figure 23).

Table 1. Material parameters for the verification problem

Inputs	Values
Young's Modulus, E (GPa)	37.5
Poisson ratio, υ	0.25
Shear Modulus, G (GPa)	15
Number of Elements	20,000

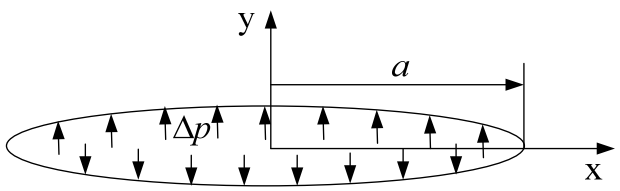

Figure 23. Uniformly pressurized crack problem

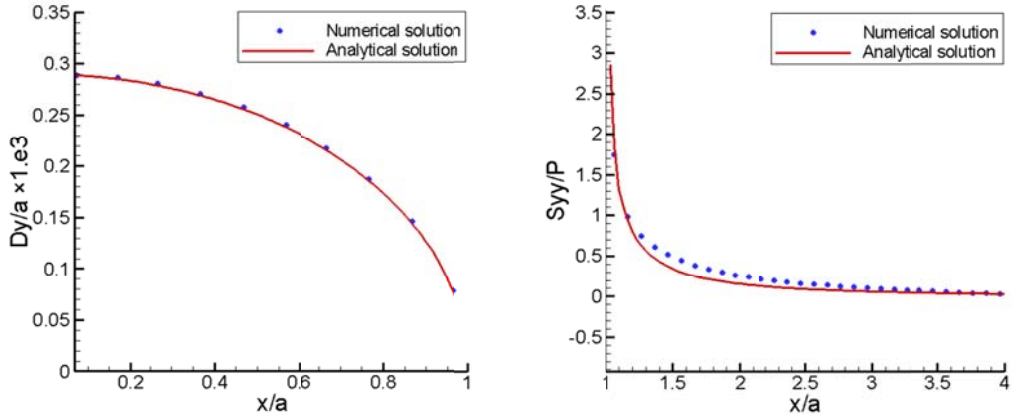

Figure 24. Comparison between numerical and analytical solutions for normalized fracture opening and normal stresses distribution.

4.1.2 2D biaxial tension

The center-cracked plane problem under uniform biaxial tension (uniform pressure, Δp=5 MPa) is shown in Figure 25. Analytical solutions of the fracture opening and the normal stresses σ_{yy} under biaxial tension are same in described in Eqn. (6.4) and (6.5) (Sneddon and Elliott, 1946). In Figure 26, it is observed that the numerical results have good agreement with the analytical solutions.

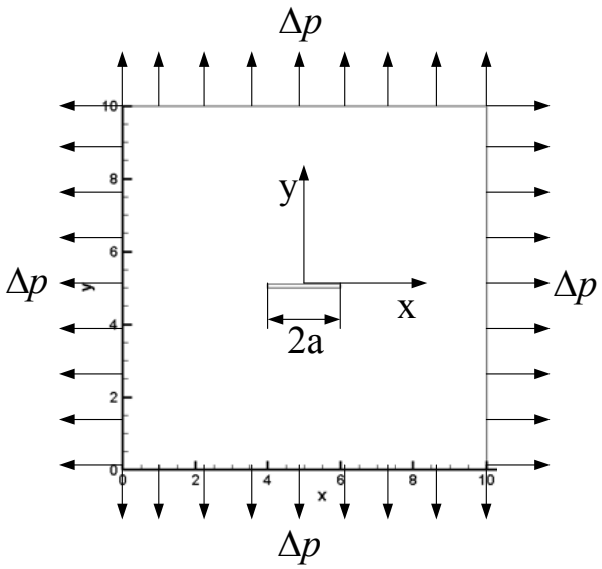

Figure 25. Center-cracked plane subjected to equally distributed biaxial tension.

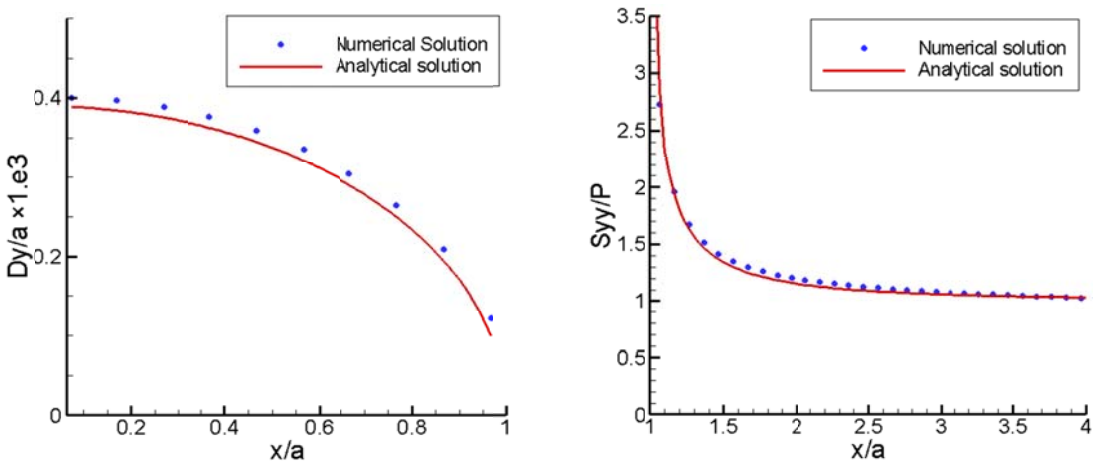

(a) (b)

Figure 26. Comparison between numerical and analytical solutions for (a) normalized fracture opening and (a) normal stresses distribution.

4.1.3 3D pressurized elliptical crack

For the model verification of the 3D model, the same material properties in Table 1 were used, but a circular crack, r=0.4 m, was placed in the center of the 2-m×2-m×2-m cubic model. Uniform pressure Δp=10 MPa was applied on the elliptical crack surface. The model included 16,000 (20×20×40) structurally meshed tetrahedron elements. Same as previous 2D examples, the numerical results of the 3D model are consistent with the analytical solutions in Figure 27.

.

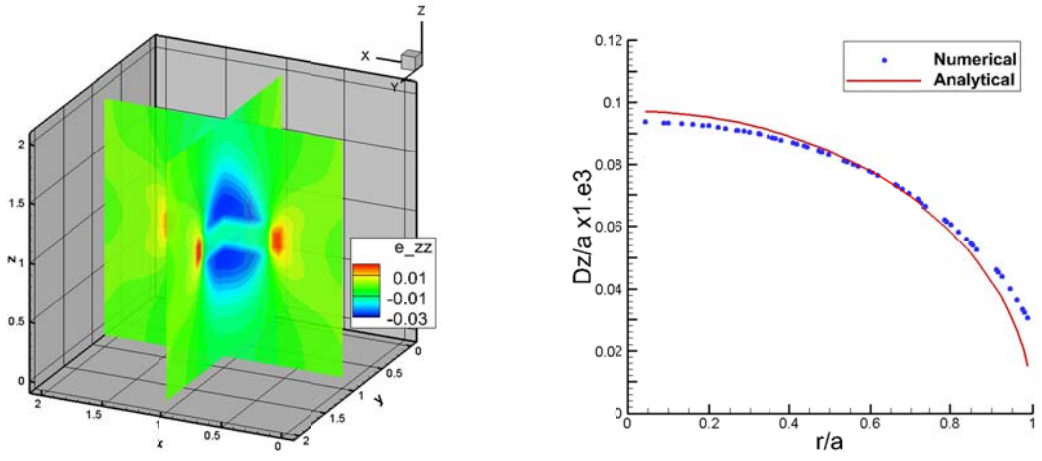

Figure 2. Comparison between numerical and analytical solutions for normalized fracture opening of the uniformly pressurized elliptical crack.

5. Numerical simulation of Compression Tests

Generally, stresses applied to brittle rock by various loading mechanisms cause crack nucleation, propagation, interaction, and coalescence in different ways. Especially, when the applied forces are compressive, the rupture paths are governed by shale-localized failures. These rupture paths are also variable and depend on material deformation properties and strength and heterogeneity (Hoek and Brown, 1990; Jaeger et al., 2007). Characterization of the fracture growth pattern in a brittle and heterogeneous reservoir is a difficult and challenging issue because of the complexity of rock properties and physical aspects of rock failure and fracture. Frequently arbitrary and randomly grown fractures are observed in well stimulation of petroleum and geothermal reservoirs. So numerical modeling of core-sample experiments is useful to investigate the suitability of the damage model of heterogeneous rocks and the numerical core analysis is applicable to use in a larger geological problem.

The elastic/brittle constitutive model of brittle rock, described in Chapter 3, is used to express the confining-dependent stress/strain relation of core samples. The multistage triaxial tests of Newberry Tuff and AltaRock Granite core samples performed by (Wang et al., 2012a). The multistage triaxial tests were performed at five different stages of confining pressure to determine the rock properties. In each stage except the last stage, the sample was unloaded when the maximum value of volumetric strain was observed on the stress-volumetric strain curve. During the last stage, the rock was loaded until complete failure to measure the compressive strength of the rock at the prescribed confining pressure. The confining-dependent stress/strain curves of the Tuff and Granite samples are listed in Figure 28-29. Tuff sample appears to be hard, inelastic and brittle, while Granite sample shows hard, elastic and brittle. Rock mechanical properties and Mohr-Coulomb parameters (friction angle, cohesion) obtained from the multistage triaxial tests (Tables 2 and 3) are used as input parameters for the numerical modeling of the triaxial compression tests. The heterogeneity of the rock was characterized using the Weibull distribution function.

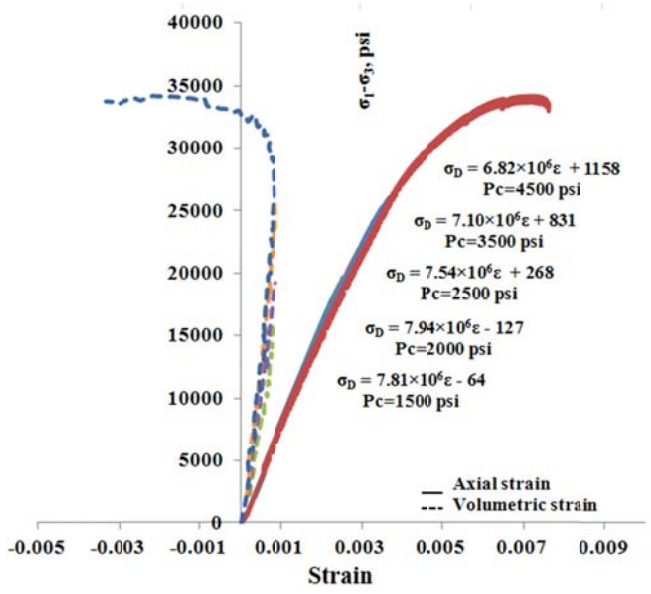

Figure 28. Stress-strain relations of Tuff after Multi-stage triaxial test (Wang et al., 2012a).

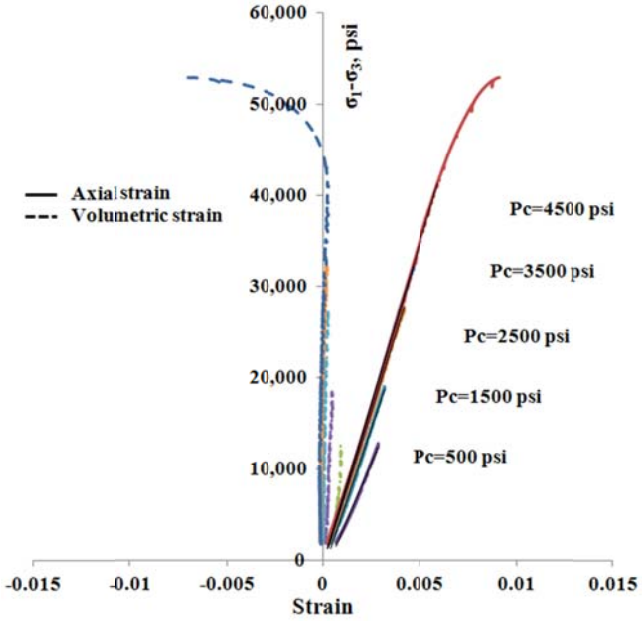

Figure 29. Stress-strain relations of Granite after Multi-stage triaxial test (Wang et al., 2012a).

5.1 Laboratory Multistage Triaxial Test of Tuff and Granite

Laboratory experiments on rock specimens give general stress/strain curves under different confining pressures Figure 28 and 29. The data used in this work came from triaxial laboratory experiments that provided input data of Young's modulus, Poisson's ratio, estimated compressive strength, uniaxial compressive strength, friction angle, and cohesion, all of which were incorporated into our numerical model. Relationships between petrophysical, mechanical and failure properties are important in reservoir development problems including wellbore stability and hydraulic fracturing.

Table 2. Multistage triaxial test data of Tuff (Wang et al., 2012a).

Pc, psi	1500 (10.34 MPa)	2000 (13.79 MPa)	2500 (17.24 MPa)	3500 (24.14 MPa)	4500 (31.03 MPa)
Compressive strength, psi	24,380 (168.14 MPa)	26,758 (184.53 MPa)	29,135 (200.93 MPa)	33,890 (233.72 MPa)	38,645 (266.52 MPa)
E, psi	7,807,493 (53.84 GPa)	7,940,565 (54.76 GPa)	7,544,256 (52.03 GPa)	7,099,090 (48.96 GPa)	6,822,836 (47.04 GPa)
Possion's ratio, υ	0.32	0.34	0.37	0.39	0.41
UCS, psi	12,818 (88.38 MPa)				
Friction angle	40.7				
Cohesion, c_F (psi)	3,955 (27.27 MPa)				
Inclination angle of failure plane, β	65.4°				

Table 3. Multistage triaxial test data of Granite (Wang et al., 2012a).

Pc, psi	500 (3.45 MPa)	1500 (10.34 MPa)	2500 (17.24 MPa)	3500 (24.14 MPa)	4500 (31.03 MPa)
Compressive strength, psi	15873 (109.47 MPa)	24,080 (166.07 MPa)	35,024 (241.54 MPa)	40,827 (281.56 MPa)	52,875 (364.65 MPa)
E, psi	4,996,970 (34.46 GPa)	6,165,314 (42.52 GPa)	6,741,385 (46.49 GPa)	6,918,957 (47.72 GPa)	6,998,963 (48.27 GPa)
Possion's ratio, υ	0.37	0.43	0.47	0.47	0.46
UCS, psi	11,246.59 (77.56 MPa)				
Friction angle	55.3				
Cohesion, c_F (psi)	1,756.36 (12.11 MPa)				
Inclination angle of failure plane, β	72.7°				

5.1.1 Heterogeneity of Tuff and Granite samples

Petrographic analyses are conducted to describe rock textures, classify and determine the relative amounts of mineral constituents, to identify minerals, and to detect evidence of mineral alteration (Wang et al., 2012a). The identification of mineral constituents and determination of texture and micro-structural features allows the recognition of rock properties that may influence the mechanical properties of the rock.

According to the petrographic analysis, the tested Tuff specimen has an aphanitic fine-grained texture (Wang et al., 2012a). In Figure 30, the images of Tuff show a heterogeneous rock containing different types of grains and various minerals. The Tuff mainly consists of two types of minerals and may have rock properties in brittle with fine-grained crystals. In addition, grain size, grain shape, texture and structure were randomly distributed. All these heterogeneity factors could affect fracture pattern creation. Effective rock properties are a function of rock composition and properties of the components. The description of petrographic images in Figure 31 is about the Granite sample and thin section of the Granite is composed of course-grained quartz, hornblende, plagioclase, biotite, and muscovite minerals with grain sizes ranging from 0.1 to 0.35 μm. The quartz, feldspar, and biotite are dispersed with various sizes. As explained previously, in order to represent the rock heterogeneity into a numerical domain. Random variables generated by Weibull distribution function are distributed to material strength and Young's modulus as multiplying the random variables at Gaussian point in an element. So, in the finite-element (FEM) formulation, the microscopic heterogeneity can be described only at the elemental scale. Therefore, further improvement, would require the correlation of Weibull parameters with rock composition from mineralogical and textural characterization. This is an important issue for the practical modeling of rock samples; however, the issue would require extensive rock mechanical and petrological analysis and is beyond the scope of this thesis.

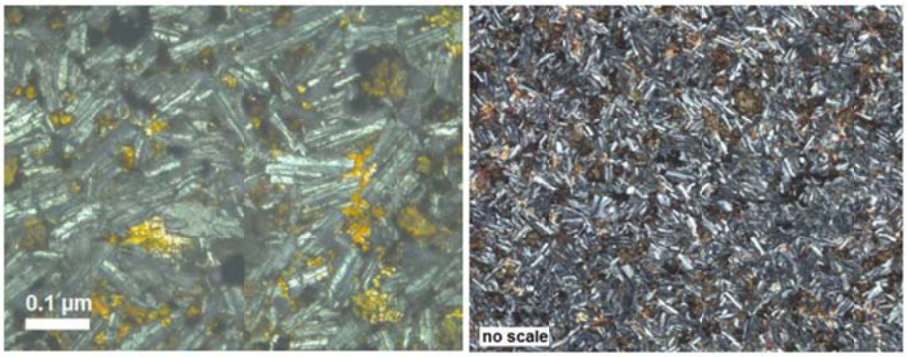

Figure 30. Petrographic images of Tuff rock from Newberry (Wang et al., 2012a).

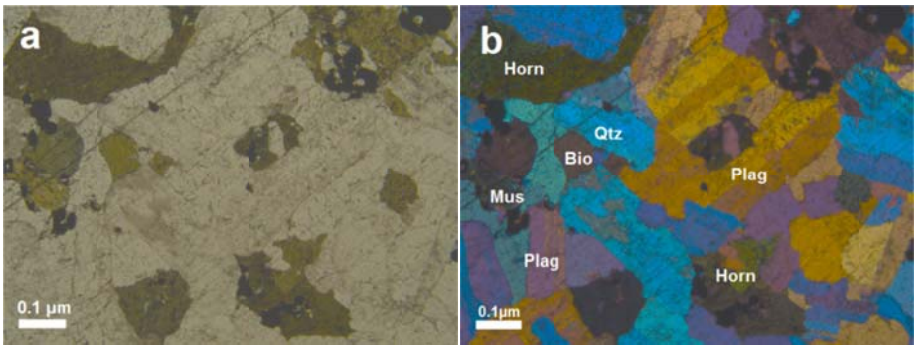

Figure 31. Petrographic images of AltaRock Granite by (Wang et al., 2012a).

5.1.2 2D numerical modeling for triaxial tests

Two-dimensional numerical domain and 10,000 uniformly meshed triangular elements were used for triaxial compression Figure 32. 2D plane strain is used to approximate an axial section through an axisymmetric triaxial test specimen. This plane strain approximation is commonly taken by other researchers (Fang and Harrison, 2002a; Tang et al., 2000; Wang et al., 2000; Yuan and Harrison, 2005). In order to express the fracture pattern of the rock specimen, the 2D plane strain approximation is suitable since 2D axi-symmetry model cannot represent a fracture pattern throughout the specimen. Ultimately 3D numerical model might be the best for the triaxial compression tests, however the 3D simulation still requires huge computational costs despite of recent development of computational capacity and lots of mathematical and numerical difficulties such as uncertainty of heterogeneity effect by three-dimensional micromechanical grains, and highly non-linear and anisotropic mathematical formation are remaining to develop 3D model. Therefore, numerically efficient 2D plane strain model is preferred to use in this research and development of suitable 3D numerical model remains for future improvement.

Boundary conditions of the compression test were that the bottom surface of the specimen was restricted in the y-direction, and force was applied on the top surface of the specimen using the same displacement increment as in an experimental test, and confining pressure was applied to both sides Figure 32(a). For heterogeneity characterization, we used random variables generated by Weibull distribution function, since it gives wide possibilities. In order to obtain approximate values of Weibull parameters, few pre-tests are performed. For example, if three cases of m_1=0.5, 1.0, 3.0 were simulated, we can estimate appropriate values of Weibull parameters. For Tuff sample, we obtained m_1=0.9, a_1=10 for stiffness distribution, and m_2=0.9, a_2=15 for strength distribution. For Granite sample, m_1=0.8, a_1=10 for stiffness

distribution, and m_2=0.9, a_2=10 for strength distribution were estimated. In Figure 32 (c), average value of stiffness is about 51 GPa, which shows that stiffness was distributed to each element by random variables. Darker colored elements represent higher stiffness, while lighter colored elements represent lower stiffness.

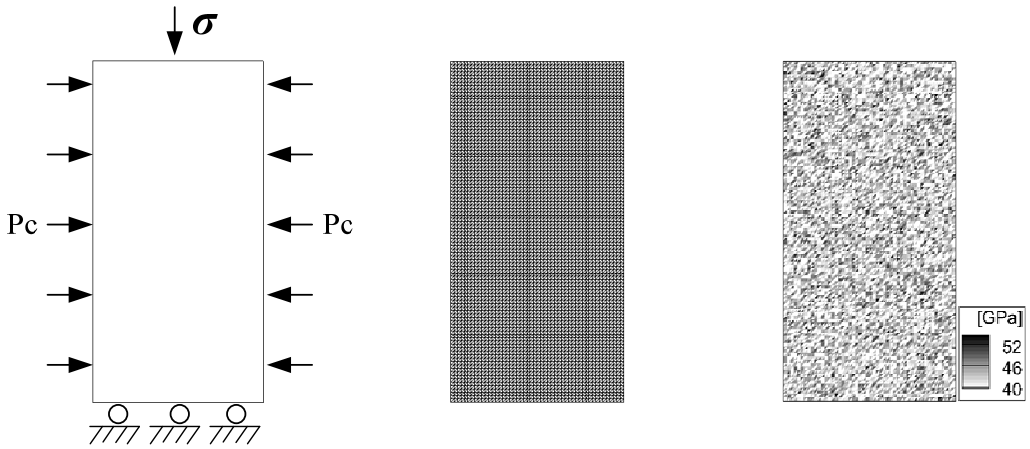

(a) (b) (c)

Figure 32. Numerical simulation model for triaxial compression tests (a) Boundary conditions, (b) Mesh (NE=10,000), (c) Heterogeneity index.

Table 4. Material parameters and input parameters for 2D triaxial.

Inputs	Values
Element type	Triangular
Young's Modulus, GPa	53.84 (Initial)
Poisson ratio	0.32 (Initial)
Num. of elements	10,000
Size of element	0.02
Aspect ratio (D:H)	1:2
Cut-off strength, MPa	15
Incremental displacement	0.1e-3
Weibull parameters	m_1=0.9, a_1=10 for stiffness(Tuff) m_2=0.9, a_2=15 for strength(Tuff) m_1=0.8, a_1=10 for stiffness(Granite) m_2=0.9, a_2=10 for strength (Granite)

Numerical simulation for Tuff at Pc=15 MPa:

The simulation result of Tuff sample about the fracture process at 15 MPa confining pressure is shown in Figure 34. The results show that local failure events initiate at random locations and gradually propagate, and then the localized failure tends to concentrate on the weaker elements of the rock specimen. The

strain localization leads to shear plane development by irreversible friction. After the shear plane takes place, the fracture surface slips and more failure is concentrated on the fracture plane.

In Figure 34, Region I is a reversible elastic zone behaving elastically; that is, the deformation is instantaneously reversed to its initial point when the forces are removed. Region II is an irreversible inelastic zone, which means the deformation could not reverse to its initial point when the forces were removed. In Region II, the rock was dilated by heterogeneous microcrack growth. Region III is a brittle fracture zone, which means sudden loss of strength happened across the fracture plane. In Region III, the deformation becomes totally irrecoverable. The fracture plane is formed when shear, compression, and tension forces break molecular bonds. As a result, the compressive forces lead to lots of microcrack growth in Region II, and then combined compressive/tensile macroscopic failures are observed in Region III (Jaeger et al., 2007). In Figure 33(a), initiation of microcracks was detected at an early stage and dilation occurred simultaneously with the microcrack growth. Then the accumulation of microcrack events hikes before reaching its peak stress. When the fracture plane was formed, both tensile and shear damages were found near the fracture plane. This is because slippage related to the shearing behavior caused tensile failures near the localized shear-fracture plane. Therefore, both tensile and shear failures occurred during the triaxial compression test, and the combined failures triggered the fracture initiation and propagation.

In Figure 33(b), the numerical result was compared with the experimental multistage triaxial result, tested at Pc=17.24 MPa. It shows general agreement between two results. Specifically, at the early stage, the strain curve has good agreement with the experiment, while at later stages the experiment's results have more inelastic behavior than the numerical result. The numerical result has less inelastic behavior than the experiment's because the volcanic Tuff sample shows hardening behavior and our constitutive model was developed based on the elastic/brittle assumption. However, the volumetric strain curve has somewhat similar behavior in both the simulation and the experiment even though the discrepancy of axial strain curves.

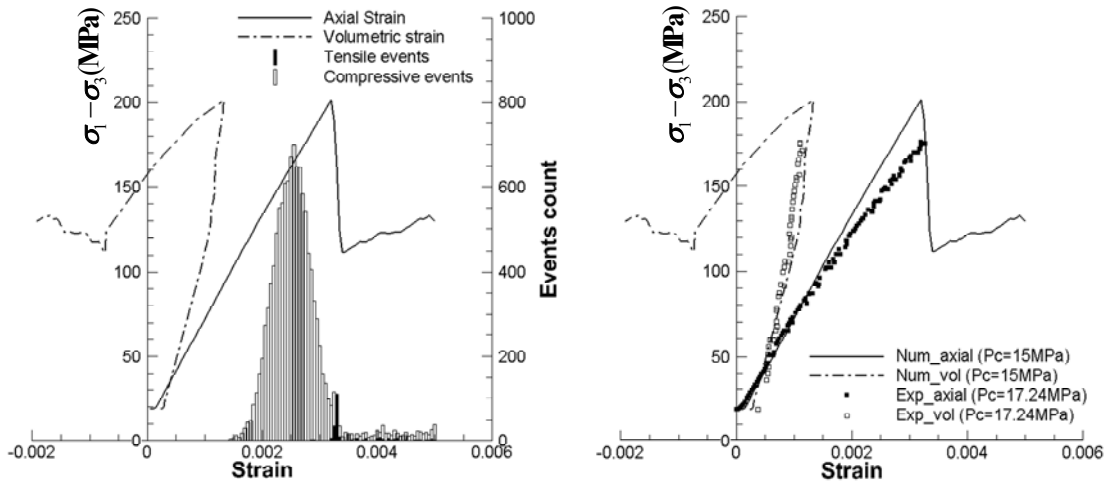

Figure 33(a) Failure events detection during fracture process at Pc=15 MPa; (b) Comparison of numerical with experimental result.

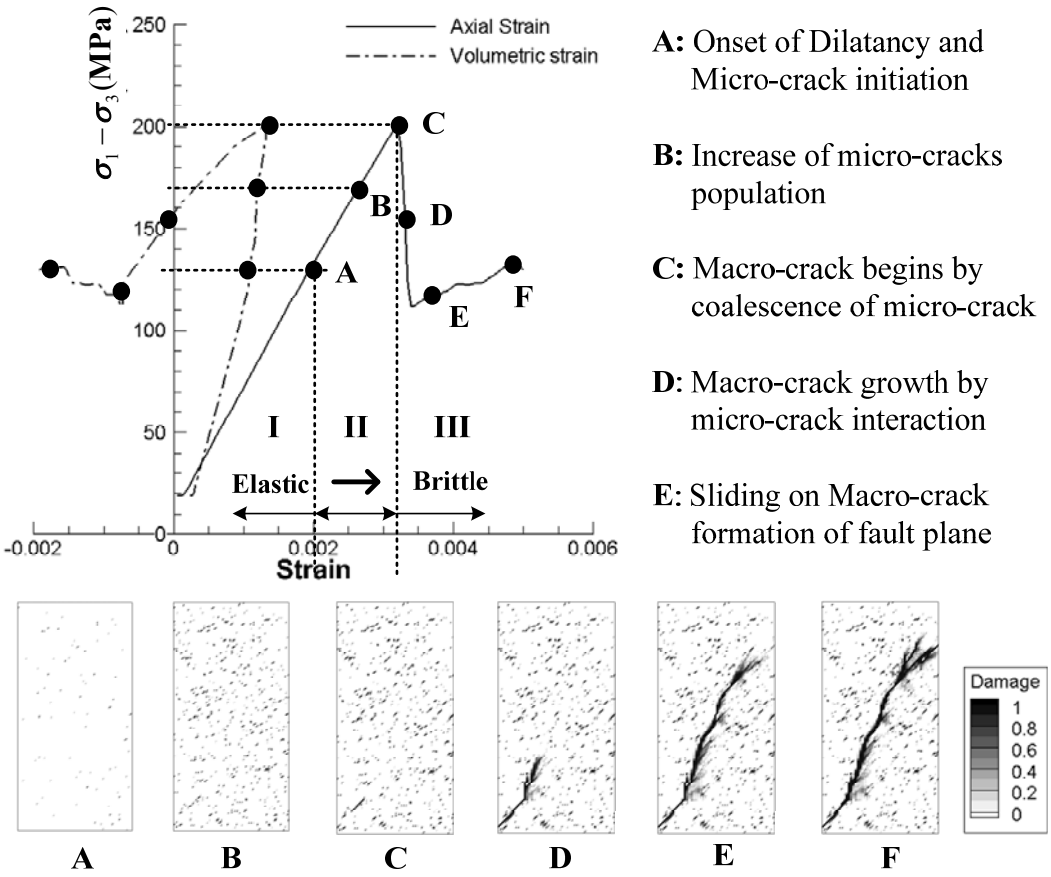

Figure 34. Axial and volumetric strain curve at Pc=15 MPa and micro/macro crack growth of brittle fractures in heterogeneous rock.

Stress-strain relations of Tuff by confining pressure:

In this section, the influence of confining pressure was studied. As discussed in Chapter 2, the stress-strain relations of a rock were highly affected by the confining pressure. Similarly, fracture patterns are also influenced by the confining pressure variation. Under uniaxial compression (i.e. no confinement), a rock tends to by failed by somewhat irregular longitudinal splitting, while with a moderate amount of confining pressure, the longitudinal fracturing is suppressed and clearly defined plane of fracture is formed through the rock specimen (Jaeger et al., 2007). The fracture plane is characterized by shearing displacement (i.e. shear fracture) and typically inclined at an angle less than 45° from the axial direction. If the confining pressure is increased highly and the rock becomes fully ductile, small shear fractures, accompanied by plastic deformation of the individual rock grains, are observed (Jaeger et al., 2007).

Numerical results show that both the stress-strain relations and the fracture pattern were affected by the confining pressure variation in Figure 35 and 36. As peak strength increases, absorbed fracture energy increases during the fracturing process. Inclination angles of the fracture plane were varied by the confining pressure. As increasing confinement, the inclination angle of the fracture plane is about 45°. Furthermore, the angle of dilation depends on the confining pressure and the angle of dilation of the higher confinement case has a larger angle than other cases.

In cases of higher confinement, more damaged events were detected and the damaged events could lead to more dilation during the failure process. This is because the angle of dilation is controlled by an amount of plastic volumetric strain developed during fracture shearing. In Figure 36, we observed that the fracture pattern after the multistage triaxial simulation has brittle fracturing patterns. Based on the study of confining pressure, the peak strength of the brittle rock undergoing deviatoric loading is highly affected by the confining pressure. The peak strength and shear dilation have strong effects on the fracture pattern.

In Figure 46, a fracture pattern of Tuff sample was observed at an angle of 62° after the multistage triaxial compression test at Pc=4500psi (≈31MPa). From the front and side view (Figure 46(b), small fractures are observed along the rock sample. However, a fracture pattern from the numerical simulation at Pc=30MPa (Figure 36) shows clearly formed fracture plane at an angle of 45°. This is because the stress-strain relation of numerical simulations at Pc=30MPa (Figure 35) has elastic-brittle behavior; on the other hand the stress-strain relation of experimental results has ductile behavior. Hence, the fracture patterns from numerical results are somewhat disagreement with the experimental results when high confining pressure is applied. However, the multi-stage triaxial test is not a good experiment to characterize the fracture pattern variation by the confining pressure, since micro-fractures could be formed due to multi-loading/unloading during the multi-stage test.

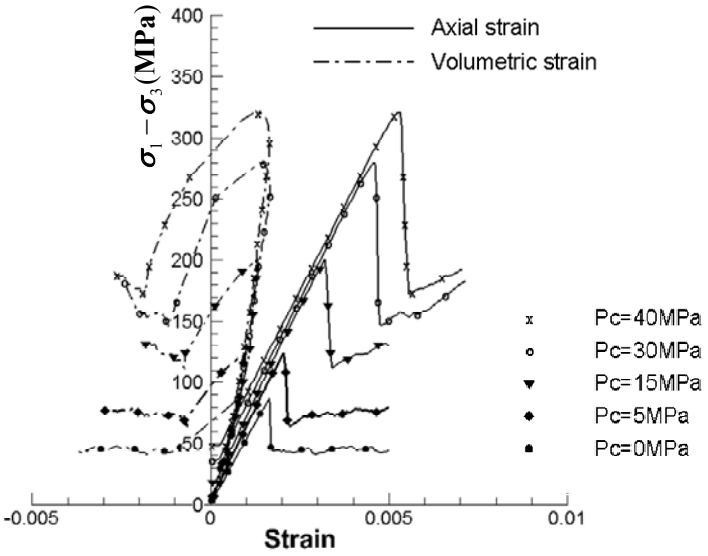

Figure 35. Stress/strain relations of Tuff by various confining pressure

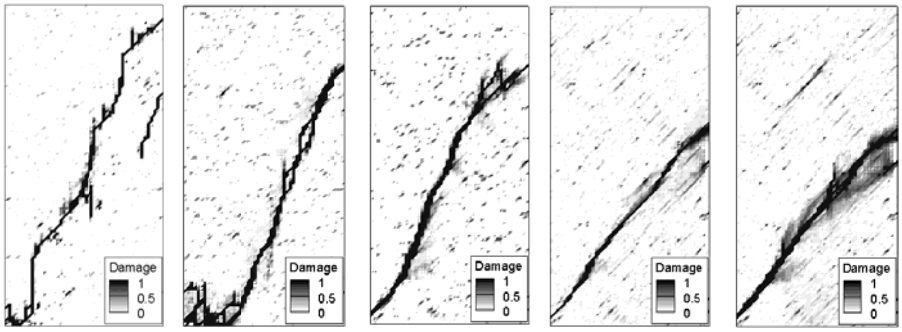

Pc= 0MPa Pc= 5MPa Pc= 15MPa Pc= 30MPa Pc= 40MPa

Figure 36. Fracture patterns of Tuff by various confining pressure at NE=10,000

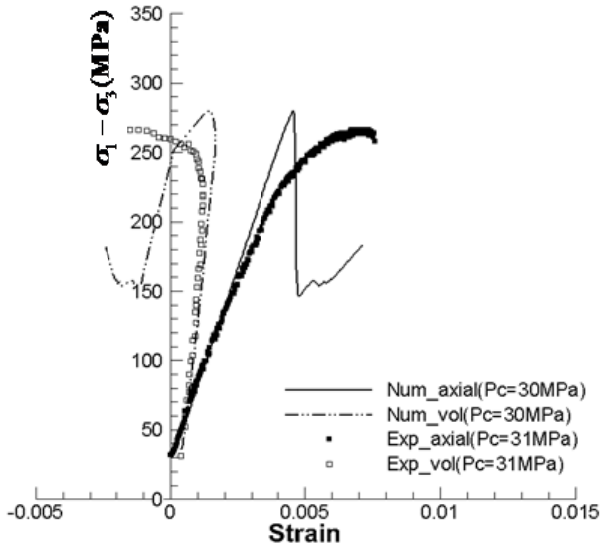

Figure 37. Stress-strain relation of Tuff at Pc=30 MPa compared with experimental result (Pc=31MPa)

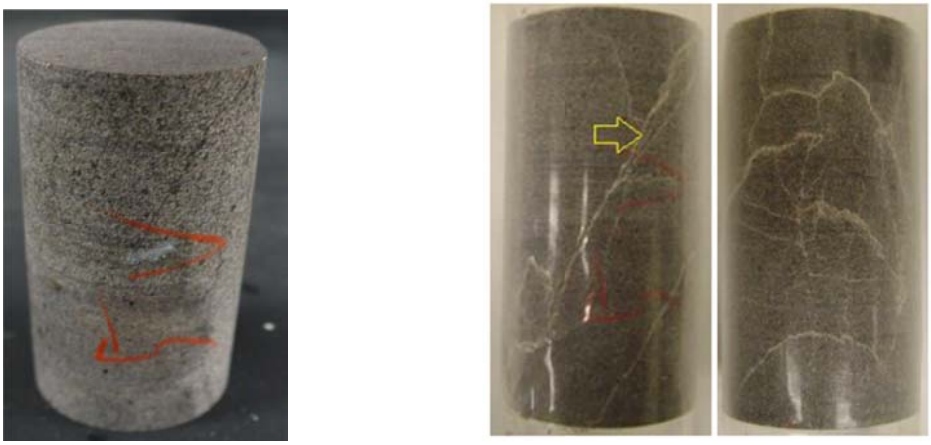

(a) Before multistage tests (b) After multistage test from side and front

Figure 38. Fracture pattern of Tuff rock before and after multistage triaxial test (Wang et al., 2012b).

Numerical simulations for Granite at Pc=25 MPa:

The simulation result of Granite sample about the fracture process at 25 MPa confining pressure is shown in Figure 39. Similar with previous Tuff example, compressive failures were mostly observed and accumulated at random locations. While the fracture plane was formed, small amount of tensile failures are observed during the shear fracturing process (Figure 39(a)). The stress-strain relation of the Granite sample shows less inelastic behavior before complete failure and brittle behavior when the rock is completely failed. These small inelastic and brittle behaviors are good agreement with the experimental results (Figure 39(b)). The Granite sample shows less ductile behavior than the Tuff sample (Figure 33(b)). So, it is found that the elastic-brittle constitutive assumption is suitable for the Granite rock sample than the Tuff sample.

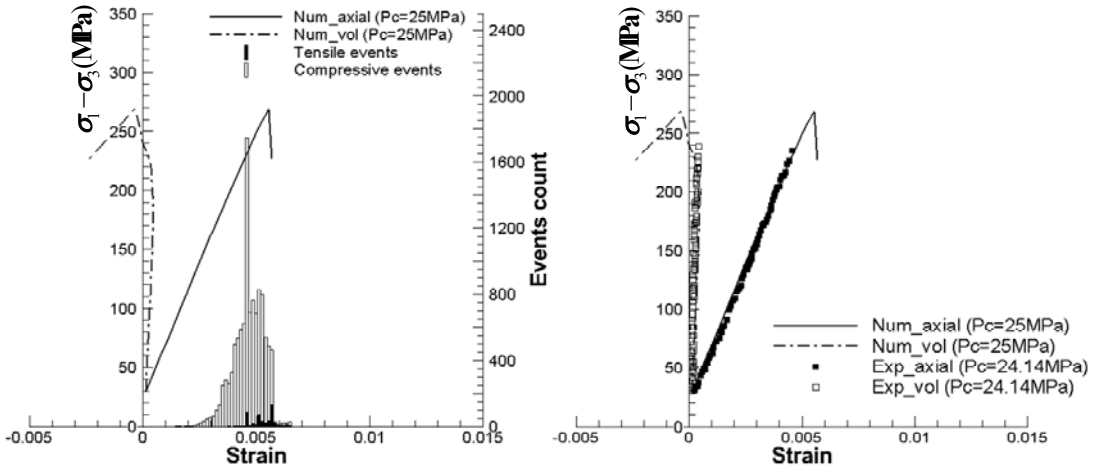

Figure 39. (a) Failure events detection during fracture process at Pc=25 MPa; (b) Comparison of numerical with experimental result.

Stress-strain relations of Granite by confining pressure:

As discussed earlier, the confining pressure is critically influencing the stress-strain relations and fracture patterns of a rock. Numerical results show that the stress-strain relations and the fracture pattern were affected by the confining pressure variation in Figure 40 and 41. The fracture patterns of the Granite sample show irrelevant results than the Tuff cases. Under uniaxial compression, somewhat longitudinal splitting fractures were found and clearly formed fracture planes were observed under various confinements. In Figure 43, a fracture pattern of Granite sample was observed at an angle of 72° after the multistage triaxial compression test at Pc=4500psi (≈31MPa). However, observed fracture pattern from the numerical simulation at Pc=32MPa was inclined at an angle of 50°. This is because a formation of rock heterogeneity is also a critical factor for the fracture plane forming. As mentioned above, the characterization of the rock heterogeneity is an important issue for the practical modeling of rock samples, but this issue is beyond the scope of this thesis, because it requires extensive research about micro-mechanical structures of the rock.

In Figure 42, the stress-strain relation of the numerical result (Pc=32MPa) and the experiments result (Pc=31.03MPa), which is the last stage of the multi-stage triaxial test was compared until complete failure. General behavior of axial and volumetric strains is almost similar in both numerical and experimental results. The experimental results show high volumetric changes when the complete failure occurred.

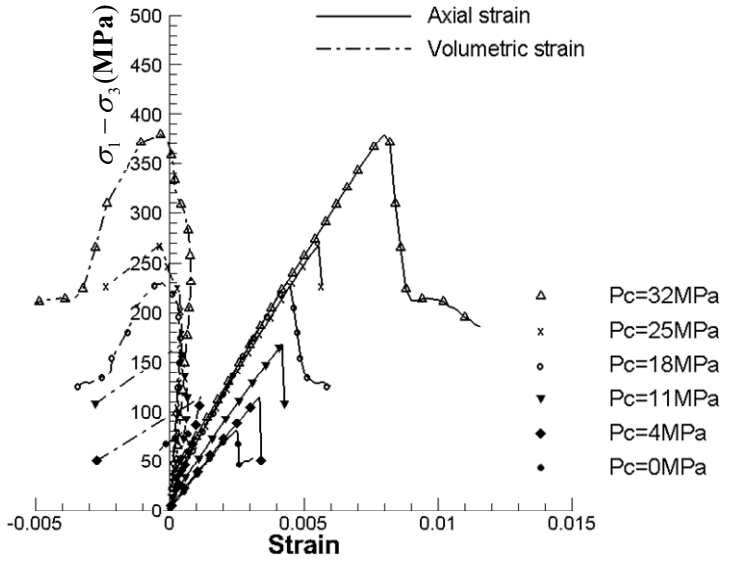

Figure 40. Stress/strain relations of Granite by various confining pressures.

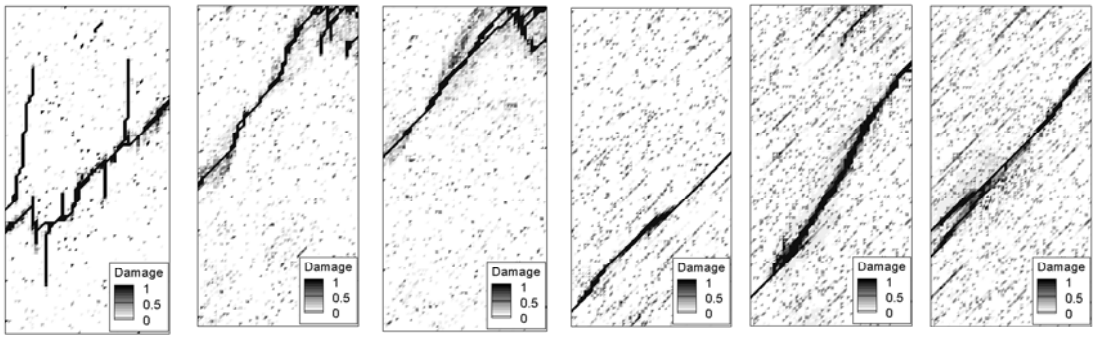

(a) Pc=0MPa (b) Pc=4MPa (c) Pc=11MPa (d) Pc=18MPa (e) Pc=25MPa (f) Pc=32MPa

Figure 41. Fracture patterns of Granite by various confining pressures.

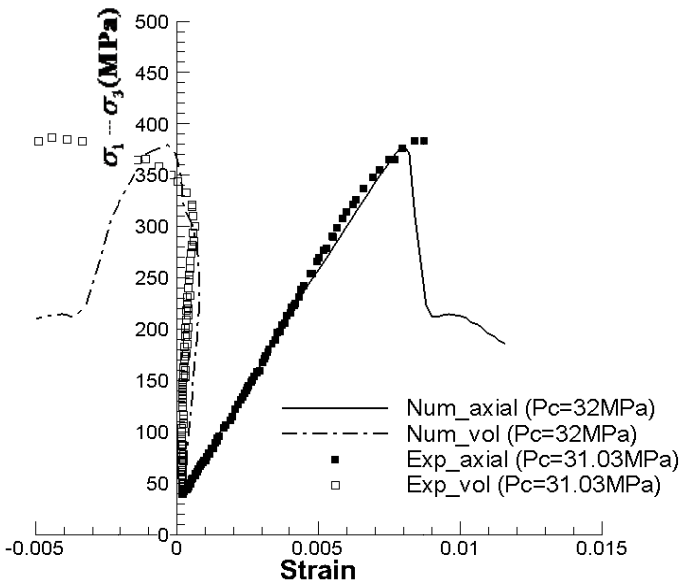

Figure 42. Stress-strain relation of Granite at Pc=32 MPa compared with experimental result (Pc=31MPa).

(a) Before multistage tests (b) After multistage test from side

Figure 43. Fracture pattern of Granite before and after multistage triaxial test (Wang et al., 2012b).

5.1.3 Numerical study of the influence of heterogeneity parameter

Because most rocks are brittle and heterogeneous, heterogeneity commonly causes multiple and randomly distributed crack propagation. The brittle rock is composed of different sizes of micrograins and different distributions of microdefects, so that correct representation of rock heterogeneity is a key factor of the numerical core analysis. However, a large part of the material properties of rock is uncertain, and it is very difficult to characterize the mechanical behavior of the heterogeneous rock in both microscopic and macroscopic views.

In this study, the Weibull distribution function was used to characterize the rock heterogeneity. The Weibull function is commonly used in rock engineering (Fang and Harrison, 2002b; Tang and Hudson, 2011), although the approach cannot be a perfectly suitable method to characterize the rock heterogeneity because its randomly generated variables cannot exactly represent texture, orientation, and shape of micrograins. However, the Weilbull distribution function may be the easiest method for generating heterogeneous properties of rock, and it is also easy to implement in an FEM formulation (Fang and Harrison, 2002a; Tang and Hudson, 2011; Tang et al., 2002; Wong et al., 2006; Yuan and Harrison, 2005). So far, no numerical method can express the complicated mineralogy and microstructures of the brittle rock perfectly, so the heterogeneity study in this section could give valuable interpretation of rock heterogeneity effects on the fracture pattern. This section discusses the simulated influence of the Weibull shape parameters on stiffness and strength distributions using numerical simulations of Tuff samples.

Stiffness mean value parameter:

Figure 45 shows different fracture patterns by controlling of Weibull parameter for average value of stiffness distribution curve. In this simulation, lower value of m_1 means the mean value of Young's modulus of rock becomes smaller, but strength of rock specimen was not changed, because it was determined by confining pressure from experimental data in our numerical model. In this section, influence of different mean values on stiffness distribution was tested without strength variation, because we generally assumed that stiffness variation does not mean corresponding change of material strength. Figure 44 shows that case of m_1=1.5 has higher compressive strength than other cases. In addition, as we discussed, fracture patterns are depend on distribution curve of random variable which means we cannot control the specific location of weaker or stronger elements. In case of m_1=0.5, fracture plane was mostly observed at upper of the specimen, while other cases have clearly inclined fracture plane. In addition, we applied same loading condition of Δd=0.1e-3, so that upper of the rock sample could be failed earlier when a rock is weaker (m_1=0.5). This is because relatively large loading condition was applied on the weaker rock sample and the high stress concentration near loading points, where a top surface of the rock sample, lead shear failures near the top surface. From observation of, both dilation angle and peak strength were influenced by the value of Weibull parameter change.

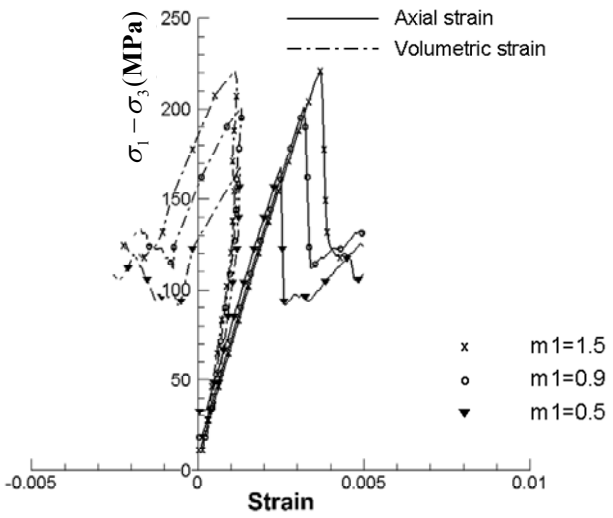

Figure 43. Stress/strain curve by stiffness mean value parameter change.

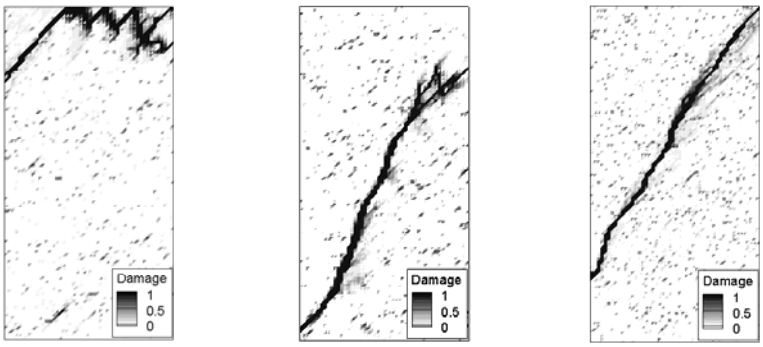

m1= 0.5 m1= 0.9 m1= 1.5

Figure 45. Fracture patterns by changing the stiffness mean value (left to right: softer rock to stiffer rock).

Stiffness shape parameter:

In this section, a shape parameter effect of the stiffness distribution was simulated with values of a_1=5, 10, 20, 100. In Figure 11, a larger value of a_1 means more homogeneity and narrow distribution, while a lower value of a_1 means more heterogeneity and wider distribution. Figure 46 and 47 show effects of the shape variation of the stiffness distribution on the fracture patterns. According to the simulation results, the influence of the stiffness shape parameter wasn't significant because two sets of Weibull parameters were used to represent the rock heterogeneity in our model. One was used for the grain-size distribution, while the other was used for the microdefects distribution. As explained earlier, we assumed that the stiffness variation did not correspond with any change of the material strength, so that the combination of the two sets has strong randomicity on the fracture patterns. That is, the distribution of the microdefects more significantly influenced the material heterogeneity. However, the stiffness shape parameter could influence crack initiation and its patterns. In Figure 47, as the shape parameter increases, the fracture plane becomes more clearly formed, since larger shape parameter represents more homogeneous

distribution. On the other hand, more randomly distributed crack growth was found when the stiffness shape parameter was small (a_1=5), which means the matrix was more heterogeneous.

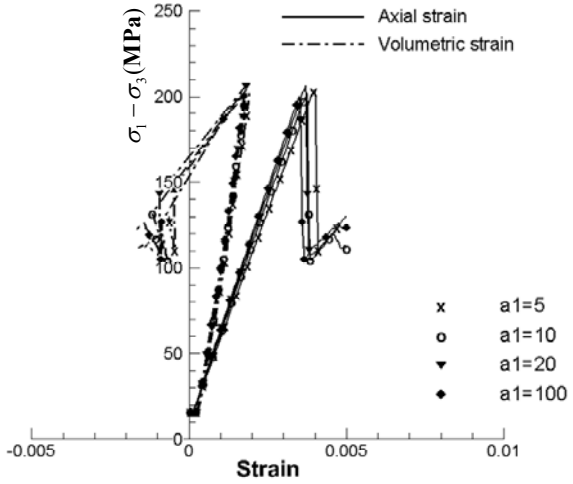

Figure 46. Stress/strain curve by stiffness shape parameter change.

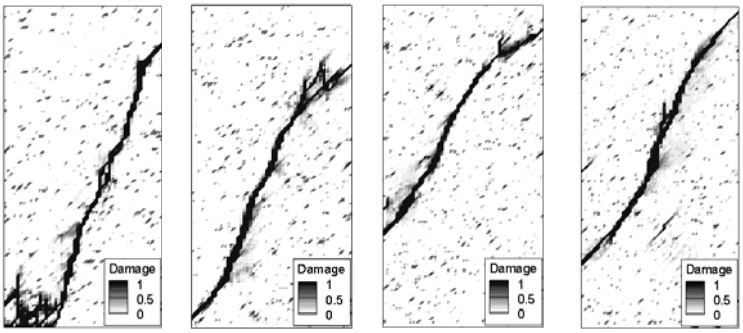

Figure 47. Fracture patterns by stiffness shape parameter change.

Strength mean value parameter:

Similar with previous section, mean values of strength distribution were changed accordingly and simulated in Figure 48. Based on material strength estimation from numerical results, Weibull parameter change on mean value of strength distribution has strong influence the material strength. It is better to compare the numerical estimation with experimental results, but it is very difficult to use same heterogeneity conditions in experimental test. In every case, fracture plane was fully ruptured through the specimen. Although dip angle and fracture pattern is different, this difference is not critical issue here because rock property has a lot of uncertainty and complexity. Due to these uncertainty and complexity of rock mechanics, it is hard to estimate fracturing phenomena of brittle heterogeneous rock.

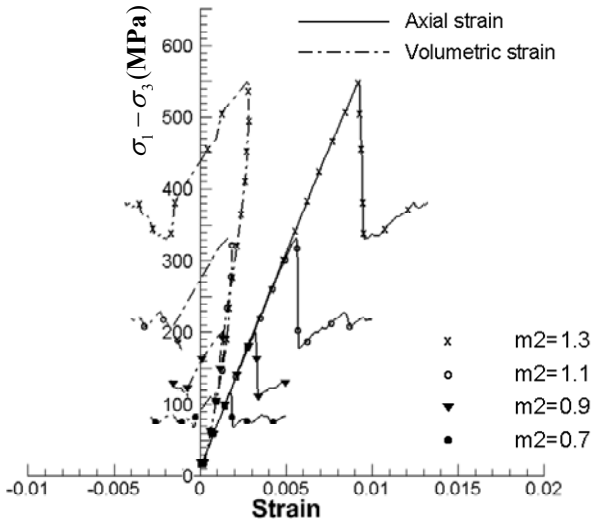

Figure 48. Stress/strain curve by strength mean value parameter change.

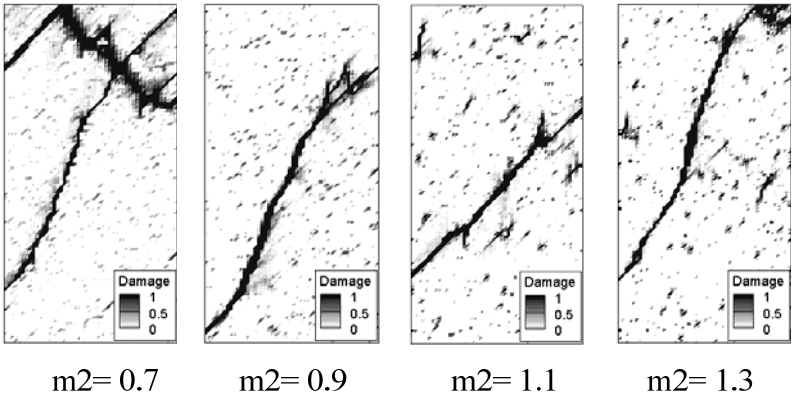

Figure 49. Fracture patterns by strength mean value parameter change.

Strength shape parameter:

In this section, the effect of the shape parameter on the strength distribution was simulated and discussed with values of a_2=5, 15, 30, 100. Figure 50 shows that the strength shape parameters of a_2=15, 30, 100 indicated a similar compressive strength, while the strength shape parameter of a_2=5 has a much lower compressive strength than other cases. As mentioned earlier, a lower Weibull parameter means that the rock has more heterogeneity. That is, the strength shape parameter change has a strong influence on the material strength. In Figure 50, fracture planes were formed differently through the fully ruptured path in the specimens. Because every case has different formations of heterogeneity, the fracture patterns are strongly influenced by the heterogeneity formation.

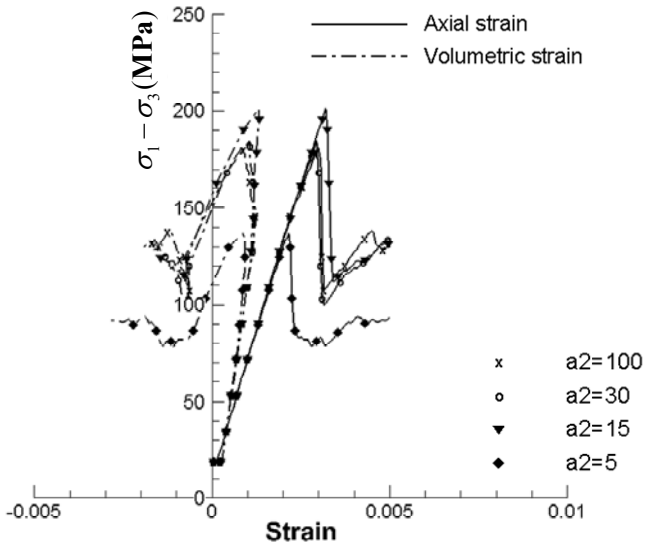

Figure 50. Stress/strain curve by strength scale parameter change.

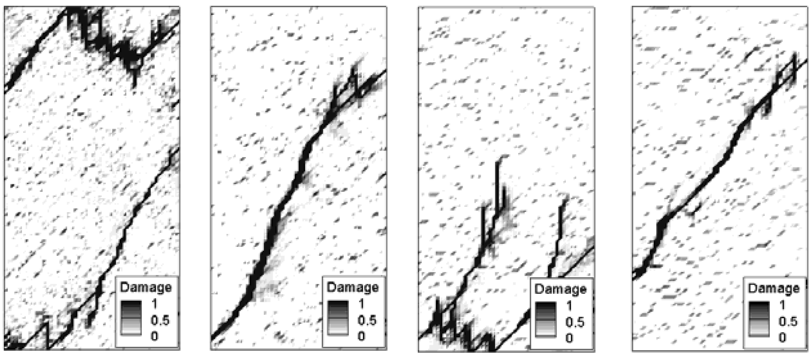

Figure 51 Fracture patterns by strength shape parameter change.

5.1.4 Numerical simulation for mesh size effects

In this section, three different sizes of mesh (0.01, 0.02, 0.04) were used for the multistage triaxial simulation (Figure 52). For rock heterogeneity, Weibull parameters of m_1=0.9, a_1=10 for stiffness distribution and m_2=0.9, a_2=15 for strength distribution were used to generate random variables; this allowed us to apply similar heterogeneity density to the numerical models. Table 5 and Figure 53 compare compressive strengths estimated by the numerical simulations, and the simulation results show that the estimated strengths generally match well with the experiments. However, the coarse mesh case shows some discrepancy in the high confinement tests, while the intermediate mesh size of 0.02 gives

better estimates than other mesh cases. In Figure 54, multiple and unconfined fractures were initiated and propagated during the triaxial compression test. When the confinement increased, the fracture patterns formed with less inclination angle. According to the simulation results, the finer mesh case can capture multiple crack growths; however, computational costs might be exponentially increased. The coarse mesh case shows inaccurate fracture patterns in Figure 56. Especially, at the high confinement cases, fracture patterns are significantly different from other mesh cases. Also, estimated compressive strength has larger errors.

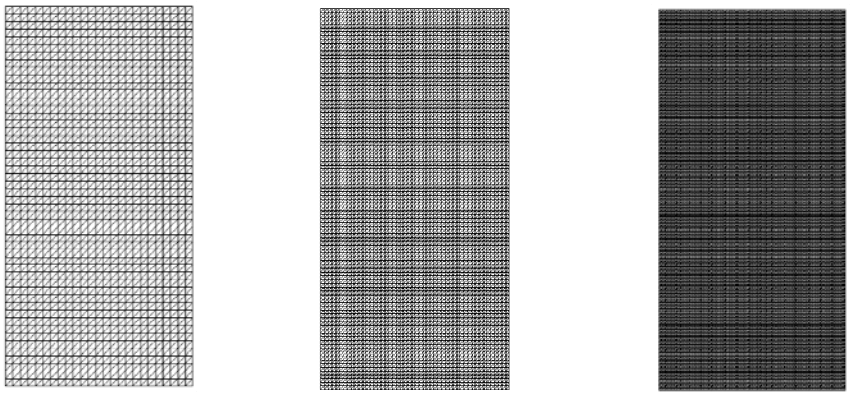

(a) size=0.04(NE=2,500) (b) size=0.02(NE=10,000) (c) size=0.01(NE=40,000)

Figure 52. Numerical models with different mesh sizes.

Table 5. Comparison of experiment and simulations of Tuff samples.

Confining Pressure (Unit=MPa)	0	5	15	30	40
Multistage Triaxial tests	88.4	126.9	190.3	261.6	309.2
NE=40,000 (size=0.01)	84.9	107.3	197.5	263.4	339.2
error(%)	4.12	18.27	3.65	0.68	8.84
NE=10,000 (size=0.02)	86.6	124.1	201.1	279.9	321.2
error(%)	2.08	2.26	5.37	6.54	3.74
NE=2,500 (size=0.04)	87.7	132.1	202.9	339.2	385.1
error(%)	0.8	3.94	6.21	22.9	19.7

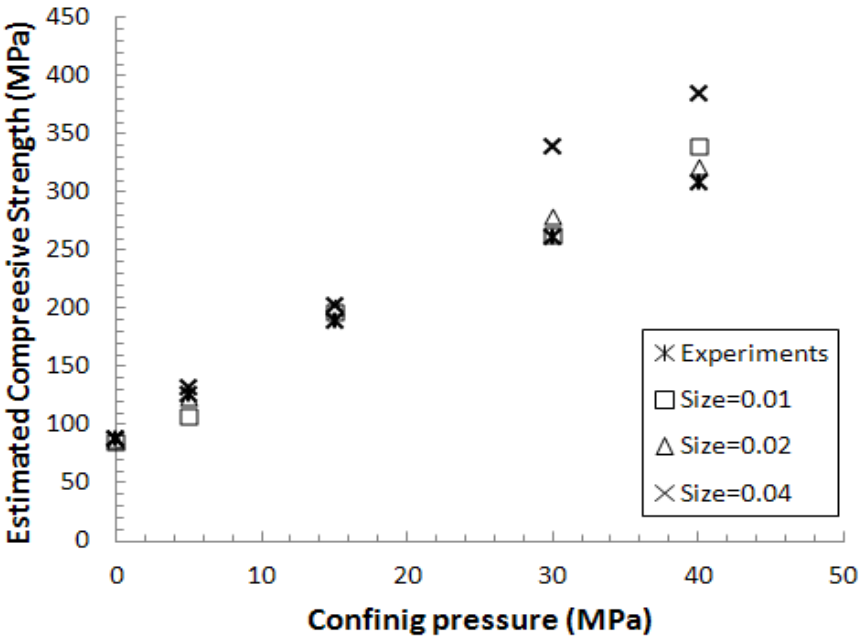

Figure 53. Comparison of estimated compressive strength by different mesh size.

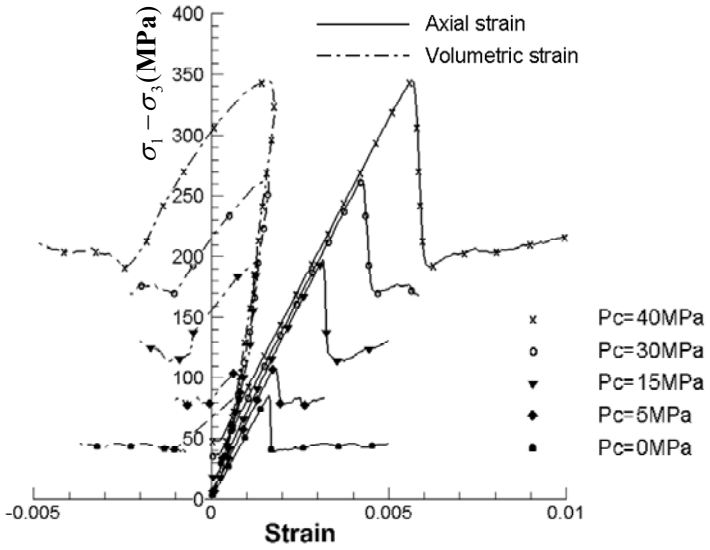

Figure 54. Stress/strain curve by various confining pressure at NE=40,000 (size=0.01).

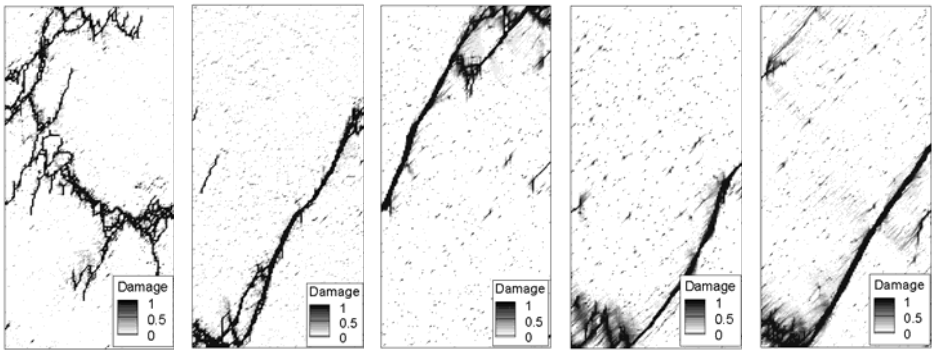

Pc= 0MPa Pc= 5MPa Pc= 15MPa Pc= 30MPa Pc= 40MPa

Figure 55. Fracture patterns by various confining pressure at NE=40,000 (size=0.01).

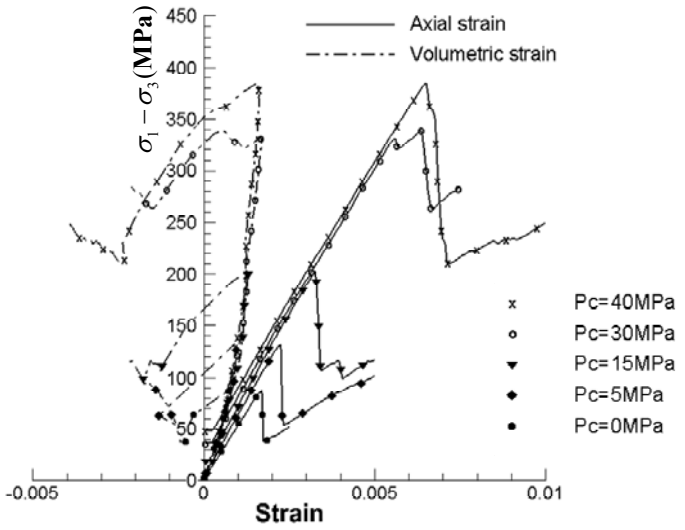

Figure 56. Stress/strain curve by various confining pressure at NE=2,500 (size=0.04).

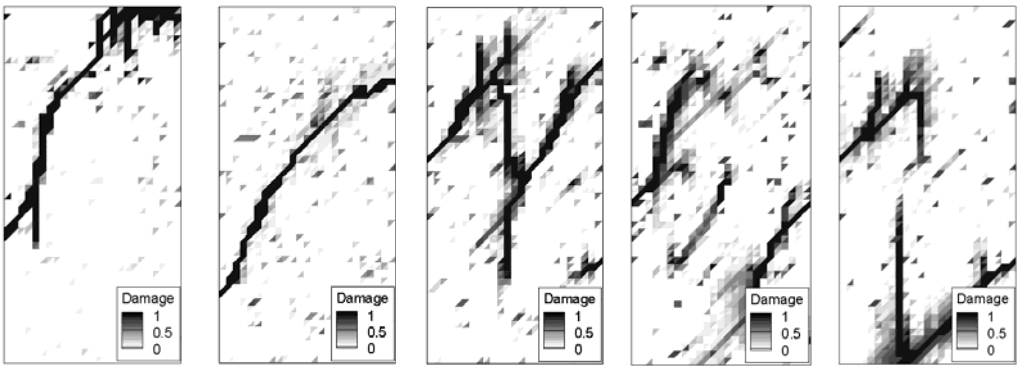

Pc= 0MPa Pc= 5MPa Pc= 15MPa Pc= 30MPa Pc= 40MPa

Figure 57. Fracture patterns by various confining pressure at NE=2,500 (size=0.04).

5.1.5 Mesh dependency issue

Mesh dependency is significant in FEM analysis. A stress-strain relation predicted in finite-element analysis usually depends on the mesh density. The mesh dependency may increase significant errors during analysis of practical problems (Pande et al., 1990). Thus, reducing mesh dependency is a critical issue in both numerical and practical aspects. In order to reduce the mesh effect, the hypothesis of equivalent energy dissipates rate was proposed and the dissipate energy based constitutive model was developed in Chapter 3. In this constitutive modeling, it is generally assumed that the energy dissipation rate required to initiate/propagate cracks should be similar regardless of finite element size. That is, initial amount of fracture energy and the energy dissipation rate per unit volume for crack initiation/propagation should be consistent in different finite element sizes. So, required fracture energy for bigger element size (NE=2500) should be four times higher than intermediate element size (NE=10000) and sixteen times higher than smallest element size (NE=40000). Also, the energy dissipation rate should be assigned same value regardless of finite element size to maintain the similar softening part of stress-strain curve to keep the fracture energy constant during crack propagation. During the triaxial compression simulation, elastic energy stored by mechanical deformation is computed at each element and the energy dissipation rate is assigned based on the confining pressure, as explained in Chapter 3. Hence, the constitutive relation of each element is governed by the elastic energy variation. When same loading and boundary conditions are applied, the stress-strain relations of three cases (NE=2500, 10000, 40000) show similar behaviors (Figure 58), because the fracture energy kept constant.

Based on this hypothesis, the damage model based on energy dissipation rate could be a possible solution for the mesh dependency problem. In Figure 58, strain-stress curves of the three different mesh sizes show similar behavior. That means total amount of dissipated energy of the three different mesh cases are similar and it indicates less mesh dependency solutions. Consequently, the mesh sensitivity issue has been successfully reduced in numerical analysis; however fracture patterns of the three different mesh cases show different patterns (Figure 59). This is because the fracture patterns are strongly related with distribution of the rock heterogeneity. In our method, the rock heterogeneity does not consist in the three different mesh cases, so that different fracture patterns are obtained in the different mesh cases. In addition, as mentioned earlier, in order to obtain proper fracture pattern and approximated compressive strength, coarse mesh case are not recommended and intermediate finite element size is recommended based on calculation of error estimation and computational cost.

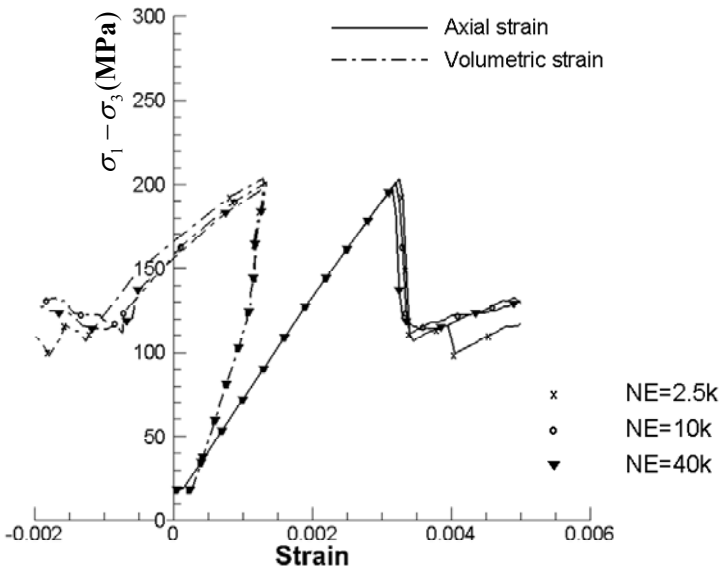

Figure 59. Stress-strain behavior at Pc=15 MPa with different element size.

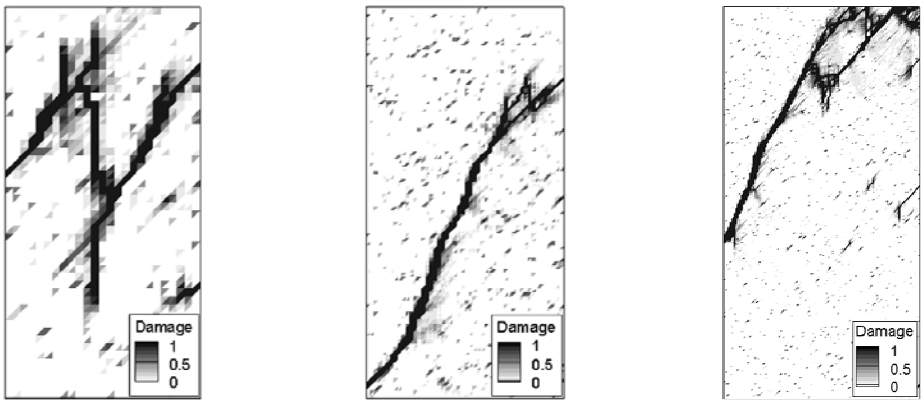

(a) size=0.04(NE=2,500) (b) size=0.02(NE=10,000) (c) size=0.01(NE=40,000)

Figure 59. Fracture pattern at Pc=15 MPa with different element size.

5.2 3D Numerical Simulation of Compression Tests

In this section, uniaxial compression test was used to study brittle fracture phenomena in a heterogeneous rock. When compressive forces are applied to the brittle rock, the fracturing patterns are complex, and replicating the shear localized fracturing patterns is challenging using numerical methods, especially for the three-dimensional simulation. The shear-faulting phenomenon depends on many parameters such as strength, heterogeneity, initial flaws, composition pattern, and grain size of rock. Because of the model's complexity, rather than attempting to consider grain size in numerical simulations, a probability distribution function was used to characterize the strength of fine- and coarse-grained rock in this study. The heterogeneity of brittle rock was characterized by the Weibull distribution function (Weibull, 1951), which was chosen for its flexibility. Random values generated by Weibull distribution function were

applied to both stiffness and compressive strength to represent the heterogeneous character of the rock. In this study, Weibull distribution parameters, m_1=1, a_1=5 for stiffness distribution and m_2=1, a_2=4 for strength distribution are used to characterize rock heterogeneity. The cylindrical specimen of rock with a size ratio of 2:1 and material properties in Table 6 were used in this simulation. The numerical domain for the uniaxial compression test is described in Figure 60. We used 57,153 uniform tetrahedron elements and applied displacement loading on the top surface of the cylindrical specimen. Boundary condition was that the bottom surface of the specimen was restricted in the z-direction, and the axial force was loaded on the top surface of the cylindrical specimen using displacement increments of $\Delta d=3.55\times10^{-3}$. Heterogeneous distribution of element stiffness was applied to each element by random variables with an average stiffness value of 73.5GPa (Figure 60). Lighter-colored elements represent weaker rock, while darker colored elements represent stronger.

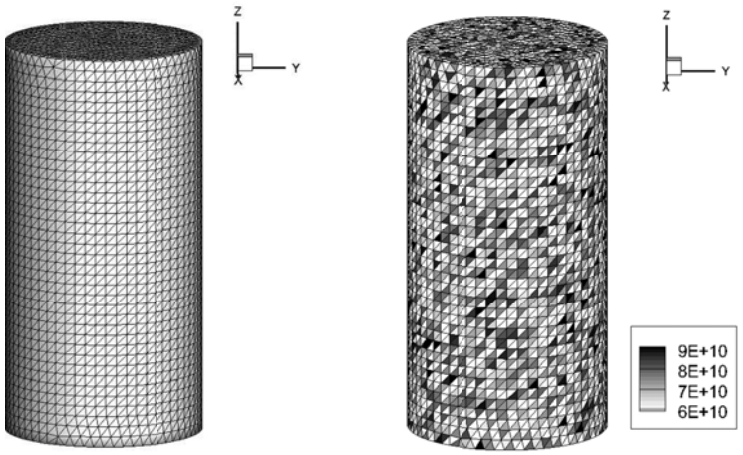

Figure 60. Numerical model and heterogeneity index (Unit=Pa).

Table 6. Material properties and input parameters for 3D uniaxial.

Inputs	Values
Element type	Tetrahedron
Young's Modulus, GPa	73.5 GPa
Poisson ratio	0.32
Num. of elements	57,153
Size of element	0.05
Aspect ratio (D:H)	1:2
Tensile strength, MPa	15-30
Incremental displacement	0.1e-3
Weibull parameters	m_1=1, a_1=5 for stiffness m_2=1, a_2=4 for strength

5.2.1 Numerical simulation of uniaxial compression

When rock heterogeneities were applied on both the stiffness and compressive strength of each element, fully penetrated cracking was found (Figure 61). Because the rock specimen was modeled as very brittle material, fully ruptured fracturing occurred in a very short period (Steps 175-195). Multiple failures were initiated at Step 175 when the total applied displacement on the top surface was $\Delta d=6.21\times10^{-1}$. Also, we can see very broad and spotted damage propagation due to the rock heterogeneity (Figure 62). The rock specimen is more damaged near the fracture plane after contact and shear faulting fully ruptured fracturing of the specimen. Figure 61 shows damage propagation with deformation over the step, so that the part with more deformation in the damaged zone is clearly visible.

In Figure 63, the maximum principal stress is mostly focused in the damaged zone and strain localization follows crack element propagation. According to the uniaxial compression simulation, the compressive failure of brittle rock predominated at the earlier period of rock fracture. The compressive stress led to shear faulting of the brittle rock after that, and the shear faulting dominated mostly during the fracture propagation.

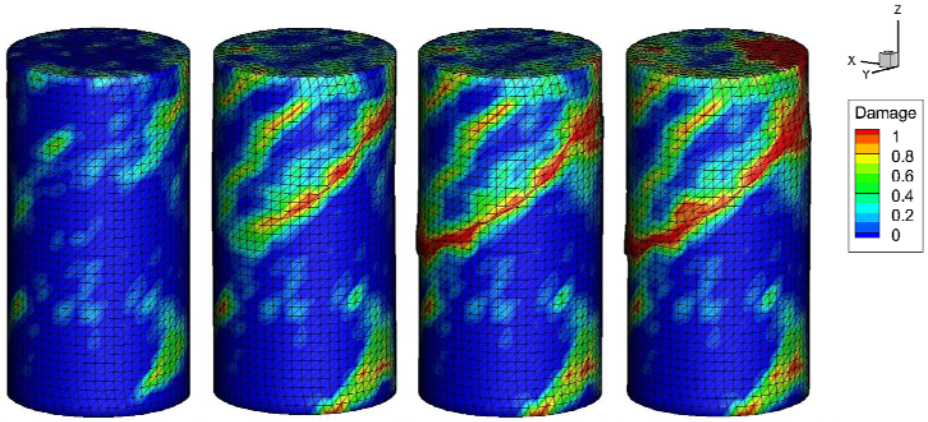

Figure 61. Damage propagation along steps with deformation (step= 175,185, 190, 200).

Figure62. Damage events during uniaxial compression (step= 175,185, 190, 200).

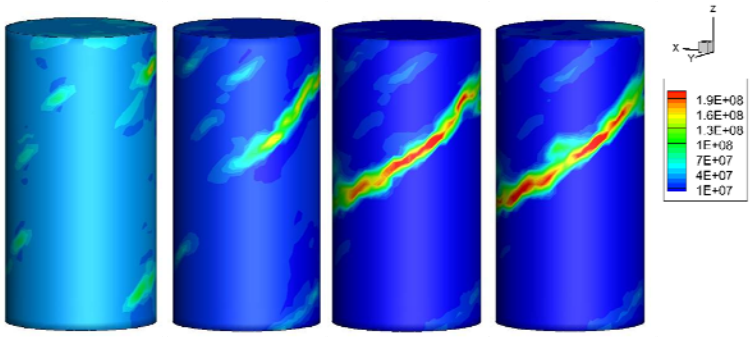

Figure 63. Principal stress propagation (Unit=Pa) (step= 175,185, 190, 200).

5.2.2 Snapback issue during triaxial compression

In this section, 3D numerical simulations were performed for triaxial compression test. Numerical model is same as previous 3D uniaxial simulation and material properties (Table 7) were used. When confinement is applied to the rock specimen, snapback issue is found Figure 64 and 65. From the numerical results, it is observed that fully ruptured fracture plane is successfully formed through the rock specimen. However, stress-strain curves show snapback behavior during crack propagation (Figure 64 and 65). The snapback behavior occurs for brittle materials when more fracture energy dissipated than the stored elastic energy during crack propagation. In the case of brittle materials, crack propagation causes sudden drop of the load and it could lead unstable response of stress-strain relation. The instability of mechanical behavior represents the snapback phenomenon. The snapback issue is normally caused by numerical destabilization, because more energy is dissipated than it actually should (Bazant and Planas, 1997). The snapback issue does not occur in 2D triaxial simulation, while only 3D triaxial simulation shows the snapback issue. This is because more energy is dissipated during crack propagation in the 3D triaxial simulation. Since we used scalar relation between the normal stress and strain for 3D constitutive modeling, the scalar degradation model could not represent the compressive failures in triaxial phenomenon, in which failure is triggered by lateral expansion and shear slip on inclined mircroplanes.
Therefore, in order to consider the triaxial variation of elemental degradation model, tensor type of damage model is recommended and the tensor damage model might be a solution of the numerical destabilization by the snapback phenomenon. However the tensor type of damage modeling is requiring complex mathematical formulation and high computational efforts. So, this issue is out of scope of our research and development of the tensor damage model is remaining for future improvement.

Table 7. Material properties and input parameters for 3D tiaxial simulation.

Inputs	Values
Young's Modulus, GPa	53.84 ~54.76 Gpa
Poisson ratio	0.32~0.34
Tensile strength, MPa	15-30
Incremental displacement	0.1e-3
Confining pressure, Pc	5MPa, 15MPa
Weibull parameters	m_1=1, a_1=9 for stiffness

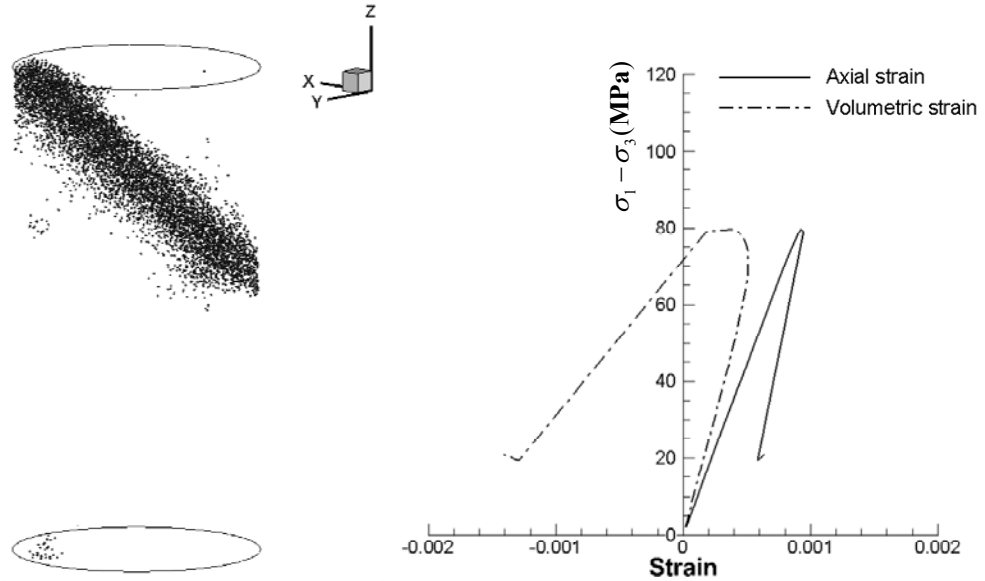

Figure 64. Plot of damage events and stress-strain curves of snapback at Pc=5MPa.

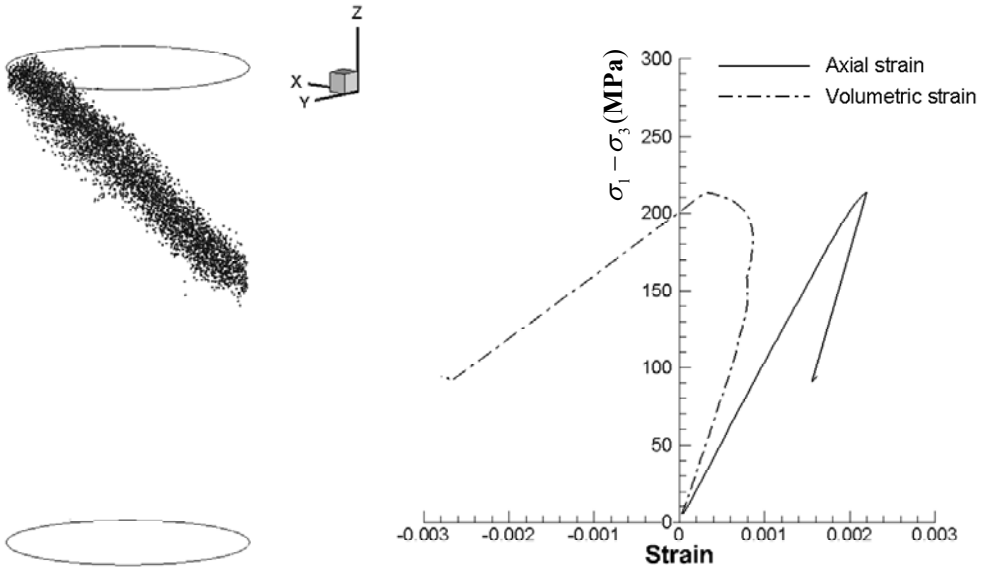

Figure 65. Plot of damage events and stress-strain curves of snapback at Pc=15MPa.

6. Numerical Simulation for Mixed-mode Fracture Propagation

Hydraulic fracturing paths, especially for fractures emanating from inclined wellbores and closed natural fractures, often involve mixed models of Mode I, Mode II, and Mode III fracture patterns. When an

embedded inclined fracture is subjected to compression, the fracture tips are restrained by the surrounding materials so that it does not propagate as predicted by a single-mode fracture (Min et al., 2011). In this section, two- and three-dimensional mixed-modes fracture growths from an initially embedded crack were studied using damage mechanics implemented within a finite element method (FEM). Especially, simulation of three-dimensional fracture propagation is complex as it often simultaneously involves all three fracture modes over a contour. Whereas in a 2D case, the zone of interest is only a point (fracture tips), in a 3D case, the fracture tip is a closed boundary, making development of a fracture criterion for predicting propagation at different points along its edges difficult.

6.1 Wing-crack Model

In this section, two-dimensional and three-dimensional wing crack growths were studied under compressive forces. As shown in Figure 67, the extension of secondary cracks in the brittle rock forms by mixed mode fracture. In 2D crack growth, the wing cracks (tensile fracture) grow towards the direction of maximum compression, while the secondary cracks (shear fracture) grow by sliding toward the lateral direction of the maximum compressive force due to the transverse shear localization. *Primary cracks*, describing of the wing crack, are originated from points of highest tension stress. *Secondary cracks*, describing of the shear fractures, are originated from points of compressive stress concentration. After the tensile stress concentration initiates the primary cracks, the compressive stresses originated from the sliding of the upper and lower areas of the pre-existing crack, and the shear concentration leads to growth of the secondary cracks opposite the primary cracks. Sequential growths of the primary and secondary cracks were observed in experimental tests (Bobet and Einstein, 1998; Lajtai, 1973; Wong and Einstein, 2009). Practically, 3D crack growth mechanism is more complicated. As shown in Figure 67, the primary cracks are originated from upper and lower areas of the pre-existing plane. By the compressive stress concentration, the secondary cracks are growing on the opposite side of the contact surface by Mode II conditions and the additional secondary crack could grow in the lateral direction due to Mode III conditions. In Figure 68 and Figure 69, the mixed modes of fracture propagation have been observed in experimental modeling (Bieniawski, 1967; Bobet and Einstein, 1998; Dyskin Av, 2003; Germanovich and Dyskin, 2000; Sagong, 2001). The experimental observations show tensile and shear crack growth in compression. The shear crack growth in compression is difficult to observe during the experiments, especially for Mode III, because the tensile mode, not the shear mode, is the dominant fracture mechanism in compression. However, when the confining pressure is high, as occurs when the rock is deep underground, the shear modes cracks may be the dominant fracture mechanism.

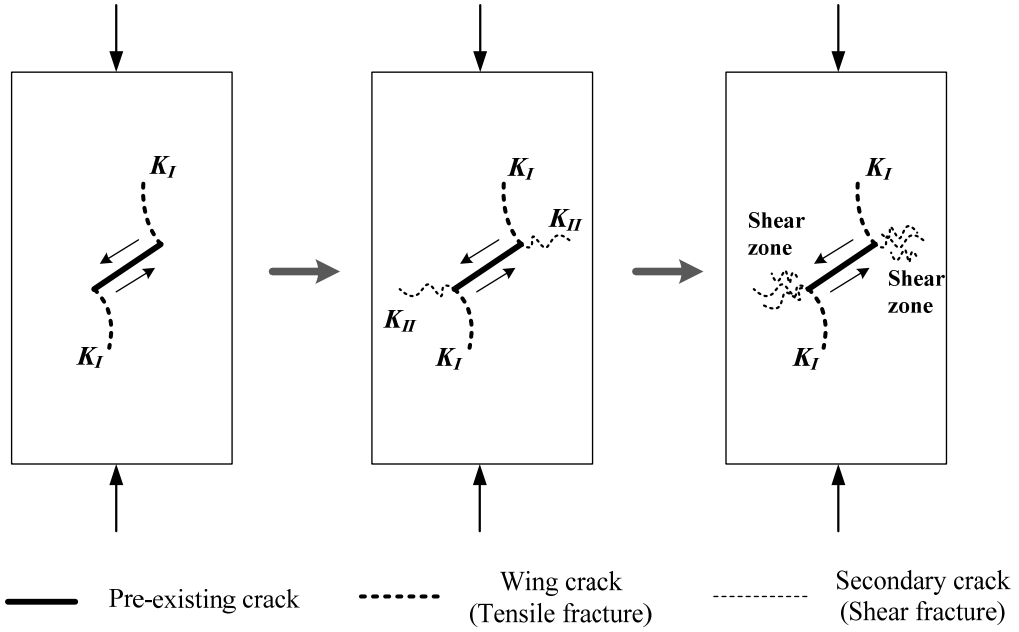

Figure 66. Evolution of 2D wing crack fractures from a pre-existing crack by (Mixed mode of K_I + K_{II}).

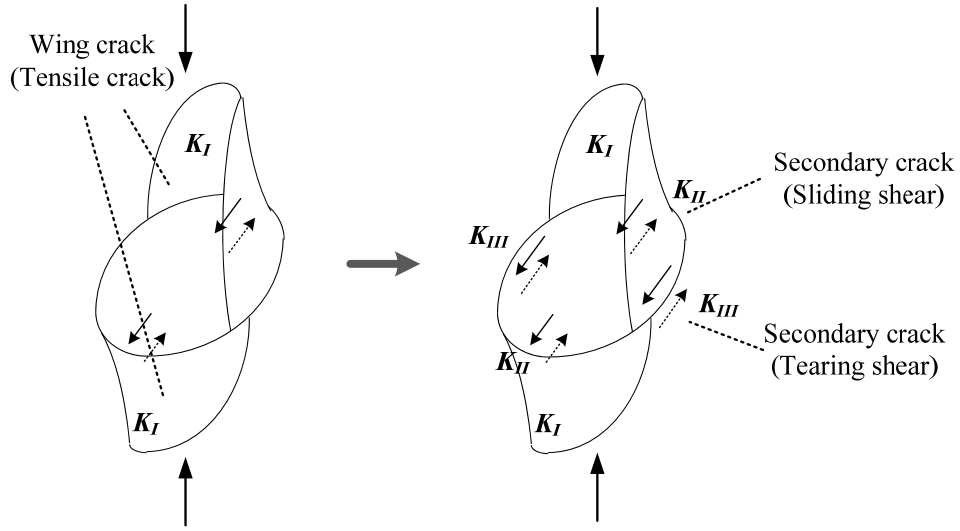

Figure 67. Evolution of 3D wing crack fractures from a pre-existing plane by (Mixed mode of K_I + K_{II}+ K_{III}).

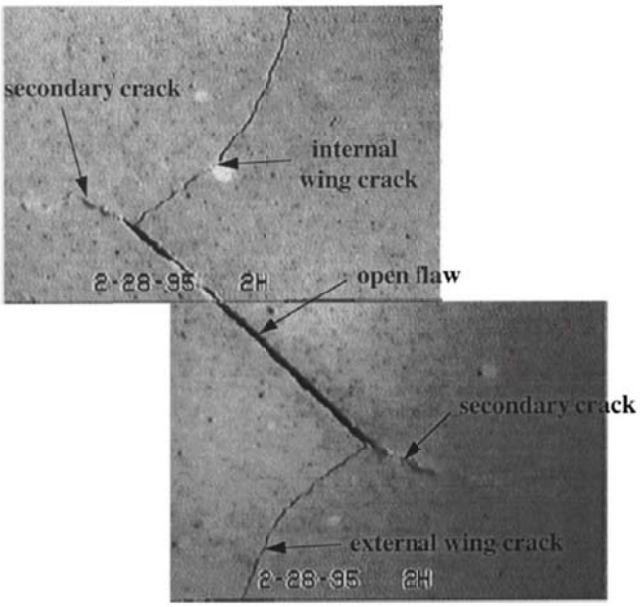

Figure 68. Crack growths of 2D wing-crack in uniaxial compression (Bobet and Einstein, 1998).

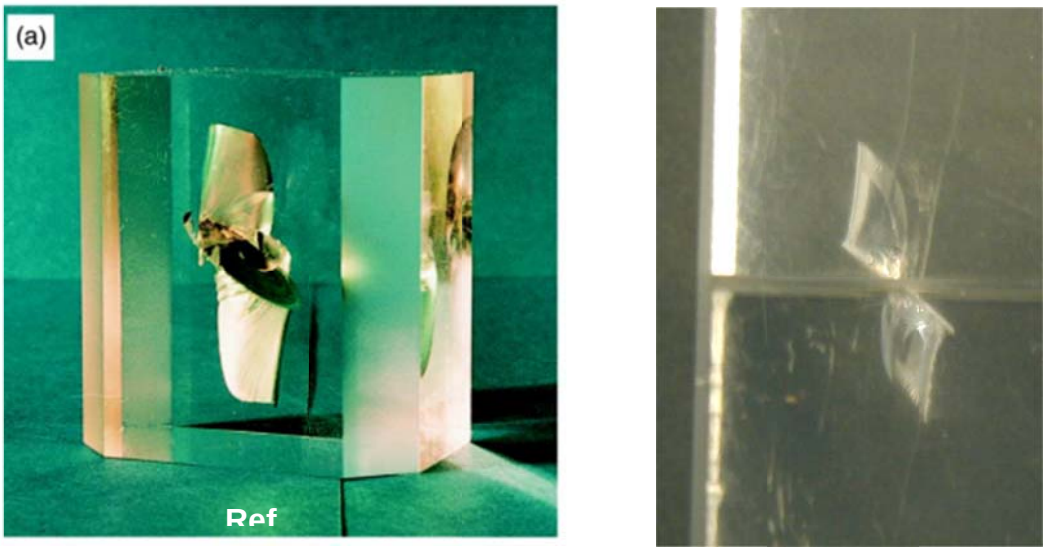

Figure 69. Crack growths of 3D wing-crack in uniaxial compression (Dyskin et al., 2003; Germanovich and Dyskin, 2000).

6.2 Numerical Results of 2D Wing Crack Model

Two-dimensional plane strain and 40,000 uniformly meshed triangular elements were used in this simulation, described in Figure 70 (b). Boundary conditions of the wing-crack model, described in Figure 70(a), were that the bottom surface of the specimen was restricted in the y-direction and the compressive force was applied on the top surface of the specimen using a displacement increment of $\Delta d=1\times10^{-3}$. Material properties and numerical input values for the 2D wing crack simulation are shown in Table 8. A pre-existing crack was located at center of the specimen with a 45° inclination angle (71(b)). The pre-existing crack is assumed an open flaw same as the experimental test (Figure 68). In order to express the

open flaw in numerical domain, crack elements overlapped with the initial crack geometry are modeled by assigning high damage variable (D=0.9). In addition, same as the experiment the crack elements are assumed as frictionless. If the pre-existing flaw is rough, crack initiation and propagation from the closed flaw are much different with the open flaw propagation. The closed flaw propagation was discussed in (Bobet and Einstein, 1998). Three cases are compared below: a tensile-dominated case, a shear-dominated case, and a mixed-modes case. The influence of various confinements on crack propagation and the mesh-dependency issue are discussed in this section.

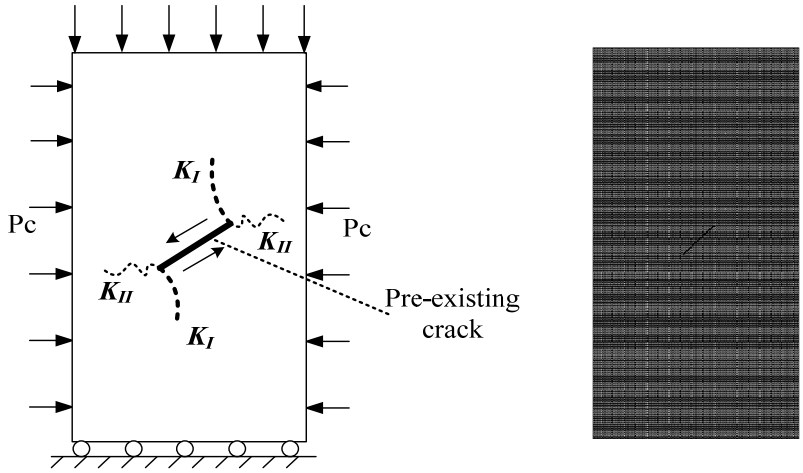

Figure 70. Numerical modeling of 2D wing crack model (a) Boundary condition (b) Meshed domain with inclined pre-existing crack.

Table 8. Material properties and input parameters for 2D Wing crack.

Inputs	Values
Young's Modulus, E (GPa)	37.5
Poisson ratio, υ	0.25
Number of Elements	40,000
Number of Nodes	20,301
Element type	Triangular
Ratio of specimen(D:H)	1:2

6.2.1 Tensile dominated wing crack growth (Mode I)

We assumed zero confining pressure applied on the specimen and Mohr-Coulomb parameters are assumed as shown in Table 9. In Figure 61, it was observed that tensile failure is a dominant failure mechanism under compression in the wing-crack model. In Figure 72, tensile stresses were concentrated at upper and lower areas of the pre-existing crack and the primary cracks (wing crack) initiated at step=25 and propagated until step=90 with the longer primary cracks. It was also observed that the maximum tensile stress concentration was following at the tensile crack tips and high compressive stress was developed at lateral directions of the pre-existing crack (Figure 71 (c)), but the secondary cracks (shear

crack) were not developing until step=90. The compressive stress eventually leads to initiation of the secondary crack (shear crack).

Table 9. Mohr-Coulomb parameters for tensile dominating crack (Mode I).

Inputs	Values
Mohr-Coulomb parameter, ϕ_f	10
Cohesion, c_F (MPa)	50
Tensile strength, σ_T (MPa)	10
Incremental displacement, Δd (mm)	1

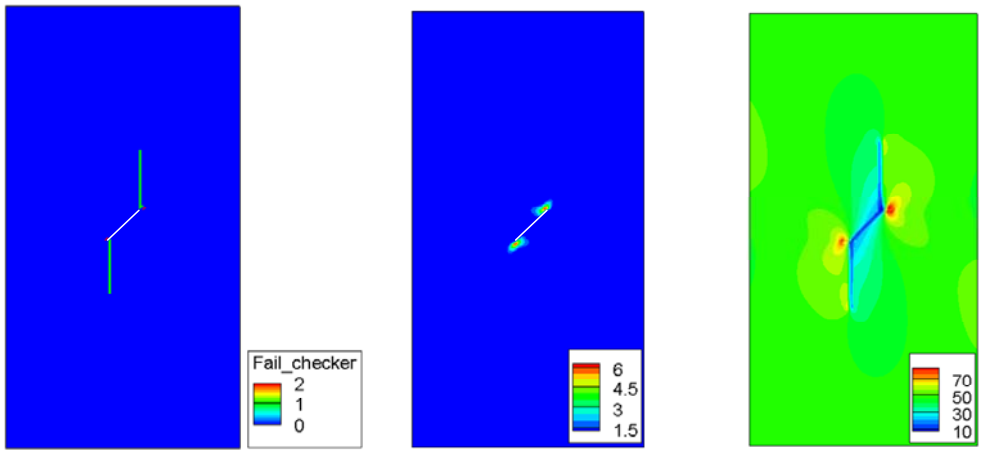

(a) step=90 (b) step=25 (c) step=90

Figure 71. (a) Failure type (1:tensile, 2: shear), (b) Maximum tensile stress (unit=MPa), (c) Maximum compressive stress (unit=MPa).

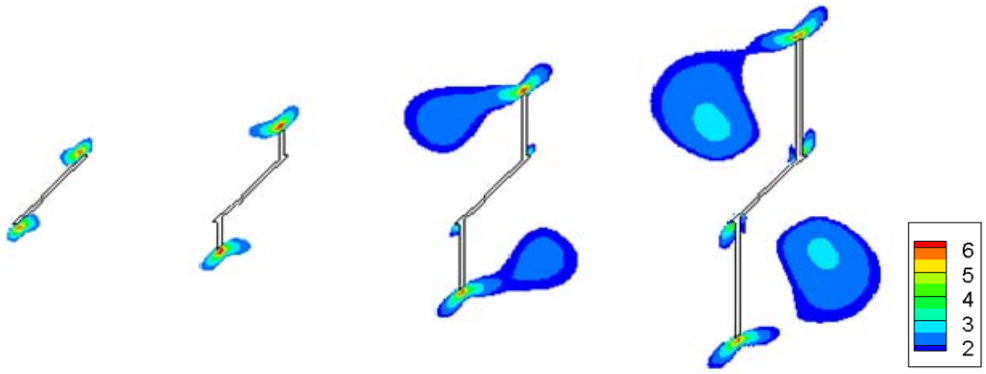

(a) step=25 (b) step=40 (c) step=60 (d) step=90

Figure 72. Maximum tensile stress (unit=MPa) with tensile crack growth.

6.2.2 Shear dominated wing crack growth (Mode II)

For the shear dominated crack simulation, we applied a confining pressure of Pc= 20 MPa on the specimen and Mohr-Coulomb parameters are assumed as shown in Table 10. When a high confining pressure is applied, shear failure becomes a dominant failure mechanism in the wing crack model and the shear dominated crack propagation can be observed (Figure 73). Since tensile cracks were restrained by the applied confining pressure, compressive stresses concentrated at the lateral areas exceeded shear failure criterion and led to initiation of the secondary cracks (shear crack). In Figure 74, the secondary cracks were initiated at the crack tips towards the lateral direction, and the shear-dominated cracks grew obliquely. The oblique shear crack growth was also observed from experiments in Figure 68 (Bobet and Einstein, 1998). The shear failure is a dominant failure mechanism when high confining pressure was applied on the rock.

Table 10. Mohr-Coulomb parameters for shear dominating crack (Mode II).

Inputs	Values
Mohr-Coulomb parameter, ϕ_f	10
Cohesion, c_F (MPa)	50
Tensile strength, σ_T (MPa)	15
Incremental displacement, Δd (mm)	1

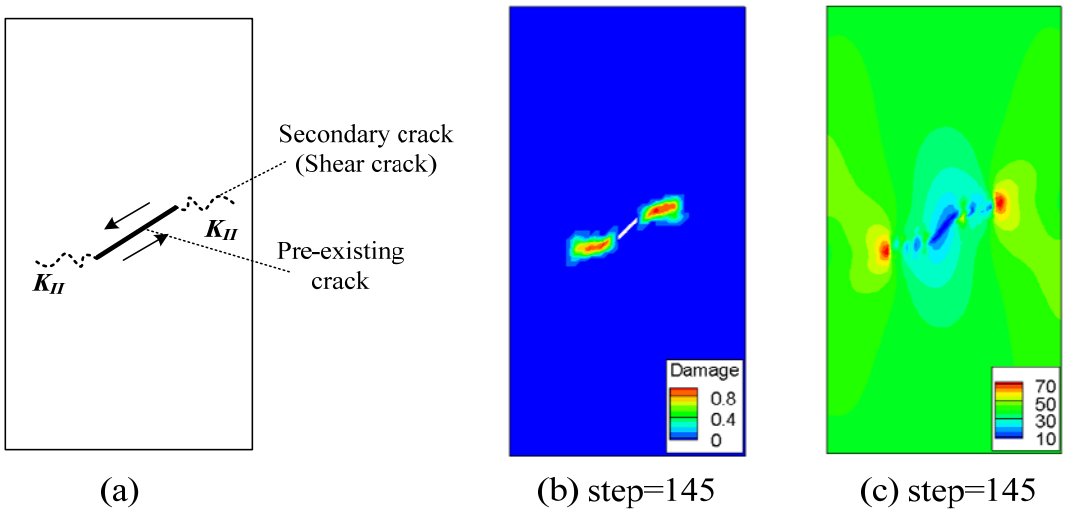

Figure 73. (a) Schematic of shear dominant crack growth (b) Damage propagation (c) Maximum compressive stress (unit=MPa).

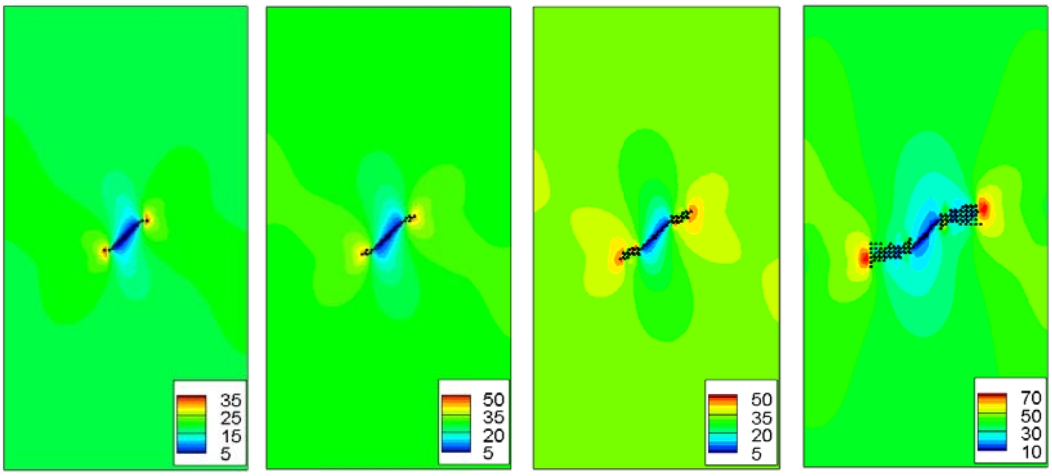

(a) step = 54 (b) step = 40 (c) step = 110 (d) step = 145

Figure 74. Maximum compressive stress (unit=MPa) with shear crack growth.

6.2.3 Mixed modes wing crack growth (Mode I+II)

In this section, we investigated a sequential growth of the primary cracks (tensile crack) and the secondary cracks (shear crack). We assumed zero confining pressure and Mohr-Coulomb parameter are assumed as shown in Table 11. In Figure 75, it was observed that the primary cracks grew first until step=70 and the second cracks were initiated from step=80. Since a tensile strength of a rock is much lower than a compressive strength, tensile failure is dominant failure mechanism at early stages. Experimental data typically shows that the ratio of the uniaxial compressive strength/the tensile strength is much greater than 2 (Jaeger et al., 2007). So, after an amount of growth of the tensile crack, the shear-induced crack was initiated from the crack tips, and it grew laterally to the pre-existing crack. The results agree with experimental observations in Figure 68 (Bobet and Einstein, 1998).

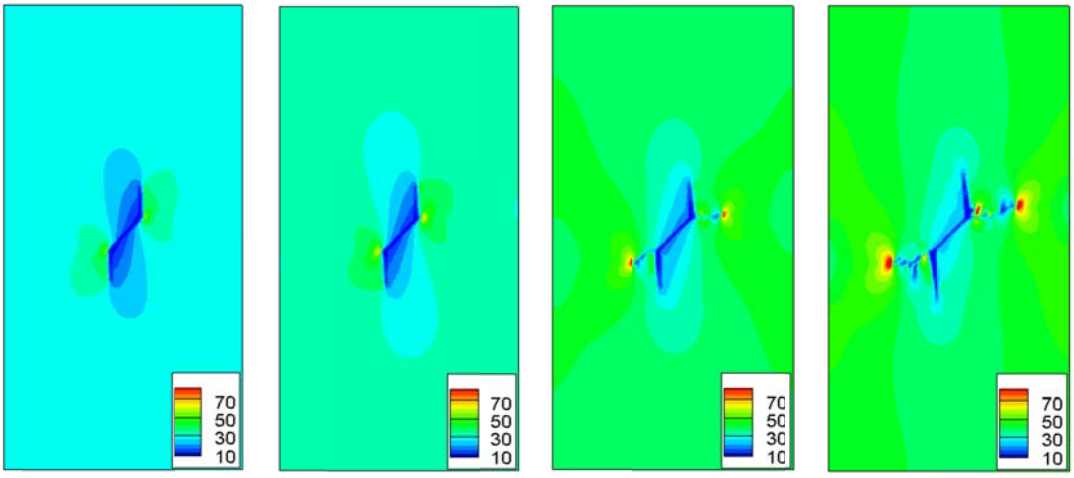

(a) step = 70 (b) step = 80 (c) step = 100 (d) step = 110

Figure 75. Maximum compressive stress (Unit=MPa) for mixed mode crack growth.

Table 11. Mohr-Coulomb parameters for Mixed modes 2D Wing crack (Mode I+II).

Inputs	Values
Mohr-Coulomb parameter, ϕ_f	10
Cohesion, c_F (MPa)	30
Tensile strength, σ_T (MPa)	10
Incremental displacement, Δd (mm)	1

6.2.4 Influence of confining pressure

As we discussed earlier, tensile crack initiation is favored over shear crack initiation because the tensile toughness of the rock type material is lower than the shear toughness (Bieniawski, 1967). However, when the confining pressure on the rock becomes higher, the confinement will constrain the tensile crack initiation; thus, the shear failure becomes dominant in failure mechanics. Especially, a rock at deep depth is under high confining pressure, and it cannot fail by one dominant mechanism. In that case, the crack propagation is highly influenced by the confining pressure. In order to investigate the influence of the confining pressure, we simulated several numerical examples of the wing-crack model with various confining pressures. We compared crack propagation patterns in Figure 76. Results of Pc=0MPa and Pc=0MPa are crack propagation at step=90, while results of Pc=0MPa and Pc=0MPa are crack propagation at step=120. The simulation results show the effect of confining pressure on a change in failure mechanism. From the simulation results, tensile cracking was dominant when the confining pressure is low, while shear cracking becomes dominant when the confining pressure is high.

Table 12. Mohr-Coulomb parameters for confining influence on 2D Wing crack.

Inputs	Values
Mohr-Coulomb parameter, ϕ_f	10
Cohesion, c_F (MPa)	35
Tensile strength, σ_T (MPa)	10
Incremental displacement, Δd (mm)	1

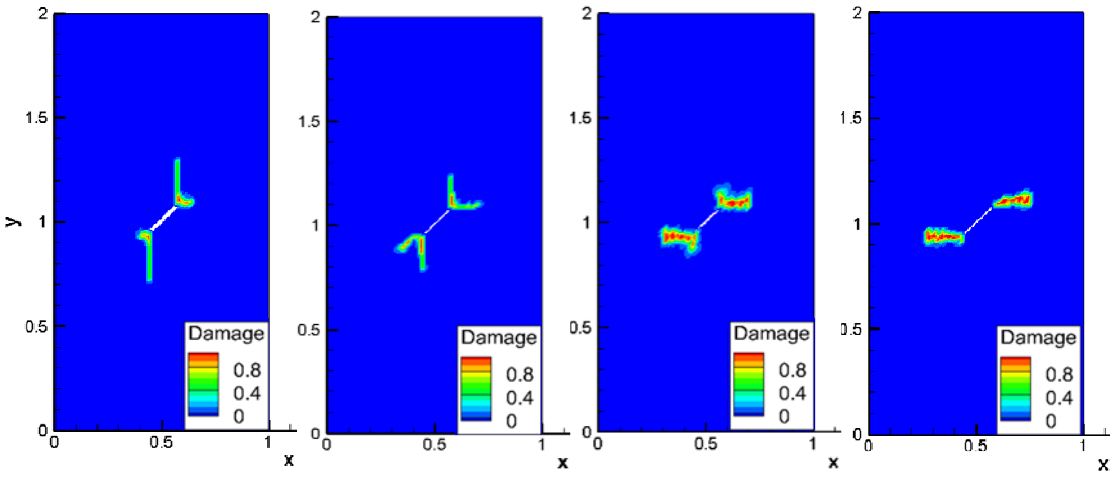

(a) Pc=0MPa (b) Pc=5MPa (c) Pc=10MPa (d) Pc=20MPa

Figure 76. Mixed modes crack propagation at various confining pressure.

Mesh dependency issue for crack propagation:

Similar with the previous sections, the mesh-dependency issue in crack propagation is an important issue in FEM analysis. If the mesh-dependency issue is not considered, crack growth rate could depend on the mesh size. Usually, finer mesh is preferred for use in crack propagation modeling, since the finer mesh can describe more realistic crack growth.

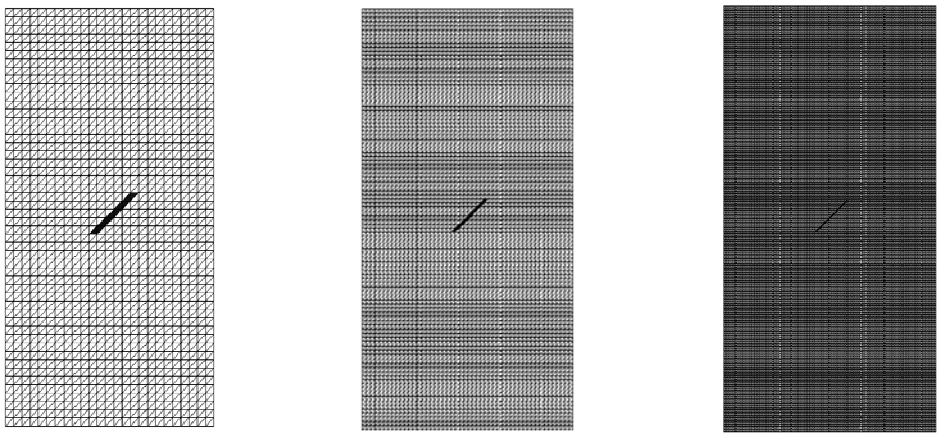

(a) size=0.04(NE=2,500) (b) size=0.02(NE=10,000) (c) size=0.01(NE=40,000)

Figure 77. Numerical model by different mesh size.

However, the finer mesh increases computational cost exponentially. Therefore, reducing the mesh dependency is important to reduce the computational cost. In this section, we compared three different mesh cases using a 2D wing-crack model. We assumed zero confining pressure and Mohr-Coulomb parameters are assumed as shown in Table 9. In Figure 77, three cases (size=0.04, 0.02, 0.01) are described with an inclined, pre-existing crack. Using the damage model developed using the hypothesis of equivalent energy dissipation rate from Chapter 3, we examined the influence of mesh size on crack growth rate. According to the simulation results in Figure 78, crack propagation rates at step=110 are similar in three cases. In all three cases, both tensile and shear crack growth are modeled by a similar pattern. However, larger size (size=0.04) shows much thicker damage zone than smaller size (size=0.01). This is because our crack propagation model is assumed that the crack is only propagating through elements. Thus, larger size case is only shown the thicker damage zone than other cases. But, growth rate of crack propagation is similar in all three cases, which means the mesh dependency was successfully reduced.

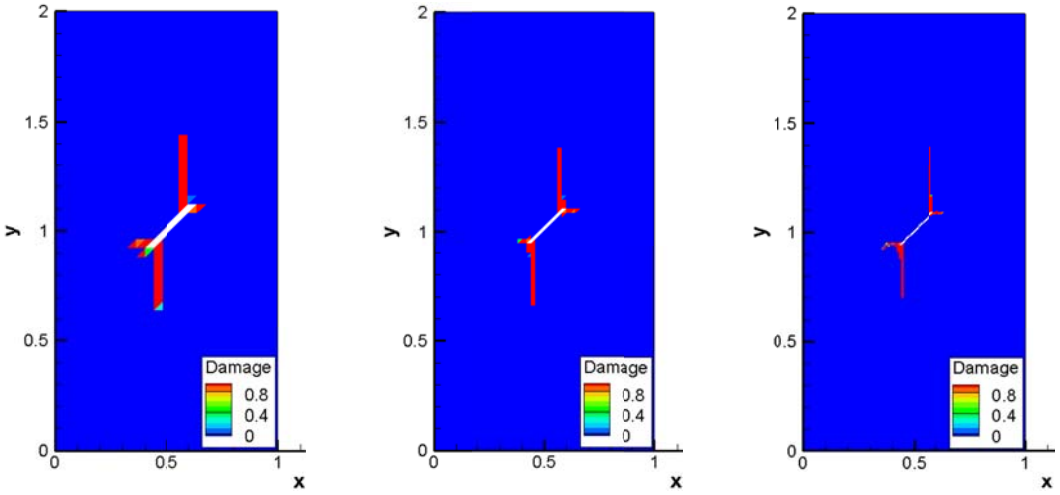

(a) size=0.04(NE=2,500) (b) size=0.02(NE=10,000) (c) size=0.01(NE=40,000)

Figure 78. Damage propagation (step=110) at different mesh size.

6.3 Numerical Results of Three-dimensional Wing Crack Model

This section explains the development of three-dimensional wing-crack growth under uniaxial compression from an initially embedded circular crack. In addition, it examines the extension of secondary cracks in a brittle rock under uniaxial compression. The failure mechanism of the three-dimensional mixed mode crack growth is more complicated than the two-dimensional model. The tensile crack (wing crack) propagates toward the direction of maximum compression, while the secondary crack grows on the opposite side of the pre-existing crack, as observed by Mode II (sliding), or in the lateral direction due to Mode III (tearing). The numerical domain has the size of 0.1-m × 0.1-m × 0.2-m, and the radius of the pre-existing circular crack is 0.02 m; inclination angle is 45°.

6.3.1 Tensile dominated wing crack growth (Mode I)

Similar to the two-dimensional wing-crack model, when tensile failure is the dominant mechanism, wing cracks are initiated from the upper and lower crack boundaries (tip contour) toward the direction of maximum compression. In Figure 79, the wing-crack growth is similar to the experimental observation in Figure 69.

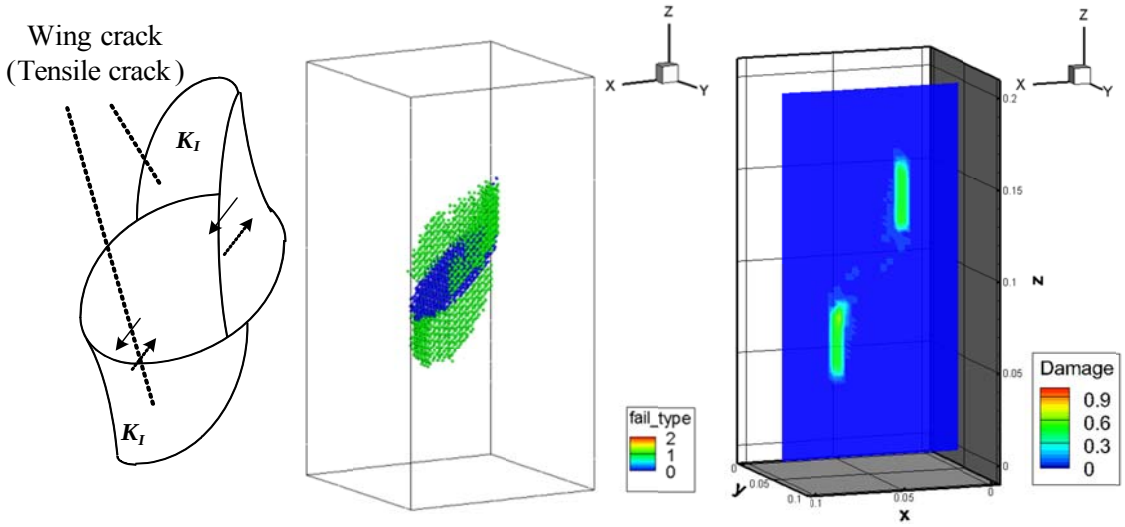

Figure 79. (a) Tensile dominated crack, (b) Failure type (1:tensile, 2: shear); (c) Damage propagation.

6.3.2 Shear dominated wing crack growth (Mode II+III)

When the brittle rock is highly confined, the tensile crack initiation is constrained and shear failure is dominant during crack propagation. Due to frictional forces on the pre-existing crack surface, shear cracks are initiated by the transverse shear localization. The shear friction force leads to growth of secondary cracks on the opposite side of the pre-existing crack. Figure 80 shows that the secondary fracture develops from the upper and lower tips by the Mode II fracture, and the secondary fracture propagates outwardly to the lateral side of specimen by Mode III. The side fracture that initiated from the side tip rotates from the initial crack tip toward the lateral side of the specimen, which represents the Mode III response. The shear-induced fracture is oblique.

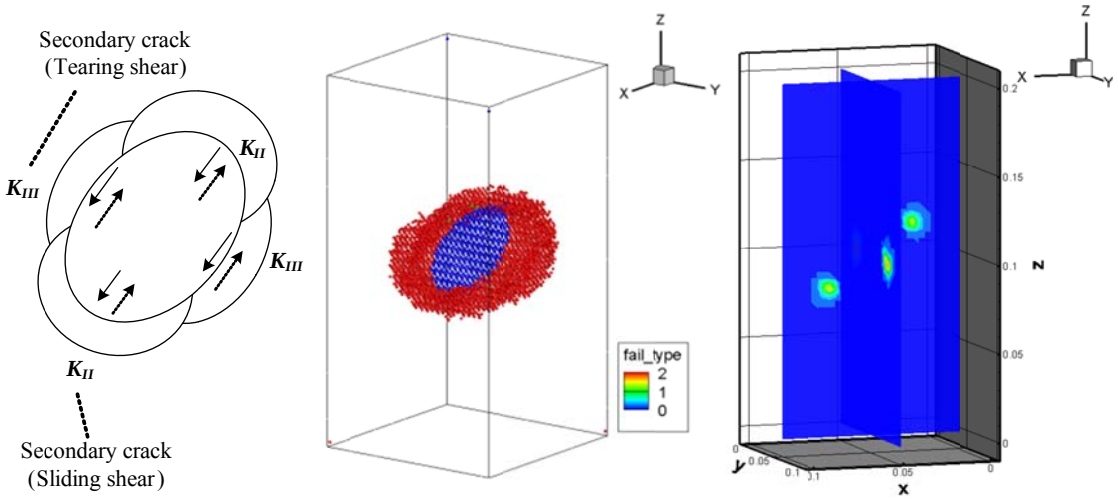

Figure 80. (a) Shear dominated crack, (b) Failure type (1: tensile, 2: shear); (c) Damage propagation.

6.3.3 Mixed modes dominated wing crack growth (Mode I+ II+III)

In Figure 81, wing cracks grow to the major compression first, and then secondary cracks grown by shear forces act on both the upper and the lower part of the pre-existing crack. However, no secondary crack appears in the lateral direction of the pre-existing crack in this example. Because only compressive force is applied on the top, the secondary crack is hard to initiate by Mode III (tearing). If confinement is applied to sides of the specimen, the failure mechanism might transition to a shear-dominant mode as shown in Section 8.2.4. This pattern of fracture propagation has been observed in experimental modeling of 3D crack growth from pre-existing circular cracks (Adams and Sines, 1978). Also, Dyskin et al. tested the wing-crack model using a brittle material and including the presence of the contact effect.

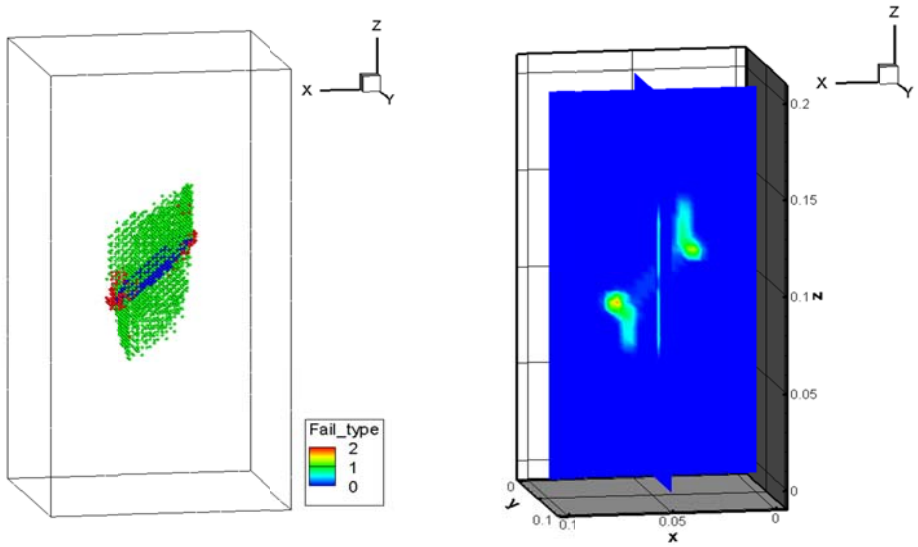

Figure 81. Mixed modes crack, (a) Failure type (1:tensile, 2: shear), (b) Damage propagation.

7. Hydraulic Fracture Propagation in Impermeable Rock

In unconventional geothermal reservoir (EGS) development, multiply-fractured reservoirs can be developed vertically or horizontally. Three areas of investigation are of special interest in the study of unconventional reservoir stimulation: the importance of mixed fracture modes and correct wellbore positioning, the estimation of crack paths from the inclined perforation, and the influence of tortuous fracture path on net injection pressure increase. In this chapter, these were investigated using models of fracture propagation induced by hydraulic pressure. Generally, when the perforations are misplaced within the maximum in-situ stress direction, high pumping pressure is required to open and initiate cracks.

7.1 Facture Propagation from Fractured Wellbore

The hydraulic fracturing treatment usually starts from an initial path for the fracture, which is created by a "perforation" technique. The perforation, a finger-like hole, is designed to give orientations. Consider a wellbore with a short initial crack on its boundary. The crack is either oriented along the maximum stress direction or is inclined as shown in Figure 82. Radius of the wellbore is 0.1 m, and it is situated in a 3m × 3m block (Figure 83). The numerical domain is meshed by 4-noded triangular elements (Figure 83). The initial crack is created by perforations before hydraulic fracturing stimulation. The length of the perforations is assumed as 0.1 m. The rock is subjected to anisotropic far-field stresses applied in the x- and y-directions and material properties of the rock are shown in Table 13. The wellbore/fracture system is pressurized incrementally using a pressure-boundary condition. The pressure level is updated at every time step and applied on both existing and newly propagated crack elements using a moving-boundary scheme. Slow fluid injection increases the hydraulic pressure uniformly over the fracture surfaces except in the crack tip area. Due to the highest fluid loss in the fluid-lag region, the applied hydraulic pressure decreases rapidly near the fracture tip (Papanastasious, 1997). Also, the low-pressure region indicates fracture-tip effects, since the fracturing fluid never quite reaches the fracture tip (Smith and Shlyapobersky, 2000). So in the simulation, the fracture tip pressure is assumed to be the zero. Except the fracture tips, we apply uniform pressurization in the fracture plane and increase incrementally until the fracture tips are propagating. Once the fracture propagated, we adjust lower uniform pressurization in the fracture and increase incrementally again until the fracture tips are propagating. It is also assumed that the process is isothermal and the rock is impermeable.

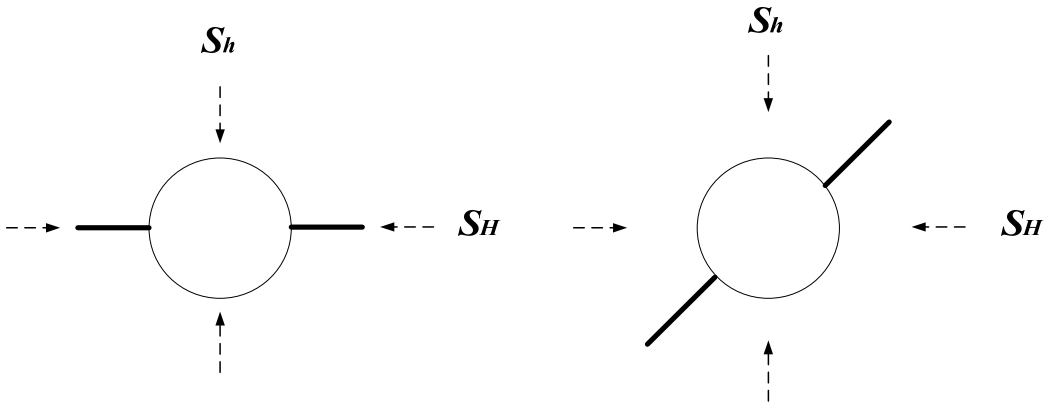

Figure 82. Fractured wellbore with perforations under in-situ stress.

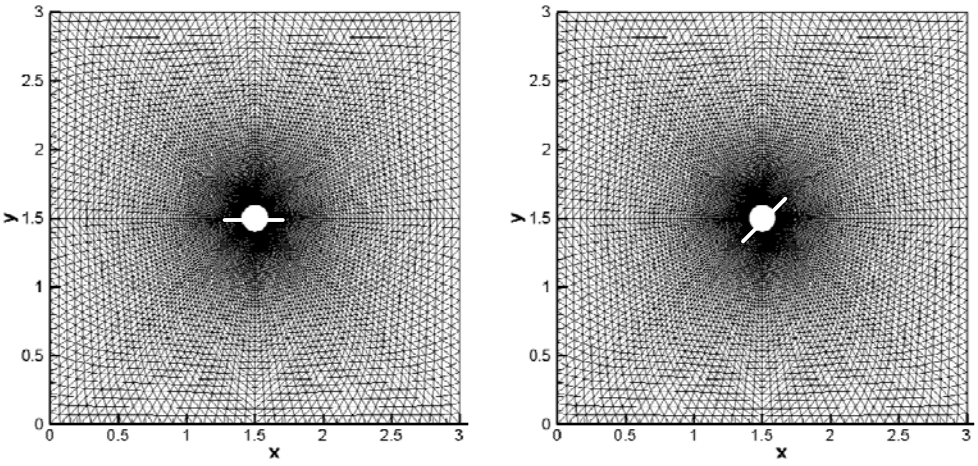

Figure 83. Numerical domains for the fractured wellbore.

Table 13. Material properties and input parameters for 2D HF model.

Inputs	Values
Young's Modulus, E (GPa)	37.5
Poisson ratio, υ	0.25
Number of Elements	19,200
Number of Nodes	9,760
Element type	Triangular
Mohr-Coulomb parameter, ϕ_f	10
Cohesion, c_F (MPa)	40
Tensile strength, σ_T (MPa)	25

7.1.1 Parallel perforated wellbore

As a boundary condition (Table 14), the far-field stresses are 4 MPa in the x-direction and 1MPa in the y-direction. As expected, the hydraulic fracture propagates toward the maximum principal stress direction (Figure 84). Note that the wellbore pressure decreases during fracture propagation. Since we used uniform pressure boundary condition (except fracture tips), required pressurization is decreasing with the growth of the fracture length. Applied total force in the fractures is increasing by multiplying the uniform pressure by the fracture length. In addition, when the injection rate remains the same during fracture propagation, the hydraulic pressure applied to the fracture surface is proportional to the fracture length. When the fracture is not propagating, the wellbore pressure increases until the fracture propagates and the wellbore pressure drops. In Figure 85, the wellbore pressure decreases continuously with fracture length. The rapid variations in the wellbore pressure profile are caused by propagation increments. The resulting aperture changes are smooth and continuously vary during crack propagation in Figure 85.

Table 14. Boundary conditions for parallel fractured wellbore.

Inputs	Values
Max. Far-field stress, S_H (MPa)	4
Min. Far-field stress, S_h (MPa)	1
Initial hydraulic pressure (MPa)	4
Incremental hydraulic pressure (MPa)	0.2

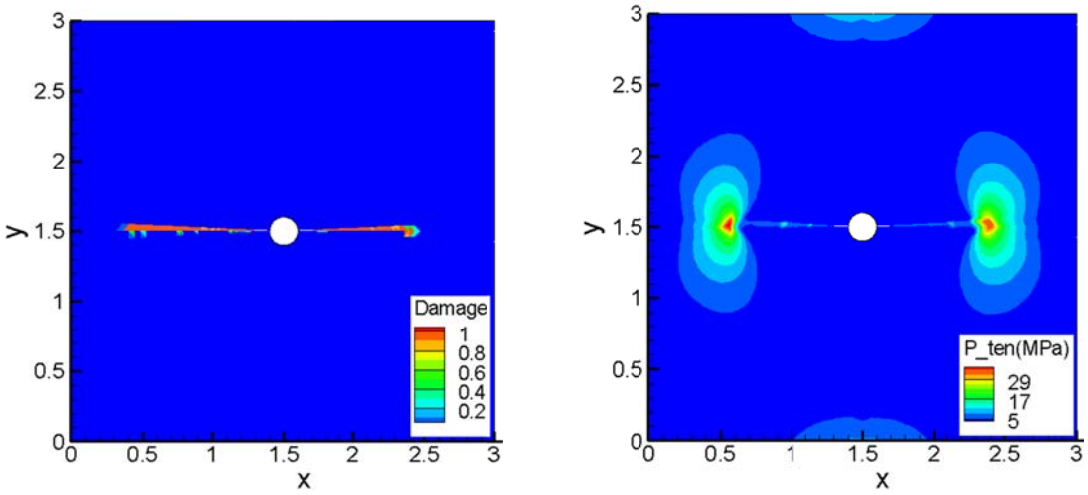

Figure 84. Damage propagation and Maximum tensile stress distribution.

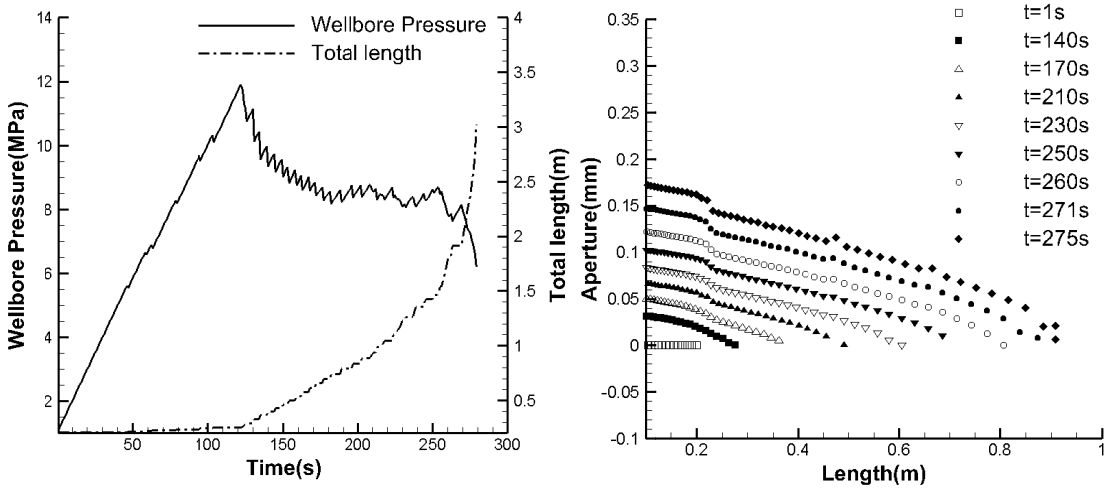

Figure 85. Wellbore pressure change and aperture change during hydraulic fracturing.

7.1.2 Inclined perforated wellbore

The inclination angle, 45°, of the initial crack is assumed in the example. As a result, the direction of crack propagation changes with increasing length as the fracture reorients itself in the maximum far-field stress direction. At early time, the hydraulic fracture is propagating with the same initial crack angle, and then the hydraulic fracture turns toward the maximum far-field stress direction. That is, the initial fracture is opened by the hydraulic pressure and slips under the anisotropic in-situ stress. So both tensile propagation and shear slip are detected near the turning zone of the crack path. As can be observed in Figure 85, the wellbore pressure is decreasing at early time when the crack propagates in its original direction, but after time steps, the wellbore pressure increases again as the crack turns, reflecting crack-path tortuosity. When the mixed mode fractures are combined during hydraulic fracturing, required wellbore pressure increases to create fracture propagation. Despite the high hydraulic pressurization, the fracture aperture change (Figure 86) is not larger than the aperture change for the straight propagation segment. The shear slip of the opened fracture causes highly compressive stress near the wellbore and the curved section of the fracture (Figure 89).

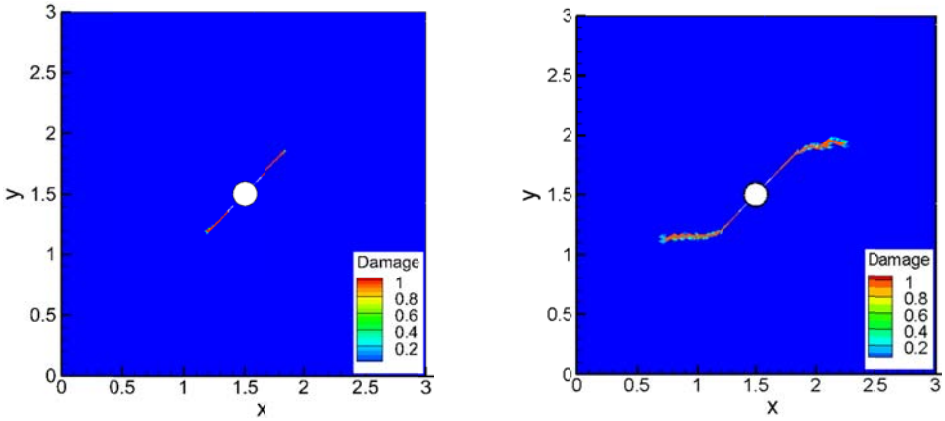

Figure86. Damage propagation at early time and later time.

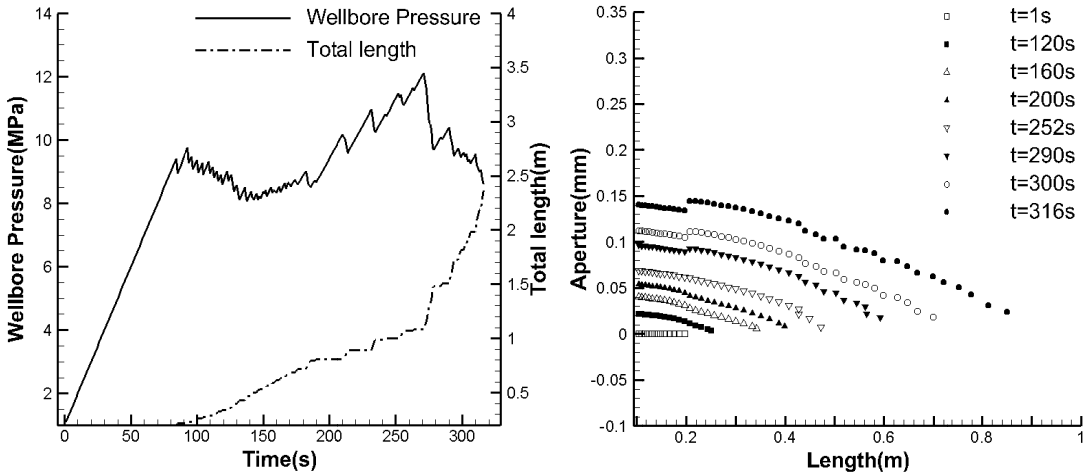

Figure 87. Wellbore pressure change and aperture change during hydraulic fracturing.

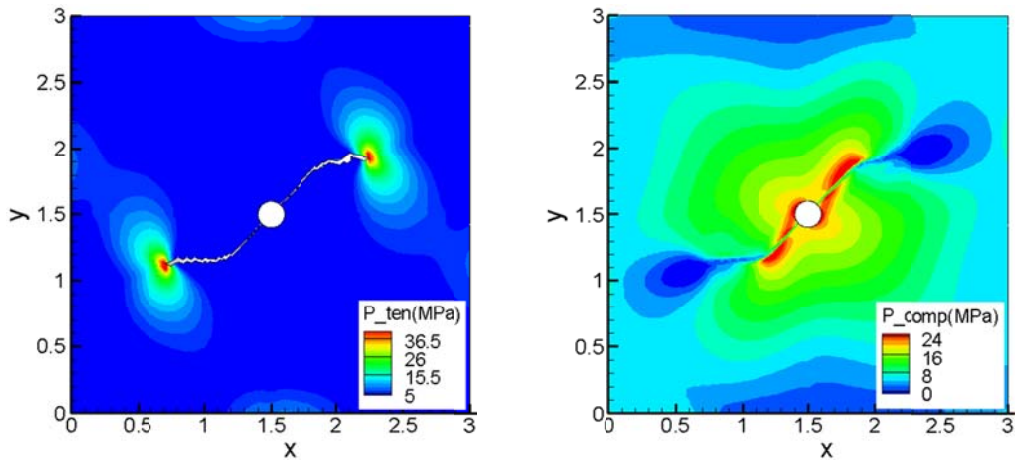

Figure 88. Principal tensile and compressive stress distributions.

7.1.3 Fracture propagation from long perforation

When the initially fractured perforation is relatively large compared with the wellbore size, the influence of the wellbore could be neglected. A larger scale reservoir model with an initial fracture is modeled 10-m × 10-m block and meshed uniformly in Figure 8.8. Material properties described in Table 13 and 20,000 uniform triangular elements were used in this simulation.

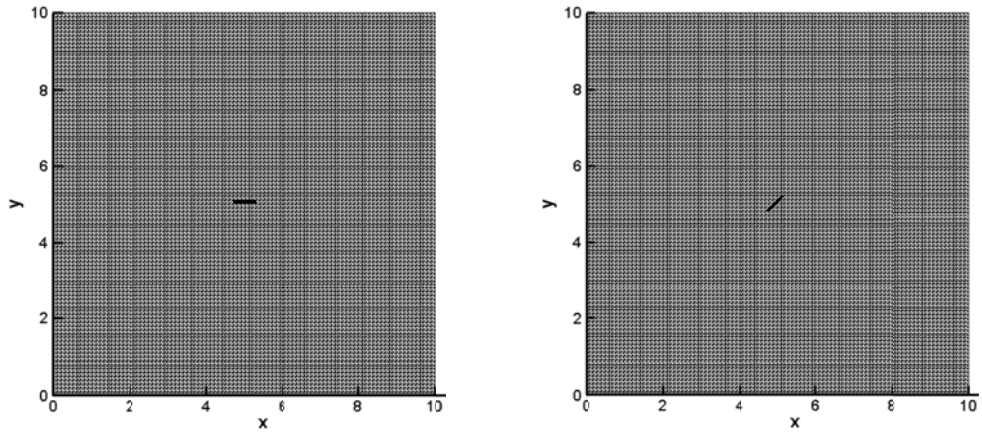

Figure 89. Schematic numerical domain of reservoir model w/o wellbore geometry.

Parallel perforation:

The initial fracture is assumed to be long enough to ignore the wellbore geometry effect. Initial fracture length is assumed as 0.6 m, and the far-field stresses are 10MPa and 5MPa in the x- and y- direction, respectively. As can be observed in Figure 90, crack propagates straight, and the wellbore pressure profile is similar with the previous simulation with a wellbore. Trend of the wellbore pressure is decreasing with the growth of the fracture length and aperture profile is gradually increasing (Figure 91). Basically, tensile failure is dominating during hydraulic fracturing, but when shear failures were combined during fracture propagation, the wellbore pressure increases to overcome the shear toughness and propagates the hydraulic fracture. Because of the mixed mode fractures, wellbore pressure is going to up and down

during hydraulic fracture propagation (Figure 91). Compared with the previous parallel fractured wellbore case, the applied max/min in-situ stress ratio is changed from 3:1 to 2:1, and due to relatively higher far-field stress contrast, the crack path shows some turns but the main crack propagating direction follows the maximum far-field stress. The simulation results show that the fracture tortuosity is not severe and the crack path is relatively straight.

Table 15. Boundary conditions for parallel perforation.

Inputs	Values
Max. Far-field stress, S_H (MPa)	10
Min. Far-field stress, S_h (MPa)	5
Initial hydraulic pressure (MPa)	7
Incremental hydraulic pressure (MPa)	0.5

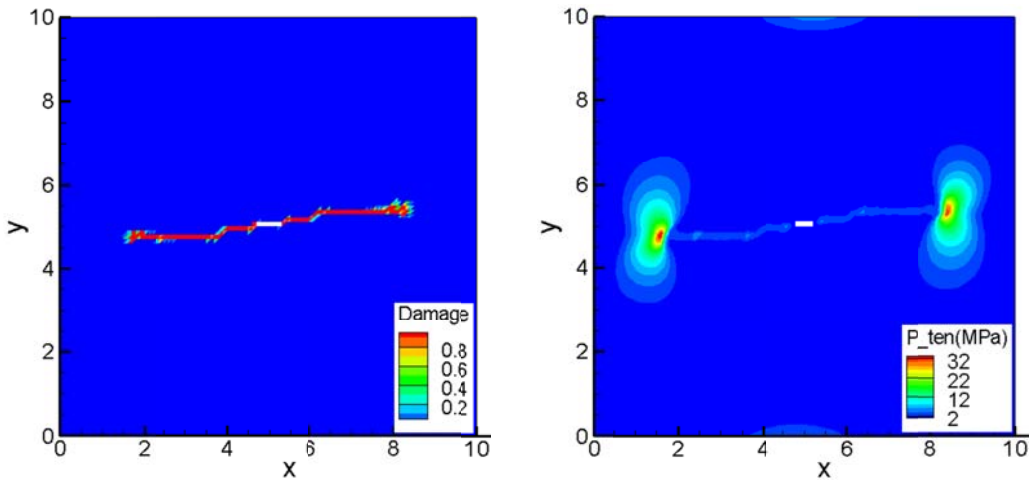

Figure 90. Damage propagtion and Maximum tensile stress distribution.

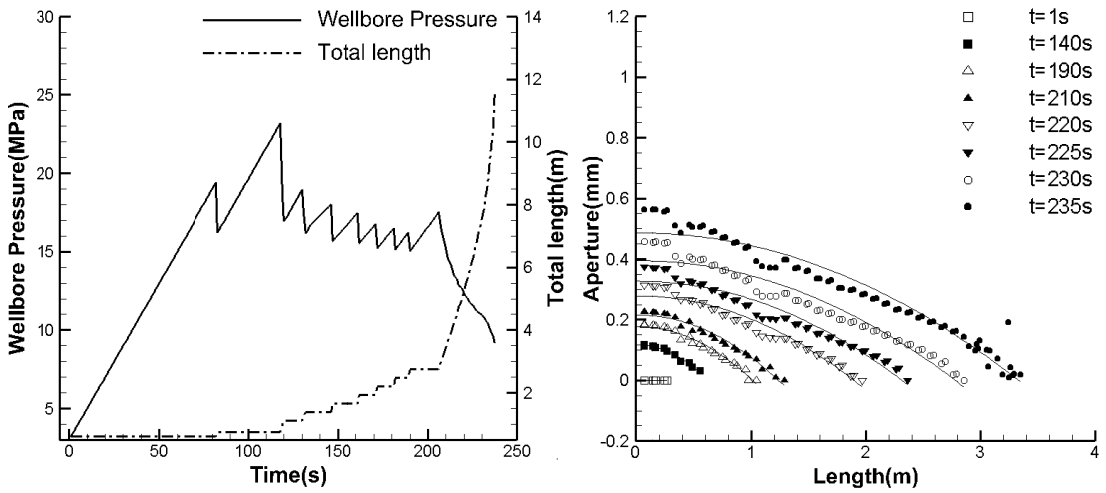

Figure 91. Wellbore pressure change and aperture change during hydraulic fracturing.

Inclined perforation:

The inclination angle, 45° and the fracture length of the initial crack are assumed as 0.55 m in the example. The reservoir dimensions are 10 m each. The far-field stress is given by 10MPa and 5MPa applied in the x- and y- directions, respectively. Similar with the previous simulation, the hydraulic fracture turns to the maximum far-field stress direction and shows tortuous crack propagation (Figure 92). At early time, tensile propagation is dominating and the hydraulic fracture is propagating with the same initial crack angle. At later time, the hydraulic fracture turns with shear slip and lots of damages are identified near the hydraulic fracture. In Figure 92, higher damage zones (red) indicate the main hydraulic fracture, while the lower damaged zone indicate secondary or microscopic fractures. As explained above, the wellbore pressure drops sharply during propagation and increases again when mixed mode fractures are combined. In addition, since the initial perforation is inclined, the wellbore pressure to overcome the anisotropic far-field stresses is higher than the parallel perforation case. In order to create tensile propagation, more pumping is required in the inclined perforation case. Therefore, it could be an indication of shear failure during hydraulic fracturing stimulation, when the wellbore pressure goes up after initial wellbore pressure drop.

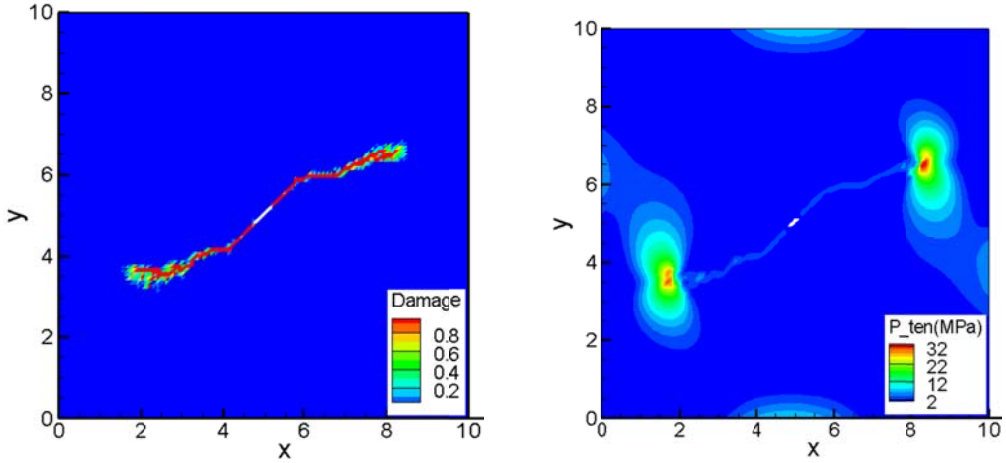

Figure 92. Damage propagtion and Maximum tensile stress distribution.

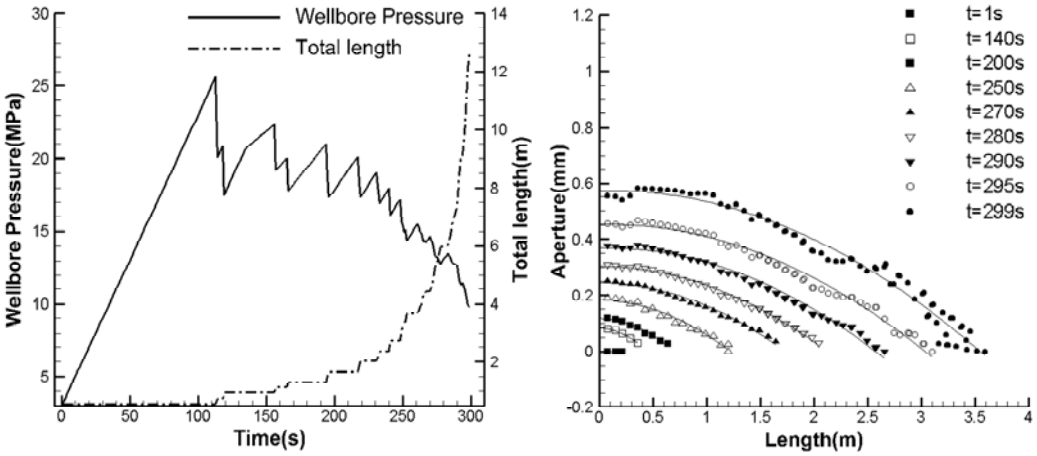

Figure 93. Wellbore pressure change and aperture change during hydraulic fracturing.

8. Hydraulic Fracture Propagation in Impermeable Rock

Hydraulic fracturing can be defined as coupled fluid-solid interaction problem. This interactive problem is very challenging to interpret via numerical methods, because of lots of numerical complexity such as the moving boundary issue, dynamic crack growth, and complex geometry. Therefore, one approach to solve the hydraulic fracture propagation problem has been quasi-static fluid-driven fracturing (Adachi et al., 2007; Boone, 1989; Papanastasious, 1997). Although the quasi-static assumption might be invalid for realistic crack growth behavior, it has given a reasonable solution so far. Hydraulic fracturing can be divided into three coupled processes of fluid flow, hydromechanical deformation, and fracture propagation. The fluid flow inside fractures is modeled using the lubrication equation, and the hydromechanical deformation of rock is solved using fully coupled poroelastic analysis. Fracture propagation is modeled as quasi-static crack growth. So at each time step we solved an iterative solution for rock deformation and fluid pressure using the coupled iterative algorithm explained in Chapter 5. In this chapter, we present 2D hydraulic fracture propagation simulation using the quasi-static fluid-driven fracturing model. The influence of reservoir heterogeneity on hydraulic fracturing stimulation is of special interest. The heterogeneous feature of the rock could affect multiple fracture propagation and fluid flow in the fracture by increasing leakoff volume, so that reservoir heterogeneity is an important factor to determine the hydraulic fracturing strategy. Through the numerical study of hydraulic fracturing, the numerical model could help to design an optimized hydraulic fracturing strategy and save developing costs in was such as minimizing unnecessary experimental tests.

8.1 Two-Dimensional Numerical Modeling

Similar to a previous simulation, a 10-m × 10-m 2D reservoir model was used. The numerical domain was meshed by 20,000 uniform triangular elements (Figure 94). The length of the perforation was assumed as 1.2 m, which is placed in the center of the numerical domain. Material properties of westerly granite were used (Table 16), and boundary conditions of the far-field stresses were 10 MPa and 5 MPa in

the x- and y-directions (Table 17). Water was used for fracturing fluid and was injected to the center of the numerical domain. Constant fluid injection rate of 24 L/min was used and applied as a point-fluid-source boundary condition into the numerical domain.

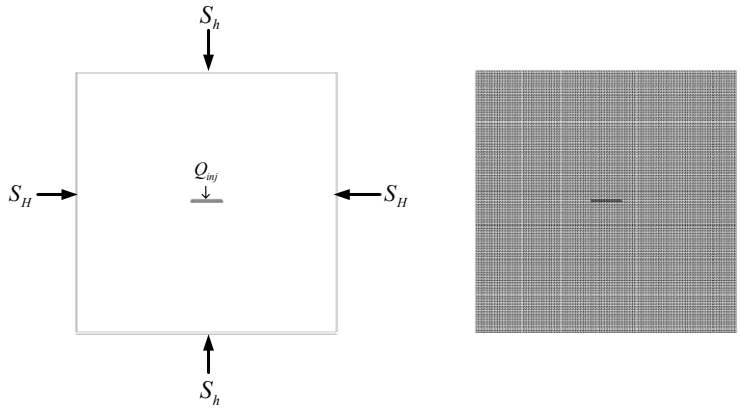

Figure 94. Numerical domain and boundary condition for Hydraulic fracturing simulation.

Table 16. Rock properties of Westerly Granite (Mctigue, 1986).

Inputs	Values
Young's Modulus, E (GPa)	37.5
Shear Modulus, G	15
Drained Poisson ratio, υ	0.25
Undrained Poisson ratio, υ_u	0.33
Biot's coefficient, α	0.44
Skempton's coefficient, B	0.82
Permeability, k (md)	0.01
Porosity	0.01
Fluid mass density, ρ_f (kg/m3)	1000
Fluid viscosity, μ (Pa·s)	1.e-3
Bulk modulus for fluid	3.291e9

Table 17. Boundary condition and input parameters.

Inputs	Values
x-dir. Far-field stress, S_H (MPa)	10
y-dir. Far-field stress, S_h (Mpa)	5
Injection rate, q_{inj} (L/min)	24
Mohr-Coulomb parameter, ϕ_f	10
Cohesion, c_F (MPa)	30
Tensile strength, σ_T (MPa)	7
Weibull distribution parameters	m_1=1, a_1=5 m_2=1.1, a_2=9

m_3=1, a_3=4

8.1.1 Hydraulic fracturing in homogeneous reservoir

According to the simulation results, the hydraulic fracture in homogeneous rock propagated toward the maximum far-field stress direction without branching or multiple crack growth (Figure 97). The small formation damage near the fracture plane limited the leakoff volume to a very small value. That is, most of the injected fracturing fluid remained inside the fracture volume. The remaining fracture volume was highly influenced by the fluid pressure distribution in the fractures. The injected fluid flow defined the fluid pressure distribution (Figure 95). The fluid pressure induced the mechanical deformation (opening) of the fractures. The fluid pressure distribution and aperture changes varied with fracturing time and fracture propagation. We solved iteratively the aperture changes and fluid pressure distribution with the fracture growth during the hydraulic fracturing treatment (Figure 96). The pore pressure at the crack tip was nearly zero due to opening modes along the fracture; while compressive fluid pressure forces pushed the pore pressure near the fracture was higher (Figure 97). Because of curvature of the hydraulic fracture path, pore pressure near the curvature area shows higher distribution. This is because compressive stresses by the hydraulic pressurization are concentrated at the curvature area. Wellbore pressure decreased and stabilized near 9MPa as the hydraulic fracture propagated (Figure 98).

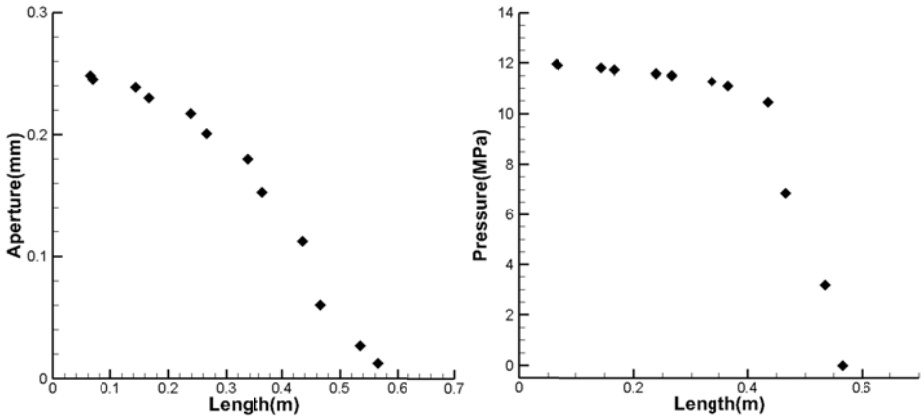

Figure 95. Aperture profile and Fluid pressure profile at first step (t=0.6seconds).

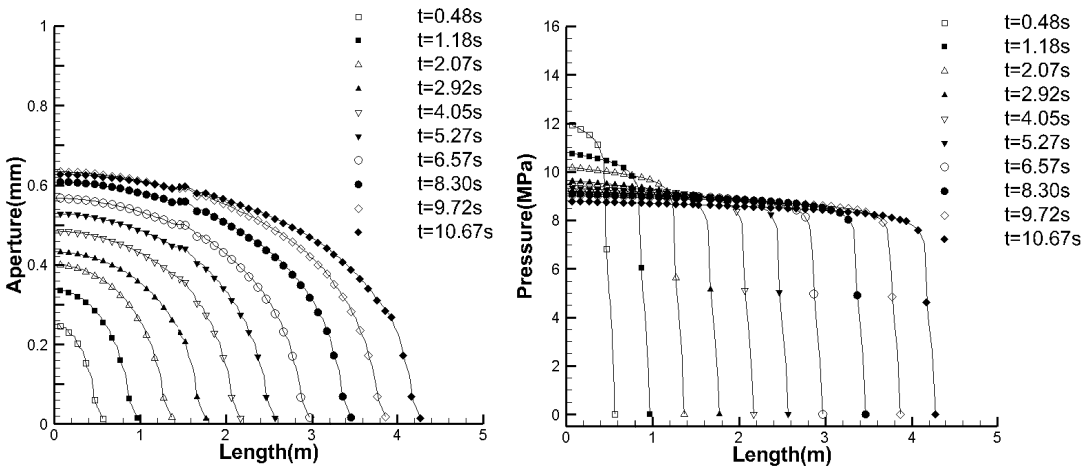

Figure 96. Aperture profile and Fluid pressure profile during hydraulic fracturing.

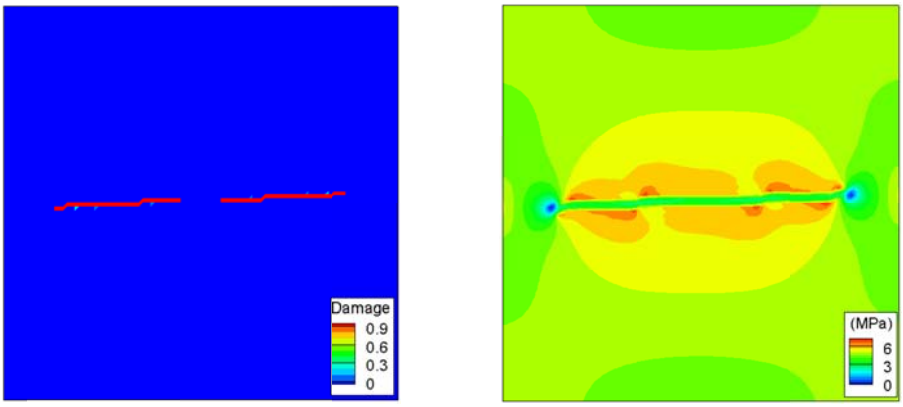

Figure 97. Crack propagation and Pore pressure distribution during hydraulic fracturing.

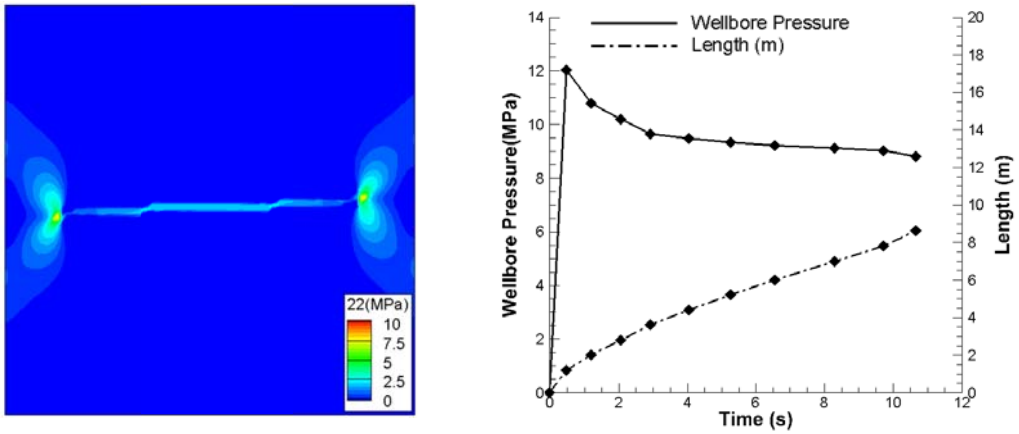

Figure 98. σ_{yy} distribution and Wellbore pressure change during hydraulic fracturing.

8.1.2 Hydraulic fracturing in heterogeneous reservoir

In this section, we investigated an influence of reservoir heterogeneity on the hydraulic fracturing design. In order to represent the reservoir heterogeneity, we assumed values of Weibull parameters Table 17 and applied to the numerical model. The random variables generated by the Weibull function are applied to distributions of material strength, Young's modulus, and matrix permeability. If the random variables were applied to porosity or Poisson's ratio, by wide distribution of the random variables the porosity could be over 1 and the Poisson's ratio could be over 0.5. There is violation of general rules, so that it is inappropriate to apply random variables to the porosity and Poisson's ratio. The combination of the distributions represents reservoir heterogeneity (Figure 99). Boundary conditions were same as in the homogeneous case. According to the simulation results, a lower wellbore pressure profile (Figure 101), a smaller opening, and lower fluid pressure distribution were obtained by the heterogeneous influence (Figure 102). Due to the heterogeneous feature, injected fluid volume and leakoff volume increased (Figure 100). Therefore, we can conclude that the hydraulic fracturing in the heterogeneous reservoir requires more fluid injection and more time to create the same length of fracture as in the homogeneous reservoir (Figure 100). In addition, breakdown pressure is lower than the homogenous case because locally distributed strength and stiffness vary randomly. The pore pressure near the fracture is varied and sparsely concentrated because of the stress heterogeneity and the pore pressure at the curvature area is higher because of compressive stress concentration (Figure 99).

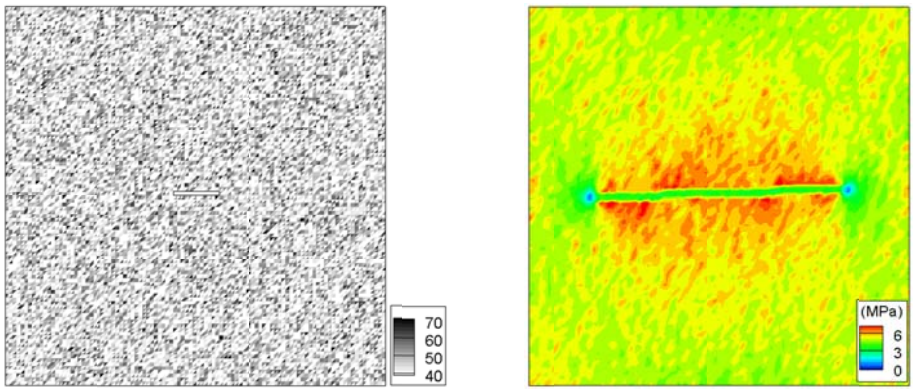

Figure 99. Heterogeneity distribution (Unit=GPa) and Pore pressure changes after fracture propagation.

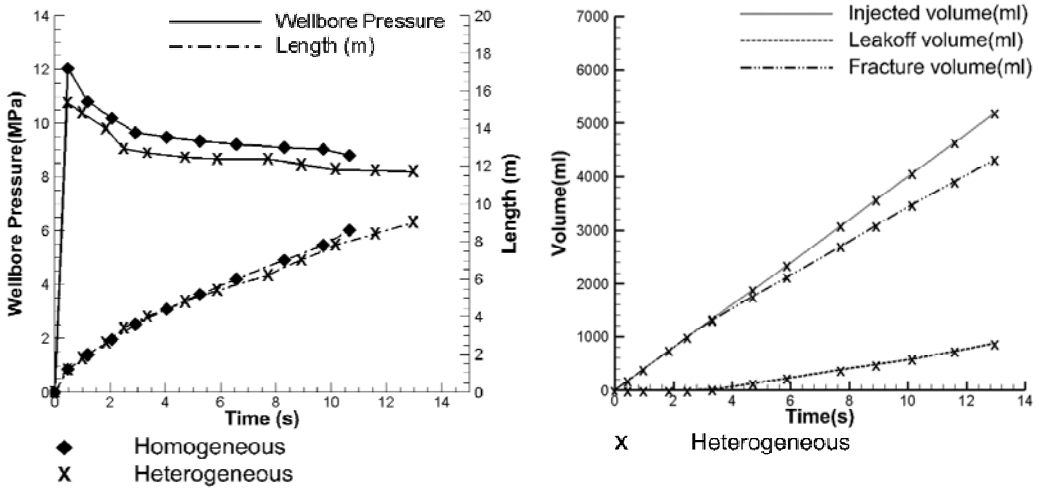

Figure 100. Comparison of wellbore pressure profile and injected fluid volume.

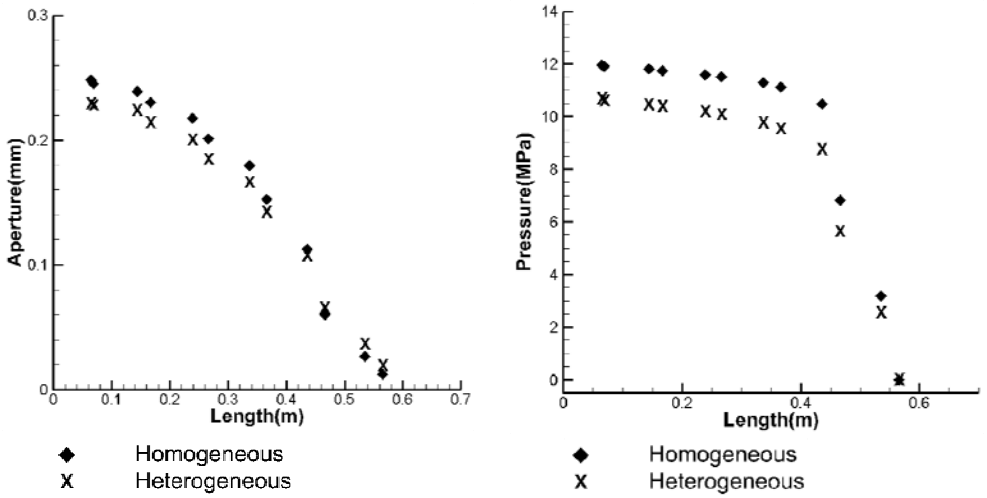

Figure 101. Comparison of aperture and fluid pressure profiles at first step (t=0.6 sec).

8.1.3 Hydraulic fracturing in highly heterogeneous reservoir

In this section, we examined the influence of the heterogeneity when the target reservoir had more heterogeneous geomechanical features. We increased the reservoir heterogeneity by modifying the Weibull parameters (m_1=1, a_1=4, m_2=1, a_2=3, m_3=1, a_3=3) (Figure 102). Based on the simulation results, when a highly heterogeneous reservoir was assumed, the fracture length propagated slowly and leakoff volume increased greatly (Figure 103). The high leakoff rate left only a small remaining fluid volume in the fracture and prevented the fluid flow from generating enough fluid pressure to create cracks. Therefore, injection efficiency also decreased and the fracture could not grow anymore. Wellbore pressure of the high-heterogenity case remained higher than the low-heterogeneity case (Figure 103) because the fracture length of the high-heterogeneity case did not increase as much as the low-heterogeneity case.

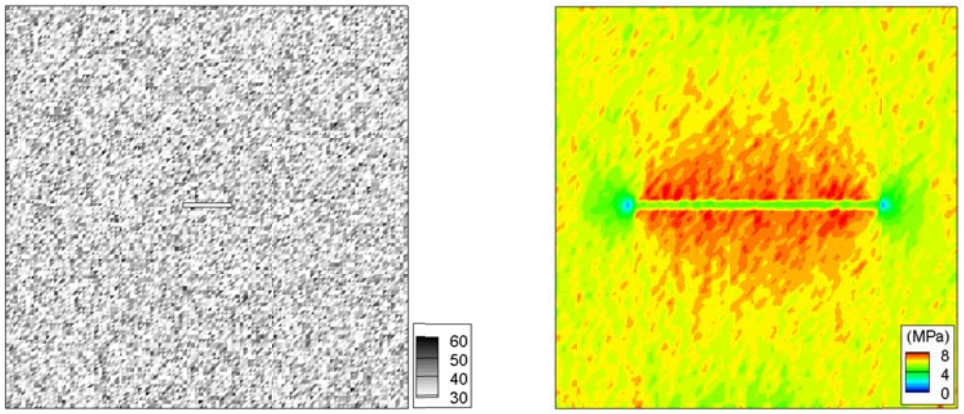

Figure 102. Heterogeneity distribution (Unit=GPa) and Pore pressure changes after fracture propagation.

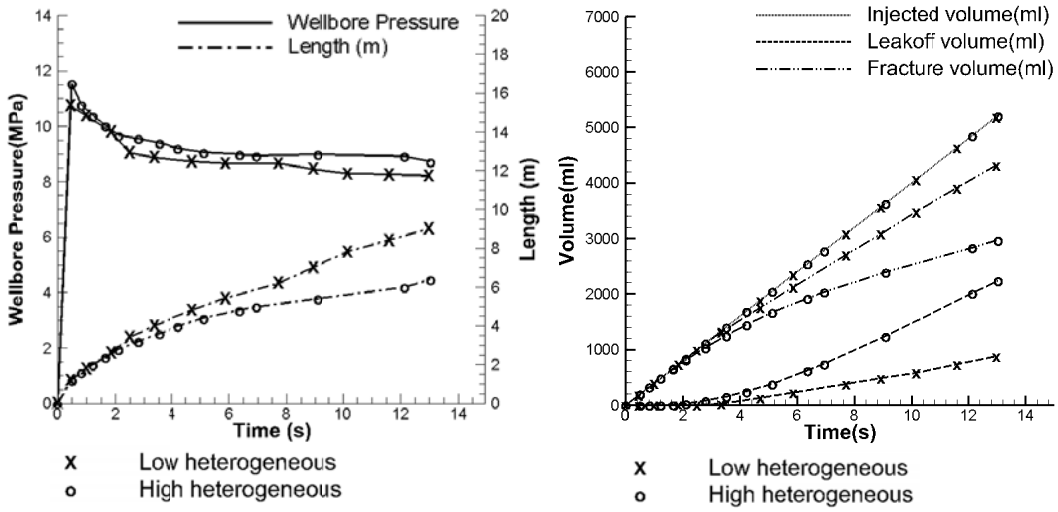

Figure 103. Comparison of wellbore pressure profile and fluid volume.

8.1.4 Hydraulic fracturing in heterogeneous reservoir with high injection

When an injection rate of fracturing fluid is increasing, faster fracture growth is expected. According to the simulation results, the treatment time decreased from 12 seconds to 4 seconds when the injection is increased from 24 L/min to 144 L/min (Figure 105). The high injection rate induced a large fluid pressure profile in the fracture, and the increased fluid pressure caused secondary fracture propagation from the primary fracture (Figure 104). The secondary fractures were initiated from crack tips of the primary facture, because concentrated tensile stresses largely exceed the tensile strength. The main trend of the fracture propagation was similar in both lower and higher injection cases, but the secondary fractures grew along with the primary fracture growth in the higher injection case (Figure 104). The creation of the multiple fractures increased the leakoff volume d twice much as the low injection case (Figure 105). In addition, breakdown pressure was as high as 14.5 MPa and the wellbore pressure quickly dropped with fracture propagation (Figure 105). The high injection rate led to large mechanical deformation (aperture profile) and high pore pressure near the fracture tips (Figure 106)).

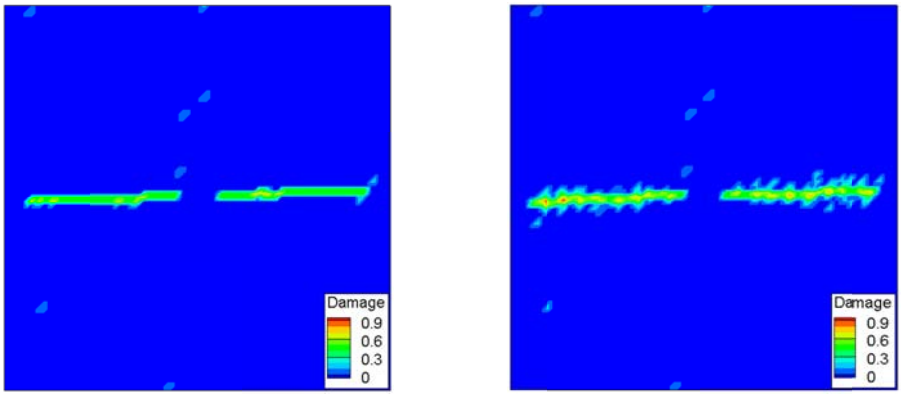

(a) q_{inj}=24L/min (b) q_{inj}=144L/min

Figure 104. Comparison of hydraulic fracture propagation at lower injection rate vs. higher injection rate.

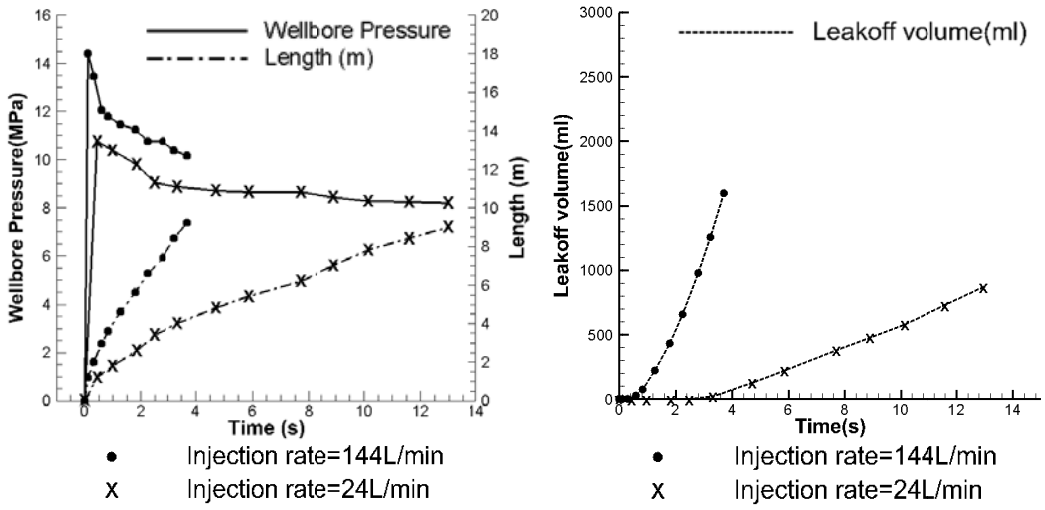

Figure 105. Comparison of wellbore pressure profile and leakoff volume change in lower injection vs. higher injection.

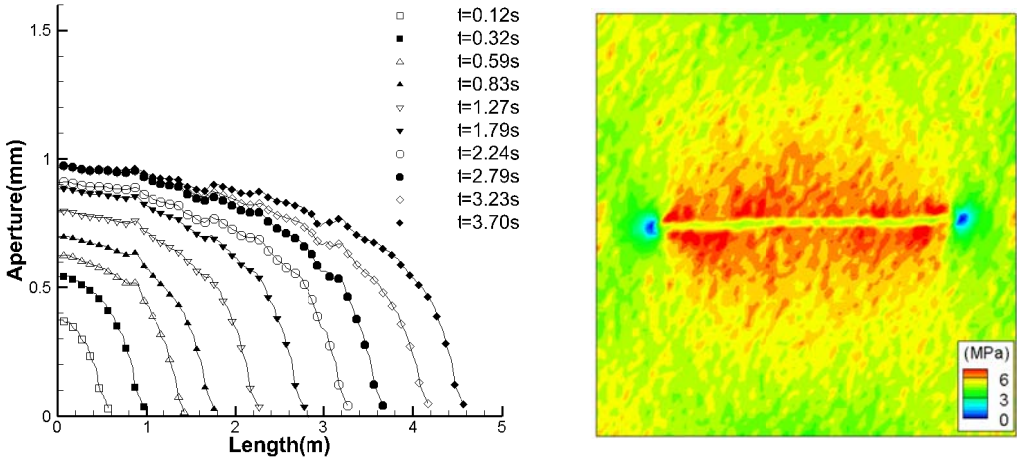

Figure 106. Aperture profile and pore pressure distribution during hydraulic fracturing of q_{inj}=144L/min.

We examined 2D hydraulic fracture propagation simulations in permeable rock and investigated the influence of the reservoir heterogeneity and the injection rate. The reservoir heterogeneity is a critical factor to determine the hydraulic fracturing strategy, because both mechanical deformation and fluid flow behavior are affected by the heterogeneity factor. Especially, high heterogeneity increases leakoff volume and reduces the injectivity of fracturing fluid. When the rock was highly heterogeneous, the injection efficiency was decreased to 0.57 Table 18. When the injection rate was increased by 6 times, the injection efficiency decreased only from 0.832 to 0.82. So that means the injection efficiency is a function of the heterogeneity factor and not a function of the injection rate. Based on the simulation results, the hydraulic fracturing strategy should carefully determine if the reservoir is highly heterogeneous.

Table 18. Comparison of fluid volume and injection efficiency.

	Time (s)	Injected volume (ml)	Fracture volume (ml)	Leakoff volume (ml)	Injection efficiency, ε_{inj}
Homogeneous	10.67	4266.39	4258.413	7.977	0.998
Low Hetero.	12.97	5189.38	4316.84	872.54	0.832
High Hetero.	13.04	5214.275	2970.55	2243.73	0.57
High injection	3.70	8878.55	7282.33	1596.225	0.82

where the injection efficiency is defined as: $\varepsilon_{\text{inj}} = \frac{V_f}{V_i} = \frac{V_i - V_l}{V_i}$.

8.2 3D Modeling of Hydraulic Fracturing Experiments

Hydraulic fracturing has continued to become more important for the oil and gas industry. Optimization of the hydraulic fracturing treatment is necessary to save developing cost. Lab experiments and numerical hydraulic fracturing models give valuable information for the optimization procedure. Laboratory-scaled hydraulic fracturing experiments have frequently been used previously. Many researchers have conducted laboratory-scaled hydraulic fracturing tests (Daneshy, 1974; Lamont and Jessen, 1963; Teufel and Clark, 1984; Zoback et al., 1977). These laboratory experiments are useful to examine an insight into the process of hydraulic fracturing treatment, because they provide guidelines for evaluating laboratory environments and the influences of different factors (e.g., injection schedule, fracturing fluid, and confining pressures) that can be monitored in the hydraulic fracturing treatment. Compared with field tests, laboratory tests can reduce developing cost significantly. Laboratory tests are also used to validate numerical hydraulic fracturing models (Bai et al., 2006). This chapter compares the fully 3D hydraulic fracturing model with the laboratory hydraulic fracturing tests of Niobrara shale that was performed by TerraTek (Ghassemi and Suárez-Rivera, 2012). The numerical simulation provides a sophisticated understanding of the complex process of hydraulic fracturing. We investigated the hydraulic fracturing simulation in both homogeneous and heterogeneous blocks.

8.2.1 Large-scale laboratory hydraulic fracturing test

The laboratory scale hydraulic fracturing test was performed in TerraTek's large block multiaxial stress frame. Using the multiaxial stress frame (Figure 107), the in-situ effective stress conditions were

generated in three principal directions by high pressure flatjacks. The tested Niobrara shale (Figure 107) was obtained from a quarry located in Colorado and prepared for 27.25-in. × 27.25-in. × 32-in. dimensions of the block. The wellbore was drilled in the middle of the testing block. Vertical completion with a cased borehole was placed, and a 7-in. long openhole section located was 15 to 22-in. from the top face of the block. Two slots of 12-mm penetration were sandblasted along the length of the openhole section to facilitate fracture initiation and breakdown. 37 acoustic sensors were installed on the faces of the block to evaluate fracture geometry and propagation during the hydraulic fracturing test. Glycerol, which has high viscosity of 1,000 cp, was used for the fracturing fluid, and a constant injection rate of 1,000 *mL*/min was pumped into the block sample subjected to anisotropic in-situ stresses.

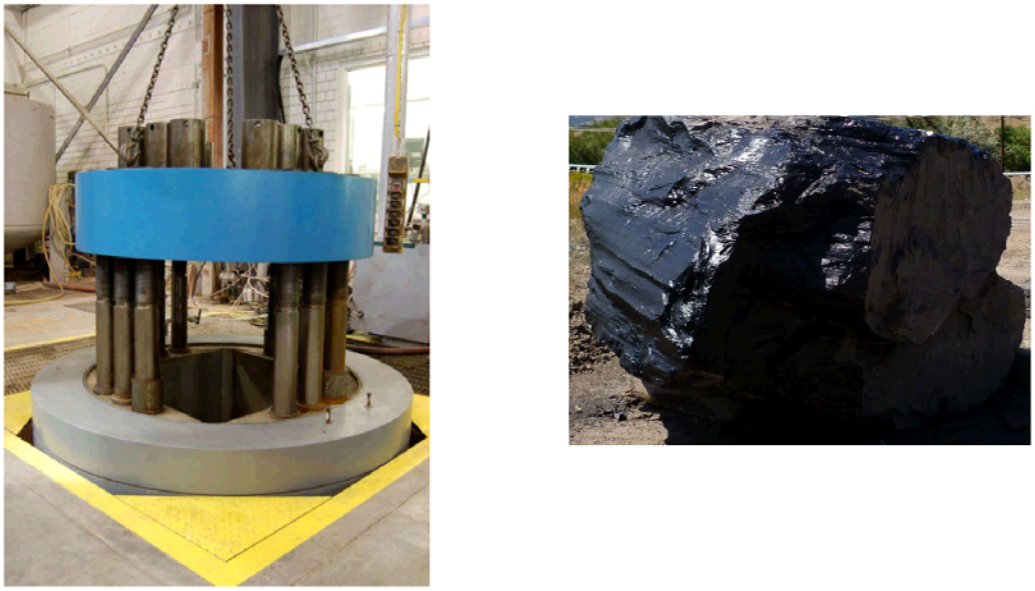

Figure 107. TerraTek's large multi-axial stress frame and Niobrara boulder acquired from the quarry in Colorado (Ghassemi and Suárez-Rivera, 2012).

8.2.2 Numerical modeling for laboratory-scaled hydraulic fracturing test

As we explained earlier, the hydraulic fracturing process was modeled using the fluid-driven fracturing problem. So rock deformation was modeled for poroelastic solids, and fracture propagation was modeled by a quasi-static assumption. The fluid flow in the propagating fracture was solved by the lubrication equation. In this 3D hydraulic fracturing simulation, the fracture propagation process is more simplified because of complexity of numerical description of fracture tip contour of the non-planar fracture growth. It is assumed that the main hydraulic fracture plane was propagated constantly with given crack increment in the direction of the maximum far-field stress. That is, the crack increment law and an angle of fracture direction are not considered in the 3D simulation. In the 3D hydraulic fracturing simulation, once the fracturing tip contour met with the maximum tensile criterion, the fracture plane is extended with the given crack increment at every time step.

The laboratory-scale large block was modeled using a 3D finite-element model and meshed using 26,400 tetrahedron elements (Figure 108). Since quasi-static planar fracture propagation is assumed, our interest zone is the middle zone of the numerical domain. So, finer mesh is applied in the middle zone to capture

the fracture plane propagation. The dimensions of the block were modeled as 1-m × 1.2-m × 1-m. We assumed a center-located pre-existing fracture plane of radius of 0.1-m for an open-hole perforation in the experiment. In the numerical domain (Figure 108(b)), elements overlapped with the initial fracture plane geometry (r=0.1m) are treated as crack elements. The crack elements are used to compute equivalent nodal forces by EPM. For quasi-static fracture propagation modeling, the crack increment is given as Δr=0.05m. A fracturing fluid injection rate of 1,000 mL/min was applied as a point-source boundary condition at the center of the propagation fracture plane. For in-situ stress conditions, the vertical stress was applied in the y-direction and the maximum and minimum in-situ stresses were applied in the x- and z-directions respectively (Table 19). Fluid properties of glycerin appear in Table 20. Since the material properties of the Niobrara shale were not given, we approximated the material properties from Colorado shale test data performed by (Regehr, 2012). Approximate material properties of the Niobrara shale are shown in Table 21 Assumed Mohr-Coulomb parameters and tensile strength also appear in Table 19.

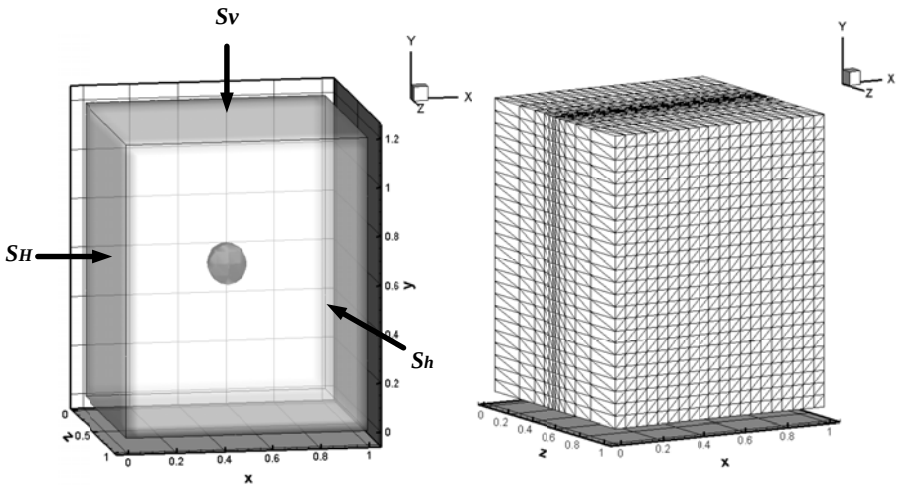

(a) Boundary conditions (b) Finite element mesh

Figure 108. 3D numerical model and meshed finite element model for laboratory-scaled hydraulic fracturing test.

Table 19. Boundary conditions and input parameters.

Inputs	Values
Vertical in-situ stress, S_v (MPa)	31(4,500 psi)
Maximum in-situ stress, S_H (Mpa)	20.7(3,000 psi)
Minimum in-situ stress, S_h (MPa)	6.9 (1000 psi)
Injection rate, q_{inj} (mL/min)	1,000
Mohr-Coulomb parameter, ϕ_f	10
Cohesion, c_F (MPa)	30
Tensile strength, σ_T (MPa)	7
Number of elements	26,400

Number of nodes	6,300

Table 20. Fluid properties for Glycerin.

Inputs	Values
Fluid mass density, ρ_f (kg/m3)	1261
Fluid viscosity, μ_f (Pa·s)	1 (1,000 cp)
Bulk modulus for fluid	4.35e9

Table 21. Rock properties of Niobrara Shale.

Inputs	Values
Young's Modulus, E (GPa)	3.7
Shear Modulus, G (GPa)	1.42
Drained Poisson ratio, υ	0.3
Undrained Poisson ratio, υ_u	0.46
Biot's coefficient, α	0.866
Skempton's coefficient, B	0.949
Permeability, k (md)	0.01
Porosity, ϕ	0.1

8.2.3 Hydraulic fracturing in homogeneous block

In a homogeneous block, only major planar fracture growth propagated (Figure 113). With the planar fracture growth, fluid pressure distributions changed with time. Figure 113 (a to h) captures continuous changes of the fracture plane and the fluid pressure distribution. In Figure 110, the fluid pressure profile changed quickly with time and the fracture aperture opened gradually. As the fracture plane grew, the fluid pressure profile stabilized.

A viscous fracturing fluid is inducing a steep rise of wellbore pressure and eventually leads the initiation of a fracture. Wellbore pressure profile (Figure 109) quickly dropped with the fracture growth. Breakdown pressure in this simulation was 30.12 MPa (4368.55 psi) and wellbore pressure stabilized around 10.6 MPa (1537.4 psi). Since the block was assumed as homogeneous, the leakoff volume was small (48 ml). In Figure 111 112, the compressive stress increased the pore pressure near the fracture plane. Pore pressures near fracture tips were nearly zero due to the opening mode of fracture. Maximum opening stresses were concentrated in this region.

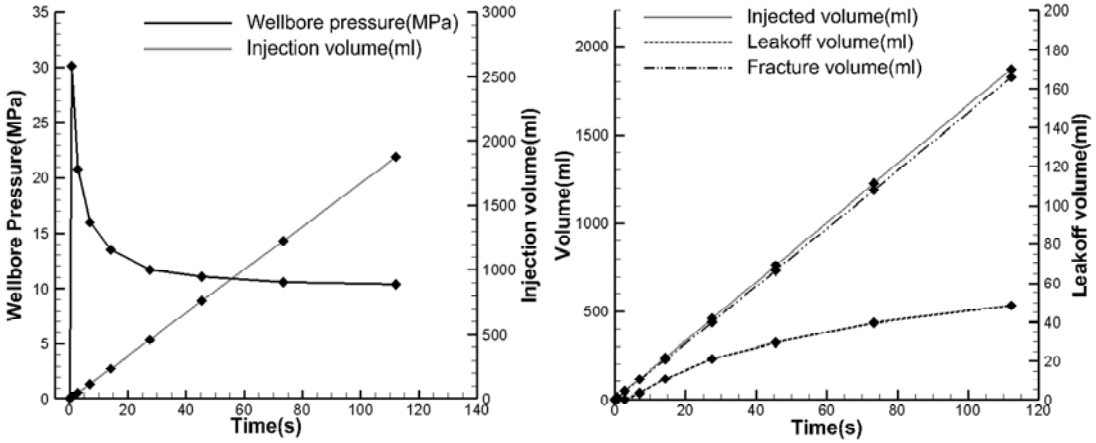

Figure 109. Wellbore pressure profile and injected fluid volume.

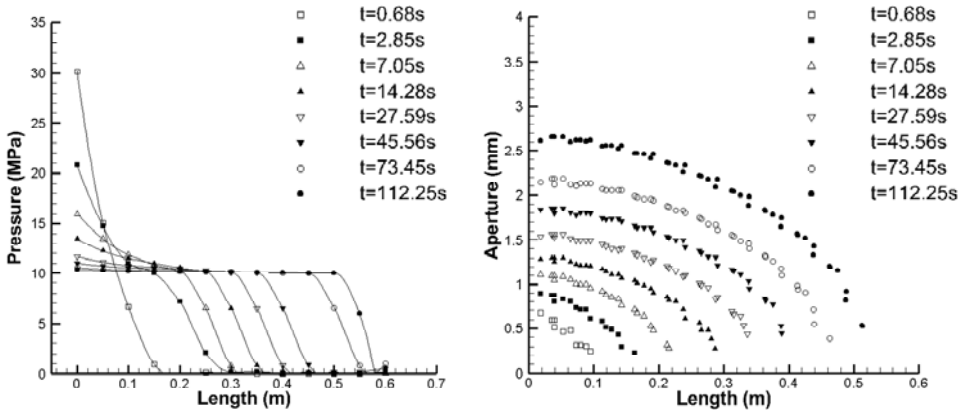

Figure 110. Fluid pressure change and aperture change during hydraulic fracturing.

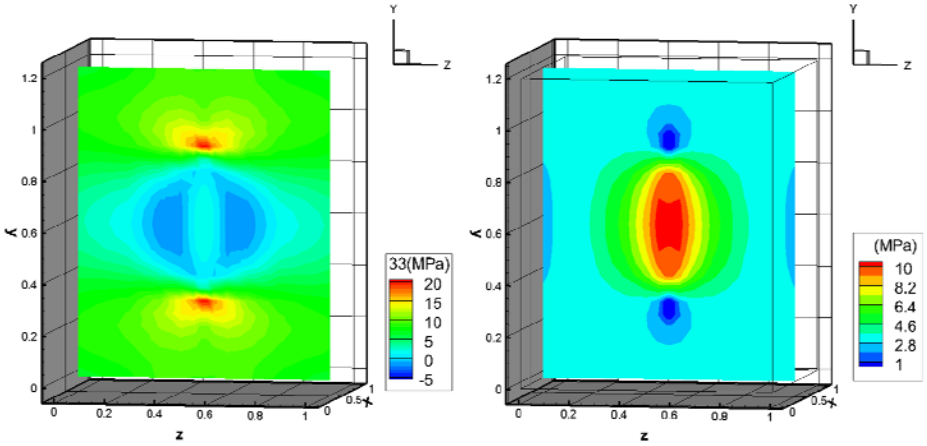

Figure 111. σ_{zz} distribution and pore pressure distribution at t=14.28 seconds in homogenous block.

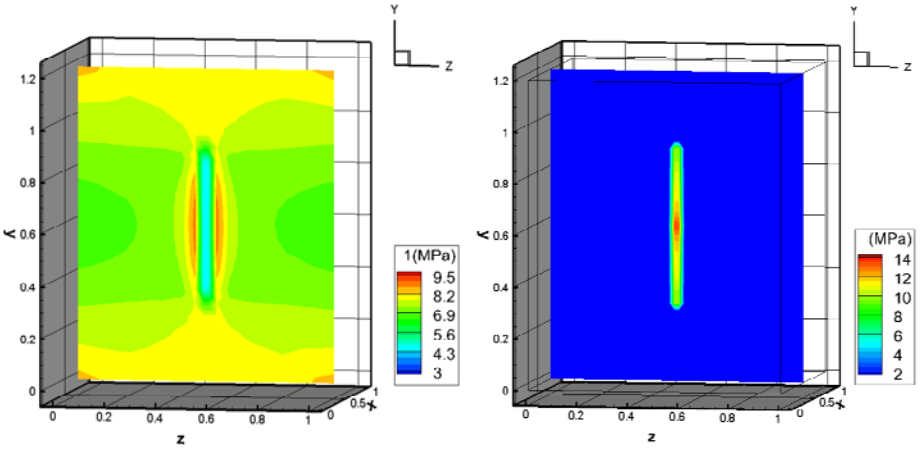

Figure 112. Maximum compressive stress and fluid pressure distribution (from center cut-view) at t=14.28 seconds in homogeneous block.

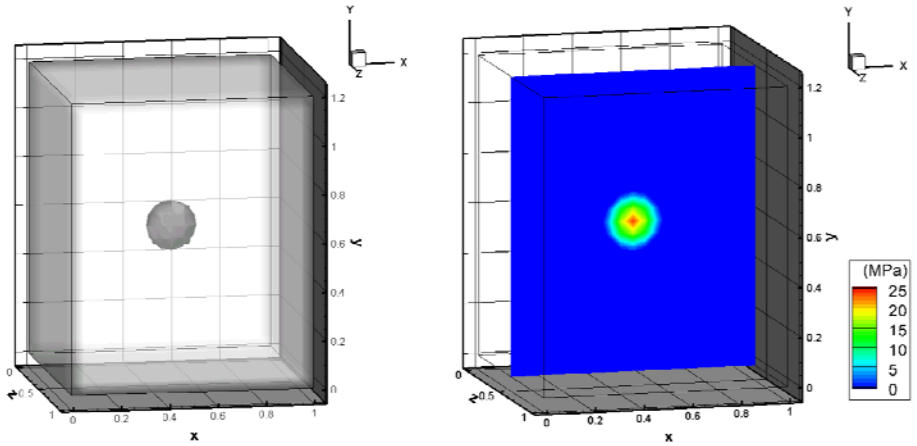

(a) t=0.68 seconds

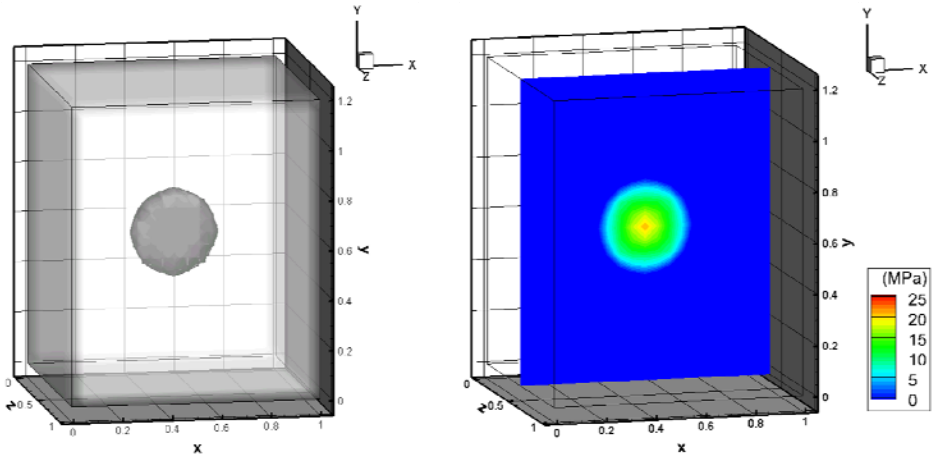

(b) t=2.85 seconds

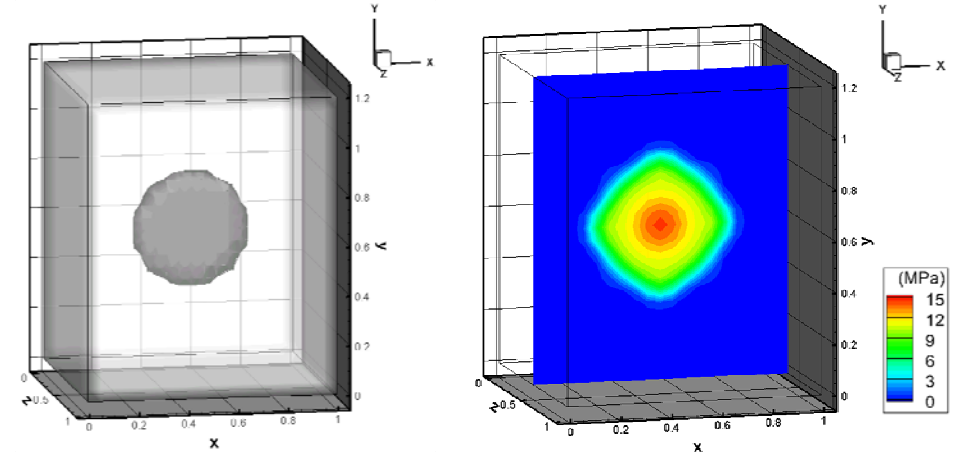

(c) t=7.05 seconds

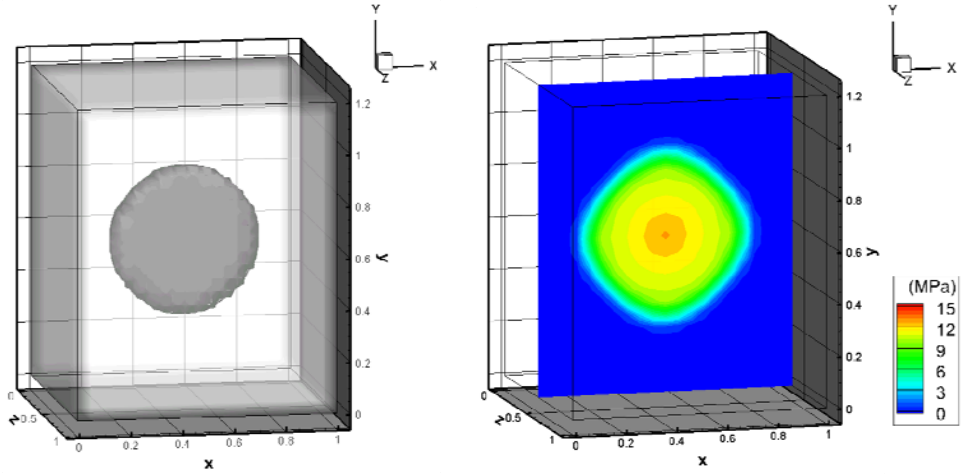

(d) t=14.28 seconds

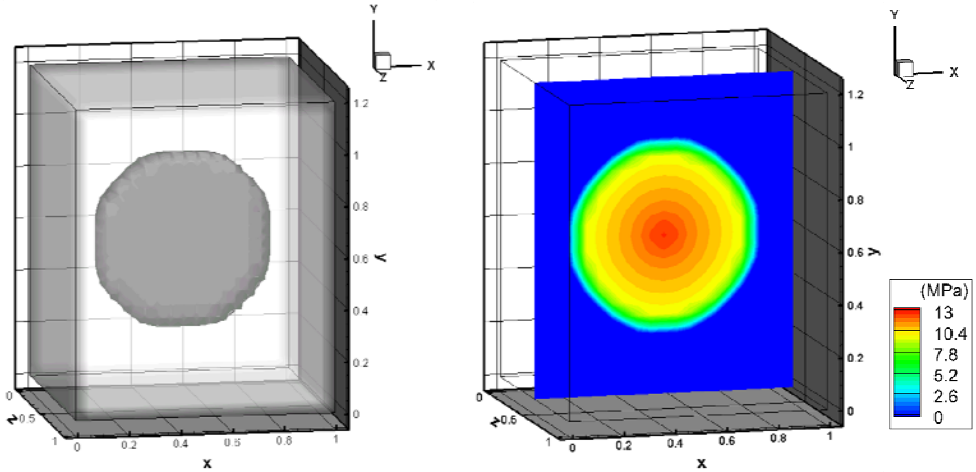

(e) t=27.59 seconds

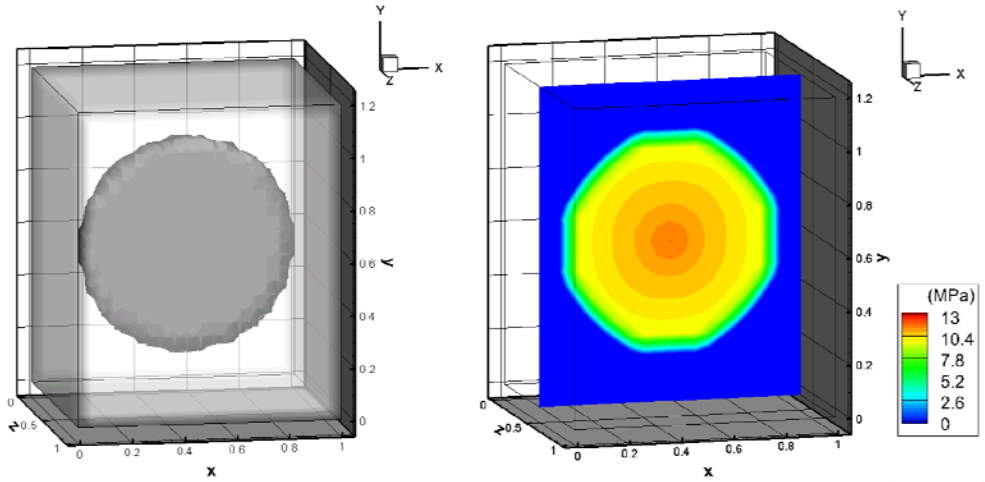

(f) t=45.56 seconds

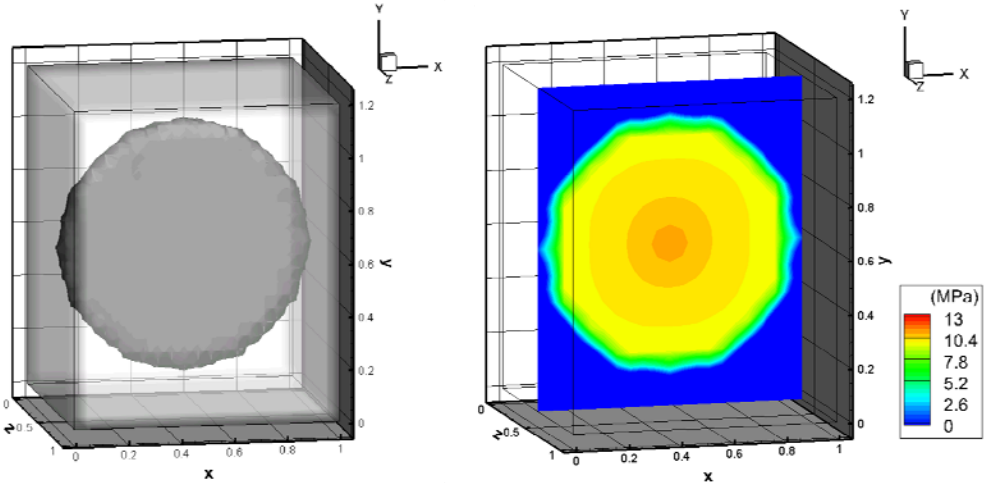

(g) t=73.45 seconds

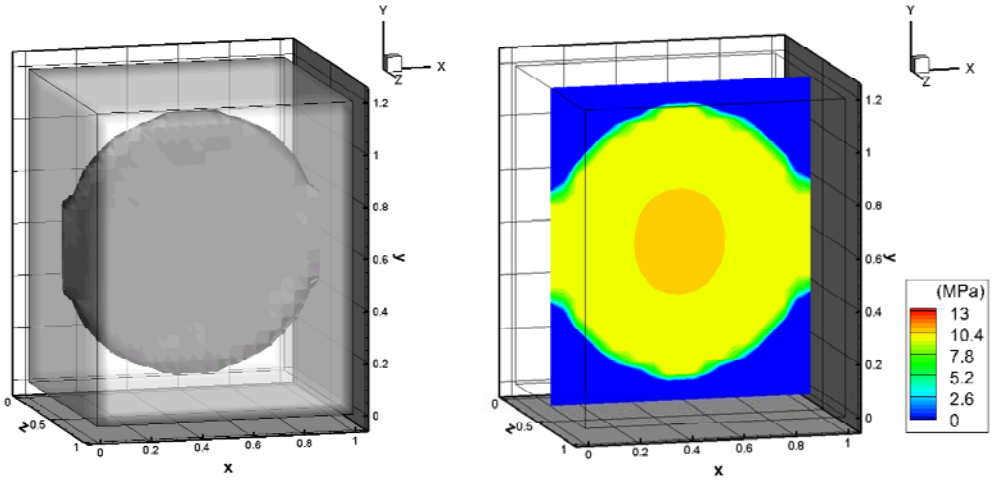

(h) t=112.25 seconds

Figure 113. Fracture plane growth and fluid pressure distribution with time.

8.2.4 Hydraulic fracturing in heterogeneous block

Because the real testing block is characterized by heterogeneous fabric, we applied the heterogeneities to the numerical block using random variables generated by the Weibull distribution function. There are no initially assigned cracks in the numerical block. Generated random variables applied to stiffness, permeability, and strength of each element for representation of the block heterogeneity. Selected Weibull parameters are shown in Table 22. The heterogeneity of the block is described in Figure 117. During hydraulic fracturing in the heterogeneous block, lots of failures were detected with the main planar fracture growth (Figure 117). The secondary failures are induced by the hydraulic pressurization in the main fracture plane. However, the spotted failures are not directly connected with the main fracture plane, so that the secondary failures could not be opened by fluid pressure. The spotted failures have been increasing with time and fracture plane growth. Figure 118 captured failures in orthogonal direction of the major fracture plane are captured. The lateral growth of the fracture is also observed in experiments.

The wellbore pressure profile (Figure 115)) was similar to the homogeneous case. Breakdown pressure in this simulation was slight lower at 28.75 MPa (4169.84 psi) and wellbore pressure is stabilized around 10.6 MPa (1537.4 psi). Because of effect of the heterogeneity, leakoff volume is increasing to 385 ml (Figure 115). In Figure (116), pore pressures near the fracture plane are high due to the compressive forces of fluid pressurization. The pore pressure is more widely distributed than the homogeneous case and the heterogeneous pore pressure increase could affect failures, because increased pore pressure moves the failure envelope left to right. The pore pressure effect triggered tensile or shear failures are. In addition, because the maximum opening stresses concentrated on the fracturing tip region, pore pressures near the fracturing tip region are nearly zero by the fracture opening.

Table 22. Weibull parameters for Block heterogeneity.

Inputs	Values
Distribution for stiffness	m_1=1, a_1=5
Distribution for permeability	m_2=1.1, a_2=10
Distribution for strength	m_3=1, a_3=6

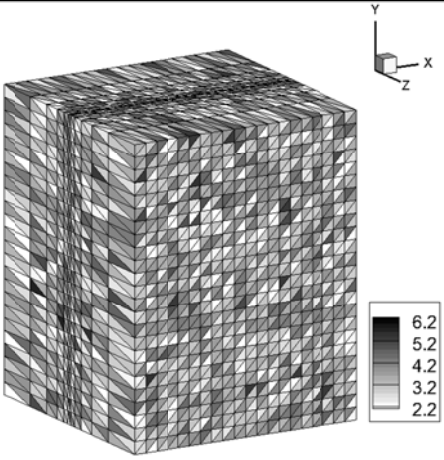

Figure 114. Representation of stiffness heterogeneity (unit=GPa).

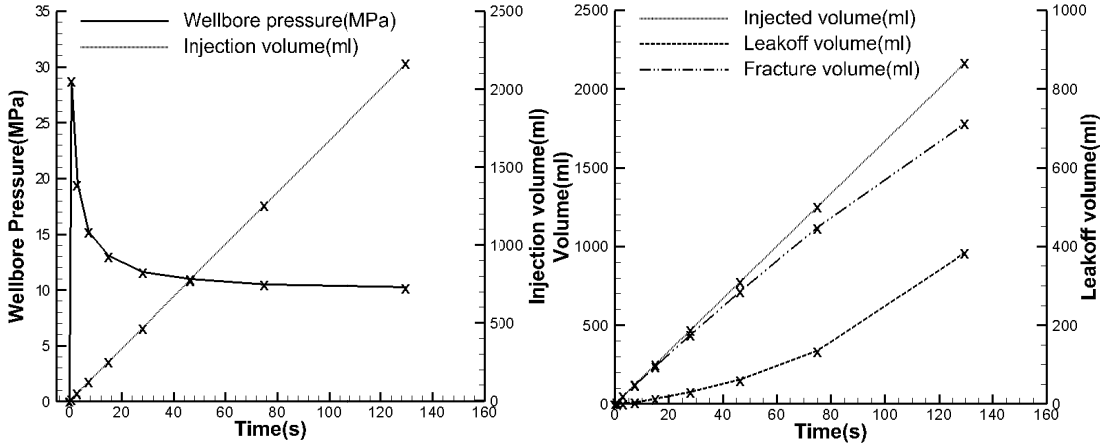

Figure 115. Wellbore pressure profile and injected fluid volume.

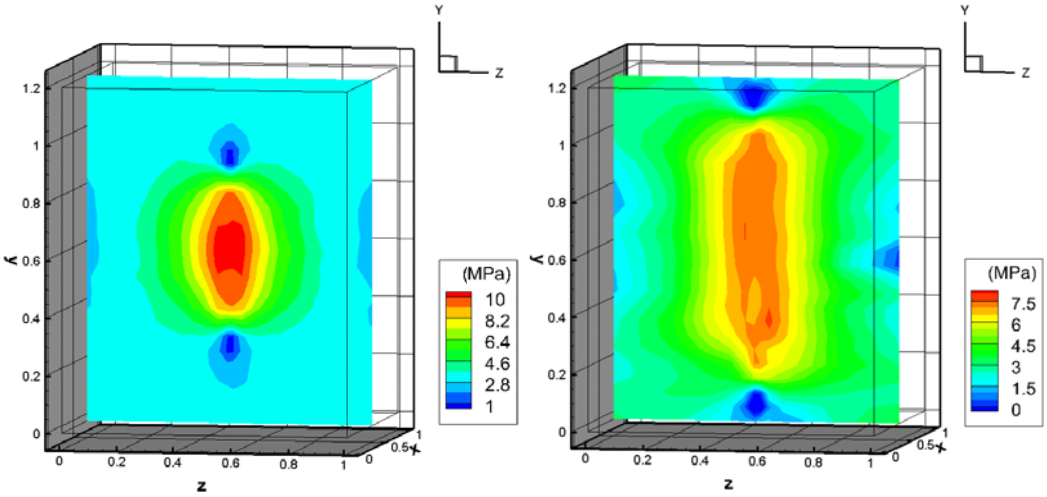

Figure 116. Pore pressure distribution at t=15.07 seconds and t=75.15 seconds in heterogeneous block.

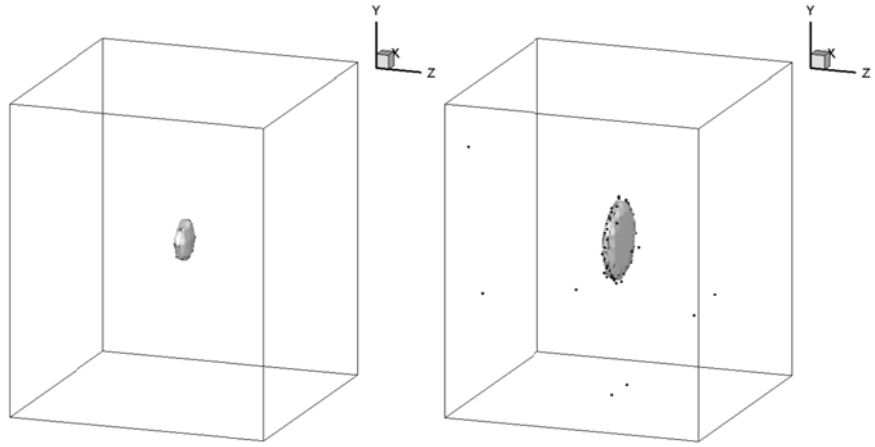

(a) t=0.73 seconds (b) t=3.02 seconds

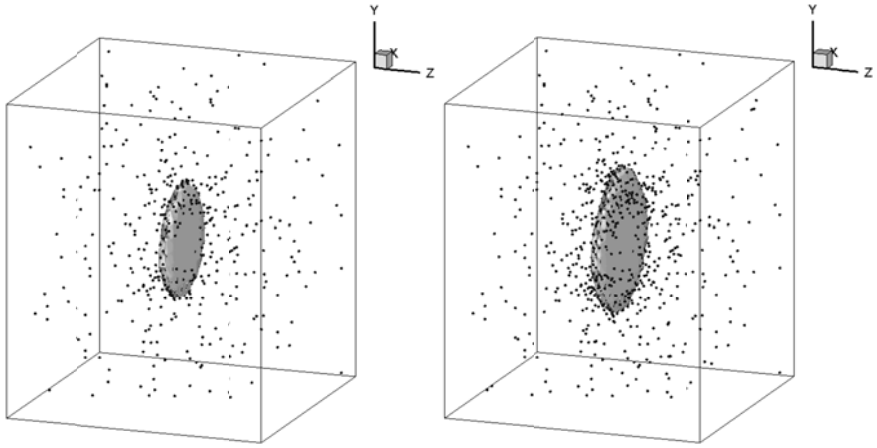

(c) t=7.48 seconds (d) t=15.07 seconds

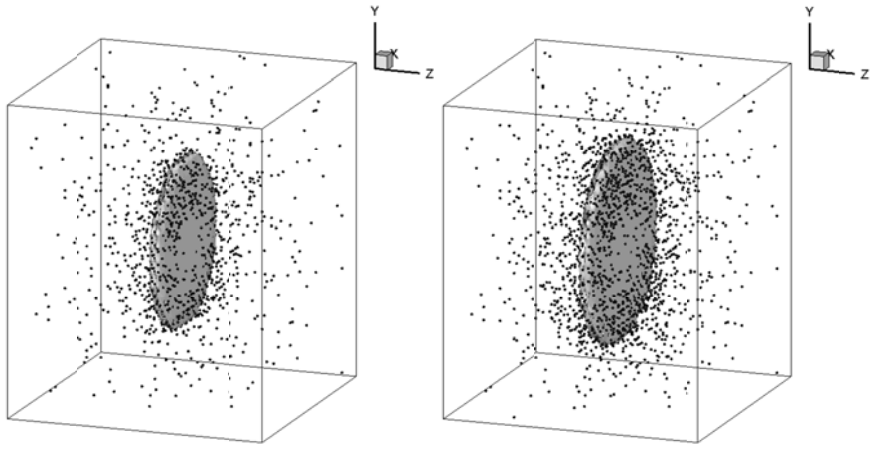

(e) t=28.10 seconds (f) t=46.48 seconds

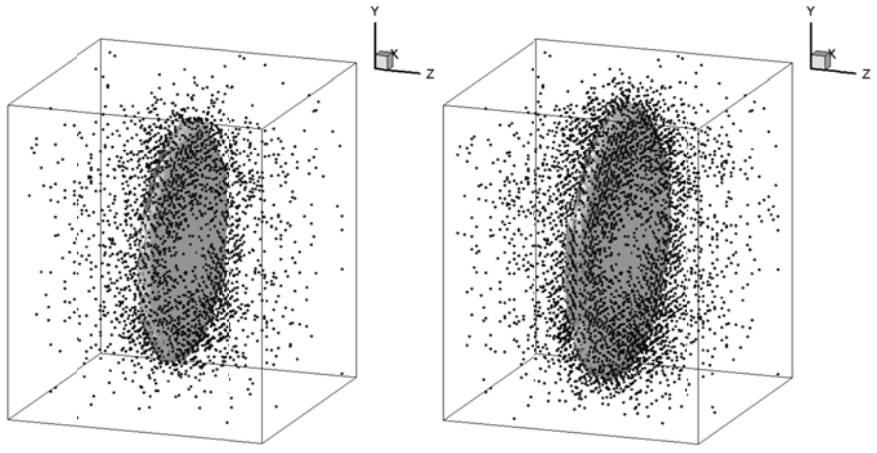

(g) t=75.15 seconds (h) t=129.8 seconds

Figure 117. Fracture plane growth and failure events in heterogeneous block.

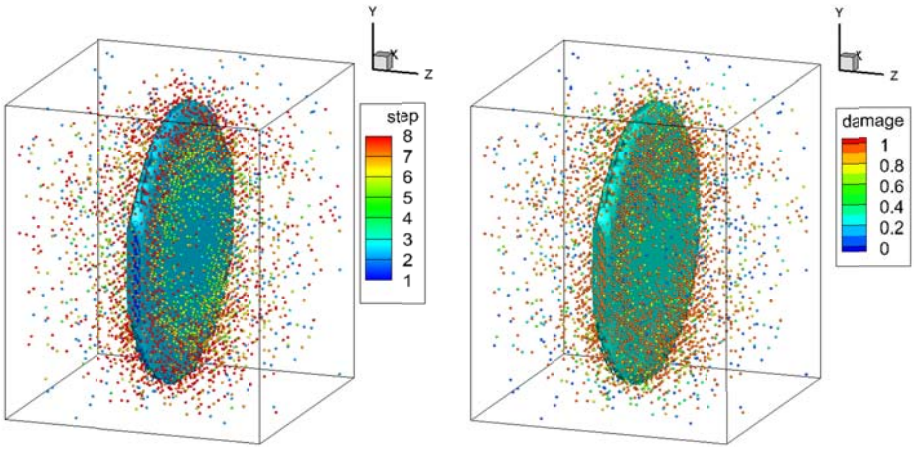

(a) Colored by step (b) Colored by damage

Figure 118. Failure events colored by step and damage at t=129.8 seconds.

In Figure 117 and 118, the main fracture plane is represented by iso-surface, while the multiple and spotted failures are indicated by points. The spotted failures have been detected by damage events during hydraulic fracturing simulation. In Figure 117(a), the initial fracture plane is pressurized by fracturing fluid injection and after a short time (t=0.73 seconds), wellbore pressure reaches breakdown pressure (P_b= 28.75MPa) and the fracture plane propagates toward the maximum in-situ stress direction. We only observe a few failures in the heterogeneous block until t=3.02 seconds and then the multiple and spotted failures are detected after t=7.82 seconds (Figure 117 (c)). After t=28.10 seconds, the multiple failures are concentrated on near the primary fracture plane toward orthogonal direction of the primary fracture plane (Figure 117 (e)-(h)). These orthogonal failures are an indication of branching of the hydraulic fracture propagation. In Figure 117 (g)-(h), the fracture plane has almost reached the boundary of the block. The fracture plane is highly opened and leakoff volumes are also increasing (Figure 115).

8.3.4 Comparison of numerical and experimental results

In Figure 119, we compared the wellbore pressure profile of the numerical simulation with the experimental results. According to the comparison, the breakdown pressure of the homogeneous block is slightly higher than in the experiments, while the breakdown pressure of the heterogeneous block is almost similar with the experiments. The simulation time of the homogeneous block case is shorter than in the experiments and the heterogeneous block (Table 23). A major difference between the wellbore pressure profile of the numerical simulation and the experiments appears after breakdown pressure. Wellbore pressure of the experiment is shown to drop more quickly than the numerical simulation. This is because we assumed the fracture propagation would grow in a quasi-static manner. However, practically speaking, the fracture grew dynamically and the speed of growth was faster than our simulation.

Table 23. Comparison of experimental results and numerical simulations.

	Breakdown pressure	Stabilized pressure	Treatment time (s)
Experimental results (by TerraTek)	28.97 MPa (4202 psi)	10.93 MPa (1585 psi)	130
Num. Homogeneous block	30.12 MPa (4368.55 psi)	10.6 MPa (1537.4 psi)	112.25
Num. Heterogeneous block	28.75 MPa (4169.84 psi)	10.6 MPa (1537.4 psi)	129.8

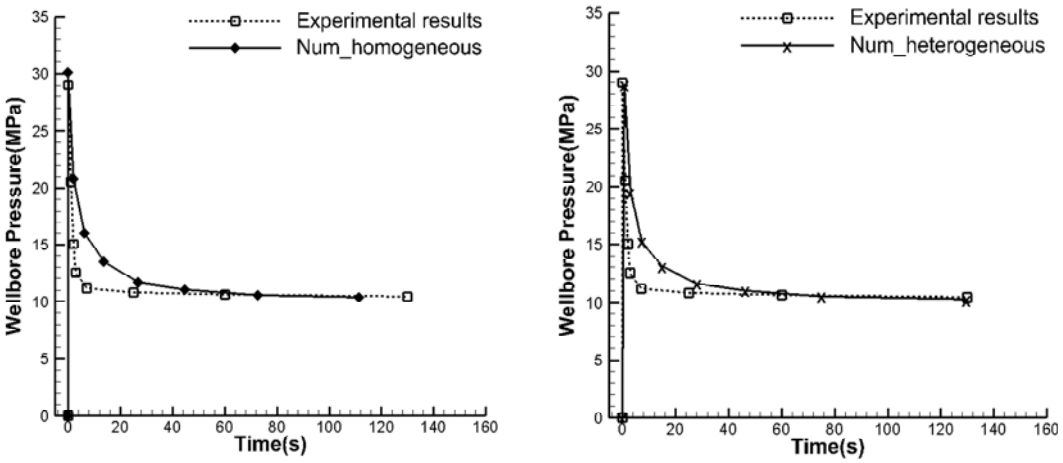

Figure 119. Comparison of wellbore pressure profile with experimental results.

8.3.5 Sensitivity of numerical model by material property

In Figure 121, we investigated the sensitivity of the 3D hydraulic fracturing simulation against Young's modulus. Since mechanical deformation of a rock is dependent on the Young's modulus of the rock, hydraulic fracturing behaviors are also influenced by the change of the mechanical deformation. When the rock was softer (E=2.7GPa), less breakdown pressure was obtained and more simulation time was required, because the fractures opened wider in the soft rock. In contrast, when the rock was harder (E=4.5GPa), breakdown pressure was higher and shorter simulation time was required, because the fractures opened less in the hard rock.

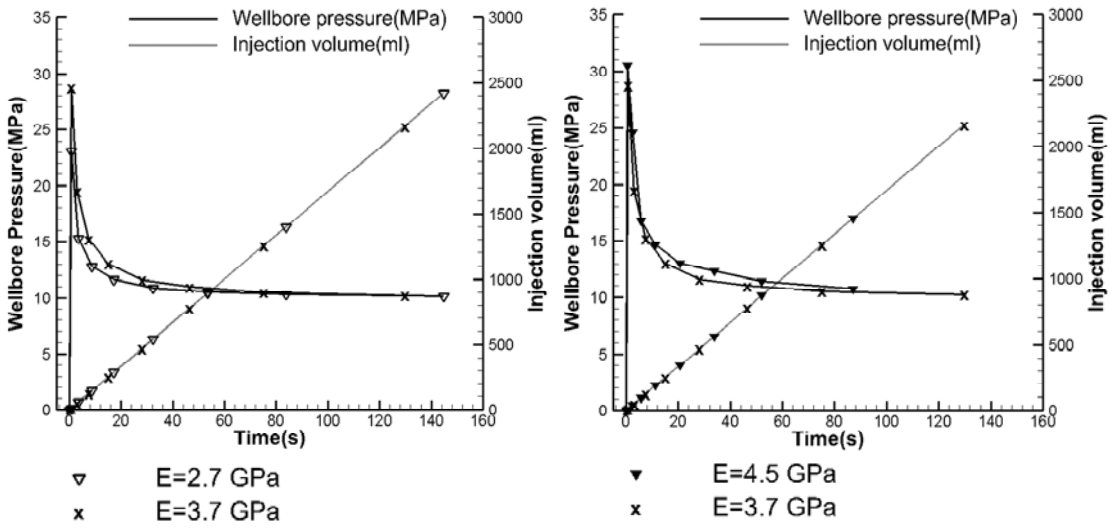

Figure 121. Comparison of wellbore pressure profile and injection volume by Young's modulus changes.

Viscosity of fracturing fluid*:* In the hydraulic fracturing stimulation, choice of fracturing fluid is another important issue, because fracture opening (i.e. aperture) is highly affected by viscosity of the fracturing fluid. Generally, high viscosity fluid opens more, while low viscosity fluid opens less. Because the high viscosity fluid induces strong tensile force, higher breakdown pressure is observed than the low viscosity fluid. In this section, influence of the fluid viscosity on the hydraulic fracturing was investigated.

Cases of μ=1000cp vs. μ=100cp:

Previously we used glycerin for the fracturing fluid, which has high fluid viscosity (μ=1000cp). Lower viscosity fluid (μ=100cp) was used instead of the glycerin. When same amount of injection rate (q_{inj}=1L/min) was used, low breakdown pressure (P_b=13MPa) was observed and the fracture plane did not propagated since the low injection rate could not induce enough tensile forces at fracturing tips (Figure 121). So, when the injection rate was changed to q_{inj}=10L/min, higher breakdown pressure (P_b=28MPa) was obeserved and the fracture plane was fully propagated (Figure 121). When the low viscosity result (μ=100cp, q_{inj}=10L/min) was compared with the high viscosity result (μ=1000cp, q_{inj}=1L/min) (Figure 121), the low viscosity case required shorter treatment time than the high viscosity case because the injection rate of the low viscosity case is ten times higher than the high viscosity case. Because of the high injection rate of the low vicosity case, amount of injected fracturing fluid (V_f=2,500mL) is higher than the high viscosity case (V_f=1,900mL).

Consequently, when the lower viscosity fluid is used, higher injection rate is required to create hydraulic fracturing. Unless the injection rate is increased, the fracture plane could not be extended. Hence, high pumping equipment is required when the fracturing fluid has low viscosity property.

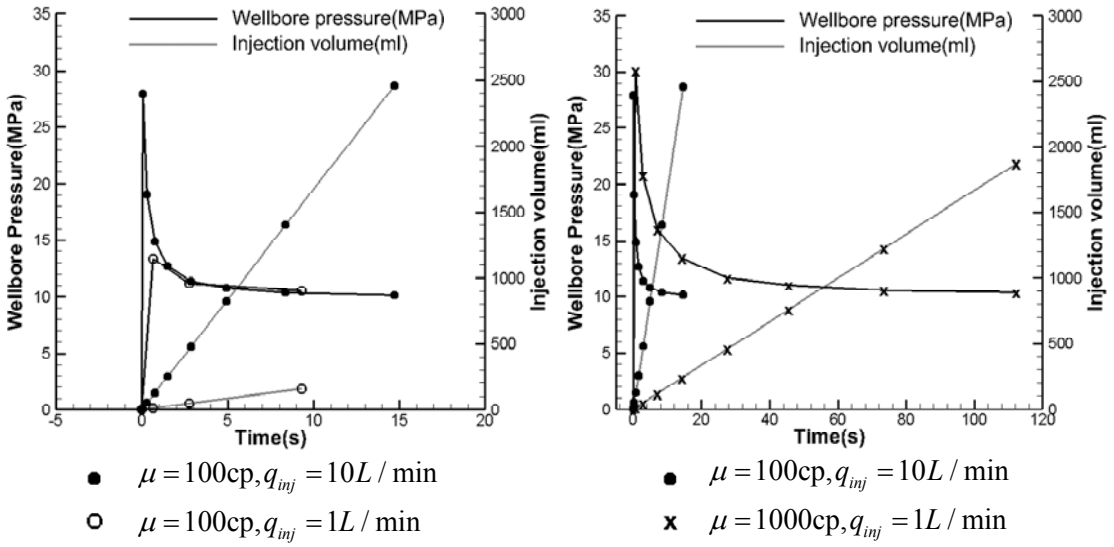

Figure 121. Comparison of wellbore pressure profile and injection volume by fracture fluid viscosity and injection rate.

In this section, development a fully 3D hydraulic fracturing model for the large-scale laboratory hydraulic fracturing test was presented. The model was successfully validated using a lab-scale experiment performed by TerraTek. Planar fracture propagation was observed in both numerical simulations and experiment, as expected. In the case of the heterogeneous block test, both main planar fracture growth and widely distributed micro-fractures were observed. The greatest difficulty of the 3D hydraulic fracturing model is tracking the crack tips, because the crack tip is no longer 2D and the 3D variation of the crack tips makes them difficult to identify. In our 3D hydraulic fracturing simulation, we assumed the main planar fracture plane was propagating toward the maximum in-situ stress direction. However, the fracture could turn or intersect natural fractures. Capturing these complex fracture interactions would require further development of the presented 3D model.

9. Three-dimensional (3D) Thermal Fracture Propagation

In geothermal reservoir development, thermal stresses arise from conductive and convective heat transfer. These stresses become important for long injection times and may result in thermal fracturing (Min and Ghassemi, 2011). Basically, three mechanisms of heat transferring—conduction, convection and radiation—could be acting on the porous rock. Conduction is transferring heat through solid material from high temperatures to low temperatures. Convection is a process of heat transfer by a flowing fluid. Radiation is a heat transfer process of electromagnetic waves moving through space, so there is negligible radiation effect through the porous rock, and usually it is not considered as an important heat transfer mechanism (Pratt, 1982). Among these three heat transfer mechanisms, heat conduction is a dominant heat transfer mechanism in porous rock (Settari, 1989). Therefore, in enhanced geothermal system (EGS) design, thermally induced stresses might be used to create reservoir permeability. When cold water was injected into the geothermal reservoir, the reservoir rock gradually lost its heat and the rock shrank due to the cooling process. Eventually, the thermally induced stresses nucleate fractures when the strain energy

from the thermal load is sufficient to create initial cracks in an intact rock mass (Tarasovs and Ghassemi, 2010). The secondary thermally induced fractures initiate perpendicular to the preexisting major fracture (Tester et al., 1989), and the creation of thermally induced fractures could provide larger contact area by increasing fracture permeability near the preexisting fracture networks, increasing injectivity and productivity of the geothermal reservoir. Especially, serial processes of cooling and heating in geothermal reservoirs could enhance reservoir permeability due to the secondary thermal fracture growth (Min and Ghassemi, 2011). We investigated the basic fracture mechanism of the thermally induced fracture growth and the role of the heterogeneity in a geothermal reservoir. The thermal stresses were calculated using the coupled thermo-hydro-mechanical (THM) analysis, and their influence on crack propagation during reservoir stimulation was simulated using numerical simulation.

The size of the section of interest is 150-m × 100-m × 80-m (Figure 122) and the upper and lower zone have 20 m and 75G Pa each, while the zone of interest is 40 m thick and has a variable modulus, between 45 and ~ 55 GPa (figure 123). In the center of the zone, a preexisting fracture is assumed, and its surface is considered cooling. The closed fractured surface is simplified as an elliptical surface as in a hydraulic fracture. In the thermal coupling part, conductive heat transfer is considered between the rock matrix and the cooled fracture. In addition, the boundary conditions of the numerical model are simplified; a zero pore-pressure boundary condition is applied to top and bottom surfaces of the model. Table 24 shows the statistically generated heterogeneities applied to the zone of interest in the geothermal reservoir. The randomly generated variables are applied to matrical stiffness, matrial strength, and permeability. Hydraulic, thermo-physical, and mechanical properties for simulation domain are described in Table 24.

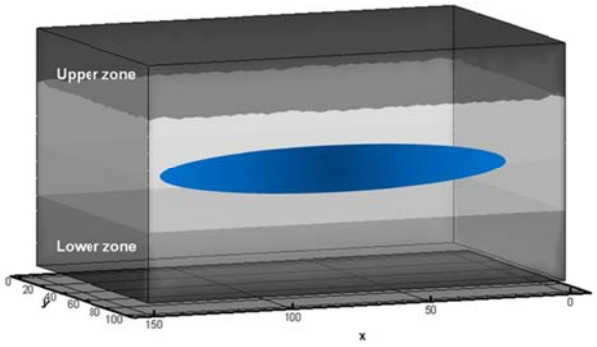

Figure 122. Schematic numerical modeling of a geothermal reservoir with a preexisting cooled fracture.

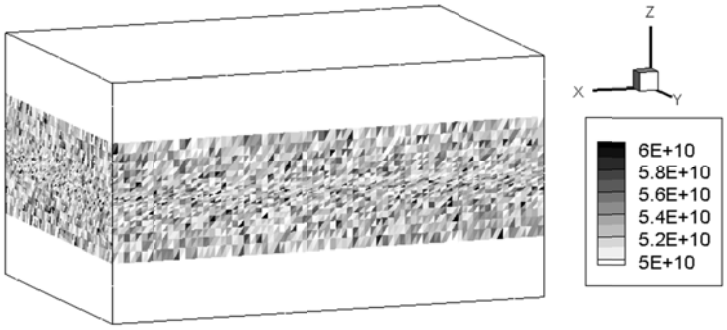

Figure 123. Representation of stiffness heterogeneity (unit=Pa).

Table 24. Material properties and input parameters for Thermal fracturing.

Inputs	Values
Young's Modulus	54.5 GPa
Poisson ratio	0.25
Permeability	0.001 md
Porosity	0.19
Biot's effective stress coefficient	0.966
Thermal diffusivity	1.6×10^{-6} m^2/s
Thermal expansion of solid phase	1.8×10^{-5} K^{-1}
Thermal expansion of fluid phase	3.0×10^{-4} K^{-1}
Num. of element	275,556
Num. of nodes	49,019
Reservoir dimension	150-m×100-m×80-m
Thermal loading	ΔT=90°C

No initial cracks were applied in our FEM model. Crack initiation and propagation were detected by both the damage variable and the maximum principal strain criterion. Pore pressure changes around the fracture surface were influenced by the temperature variation through thermo-poroelastic effects. The cooling zone was extended by the cooling injection over time (Figure 123), the distribution of ε_{zz} and the maximum tensile value of ε_{zz} were concentrated on the fracture surface, and the tensile-strain concentration led to crack growth perpendicular to the preexisting fracture surface (Figure 125). When the heterogeneous reservoir was subjected to temperature change, the fracture volume increased; the amount of the volume change was dependent on the thermal expansion coefficient of the rock. The considerable difference of thermal expansion coefficient between damaged rock and intact rock will increase the effective volumetric stress in the heterogeneous reservoir. The volumetric stress change will initiate thermal fractures and increase a significant positive pore pressure in the thermally induced fractures. And the continuous change of volumetric expansion of the pore space will cause further propagation of the thermal fractures. Figure 126 shows crack initiation at early (a) and later (b) stages of cooling. Clearly, the longer cracks grew mostly in the central area of the main fracture surface. The length of the fracture was limited by the extent of the cooled zone. Tension failure by thermal loading created several cracks perpendicular to the major fracture surface at various locations due to the heterogeneous nature of the rock matrix. . In this simulation, we assumed that the initial pore pressure of the rock matrix was 20 MPa and the pore pressure of the fractured element was 25 MPa. However, the low matrix permeability prevented rapid communication of the hydraulic pressure with the rock matrix until the thermal fractures grew. The pore-pressure distribution at this stage is shown in Figure 127.

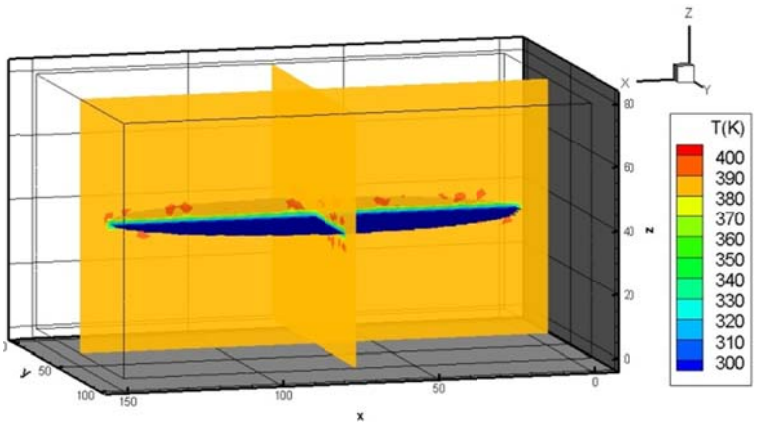

(a) Time = 2 hours

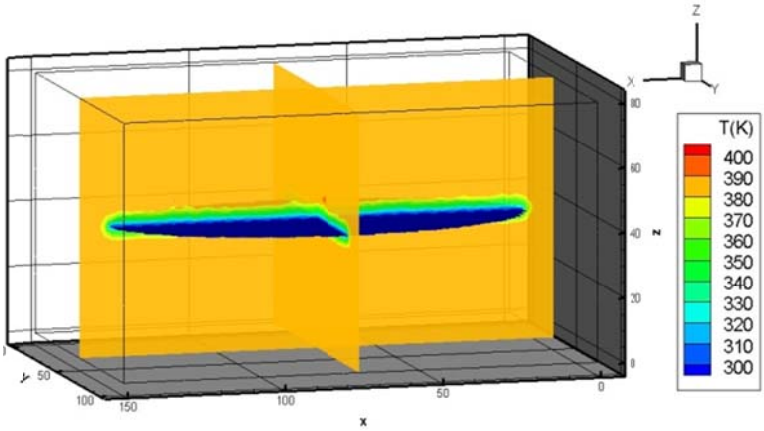

(b) Time = 173 days

Figure 124. Temperature distribution changes by cooling injection.

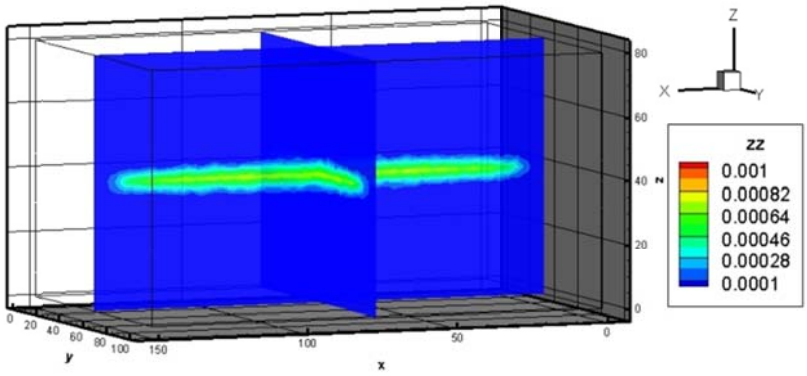

(a) Time = 2 hours

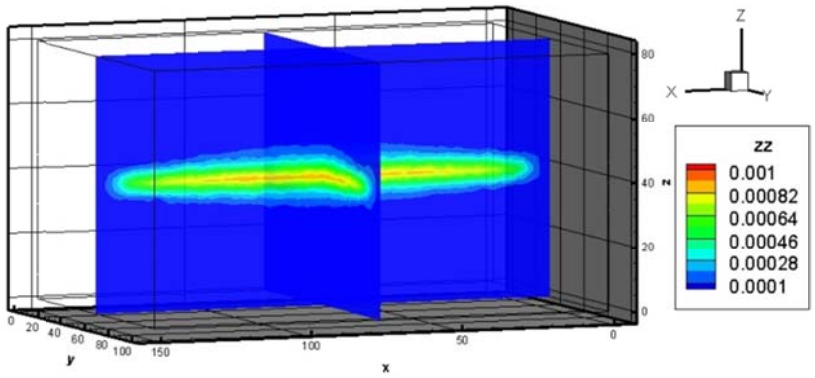

(b) Time = 173 days

Figure 125. Distribution of ε_{zz} changes by cooling.

In this simulation, the minimum element size was about 0.2 m. This means that the minimum crack length growth at each step was at least 0.2 m, so it was difficult to see thermal fracture growth clearly in this coarse mesh. In Figure 128, crack propagation is scattered at early stages, while the spacing of the cracks decreases at the later stages of fracturing. Red spots indicate early crack growth and orange spots indicate later crack growth. Since tensile stresses were concentrated in the center of the fracture surface, cracks nucleated mostly from the interior regions of the fracture surface, and later cracks initiated from the outer boundary of the closed fracture as the tensile region transferred to the edge of the cooled fracture surface. However, the fracture spacing should eventually increase as the fractures interact and some cease to propagate.

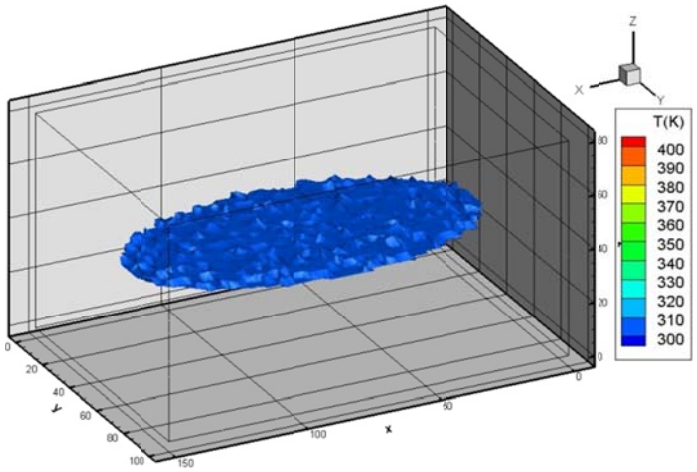

(a) Crack initiation stage

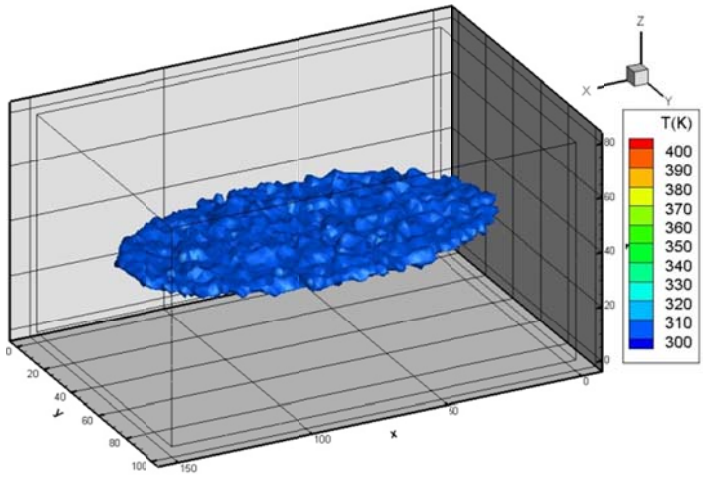

(b) Crack propagation stage

Figure 126. Thermal fracture growth represented by the isothermal surface.

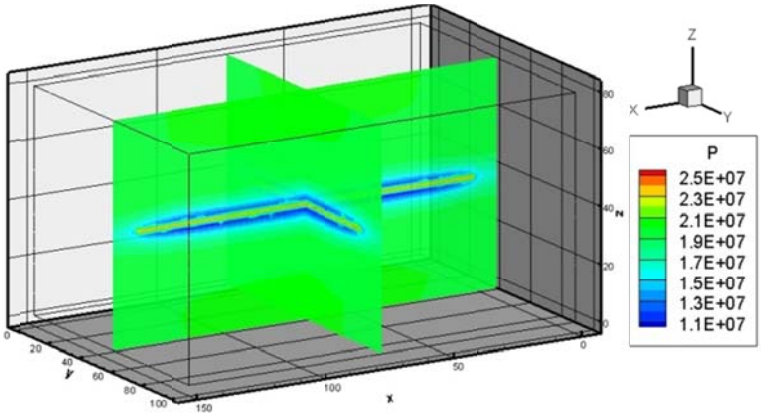

(a) Pore pressure distribution at the early stage of thermal fracturing.

1.

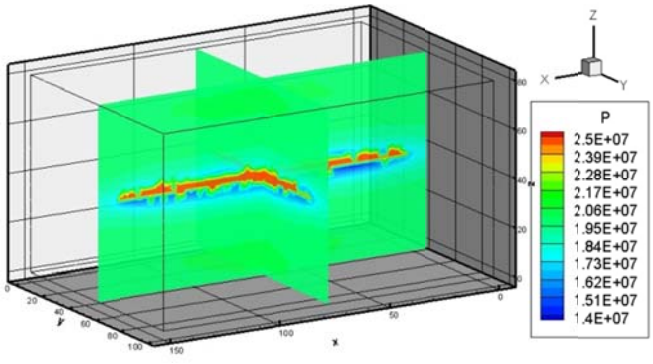

(b) Pore pressure distribution at the later stage of thermal fracturing

Figure 127. Pore pressure distribution during thermal fracturing.

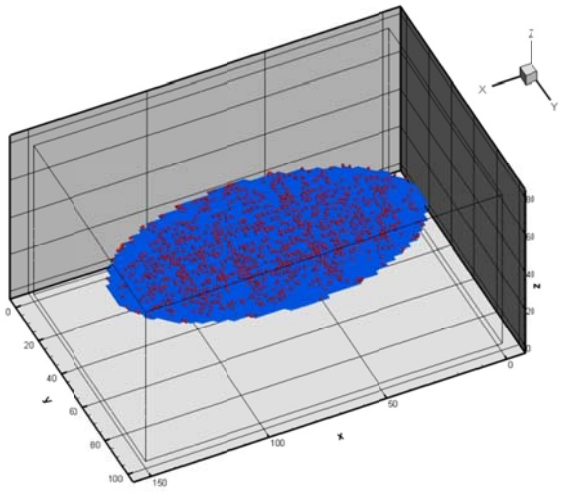

(a) Crack growth at the early stage

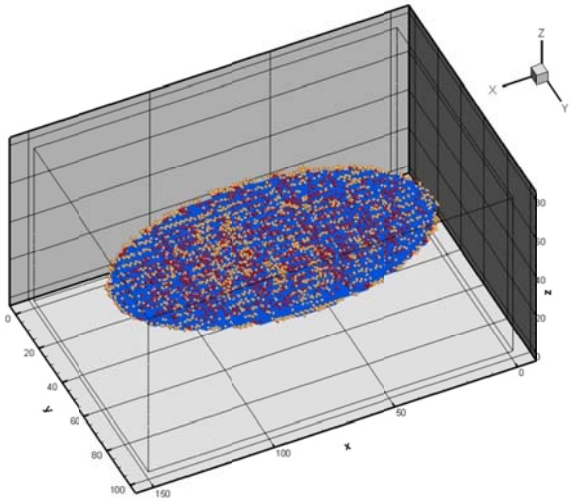

(b) Crack growth at the later stage

Figure 128. Thermal fracturing growth using scatter image in sequential stages.

This evaluation showed that thermal fractures propagate perpendicular to the original natural fracture. Because of heterogeneity, some fractures align differently, but the major trend of thermal fracturing is similar to previous work (Tarasovs and Ghassemi, 2010). Characterization of the thermal fracture spacing is difficult with the current simulations. The major difficulty of thermal fracturing characterization is applying a crack-propagation and branching scheme. In many cases, simulation results produce unstable configurations when propagation is very fast. Thus, it is necessary to carefully determine the step size and the critical criterion for crack propagation and branching. Also, to characterize very small fracture growth from a large fracture surface, a finer mesh is needed; however, a drawback of the finer mesh model is increasing computational cost. For future research, long-term thermal fracturing growth will be simulated and characterized using a finer mesh case.

10. References

Aboustit, B.L., Advani, S.H., and Lee, J.K., 1985. Variational Principles and Finite Element Simulations for Thermo-Elastic consolidation. *Int J Numer Anal Methods Geomech*. 19, 49-69.

Adachi, J., and Detournay, E., 2008. Plain strain propagation of a hydraulic fracture in permeable rock. *Engineering Fracture Mechanics*. 75(16), 4666-4694.

Adachi, J., Siebrits, E., Perice, A., and Desroches, J., 2007. Computer simulation of hydraulic fractues. *International Journal of Rock Mechanics and Mining Sciences*. 44, 739-757.

Adams, M., and Sines, G., 1978. Crack extension from flaws in a brittle material subjected to compression. *Tectonophysics*. 79, 97-118.

Al-Rub, R.K. Abu, and Darabi, M.K., 2010. A straightforward numerical technique for finite element implementation of non-local gradient-dependent continuum damage mechanics theories *International Journal of Theoretical and Applied Multiscale Mechanics*. 1(4), 352-385.

Bai, M., Green, S., Casas, L.A., and Miskimins, J.L., 2006. 3-D Simulation of Large Scale Laboratory Hydraulic Fracturing Tests. *Presented at 41st U.S. Symposium on Rock Mechanics (USRMS)*. Golden, Colorado USA.

Batchelor, G.K., 1967. *An introduction to fluid mechanics*. Cambridge: Cambridge University Press.

Bather, K.J., 1996. *Finite Element Procedure*. New Jersey: Pretice Hall.

Bazant, Z.P., 1986. Mechanics of Distributed Crackings. *Applied Mechanics Review*. 39(5), 675-705.

Bazant, Z.P., and Pijaudier-Cabot, G., 1988. Nonlocal continuum damage, Localization instability and convergence. *Journal of Applied Mechanics*. 55, 287-293.

Bazant, Z.P., and Planas, J., 1997. *Fracture and Size effect in concrete and other quasibrittle material*. Boca Raton: CRC Press.

Belytschko, T., and Black, T., 1999. Elastic crack growth in finite elements with minimal re-meshing. *Int J Numer Methods Eng*. 45, 601-620.

Belytschko, T., Moës, N., Usui, S., and Parimi, C., 2001. Arbitrary discontinuities in finite elements. *Int J Numer Methods Eng*. 50, 993-1013.

Bieniawski, ZT., 1967. Mechanism of brittle fracture of rock part II—experimental studies. *Int J Rock Mech Min Sci Geomech Abstr*. 4, 407-423.

Biot, M.A., 1941. General Theory of Three-Dimensional Consolidation. *Journal of Applied Physics*. 12.

Bobet, A., and Einstein, H.H., 1998. Fracture Coalescence in Rock-type Materials under Uniaxial and Biaxial Compression. *International Journal of Rock Mechanics & Mining Sciences*. 35(7), 863-888.

Boone, T.J., 1989. *Simulation and visualization of hydraulic fracture propagation in poroelastic rock.* Cornell University. Ithaca.

Boone, T.J., and Ingraffea, A.R., 1989. An investigation of poroelastic effects related to hydraulic fracture propagation in rock and stress measurement techniques. in A.W.Khair, (ed.). *Rock Mechanics as a Guide for Efficienct Untilization of Natural Resources*. Rotterdam: Balkema.

Boone, T.J., and Ingraffea, A.R., 1990. A Numerical Procedure for Simulation of Hydraullcally-driven Fracture Propagation in Poroelastic media. *Int J Numer Anal Methods Geomech*. 14, 27-47.

Boone, T.J., Ingraffea, A.R., and Roegiers, J.C., 1991. Simulation of Hydraulic Fracture propagation in Poroelastic Rock with application to stress measurement techniques. *International Journal of Rock Mechanics and Mining Sciences*. 28(1), 1-14.

Börgesson, L., Chijimatsu, M., Fujita, T., Nguyen, T.S., Rutqvist, J., and Jing, L., 2001. Thermo-hydro-mechanical characterization of a bentonite-based buffer material by laboratory tests and numerical back analysis. *International Journal of Rock Mechanics and Mining Sciences*. 38(1), 95-104.

Brace, W.F., 1961. Dependence of fracture strength of rocks on grain size. *Presented at the 4th Symposium on Rock Mechanics*. University Park.

Budiansky, B., and O'Connell, R.J., 1976. Elastic Moduli of a Cracked Solid. *International Journal of Solids and Structures*. 12(2), 81-97.

Camacho, G., and Ortiz, M., 1996. Computational modeling of impact damage in brittle materials. *International Journal of Solids and Structures*. 33, 2899-2938.

Carrier, B., and Granet, S., 2012. Numerical modeling of hydraulic fracture problem in permeable medium using cohesive zone model. *Engineering Fracture Mechanics*. 79, 312-328.

Christian, J.T., 1977. Two- and Three dimensional consolidation. in Desai and Christian, (eds.). *Numerical Methods in Geomechanical Engineering*. London: McGraw-Hill. pp. 399-426.

Cleary, M.P., 1976. *Fundamental solutions for fluid-saturated porous media and application to localized rupture phenomena.* Brown University. Providence.

Cleary, M.P., 1977. Fundamental solutions for a fluid-saturated porous solid. *International Journal of Solids and Structures*. 13(785).

Combarnous, N.A., and Bories, S.A., 1975. Hydrothermal convection in saturated porous media. *Advances in Hydroscience*. 10, 231-307.

Courant, R., 1943. Variational methods for the solution of problems of equilibrium and vibration. *Bulletin of the American Mathematical Society*. 49, 1-43.

Daneshy, A.A., 1974. Hydraulic Fracture Propagation in the Presence of Planes of Weakness. *Presented at SPE-European Meeting*. Amsterdam, Netherlands.

Detournay, E., 2004. Propagation Regimes of Fluid-driven Fractures in Impermeable rocks. *International Journal of Geomechanics*. 4(1), 35-45.

Devloo, P.R.B., Rylo, E.C., and Demkowicz, L., 2002. An HP-adaptive refinement strategy for the finite element method. *Presented at Fifth World Congress on Computational Mechanics*. Viena, Austria.

Dyskin, A.V., Sahouryeh, E., Jewell, R.J., Joer, H., and Ustinov, K.B., 2003. Influence of shape and locations of initial 3-D cracks on their growth in uniaxial compression. *Engineering Fracture Mechanics*. 70(15), 2115-2136.

Dyskin AV, Sahouryeh E, Jewell RJ, Joer H, Ustinov KB, 2003. Influence of shape and locations of initial 3-D cracks on their growth in uniaxial compression. *Engineering Fracture Mechanics*. 70(15), 2115-2136.

Economides, M.J., and Nolte, K.G., 2000. *Reservoir simulation*. Chichester: Wiley.

Erigen, A.C., and Edelen, D.G.B., 1972. On Nonlocal Elasticity. *International Journal for Engineering Science*. 10, 233-248.

Fang, Z., and Harrison, J.P., 2002a. Application of a local degradation model to the analysis of brittle fracture of laboratory scale rock specimens under triaxial conditions. *International Journal of Rock Mechanics and Mining Sciences*. 39, 459-476.

Fang, Z., and Harrison, J.P., 2002b. Development of a local degradation approach to the modeling of brittle fracture in heterogeneous rocks. *International Journal of Rock Mechanics & Mining Sciences*. 39, 443-457.

Fjær, E., Holt, R.M., Horsrud, P., Raaen, A.M., and Risnes, R., 2008. *Petroleum Related Rock Mechanics 2nd Edition*. Elsevier.

Fredrich, J., Evans, B., and Wong, T.F., 1990. Effects of grain size on brittle and semi-brittle strength, implications for micromechanical modelling of failure in compression. *J. Geophys. Res.* 95(B7), 10907-10920.

Garagash, D.I., and Detournay, E., 2000. Near tip processes of a fluid-driven fracture. *Journal of Applied Mechanics*. 67, 183-192.

Geertsma, J., and Klerk, F. de, 1969. A rapid method of predicting width and extent of hydraulic induced fractures. *Journal of Petroleum Technology*. 246, 1571-2581.

Germanovich, L.N., and Dyskin, A.V., 2000. Fracture mechanisms and instability of openings in compression *International Journal of Rock Mechanics and Mining Sciences*. 37(1-2), 263-284.

Ghassemi, A., Cheng, A., Diek, A., and Roegiers, J.C., 2001. A complete plane strain fictitious stress boundary element method for poroelastic media. *Eng Anal Boundary Elements*. 25, 41-48.

Ghassemi, A., and Diek, A., 2003. Linear Chemo-poroelasticity for swelling shales: theory and application. *Journal of Petroluem Science Engineering*. 38, 199-212.

Ghassemi, A., and Suárez-Rivera, R., 2012. *Sustaining Fracture Area and Conductivity of Gas Shale Reservoirs for Enhancing Long-Term Production and Recovery*. Final Report to RPSEA Unconventional Onshore Program Under Contract 08122-48.

Ghassemi, A., Tao, Q., and Diek, A., 2009. Influence of coupled chemo-poro-thermoelastic processes on pore pressure and stress distribution around a wellbore in swelling shale. *Journal of Petroluem Science Engineering*. 67, 57-64.

Graham, S., and Yang, N., 2003. Representative volumes of materials based on microstructural statistics. *Scripta Materialia*. 48, 269-274.

Grebe, JJ., and Stoesser, M., 1935. Increasing crude production 20,000,000 bbl from established fields. *World Petroleum J*. August(473-82).

Hallquist, J.O., 1998. "LS-DYNA theory manual". City: Livemore software technology corporation: Livermore.

Harrison, J.P., and Hudson, J.A., 2000. *Engineering rock mechanics. Part 2 Illustrative workable examples*. Oxford: Pergamon.

Hoek, E., and Brown, E.T., 1990. *Underground excavations in rock*. London: Inst of Min and Metall, Tayer & Francis.

Huang, K., and Zhang, Z.N., 2010. Three dimensional element partition method and numerical simulation for fracture subjected to compressive and shear stress. *Engineering Mechanics*. 27(12), 51-58.

Hughes, J.R., 1987. *The Finite Element Method - Linear Static and Dynamic FEA*. New Jersey: Prentice-hall.

Irwin, G., 1958. *Fracture. Hanbuch der Physik*. Springer.

Jaeger, J.C., Cook, N.G.W., and Zimmermann, R.W., 2007. *Fundamentals of rock mechanics*. London: Blackwell Publishing Ltd.

Jing, L., 2003. A review of techniques, advances and outstanding issues in numerical modelling for rock mechanics and rock engineering. *International Journal of Rock Mechanics & Mining Sciences*. 40, 283-353.

Jing, L., and Hudson, J.A., 2002. Numerical methods in rock mechanics. *International Journal of Rock Mechanics and Mining Sciences*. 39, 409-427.

Jing, L., Stephansson, O., Rutqvist, J., Tsang, C.F., and Kautsky, F., 1993. *DECOVALEX-Mathematical models of coupled T-H-M processes for nuclear waste repositories, Phase I report*. Stockholm.

Jing, L., Stephansson, O., Rutqvist, J., Tsang, C.F., and Kautsky, F., 1995. *DECOVALEX-Mathematical models of coupled T-H-M processes for nuclear waste repositories, Phase II report*. Stockholm.

Jing, L., Stephansson, O., Rutqvist, J., Tsang, C.F., and Kautsky, F., 1996. *DECOVALEX-Mathematical models of coupled T-H-M processes for nuclear waste repositories, Phase III report*. Stockholm.

Jirasek, M., 2004. Non-local damage mechanics with application to concrete. *Revue Française de Génie Civil*. 8(5-6), 683-707.

Jirasek, M., and Zimmermann, T., 1998. Rotating crack model with transition to scalar damage. *Journal of Engineering Mechanics*. 124(3), 277-284.

Kachanov, L.M., 1986. *Introduction to continuum damage mechanics*. The Netherlands: Martinus Nijhoff Publishers.

Khoei, A.R., Azadi, H., and Moslemi, H., 2008. Modeling of crack propagation via an automatic adaptive mesh refinement based on modified superconvergent patch recovery technique. *Engineering Fracture Mechanics*. 75, 2921-2945.

Khristianovic, S., and Zheltov, Y., 1955. Formation of vertical fractures by means of highly viscous fluids. *Presented at 4th World Petroleum Congress*. Rome.

Krajcinovic, D., 1989. Damage Mechanics. *Mechanics of Materials*. 8, 117-197.

Krajcinovic, D., 2000. Damage mechanics: accomplishments, trends and needs. *International Journal of Solids and Structures*. 37, 267-277.

Krajcinovic, D., and Fonseka, G.V., 1981. The Continuous Damage Theory of Brittle material. *Journal of Applied Mechanics*. 48(809-815).

Kunin, I. A., 1968. The Theory of Elastic Media with Microstructure and the Theory of Dislocations. in Kroger, (ed.). *Mechanics of General Continua*. Heidelberg: Springer-Verlag. pp. 321-328.

Kurashige, M., 1989. A thermoelastic theory of fluid-filled porous materials. *International Journal of Solids and Structures*. 25(9), 1039-1052.

Lajtai, E.Z., 1973. Brittle fracture in compression. *International journal of Fracture*. 10, 525-536.

Lamont, N., and Jessen, F.W., 1963. The Effects of Existing Fractures in Rocks on the Extension of Hydraulic Fractures. *SPE*. 419, 203-209.

Lee, S.H., 2011. *Thermo-Poroelastic Modeling of Reservoir Stimulation and Microseismicity using Finite Element Method with Damage Mechanics* Ph.D dissertation. Texas A&M University. College Station.

Lee, S.H., and Ghassemi, A., 2010. Themo-poroelastic analysis of injection-induced rock deformation and damage evolution. *Presented at Stanford Geothermal Workshop*. Stanford University, CA.

Lemaitre, J., 1984. How to use Damage Mechanics. *Nuclear Engineering and Design*. 80(2), 233-245.

Li, Xu, 1998. *Thermoporomechanical Modelling of Inclined Boreholes.* Univeristy of Oklahoma. Norman.

Liu, H.Y., Roquete, M., Kou, S.Q., and Lindqvist, P.A., 2004. Characterization of rock heterogeneity and numerical verification. *Engineering Geology*. 72, 89-119.

Loehner, R., 2001. *Applied CFD techniques: an introduction based on finite element methods*. New York: Wiley.

Lubarda, V., and Krajcinovic, D., 1993. Damage Tensors and the Crack Density Distribution. *International Journal of Solids and Structures*. 30(20), 2859-2877.

Mahabadi, O.K., Randall, N.X., Zong, Z., and Grasselli, G., 2012. A novel approach for micro-scale characterization and modeling of geomaterials incorporating actual material heterogeneity. *Geophys. Res. Lett.* 39(L01303).

Mazars, J., and Pijaudier-Cabot, G., 1989. Continuum Damage Theory: Application to Concrete. *Journal of Engineering Mechanics*. 115(2), 345-365.

McTigue, 1986. Thermoelastic response of fluid-saturated porous rock. *Journal of Geophysical Research*. 91, 9533-9542.

Millard, A., 1996. Short description of CASTEM 2000 and TRIO-EF. *Developments in Geotechnical Engineering*. 79, 559-564.

Min, K.S., and Ghassemi, A., 2011. A Three-dimensional Numerical Analysis of Thermal Fracturing in Rock *Presented at 45th US Rock Mechanics / Geomechanics Symposium* San Francisco.

Min, K.S., Huang, K., and Ghassemi, A., 2011. A study of numerical simulations of mixed-mode fracture propagation in rock *Presented at Thirty-Sixth Workshop on Geothermal Reservoir Engineering*. Stanford University, Stanford, CA USA.

Mogi, K., 2007. *Experimental Rock Mechanics*. London: Taylor & Francis.

Nguyen, V.P., Rabczuk, T., Bordas, S., and Duflot, M., 2008. Meshless methods: A review and computer implementation aspects. *Mathematics and Computers in Simulation*. 79, 763-813.

Noorishad, J., and Tsang, C.F., 1996. Coupled Thermohydroelasticity Phenomena in variably saturated fractured porous rock - Formation and Numerical solution. in Stephansson, Jing, and Tsang, (eds.). *Coupled Thermo-Hydro-Mechanical processes of Fractured Media*. Amsterdam: Elsevier Science.

Noorishad, J., Tsang, C.F., and Witherspoon, P.A., 1992. Theoretical and field studies of coupled hydromechanical behaviour of fractured rocks—1. Development and verification of a numerical simulator. *International Journal of Rock Mechanics and Mining Sciences*. 29(4), 401-409.

Nordgren, R., 1972. Propagation of vertical hydraulic fractures. *Journal of Petroleum Technology*. 253(306-314).

Palciauskas, V.V., and Domenico, P.A., 1982. Characterization of Drained and Undrained Response of Thermally Loaded Respository Rocks. *Water Resources Research*. 18, 281-290.

Pan, E., and Maier, G., 1997. A symmetric integral approach to transient poroelastic analysis. *Computation Mechanics*. 19, 169-178.

Pande, G.N., Beer, G., and Williams, J.R., 1990. *Numerical methods in rock mechanics*. Chichester: Wiley.

Pandolfi, A., Guduru, P.R., Ortiz, M., and Rosakis, A.J., 2000. Three dimensional cohesive-element analysis and experiments of dynamic fracture in C300 steel. *International Journal of Solids and Structures*. 37, 3733-3760.

Papanastasious, P., 1997. The influence of plasticity in hydraulic fracturing. *International Journal of Fracture*. 84, 61-79.

Paris, P., and Erdogan, F., 1963. A critical analysis of crack propagation laws. *Journal of Basic Engineering*. 85, 528-534.

Park, K., Pereira, J.P., Duarte, C.A., and Paulino, G.H., 2009. Integration of singular enrichment functions in the generalized/extended finite element method for three-dimensional problem. *International Journal for Numerical Methods in Engineering*. 78, 1220-1257.

Perkins, T., and Kern, L., 1961. Widths of hydraulic fractures. *Journal of Petroleum Technology*. 222(937-949).

Picard, Emile, 1890. *Jour. de Math*. 4(6), 145-210.

Pijaudier-Cabot, G., and Bazant, Z.P., 1987. Nonlocal Damage Theory. *Journal of Engineering Mechanics*. 113(10).

Pratt, M., 1982. *Thermal Recovery*. SPE Monograph.

Rabczuk, T., Bordas, S., and Zi, Goangseup, 2007. A three-dimensional meshfree method for continuous multiple-crack initiation, propagation and junction in statics and dynamics. *Computation Mechanics*. 40, 473-495.

Rabczuk, T., Bordas, S., and Zi, Goangseup, 2008. A three-dimensional modelling of crack growth using partition of unity methods. *Computers and Structures*.

Regehr, M., 2012. A Reservoir and Geomechanical Model of the Colorado Shale, Western Canadian Sedimentary Basin. *Presented at SPWLA topical conference*.

Renshaw, C.E., and Pollard, D.D., 1994. Numerical simulation of fracture set formation: a fracture mechanics model consistent with experimental observations. *Journal of Geophysical Research*. 99, 9359-9372.

Rice, J.R., and Cleary, M.P., 1976. Some basic stress-diffusion solutions for fluid saturated elastic porous media with compressible constituents. *REVIEWS OF GEOPHYSICS*. 14, 227-241.

Rutqvist, J., Börgesson, L., Chijimatsu, M., Kobayashi, A., Jing, L., Nguyen, T.S., Noorishad, J., and Tsang, C.F., 2001. Thermohydro-mechanics of partially saturated geological media: governing equations and formulation of four finite element models. *International Journal of Rock Mechanics and Mining Sciences*. 38(1), 105-127.

Sagong, M., 2001. *The Study on the Fracture of Multiple Flaw Specimens.* Purdue University. West Lafayette, IN USA.

Samieh, AM, and Wong, RCK, 1997. Deformation of Athabasca oil sand at low e!ective stresses under varying boundary conditions. *Canadian Geotechnical Journal*. 34, 985-990.

Sarris, E., and Papanastasiou, P., 2012. Modeling of Hydraulic Fracturing in a Poroelastic Cohesive Formation. *International Journal of Geomechanics*. 12, 160-167.

Sarris, E., and Papanastasious, P., 2011. The influence of the cohesive process zone in hydraulic fracturing modelling. *International journal of Fracture*. 167, 33-45.

Schrefler, B.A., 2001. Computer modelling in environmental geomechanics. *Computers and Structures*. 79, 2209-2223.

Settari, A., 1989. Physics and Modeling of Thermal Flow and Solid Mechanics in Unconsolidated Porous Media. *Presented at SPE Symposium On Reservoir Simulation*. Houston, Texas.

Skempton, A.W., 1954. The pore pressure coefficients a and b. *Geotechnique*. 4, 143-147.

Smith, M.B., and Shlyapobersky, J.W., 2000. Basics of Hydraulic Fracturing. in Economides and Nolte, (eds.). *Reservoir Stimulation*. Chichester, UK: John Wiley & Sons Ltd. pp. 5-1,5-29.

Sneddon, I. N., 1946. The Distribution of Stress in the Neighbourhood of a Crack in an Elastic Solid. *Proceedings of the Royal Society of London. Series A, Mathematical and Physical*. 187(1009), 229-260.

Sneddon, I.N., and Elliott, H.A., 1946. The opening of a Griffith crack under internal pressure. *Applied Mechanics Review*. 4, 262-268.

Song, J.-H., Wang, H., and Belytschko, T., 2008. A comparative study on finite element methods for dynamic fracture. *Computation Mechanics*. 42, 239-250.

Stephansson, O., Jing, L., and Tsang, C.F., 1996. *Coupled Thermo-Hydro-Mechanical Processes of Fractured Media*. Elsevier Science.

Taleghani, A.D., 2009. *Analysis of hydraulic fracture propagation in fractured reservoirs: an improved model for the interaction between induced and natural fractures.* University of Texas at Austin. Austin.

Tang, C.A., and Hudson, J.A., 2011. *Rock Failure Mechanism*. London: Tayler & Francis.

Tang, C.A., Jiu, H., Lee, PKK., Tsui, Y., and Tham, LG., 2000. Numerical studies of the influence of microstructure on rock failure in uniaxial compression—part I: effect of heterogeneity. *Int J Rock Mech Min Sci*. 37, 555-569.

Tang, C.A., Tham LG., Lee PKK., Yang TH., and Li LC., 2002. Coupled Analysis of flow, stress and damage (FSD) in rock failure. *International Journal of Rock Mechanics & Mining Sciences*. 39, 1231-47.

Tarasovs, S., and Ghassemi, A., 2010. A Study of Propagation of Cooled Cracks in a Geothermal Reservoir. *Presented at Geothermal Resources Council Annual Meeting*. Sacramento, CA.

Terzaghi, K., 1923. Die berechnug der Durchlässigkeitsziffer des Tones aus dem Verlauf der hydrodynamischen Spannungserscheinungen. *Sitzungsber Akad Wiss Math-Naturwiss Section IIa*. 132(3/4), 125-138.

Tester, J.W., Murphy, H.D., Grlgsby, C.O., Potter, R.M., and Robinson, B.A., 1989. Fractured Geothermal Reservoir Growth Induced by Heat Extraction. *SPE Reservoir Engineering*. 4(1), 97-104.

Teufel, L.W., and Clark, J.A., 1984. Hydraulic Fracture Propagation in Layered Rock: Experimental Studies of Fracture Containment. *SPE* (9878), 19-32.

Tsang, C.F., 1987. *Coupled processes associated with nuclear waste repositories*. New York: Academic Press.

Tsang, C.F., 1991. Coupled hydromechanical-thermochemical processes in rock fractures. *REVIEWS OF GEOPHYSICS*. 29(4), 537-551.

Tsang, C.F., Stephansson, O., Kautsky, F., and Jing, L., 2004. Coupled THM processes in geological systems and the DECOVALEX project. in Stephansson, Hudson, and Jing, (eds.). *Coupled Thermo-Hydro-Mechanical-Chemical Processes in Geo-systems*. Oxford: Elsevier.

Voyiadjis, G.Z., and Kattan, P.I., 2009. A comparative study of Damage variables in Continuum Damage Mechanics. *International Journal of Damage Mechanics*. 18(315).

Wang, J., Jung, W., and Ghassemi, A., 2012a. Deformation and Failure Properties of Newberry Welded Tuff. *Presented at 46th US Rock Mechanics / Geomechanics Symposium*. Chicago, IL.

Wang, J., Jung, W., and Ghassemi, A., 2012b. *Petrophysical and Rock Mechanical Properties of Rock from Newberry*. Department of Petroleum Engineering at Texas A&M University DOE annual report.

Wang, J.S.Y., and Narasimhan, T.N., 1985. Hydrologic mechanisms governing fluid flow in a partially saturated, fractured, porous medium. *Water Resources Research*. 21(1861).

Wang, YC., Yin, XC., Ke, FJ., Xia, MF., and Peng, KY., 2000. Numerical simulation of rock failure and earthquake process on mesoscopic scale. *Pure Appl Geophys*. 157, 1905-1928.

Weibull, W., 1939. A statistical theory of the strength of materials. *Ing Vetenskaps Akad Handl*. 151, 5-44.

Weibull, W., 1951. A statistical distribution function of wide applicability. *Journal of Applied Mechanics*. 18, 293-7.

Witherspoon, P.A., Wang, J.S.Y., Iwai, K., and Gale, J.E., 1980. Validity of Cubic law for Fluid flow in a deformable rock fracture. *Water Resources Research*. 16(6), 1016-1024.

Wong, L.N.Y., and Einstein, H.H., 2009. Systematic evaluation of cracking behavior in specimens containing single flaws under uniaxial compression. *International Journal of Rock Mechanics & Mining Sciences*. 46, 239-249.

Wong, T., H., Robina., Wong, C., Chau, K.T., and Tang, C.A., 2006. Microcrack statistics, Weibull distribution and micromechanical modeling of compressive failure in rock. *Mechanics of Materials*. 38, 664-681.

Wulf, J., Schamuder, S., and Fishmeister, H.F., 1993. Finite element modelling of crack propagation in ductile fracture. *Computational Materical Science*. 1, 297-301.

Xu, X-P., and Needleman, 2006. Numerical simulation of fast crack growth in brittle solids. *Journal of Mechanics, Physics, Solids*. 42, 1397-1434.

Yamamoto, K., Gutierrez, M., Shimamoto, T., and Maezumi, S., 2000. Verification of a 3D Hydraulic Fracturing Model against a Field case. *Presented at SPE/DOE Improved Oil Recovery Symposium*. Tulsa.

Yuan, S.C., and Harrison, J.P., 2005. Development of a hydro-mechanical local degradation approach and its application to modelling fluid flow during progressive fracturing of heterogeneous rocks. *International Journal of Rock Mechanics and Mining Sciences*. 42, 961-984.

Zhang, Z.N., and Chen, Y., 2008. Simulation of fracture propagation subjected to compressive and shear stress field using virtual multidimensional internal bonds. *International Journal of Rock Mechanics & Mining Sciences*.

Zhou, X., and Ghassemi, A., 2009. Finite Element analysis of coupled chemo-poro-thermo-mechanical effects around a wellbore in swelling shale. *International Journal of Rock Mechanics & Mining Sciences*. 46, 769-778.

Zi, Goangseup, and Belytschko, T., 2003. New crack-tip elements for XFEM and applications to cohesive cracks. *International Journal for Numerical Method in Engineering*. 57, 2221-2240.

Zienkiewicz, O.C., and Taylor, R.L., 1967. *The Finite Element Method for Solid and Structural Mechanics*. London: McGraw-Hill.

Zoback, M.D., Rummel, F., Jung, R., and Raleigh, C.B., 1977. Laboratory Hydraulic Fracturing experiments in Intact and Pre-fractured rock. *International Journal of Rock Mechanics*. 14, 49-58.

Chapter 3. SUMMARY AND CONCULUSIONS

The objective of this work was to develop advanced numerical models for better understanding of brittle fracture process including mixed fracture propagation and hydraulic fracturing treatment considering rock heterogeneity. The research work carried out included numerical description and interpretation of rock properties and fracture patterns, and analysis of triaxial experiments; improved understanding of complex fractures affected by brittle/ductile behavior of rock; 2D and 3D hydraulic fracturing models for laboratory block experiments and its application to larger-scale problem

Hydraulic fracturing process was modeled using fluid-solid interaction analysis incorporating fluid flow, fracture mechanics, rock deformation and moving boundary problem. The hydraulic fracture propagation and moving boundary scheme were modeled using the VMIB and damage mechanics with the element splitting technique applied to three-node tetrahedron and four-node tetrahedron elements. The 3D hydraulic fracturing models were validated using large scale hydraulic fracture laboratory experiments.

Numerical simulation of 3D fracture propagation in brittle rock was studied using the VMIB evolution function at the micro scale. The results showed that typical features of 3D tensile and compressive fracture propagation can be well represented. Especially, simulation results by 3D VMIB and 3D EPM demonstrated the propagation of Mode III fracture. Such simulations improve understanding of 3D fracture propagation mechanism and provide a means of designing multiple hydraulic fractures for reservoir stimulation. Furthermore, 3D simulation of multiple hydraulic fractures showed good agreement with the results of theoretical analysis. In addition, an interesting manner of hydraulic fracture propagation in Mode III has been observed showing the formation of multiple fractures from the original crack.

The influences of coupled processes (poroelastic and thermoelastic) on fracture propagation were simulated using VMIB and Continuum Damage Mechanics (CDM) along with the discontinuous crack propagation algorithm. Numerical simulation of 3D thermal fracture propagation in brittle rock was studied using the VMIB model combined with 3D EPM method. In VMIB theory, the macro behavior of material is attributed to the strength evolution of micro virtual bonds subjected to applied loads. With this hypothesis, thermally induced failure of rock was simulated in this work, showing the advantages of VMIB in simulating the failure process. Nonlinearities of mechanical behavior and thermal parameters of the rock material were captured by introducing a nonlinear VMIB constitutive model. A 3D EPM associated with thermal parameters modification for fractured elements provided a simple way to represent the pre-existing fracture in a structured mesh. The advantage of the 3D EPM is that it is unnecessary to mesh the fractures and thus, remeshing is not needed during fracture propagation. This is a major convenience especially for multiple fractures in complex geometry.

Several examples were provided to test the functionality of the model and to provide evidence for its verification. Test I showed reasonable results for the nonlinear thermal deformation and fracture of rock when subjected to uniform cooling. Test II which was designed to check the model's ability to treat a randomly distributed set of fractures with a structured mesh was also successful, and illustrated the interaction and growth of fractures in a cluster under thermal loading. The final example illustrated the behavior of fractures emanating from a wellbore and showed the model captures the impact of cooling and the in-situ stress on the propagation patterns.

Special algorithms were developed and used to address the mesh-sensitivity of the VMIB approach. In particular, the fracture energy conservation was considered in the proposed VMIB model. Through incorporation of the fracture energy in the bond evolution function, the mesh-size sensitivity was minimized for the element size simulated in this work. The model served as a mechanical constitutive relation in a fully 3D hydraulic fracturing model to simulate laboratory scale experiments. Taking advantage of 3D EPM, the pre-existing fractures were treated as "joints" so that the contact and reopening behaviors were captured when interacting with a propagating fracture. For each case, curved and parallel growth of fractures under different confining stresses was captured with reasonable agreement with experimental observations. The critical element size, however, limits the maximum size that satisfies fracture energy conservation and the effectiveness of the model. Therefore, it limits the size of simulation domains to small and possibly meso-scale.

Continuum Damage Mechanics (CDM) was also used to describe the inelastic response of micro-crack growths and the macroscopic fracture (in 2D and 3D). Damage mechanics allowed representation of both micro and macro crack propagation and severely damaged zone. The brittle failure mechanism of heterogeneous rock was studied using CDM within FEM formulation. Generally, rock fractures in mixed mode which requires complex criteria for predicting the failure/fracture; however theoretical approaches are not sufficient to do it. So, simplified constitutive relations were proposed to describe the general strain-softening behavior corresponding with confining pressure, although it is more ideal to use different constitutive relations for different types of material to give a more realistic physical interpretation. In addition, an isotropic damage variable was used to represent stiffness degradation and crack initiation/propagation for simplicity of numerical implementation. The elastic/brittle constitutive model of the brittle rock was developed and simulated to study the influence of confining pressure through calibration with the multistage triaxial experiments. The numerical results showed a reasonable approximation for the stress-strain relations and fractured behavior with core samples after the triaxial test. Also, the three basic types of mechanical deformation processes—reversible elastic, irreversible inelastic, and irreversible friction—were generally captured. The elastic-brittle constitutive assumption is suitable for rock material such as granite, but not for Newberry tuff, because as confining pressure increases tuff becomes more ductile and the fracture plane is affected. The model did not include plastic hardening deformation, so the stress-strain relation did not perfectly match laboratory experiment results. Thus, to consider ductile behavior, it is necessary to introduce plasticity into the elastic/brittle constitutive model, along with an additional damage variable that could represent the plastic hardening behavior. Rock heterogeneity was represented by spatial distribution curves using Weibull function.

Numerical simulations of mixed modes fracture propagation in brittle rock was studied using 2D and 3D wing-crack models. In 2D simulation, mixed modes fracture of Mode I and II and the influence of confinement on the crack growth were studied. The dominant failure mechanism depends on the confinement and the local stress conditions determine the direction of crack propagation. In 3D simulations, a wing crack has initially grown in the major compression direction, but its direction changed due to the presence of the free surface of the 3D specimen. In 2D case, since there is no Mode III fractures, the secondary crack could grow farther toward the compression direction, but 3D secondary crack growth from the pre-existing circular crack involves mixed modes (II and III), so that 3D fracture propagation becomes more complicated. It is necessary to further study 3D crack propagation to improve understanding of the fracture propagation mechanism for designing multiple hydraulic fractures.

Moreover, hydraulic fracture propagation in permeable rock was simulated to investigate the influence of the reservoir heterogeneity and the injection rate. The reservoir heterogeneity is a critical factor because both mechanical deformation and fluid flow behavior are affected by rock heterogeneity. Especially, high heterogeneity increases leakoff volume and reduces the injectivity of fracturing fluid. When the rock was highly heterogeneous, the injection efficiency was decreased to 0.57. When the injection rate was increased by 6 times, the injection efficiency decreased very little.

3D hydraulic fracturing modeling of laboratory block experiment was simulated using the coupled fluid-solid interaction analysis. This problem was very challenging to interpret via numerical modeling, because of numerous complexities such as the moving boundary issue, dynamic crack growth, and complex geometry. Therefore, the hydraulic fracture propagation problem was treated in a quasi-static manner. The hydraulic fracturing process was divided into three coupled processes of fluid flow, hydromechanical deformation, and fracture propagation. The fluid flow inside fractures was modeled using the lubrication equation, and the hydromechanical deformation of rock was solved using fully coupled poroelastic analysis. Fracture propagation was modeled as quasi-static crack growth. A coupled iterative algorithm was introduced to solve the coupled rock deformation and fracture pressure. The coupled iterative solution for the fluid-driven fracture propagation problem is very difficult to construct, because of the nonlinear relationship of rock deformation and fluid flow in fractures. Hence, the rock deformation, computed by a fully coupled THM analysis was iteratively coupled with the fluid flow behavior, which was computed by using the lubrication equation. Numerical study of the coupled hydraulic fracturing simulation was successfully validated using a large-scale laboratory hydraulic fracturing experiment performed by TerraTek.

3.1 Publications

1. Zhang, Z., and Ghassemi, A. 2011. Simulation of hydraulic fracture propagation near a natural fracture using virtual multidimensional internal bonds. Int. J. Num. Anal. Methods. Geomech. 35 (4), 480–495.
2. Huang, K., and Ghassemi , A. 2016. Modeling 3D thermal fracture propagation by transient cooling using virtual multidimensional internal bonds. Int. J. Num. and Anal. Methods in Geomech. doi: 10.1002/nag.2526.
3. Zhang, Z. Ding, J., Ghassemi, A., Ge, X. 2015. A hyperelastic-bilinear potential for lattice model with fracture energy conservation. Engineering Fracture Mechanics. 142, 220–235.
4. Tarasovs, S. and Ghassemi, A. 2014. Self-similarity and scaling of thermal shock fractures. Physical Review E 90 (1), 012403-1-6.
5. Huang, K., Zhang, Z., Ghassemi, A. 2013. Modeling three-dimensional hydraulic fracture propagation using virtual multidimensional internal bonds. Int. J. Numer. Anal. Meth. Geomech. 37:2021–2038
6. Sesetty, V., Ghassemi, A. 2012. Modeling and analysis of stimulation for fracture network generation, Proc. 37th Stanford Geothermal Workshop on Geothermal Reservoir Engineering, Stanford University, California.
7. Min K.S., Ghassemi, A. 2012. Simulation of fracture clusters in unconventional reservoir using fully coupled Thermo-Hydro-Mechanical FEM analysis. 46th ARMA Conf., Chicago, Illinois, USA.
8. Huang, K. and Ghassemi, A. 2012. Modeling 3D hydraulic fracture propagation and thermal fracturing using virtual multidimensional internal bonds. Proc., 37th Workshop on Geothermal Reservoir Engineering, Stanford University, CA.

9. Min K.S., Huang K., Ghassemi A. 2011. A Study of numerical simulations of mixed-mode fracture propagation in rock. Proc, 36th Workshop on Geothermal Reservoir Engineering, Stanford University, 2011.
10. Min, K.S., Huang, K., and Ghassemi, A. 2011. A study of numerical simulations of mixed-mode fracture propagation in rock. 36th Stanford Geothermal Workshop, Stanford, California, USA
11. Huang, J., and Ghassemi, A. 2011. Poroelastic analysis of gas production from shale. 45th ARMA Conf., San Francisco, California, USA.
12. Min K.S., Ghassemi A. 2011. Three-dimensional numerical analysis of thermal fracturing in rock. 45th ARMA Conf., San Francisco, California, USA
13. Zhang, Z.Z., and Ghassemi, A. 2010. Three-dimensional fracture simulation using the virtual multidimensional internal bond. Proc. 44th US Rock Mechanics Symp., Salt Lake City, UT.
14. Zhennan, Z., Ghassemi, A. 2010. Three-dimensional fracture simulation using virtual multidimensional internal bond. Proc. 44th US Rock Mech. Symposium, Salt Lake City.
15. Min, K.S., Zhennan Z., and Ghassemi, A. 2010. Hydraulic fracturing propagation in heterogeneous rock using the VMIB method. Proc. 35th Workshop on Geothermal Res. Engrg. Stanford University, Ca.
16. Min, K.S., Zhennan Z., and Ghassemi, A. 2010. Numerical Analysis of Multiple Fracture Propagation in Heterogeneous Rock. 44th US Rock Mechanics Symposium and 5th U.S.-Canada Rock Mechanics Symp. held in Salt Lake City, UT June 27–30, 2010.